BIOPHYSICAL PROBES OF IRON METABOLISM IN YEAST CELLS, MITOCHONDRIA, AND MOUSE BRAINS

A Dissertation

by

GREGORY PAUL HOLMES-HAMPTON

Submitted to the Office of Graduate Studies of
Texas A&M University
in partial fulfillment of the requirements for the degree of

DOCTOR OF PHILOSOPHY

August 2012

Major Subject: Chemistry

Biophysical Probes of Iron Metabolism in Yeast Cells, Mitochondria, and Mouse Brains

BIOPHYSICAL PROBES OF IRON METABOLISM IN YEAST CELLS, MITOCHONDRIA, AND MOUSE BRAINS

A Dissertation

by

GREGORY PAUL HOLMES-HAMPTON

Submitted to the Office of Graduate Studies of
Texas A&M University
in partial fulfillment of the requirements for the degree of

DOCTOR OF PHILOSOPHY

Approved by:

Chair of Committee,	Paul A. Lindahl
Committee Members,	Frank M. Raushel
	Paul S. Cremer
	Christian Hilty
Head of Department,	David H. Russell

August 2012

Major Subject: Chemistry

ABSTRACT

Biophysical Probes of Iron Metabolism in Yeast Cells, Mitochondria, and Mouse Brains. (August 2012)

Gregory Paul Holmes-Hampton, B.S., Illinois State University

Chair of Advisory Committee: Dr. Paul A. Lindahl

Iron is essential in nearly all organisms. It is a cofactor in many proteins and enzymes. This transition metal can also be toxic because it participates in reactions which produce reactive oxygen species. To avoid these toxic effects while still being used for essential processes, the cell must regulate tightly iron import, metabolism, trafficking, and homeostasis. These processes were studied using biophysical methods centered on Mössbauer spectroscopy supplemented by electron paramagnetic resonance, electronic absorption spectroscopy, and inductively coupled plasma mass spectrometry. This integrated biophysical approach was applied to yeast cells, isolated yeast mitochondria, and mouse brains. We determined the concentration of Fe, and the proportion of that Fe present as iron-sulfur clusters, heme centers, mononuclear nonheme centers, and as Fe^{3+} oxyhydroxide (phosphate) nanoparticles for each system.

In yeast, the dependence of metabolic mode of growth and iron in the growth medium on this distribution was studied. Approximately three-quarters of the iron in fermenting cells was located in vacuoles, where it was present as high-spin mononuclear Fe^{3+} species with rhombic symmetry. The remaining quarter was present in the

mitochondria. In fermenting mitochondria 4 distinct species of iron were observed, including $[Fe_4S_4]^{2+}$ clusters and low-spin Fe^{2+} hemes arising from respiratory complexes, non-heme high spin (NHHS) Fe^{2+} species, high spin nonheme Fe^{3+} species, and nanoparticles. These distributions (in both the cells and mitochondria) change when the cells are grown on iron deficient medium but remained relatively unaltered as iron in the growth medium was increased. Respiring cells had less Fe associated with vacuoles, and more Fe present as HS Fe^{2+}. Respiring mitochondria contain more $[Fe_4S_4]^{2+}$ clusters and low-spin Fe^{2+} hemes, more S = ½ $[Fe_2S_2]^{1+}$ clusters, and less NHHS Fe^{2+}, HS Fe^{3+} species and Fe^{3+} nanoparticles. These changes were rationalized by assuming that the NHHS Fe^{2+} and Fe^{3+} species, and the nanoparticles were in equilibrium within the matrix of the mitochondria, and that the Fe^{2+} species served as feedstock for the synthesis of iron-sulfur clusters and heme centers.

The iron in the mouse brain consisted mostly of $[Fe_4S_4]^{2+}$ clusters and Fe^{2+} hemes from mitochondria respiratory complexes, and of ferritin, an Fe storage protein complex. NHHS Fe^{2+} and Fe^{3+} species were also observed. The ratio of stored Fe to mitochondrial Fe was sensitive to age. The brains of prenatal animals were dominated by ferritin. Following birth up to the first 4 weeks of life, there was an increase in mitochondrial Fe and a decline of ferritin Fe. Beyond 4 weeks up to 58 weeks, levels of ferritin increased and mitochondrial Fe remained constant. The brains of mice fed an Fe-deficient diet were also studied; most of the Fe in these brains was present as mitochondrial Fe, with little stored as ferritin. A model was developed to explain these changes.

ACKNOWLEDGEMENTS

I would first like to acknowledge my advisor, Dr. Paul A. Lindahl. The countless discussions we have had over the years have been not only helpful but insightful. It has truly been an honor to work in your lab and get to learn so many new techniques and interact with so many people. I am also grateful for the numerous opportunities you have facilitated in my young career including manuscript preparation, grant writing, and participation in conferences both as a poster presenter and as an oral presenter. Your enthusiasm in both teaching and research are truly an inspiration.

I would also like to acknowledge my committee members. I am grateful to Dr. Frank Raushel for the opportunity to use biophysical methods on an enzyme, adenine deaminase. The rich collaborative efforts have been insightful in using these techniques on additional systems to provide mechanistic details for a single protein as opposed to the systems-level analysis presented in this dissertation. I am also grateful to all my committee members including Dr. Paul Cremer and Dr. Christian Hilty in addition to Dr. Raushel for the rich discussions we have had concerning my research.

I am also grateful to a number of past members of the Lindahl lab. Chief among these are Dr. Ren Miao and Dr. Jessica Garber Morales. At the time I joined the lab these two were the only graduate students and I learned a lot from both of them. They also helped provide a fun and enjoyable work environment. I am also grateful to numerous post-doctoral researchers that have been part of the laboratory while I have

been here. In particular I would like to acknowledge Dr. Ivan Surovstev and Dr. Marco Villa.

I would also like to acknowledge the current members of the lab for their contributions over the years and facilitating an enjoyable work environment. I am grateful to Allison Cockrell, Sean McCormick, Nema Jhurry, Jink-Yu Park, and Dr. Mrinmoy Chakrabarti. I have truly enjoyed working with all of you and appreciate insightful conversations I have shared with all of you. I would also like to thank Dr. Lora Lindahl, she has been instrumental in the transition from studying iron metabolism in yeast cells to studying these processes in mice.

I am also grateful to those we have collaborated with over the years. Among these are Dr. Eckard Münck (Carnegie Mellon University) and Yisong "Alex" Guo, their assistance in Mössbauer spectral analysis has been helpful and a great learning experience. I am also grateful to Dr. Jerry Kaplan (University of Utah) for providing several yeast strains and antibodies over the years. Also I am grateful to Siddhesh Kamat from the Raushel lab. Without him the collaborations on the adenine deaminase project would not be possible. Finally, I am grateful to Dr. Louise Abbott (Texas A&M University) for her assistance along with Dr. Lora Lindahl in the transition to studying higher eukaryotes, mice.

I am grateful to the entire support staff here at Texas A&M University but in particular I would like to mention Will Seward from the machine shop. Will's expertise has been heavily utilized by not only me over the years but the entire lab. Without him

building parts each week (although at times it seems each day), we could not have done many of the experiments presented here.

I am also grateful to my family and friends. It has been tough being away from home but the love and pride of my family has been helpful toward me achieving this goal. The strength of my grandfather has always been a true inspiration to me and I am thankful to have such a role model in my life. I am also thankful to the many people I am proud to call my friends your help and support have always been appreciated. In particular I would like to acknowledge Morgan Shirley for putting up with me. I am especially thankful for the love and support she has shown me over the last 4 years.

Finally I am grateful for the funding agencies that have facilitated the research over the years. I am grateful to the National Institutes of Health and the Robert A. Welch Foundation. In particular am thankful to the NIH for funds which allowed me to participate in the Chemistry Biology Interface training program.

NOMENCLATURE

Aft1-1^{up}	a yeast strain in which the transcription factor Aft1p constitutively upregulates iron regulon genes, regardless of Fe_{medium} concentration
BPS	Bathophenanthrolinesulfonate
Ccc1p	Fe importer on the vacuolar membrane
Compound 5	a fluorescent compound described in *(228)*
CPY	carboxypeptidase Y
DDDI	double-distilled and deionized
DTT	Dithiothreitol
EPR	electron paramagnetic resonance
Fe_{medium}	iron contained in the growth medium
Gal-YAH1	a yeast strain in which expression of the ferredoxin Yah1 is controlled by the carbon source in the growth medium (galactose promotes expression; glucose represses it)
HS	high spin
ICP-MS	inductively coupled plasma mass spectrometry

IM	inner membrane of the mitochondria
ISC	iron−sulfur cluster
LS	low spin
Mrs3p and Mrs4p	Fe importers on the IM
ND	not determined
PGK	phosphoglycerate kinase
ROS	reactive oxygen species
TMG	trace metal grade
WT	wild type
YPD	standard rich medium containing glucose
δ	isomer shift
ΔE_Q	quadrupole splitting

TABLE OF CONTENTS

CHAPTER Page

CHAPTER Page

CHAPTER Page

Page

LIST OF FIGURES

LIST OF TABLES

Page

CHAPTER I

INTRODUCTION AND LITERATURE REVIEW

Introduction

Iron is an essential element for numerous aspects of cell biology. This transition metal acts as a cofactor for many different proteins from the relative simplicity of a mononuclear site to the complexity of an iron-sulfur cluster (Figure 1.1) or a heme (Figure 1.2). In such centers iron catalyzes an assortment of reactions such as those involved in respiration (*1-3*), electron transfer (*4-6*), DNA replication and repair (*7-10*), and diatomic gas storage, transfer, and sensing (*11-13*). The ability to gain or lose electrons allows for the diverse range of reactions catalyzed by iron containing proteins.

In spite of its utility in cells iron can also be detrimental through the Fenton reaction [$Fe^{2+} + H_2O_2 \rightarrow Fe^{3+}(OH) + {}^{\bullet}OH$] whereby reactive oxygen species (ROS) can be made (*14*). Such species, as the name implies, are highly reactive and can damage numerous cellular components including lipids (*15*), proteins (*16*), and DNA (*17*). In light of this two-sided nature of iron, wherein it is vital to life but still quite dangerous, iron uptake, trafficking, and homeostasis are especially important. These aspects of the budding yeast cell *Saccharomyces cerevisiae* and the mouse brain are the focus of this dissertation.

Iron Acquisition in the Yeast Cell

Yeast serves as a model system for eukaryotic cells because they are the simplest

---

This dissertation follows the format of *Biochemistry.*

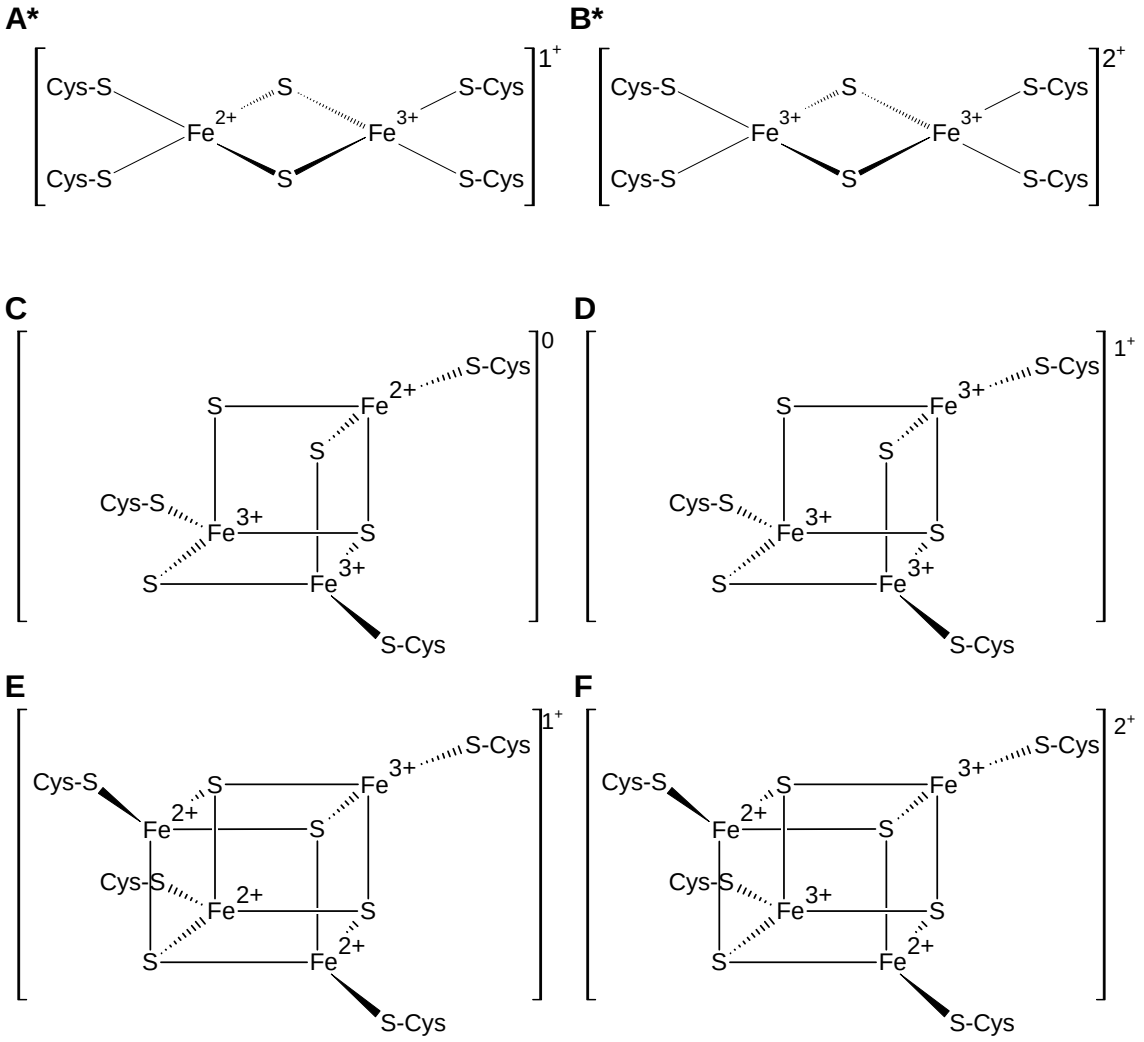

Figure 1.1. Common iron-sulfur clusters . Structures of the most common iron-sulfur clusters in their most common oxidation states. A,B, $[Fe_2S_2]$ clusters in the reduced (1+) and oxidized (2+) state, C,D, $[Fe_3S_4]$ clusters in the reduced (0) and oxidized (1+) state, E,F, $[Fe_4S_4]$ clusters in the the reduced (1+) and oxidized (2+) state. *The $[Fe_2S_2]$ clusters can have two N-His ligands in place of the S-Cys and this is referred to a Rieske center (*18*).

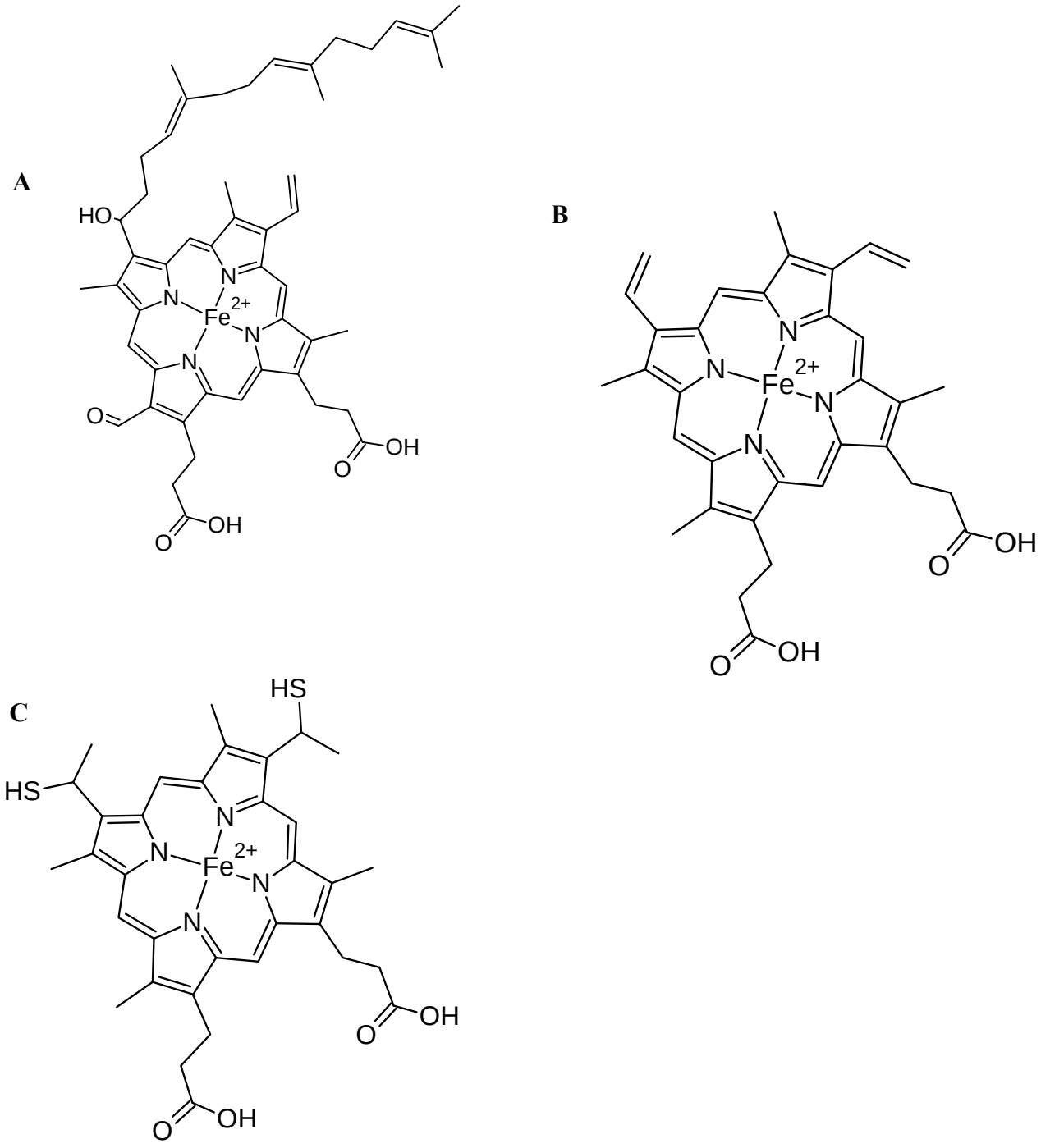

Figure 1.2. Heme centers. Structures of the most common heme centers found in cells A, heme *a*; B, heme *b*; C, heme *c*. These centers are typically found in the Fe^{2+} or Fe^{3+} oxidation state.

cell, and are easy and inexpensive to grow and manipulate genetically. Yeast possesses three major pathways of iron uptake. The pathways are comprised of a feroxidase/permease complex, ferrous transporters, and siderophore receptors and importers. Each pathway internalizes ferric ions from the growth medium across the plasma membrane into the cytosol of the cell.

The ferroxidase/ permease pathway is the "high affinity" system of iron uptake (*19*). The pathway is termed high affinity because of its ability to acquire iron when the concentration of iron in the growth medium is low. The first step of this process is to reduce Fe^{3+} to Fe^{2+} using ferric reductases Fre1p or Fre2p (*20*). Following reduction, iron is accepted by the Fet3p/Ftr1p complex. Fet3p is a multicopper oxidase (*21*), and Ftr1p is a permease (*22, 23*). These two proteins work together in that Ftr1p will not localize to the plasma membrane in the absence of Fet3p, and Fet3p will not accept the necessary copper cofactor in the absence of Ftr1p (*22*). This pathway is essentially non-functional under anaerobic growth conditions, perhaps because of an inability of the copper to undergo redox changes in the absence of O_2 (*23*).

The ferrous transport pathway, comprised of Fet4p, is the "low affinity" system of iron uptake. This pathway requires higher concentrations of iron in the growth medium than does the Fet3p/Ftr1p system (*24*). Fet4p is a divalent metal transporter which internalizes Fe^{2+} in addition to other divalent metals (*25, 26*). This pathway is upregulated under anaerobic conditions compensating for the reduced ability of the high affinity pathway to acquire iron. Under such conditions iron in the growth medium can be in the ferrous state allowing the protein to internalize it (*23*). In aerobic conditions the

Fet4 system of iron uptake is ~100 times less effective at binding and importing iron than the Fet3/Ftr1 complex (*24*). In aerobic conditions the cell must use a reductase such as Fre1p or Fre2p to internalize iron via Fet4p. Aerobically grown cells lacking the high affinity system show no signs of iron deficiency as long as the concentration of iron in the media is 50 μM or higher (*24*). Under these conditions the Fet4p system will internalize the iron.

Siderophores are low-molecular weight organic molecules which bind ferric ions tightly; they are especially useful when the concentration of iron in the growth medium is low. Yeast have receptors, Arn1-4p (*27-29*), which recognize such species. In spite of the ability of yeast to acquire iron from siderophores, they do not synthesize them, making this a system to scavenge iron from other organisms. Yeast internalize siderophore iron with a permease (following reduction by Fre3p or Fre4p (*30*)) or via endocytosis (*31, 32*).

Control of Iron Acquisition by Aft1p and Aft2p

These iron import pathways are tightly regulated on the transcriptional level by two transcription factors called Aft1p and Aft2p (*33*) (*34*). These proteins localize to different compartments of the cell depending on the concentration of iron in the cytosol. Under low iron conditions they are found in the nucleus where they activate the genes of the iron regulon. The iron regulon includes the genes which synthesize the proteins of the iron import pathways. Through this mechanism Aft1p and Aft2p control the import of iron into the cell. Conversely, when iron levels are replete, Aft1/2p localize in the cytosol and the iron regulon deactivates.

The mechanism of Aft1p localization is unclear, but recent studies on Aft2p indicate protein:protein interactions may play a role. Outten and coworkers have identified a pair of monothiol glutaredoxins (Grx3p and Grx4p) that form a bridging [Fe_2S_2] cluster with a BolA-like protein called Fra2p (*35*). Aft2p may bind this complex (*34*). When iron levels become depleted, this cluster may not form, decreasing the affinity for Aft2p to the complex. This would allow localization in the nucleus and an upregulation of the iron regulon. Localization of Aft1p may also be controlled by protein:protein interactions. A strain (Aft1-1^{up}) has a single point-mutation, C291F, which may be involved in such interactions. This strain has a constitutively activated iron regulon (*33*) (see chapter 5). The mutated cysteine may have other roles that lead to its localization in the nucleus such as acting as a ligand in an ISC or in forming a disulfide bond.

Fates of Iron in the Yeast Cell

Many yeast organelles contain iron, including the nucleus (*7, 9, 36-41*), the endoplasmic reticulum (ER) (*39, 42, 43*), the vacuole, and the mitochondrion (the latter two will be discussed below). The iron acquisition pathways first transport iron to the cytosol prior to being trafficked to other organelles (*44, 45*). Little is known about the iron content of the cytosol, the aqueous environment inside the plasma membrane which houses these organelles. This is compounded by the difficulty of studying cytosolic material (*24*). There are established protocols for isolating organelles (specific protocols for mitochondria will be discussed in chapter 2.) The cytosol is encapsulated only by the plasma membrane which will be disrupted during isolation of organelles or cytosolic

material. This means that studying cytosolic material would involve removing all contaminating organelles. This task in itself is difficult but studying iron in the cytosol involves removing iron associated with these organelles. This is complicated by the tendency of iron to leach out during organelle removal, or be released during inadvertent organelle disruption. In spite of this, several ISC (*34, 38, 46-50*) and mononuclear iron (*51, 52*) proteins have been identified in the cytosol. The clusters in cytosolic ISC containing proteins are made (at least in part) by the cytosolic iron sulfur cluster assembly machinery (CIA) (*38, 53-55*).

The Vacuole as a Storage Site for Iron in the Yeast Cell

The vacuole is an organelle that is specific to plant and fungal cells. Vacuoles are similar in function to the lysosomes found in higher eukaryotes. The vacuole plays a major role in yeast iron trafficking and homeostasis (*56*). It stores and detoxifies iron thereby avoiding ROS formation. Vacuoles store iron that is used when the cell is in an iron deficient environment (*57*). They may also provide iron for a shift in metabolism (a diauxic shift) from fermenting to respiring conditions (*58*).

The vacuolar lumen is more acidic than the surrounding cytosol, giving rise to a more oxidizing environment (*58, 59*). The majority of iron in the vacuole has been hypothesized to be in the ferric state ligated by hydroxide, phosphate and or polyphosphate ligands (*58-60*). Previous reports have indicated the vacuolar iron content is ~ 0.2 μg Fe/mg protein (*59, 61*). Reporting numbers in this fashion is confusing in that it does not indicate the concentration of iron, only the ratio of iron concentration to the protein concentration in the organelle. By reporting the amount of iron as a ratio of the

amount of protein, there is the possibility that changing protein content can make the organelle appear to have more or less of the metal. This is a common problem in studies of metals in cell biology; it is not limited to vacuoles but rather is applicable to any organelle.

There are a number of vacuolar proteins which have been identified in iron homeostasis. The first is the protein ccc1p which is the primary importer of iron into the vacuole (*62, 63*). Ccc1p imports ferrous ions from the cytosol (*57, 61, 64*). Vacuoles also undergo endocytosis indicating a second pathway for iron acquisition. However, vacuoles lacking the ability to endocytose do not show a considerable change in iron content. This indicates that the majority of the iron is imported by ccc1p (*62*). Ccc1p is the only identified importer of iron into the vacuole and genetic deletion of this protein greatly decreases the iron content of the vacuoles (*61*).

Other identified proteins involved in iron homeostasis in the vacuole are involved in the export of iron. Two Fe export systems have been identified. The first system uses a permease/oxidoreductase pair, Fet5/Fth1p (*65*), homologous to Fet3/Ftr1 system of iron acquisition across the plasma membrane. The other system of iron export includes Smf3p which is a divalent metal transporter (*66*). Both of these proteins rely on a metalloreductase Fre6p homologous to the plasma membrane proteins Fre1-4p (*59*). This reductase is necessary for export of iron from the vacuole, further substantiating the hypothesis that iron is stored in the ferric form in the vacuole. These systems of iron export allow the release of iron from the vacuole. Without such systems the vacuoles would simply sequester iron rather than store it.

Yap5p is a transcription factor which modulates the activity of vacuolar importers and exporters. Yap5p is responsible for differential expression of Ccc1p; this process is mediated by the concentration of iron in the cell. Ccc1 protein levels are upregulated when the concentration of iron in the cell is high and the Ccc1p levels will decline under iron depletion (*67*). The proteins Cth1p and Cth2p also appear to be involved in this process; however the direct connection and roles have not been established (*68*). This response to iron content of the cell allows the vacuoles to import more (or less) iron under iron replete (or depleted) conditions. There may also be a connection to the exporters of the vacuole to mobilize iron when the cell needs this metal but again this phenomenon is not well investigated.

Mitochondria as "Hubs" of Iron Metabolism

The mitochondria are major hubs of iron metabolism in the cell. Within this organelle all hemes and ISCs (excluding those made by the CIA) are synthesized. Mitochondria are the site of the citric acid cycle used during cellular respiration and harbor the proteins of the electron transport chain (ETC) and oxidative phosphorylation. Mitochondria contain 4 distinct structural components including an outer membrane (OM), an inner membrane (IM), an inner membrane space (IMS) and the matrix (Figure 1.3). The OM is highly porous allowing the free flow of small molecules and nutrients across the membrane (*69*). The inner membrane is much harder to transverse. Both the OM (*70-72*) and IM (*73-76*) make use of specific translocases to move materials into the mitochondria. The IM is heavily invaginated with the cristae or folds of the IM being

Figure 1.3. Electron microscopy image of mitochondria isolated from rat brains. The Blue arrow indicates the OM, the red arrow indicates the IM at the location of cristae, the IMS is the space between these two areas and the matrix constitutes the rest of the structure.

composed primarily of protein including those used for oxidative phosphorylation and the ETC (*77*).

Iron import into the Mitochondria

Iron is imported into the mitochondria through a pair of homologous proteins, Mrs3p and Mrs4p. These proteins were first identified as solute carriers (*78*) and were later identified as the high affinity importers of iron for the mitochondria (*79, 80*). Mrs3/4p are thought to import ferrous ions from the cytosol (*80*). Deletion of these proteins leads to a decrease in mitochondrial iron (*81*) and inhibited heme and ISC synthesis (*79*).

There is no evidence for oxidation of this iron concurrent with import and for at least the last 35 years efforts have been made to quantify the amount of "chelatable" ferrous iron in the mitochondria. Starting with studies by Flatmark and Tangeras, mitochondria were incubated with bathophenanthroline sulfonate (BPS). The investigators found that ~25% of the mitochondrial iron was chelatable (*82*). More recent studies by Petrat and co-workers indicated a much lower concentration of chelatable iron using mitochondrial specific fluorescent chelators. These experiments involved a pre-incubation with chelators whose fluorescence will quench upon binding iron followed by incubation with phenanthroline which binds iron tighter than the fluorescent molecule. By monitoring the change in fluorescence the investigators found that only 12-17 μM of iron in the mitochondria of mouse liver cells was in this chelatable form (*83-86*). How these studies relate to the mitochondria in yeast cells is uncertain.

Both of these methods are complicated by the use of chelators; the Flatmark studies reported on the formation of the $Fe(BPS)_3$ complex which has a well-defined extinction coefficient of 23,141 M^{-1} (*87*), while the Petrat methods reported on the fluorescence of the phenanthroline derivative Phen-Green SK when iron is not bound. The problem is that neither method *directly* probes the endogenous iron complexes. By probing an iron species with a chelator, one is methodically defining what is being probed. When using a chelator which is sufficiently strong to remove iron from ISCs or mononuclear sites, there is a possibility that more than just iron ligated by small molecules may be probed by these methods yielding a higher concentration of chelatable iron than would otherwise be found. Conversely, if one were to use a chelator weaker than the endogenous ligands of the small molecules of interest, the concentration of chelatable iron would appear lower than would be apparent using a stronger chelator. Using a chelator based method also relies on using appropriate concentrations of the chelator. Finally, chelator-based methods will destroy the endogenous cellular complexes and thus destroy any chance of identifying the endogenous ligands attached to the iron.

Mitochondrial Iron-Sulfur Cluster Biosynthesis

Mitochondria utilize a number of proteins to make ISCs. The scaffold proteins Isu1/2p are central to this process. The yeast homolog of frataxin Yfh1p is also necessary, but its role is elusive. It has been assigned as an iron chaperone for this process (*88-90*). However, recent work suggests Yfh1p is an activator of the process as evidenced by the decreased *in vitro* ability of the constituents of the mitochondrial ISC

machinery to make a cluster in the absence of Yfh1 (*91*). A recent study on the *E. coli* counterpart CyaYp has shown that frataxin is an inhibitor of ISC biosynthesis (*92*). There is no evidence to support this in eukaryotic systems. The sulfur associated with the cluster originates from the protein complex Nfs1/Isd11. Nfs1p has been identified as a cysteine desulfurase which catalyzes the conversion of cysteine to alanine via a persulfide intermediate (*93*). Isd11p does not have an established role but is necessary for Nfs1p activity and/or stability (*91, 94*). Reducing equivalents are also necessary to making the bridging sulfides. These reducing equivalents come from NADPH via the oxidoreductase Arh1p (*95, 96*) and are shuttled through Yah1p (*97*).

Downstream of this process are a number of chaperone proteins presumably involved in transfer of the newly formed cluster to the apo-protein targets. These include Ssq1p, a 70 kDa heat shock protein which appears to have a role in Yfh1p maturation (*98-100*), Jac1p, a J-protein which interacts with Ssq1p (*101*), Mge1p which acts as a release factor for Ssq1 following ATP hydrolysis (*102*), and Grx5p, a glutaredoxin necessary for ISC maturation (*103*). Even further downstream is Atm1p, an ATP-binding cassette (ABC) transporter protein on the IM that exports an unknown compound necessary for CIA function (*104, 105*).

Nanoparticles in ISC Mutants

Disruption of the ISC biosynthetic pathway affords similar phenotypes in Δyfh1, Δyah1, and Δatm1 strains. This includes the massive accumulation of iron in the mitochondria in the form of ferric nanoparticles and the disruption of both mitochondrial and cytosolic ISC biosynthesis (*105-107*). These nanoparticles have been studied by

numerous biophysical techniques (many of which will be described in detail in Chapter two). The data suggests that this species is comprised of O, P, and Fe but not C or N. These ferric ions interact magnetically to afford a repeated structure that is similar to that shown in figure 1.4.

Studies on Δyah1 and Atm1-depeleted cells indicate that formation of the nanoparticles requires molecular oxygen as anaerobic growth of these strains does not yield ferric nanoparticles (*105, 107*). The Δatm1 strain appears to have normal mitochondrial ISC levels under anaerobic growth unlike Δyah1 (*105, 107*). This is indicative of a damaging secondary effect of oxidative stress to the mitochondrial ISC machinery under aerobic conditions. ROS generation may occur concurrently with the production of the ferric nanoparticles. The ability of Δatm1 cells to make mitochondrial but not cytosolic ISCs under these conditions is consistent with functional mitochondrial ISC machinery and the downstream role of Atm1p in ISC biosynthesis.

Heme Biosynthesis

Mitochondria are the exclusive site of heme biosynthesis in the cell although not all steps in the pathway occur therein. The first step utilizes succinyl CoA, an intermediate of the citric acid cycle. Rather than converting this molecule to succinate, the substrate for the citric acid cycle reaction of succinate dehydrogenase, succinyl CoA is converted to δ-aminolevulinic acid and transferred to the cytosol where the porphyrin ring is built. Protoporphyrinogen III is transported back into the mitochondria where it is converted to protoporphyrinogen IX. Iron is inserted into this intermediate in a reaction catalyzed by Hem15p, ferrocheletase (*108*). This yields heme *b* a portion of

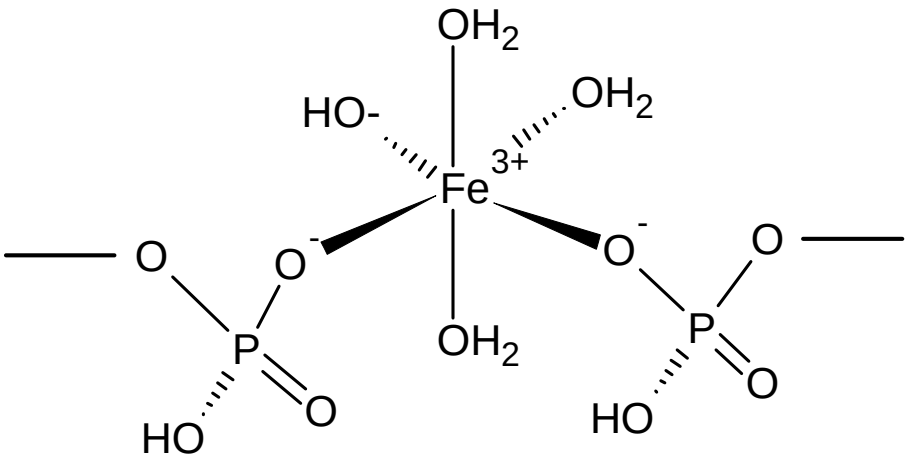

Figure 1.4. Candidate structure for the ferric nanoparticles. This candidate structure in adapted from (*105*) used data collected from Atm1p-depleted mitochondria. Other geometries are possible. Other protonation states for water and hydroxide ligands are also possible, as long as overall charge neutrality is maintained.

which is converted to heme *a* by the enzyme heme *a* synthase (*109*). Another portion of the heme b population is converted to heme *c* through covalent linkages to the hemeprotein by heme *c* lyase (*110*). The changes for heme *a* and heme *c* relative to heme *b* are shown in Figure 1.2.

Mitochondrial Use of ISCs and Hemes

The citric acid cycle uses 10 enzymes (two of which have iron active sites) to convert acetyl-CoA to CO_2. The first of these iron containing enzymes, aconitase, is a $[Fe_4S_4]$ cluster containing protein which contains a labile iron the loss of which yields an $[Fe_3S_4]$ cluster. This enzyme is responsible for the conversion of citrate to isocitrate. The second Fe-containing enzyme of the cycle, succinate dehydrogenase, is a multi-subunit complex containing 3 ISCs (2 $[Fe_4S_4]$ clusters, one with a labile iron making a $[Fe_3S_4]$ cluster, and a $[Fe_2S_2]$ cluster) and a heme *b* group that converts succinate to fumarate.

Succinate dehydrogenase is also found in the electron transport chain and is termed complex II (yeast lack a complex I) (*111, 112*). Complex II shuttles electrons to complex III, also referred to as cytochrome bc_1. Complex III contains two heme *b*'s, a heme *c,* and a $[Fe_2S_2]$ Rieske center (*113*). The final protein complex in the ETC is cytochrome *c* oxidase (complex IV) which contains two heme centers, heme *a* and heme a_3, and two copper sites referred to as Cu_A and Cu_B. Heme a_3 functions with Cu_B to bind and reduce O2 to water. The electrons used in this process are passed from heme *c* of cytochrome c via the Cu_A site and the heme *a* site of cytochrome c oxidase (*114*). Electron transfer is coupled to oxidative phosphorylation, which uses ATP synthase to

generative massive amounts of ATP. Dangerous ROS is generated during respiration (*115*).

A Systems-Level Study of Iron in Cells and Organelles

Biophysical methods have been utilized to study individual iron containing proteins (*93, 116-120*). Such methods can give insight into the mechanism of an enzyme. These methods, however, have been rarely applied to studying the iron in an organelle or cell. The motivation of this dissertation was to determine whether biophysical spectroscopy, with Mossbauer spectroscopy playing the dominant role, could be used to understand iron metabolism from a systems-level perspective. This is a different use of the techniques. As will be demonstrated in this dissertation, this systems-level biophysical approach is indeed useful in probing issues of iron trafficking, regulation and homeostasis in cells.

In chapter 2, we describe the biophysical approach. In chapter 3, we biophysically characterize mitochondria isolated from fermenting cells. In chapter 4, we describe the biophysical differences in mitochondria isolated from different metabolic modes of growth. In chapter 5, we biophysically describe the whole yeast cell, vacuoles isolated from fermenting cells, and the differences to cellular iron distribution when Aft1 constitutively expresses the genes of the iron regulon. In chapter 6, we describe the changes to the iron content of yeast cells and mitochondria when cells are grown under fermenting and respiring mitochondria with high and low concentrations of iron in the growth medium.

Iron in the Mouse Brain

The second major focus of this dissertation is to use the same systems-level biophysical approach to study an even more complex system – namely the iron content of the mouse brain. The main issue is whether the integrative biophysical approach developed to study the iron in yeast cells and organelles will be useful in understanding aspects of brain Fe metabolism.

Iron is critical for brain metabolism. Iron is found in hemoglobin, necessary for the transport of O_2 into the brain. Inside the brain iron is found in a number of different centers. Iron rich mitochondria house a number of hemes and ISCs in respiratory complexes homologous to those discussed above in yeast. These complexes help provide the majority of the chemical energy needed for the brain to function (*121*). Iron is also found at the active site of a number of metalloenzymes in the brain. Among these are tyrosine and tryptophan hydroxylases which harbor roles in the biosynthesis of neurotransmitters (*122, 123*). Iron is also critical for myelin biosynthesis (*124, 125*).

Trafficking of Iron into the Brain

Iron is trafficked into the brain by the protein transferrin. Transferrin binds two ferric ions with high affinity (*126*). Iron loaded transferrin is bound by a receptor on the cellular membrane which promotes endocytosis of the protein bound iron (*127*). In turn, the iron is released and the transferrin returns to the extracellular space (*128*). Iron as well as most other molecules must traverse the blood brain barrier (BBB) for import into the brain (*129*). This barrier is the result of tight junctions between endothelial cells. The cells of the BBB have a number of highly selective active transport systems for

importing molecules like iron or metabolites such as glucose. This basically establishes a mechanism whereby the BBB can control which molecules enter the brain.

Cellular Export of Iron

Neuronal cells have the ability to release iron (*130, 131*). Cells of the spleen, kidney, and placental syncytiotrophoblast also have a similar capacity to release iron (*130, 132*). Most cells (excluding neuronal cells) export iron using ceruloplasmin, a multicopper oxidase, and ferroportin. Neuronal cells lack ceruloplasmin (*133*); instead the β-amyloid protein precursor harbors a ferroxidase activity in such cells.

Proteins of Iron Storage

Neuronal cells have a number of proteins capable of storing large amounts of iron including neuromelanin, ferritin, and hemosiderin. Neuromelanin is a pigment found in regions of the brain including, most notably, the substantia nigra. This pigment has a high affinity for chelating metals (*134*) and accumulates with age (*135*) because it is not effectively degraded (*136*). Elevated levels of cellular iron have been found in Parkinson's disease and appear to be in a form related to neuromelanin (*137-139*).

Ferritin is widely distributed throughout the body with the established role of binding massive amounts of iron. Ferritin is a globular protein with 24 subunits of L (light chain) and H (heavy chain) ferritin monomers. H-ferritin has a ferroxidase activity that is lacking in the L-chain ferritin subunit. As many as 4500 iron ions may be bound to a single ferritin complex (*140, 141*). The iron is found in the ferric form in magnetically interacting ferric (oxidized by the H-chain ferritin subunits) nanoparticles in the protein core (*142*). Ferritin protects the cell from potential iron overload and ROS

formation. Mitoferritin is a functionally and physically similar protein which localizes to the mitochondria (*143*). Hemosiderin is also functionally similar to ferritin but is often associated with hemorrhaging (*144*).

Methods for Studying Iron in the Brain

Traditionally iron has been visualized by staining methods. The two most common methods are Perl staining and Turnbull staining. Both methods involve staining brain slices and monitoring complex formation between the stain and iron in the sample. Both methods are based on ferricyanide, with the Perl stain detecting ferric iron, and the Turnbull stain detecting ferrous iron. Typically such methods are used to study neurodegenerative states (*145*). Staining gives good spatial resolution as the stain will diffuse throughout the slice and a change in color will occur upon iron binding. These stains, used in conjunction, give the ability to distinguish ferrous from ferric ions. Not all of the iron in the brain will be stained with these methods. These methods can only detect iron that is chelated by the reagent. Staining also destroys endogenous complexes, just as with the chelator based studies.

X-ray fluorescence (XRF) (*146*) has also been used to probe iron in the brain. Using XRF, changes in iron levels associated with disruption of the prion protein were studied (*147*). XRF will give information about the amount of iron in a sample but not the form of it. Essentially XRF involves bombarding a sample with energy in the form of x-rays which disperses electrons from the atom. The atom will move an electron from an outer orbital to a vacant orbital, causing a photon to be emitted. This emitted energy is different for different elements allowing elements in the sample to be distinguished.

Because of the high energy used in the technique, the endogenous ligands to an iron complex may be lost. The technique involves sectioning of the brain so spatial resolution is gained by the number of sections used. X-ray fluorescence is sensitive, with detection limits of 10-100 parts per billion (ppb). With a large number of sections, this technique has the ability to give excellent spatial resolution but not *spectral* resolution.

High field magnetic resonance imaging (MRI) has also been used to study iron in the brain (*148-150*). MRI has excellent spatial resolution of intact samples. The sensitivity of the technique is dictated by the field strength of the instrument and the length of the scan. MRI is a nondestructive technique. Unlike other techniques mentioned, MRI can be used on living samples. For such samples the length of the scan becomes an important experimental parameter. If the scan time is too long the sample may move, diminishing S/N (*151*). Like X-ray fluorescence MRI does not detect individual iron centers like an ISC or a heme. In fact, MRI probes relaxation properties of water in the body which are iron sensitive. The technique is most useful for studying samples that accumulate iron.

Mössbauer spectroscopy has also been used to study iron in the brain (*142, 152-158*). This technique will be discussed in detail in chapter two. Mössbauer lacks spatial resolution unless the brain was sectioned. The strength of Mössbauer spectroscopy is its ability to distinguish types of iron. For example, an ISC will be easily distinguished from ferritin associated iron. The major drawbacks of Mössbauer are that it only probes ^{57}Fe and the technique is insensitive. The majority of the studies presented previously suffer from poor S/N. Because of this, use of the technique has been limited to samples with

high levels of iron, or specific regions of the brain with high levels of iron. As a result most of the collected Mössbauer spectra of brains tend to be dominated by storage forms of iron.

Diseases arising from Iron in Higher Eukaryotes

The methods mentioned above are typically utilized to study iron associated with diseases. Iron will accumulate in the brain in several neurodegenerative diseases. By studying diseased samples and comparing them to healthy samples, the change in iron distribution can be detected. Often times techniques such as MRI can aid in diagnosing neurodegenerative diseases (*159*).

There are many diseases associated with iron. In general diseases associated with iron originate from an overload or a deficiency in the cell. One in 200 people suffer from hemochromatosis, the most common form of iron overload. The disease results from either a genetic or metabolic disorder (*160*). The symptoms include accumulation of iron in several tissues which can lead to cirrhosis (*161*), adrenal insufficiency (*162*), diabetes (*163*), and heart failure (*164*).

More prevalent than iron overload are diseases of iron deficiency or anemia. Usually this occurs when patients cannot acquire enough iron from the diet, a condition found in one in 6 people worldwide. Anemia can be related to a simple dietary deficiency and in some cases can be alleviated by supplementing the diet with iron (*165, 166*). Anemia can also arise from genetic dysfunction with red blood cells and this form is much harder to alleviate. While anemia is often manageable in otherwise healthy individuals, the greatest dangers associated with anemia arise during pregnancy.

Expecting mothers have an increased dietary need for iron and failure to meet this need can lead to problems with the fetus including mortality, premature birth, neurological disorders and other complications (*167*).

Iron is involved in several neurodegenerative diseases as well including Parkinson 's disease (PD) and Alzheimer's disease (AD.) PD involves neuronal cell death in the substantia nigra (SN), and iron accumulation in the same cell types (*139*). Decreased melanin levels in PD patients leads to a diminished chelating ability. The increase in iron accelerates fibril formation which leads to cellular dysfunction (*168*). Ferritin and neuromelanin appear to contribute to protection from this additional iron (*169*). Overexpression of ferritin in mouse PD models diminishes the effects (*170*). In AD, the β-amyloid protein precursor is often mutated which results in the accumulation of β-amyloid plaques. The mentioned role of the β-amyloid protein precursor protein in the export of iron may lead to the reported accumulation of iron in AD (*171*). The accumulated iron would make the cell susceptible to ROS formation perpetuating the effects of the disease.

There are also mitochondrial diseases that involve Fe overload, including Friedreich's ataxia (*172*) and X-linked sideroblastic anemia (*173*). Friedreich's ataxia is a disease where the protein frataxin (yfh1 in yeast) is mutated. The disease affects about one in 50,000 people (*174, 175*). This mutation leads to cells deficient in ISC proteins. Patients with Friedreich's ataxia display a loss of sensory neurons in the spinal cord and dorsal root ganglia (*176*). Patients succumb to the disease at a median age of 35, typically as a result of cardiomyopathy.

In X-linked sideroblastic anemia the protein ABCB7 (atm1 in yeast) is mutated (*177*). In this disease, heme production is decreased and the connection to ISC biosynthesis promotes the accumulation of iron in the mitochondria. Often X-linked sideroblastic anemia will be accompanied by late onset (age 40-50) ataxia which can confine patients to wheel chairs. Most commonly the disease can be associated with heart disease, liver damage, and kidney failure.

Iron has also been implicated in processes related to ageing in healthy individuals. Often increased levels of iron are found in the brain with age. This may lead to destructive processes such as ROS formation. In addition, the regulation of iron may also decline with age (*142, 178-182*).

A Systems-Level Analysis of the Iron Content of the Mouse Brain

Chapters 3-6 of this dissertation demonstrate the ability of biophysical probes to gain insight into issues of iron trafficking, regulation, and homeostasis in yeast organelles and cells. In chapter 7 we present data which suggests that the same techniques can be applied to an even more complex system, the brains of mice. As in the yeast based studies, we use an integrated biophysical approach centered on Mössbauer. Although these are not the first Mössbauer based studies on brains, they demonstrate that a substantial portion of iron can be found in forms other than those associated with iron storage. This is a novel characterization of the mouse brain. Furthermore the studies presented in chapter 7 discuss changes to the distribution of iron in the mouse brain as it is developing.

CHAPTER II

MATERIALS AND METHODS

Biophysical Methods Used in These Studies

Several biophysical methods were used in an integrative fashion to probe cells and organelles from a systems level perspective. Mössbauer spectroscopy was the core of our approach, with electron paramagnetic resonance (EPR) and electronic absorption spectroscopy (UV-vis) serving auxiliary roles. Inductively coupled plasma-mass spectrometry (ICP-MS) was used to determine metal concentrations.

Inductively Coupled Plasma-Mass Spectrometry

ICP-MS does not have the ability to resolve Fe into different types but is extremely sensitive in determining Fe (and other metal) concentrations. The technique has exceedingly low detection limits and a large linear dynamic range. The low detection limit is in the ppt and the upper limit is in the high ppm. This dynamic range allows the measurement of samples without the need for serial dilutions prior to analysis.

Since the detection of ICP-MS is based on mass, different isotopes of the same element can be measured. For Mössbauer spectroscopy samples must be enriched with the isotope ^{57}Fe as discussed below. This isotope, which is only 2% natural abundant, can be quantified relative to other iron isotopes using ICP-MS.

Traditionally the most widespread technique for discriminating iron ions in a sample has been to use radioactive iron coupled with scintillation counting. Many experiments involving trafficking of iron into a cell monitor ^{59}Fe or ^{55}Fe by scintillation

counting *(183)*. Similar experiments can be performed using ICP-MS but without the need for radioactive isotopes.

Spin States of Iron

The remaining techniques to be discussed will focus on the characterization of iron centers in a sample. For mononuclear iron sites including those found in the active sites of proteins as well as in heme centers the most common oxidation states of Fe will be Fe^{2+} (ferrous) and Fe^{3+} (ferric). Either oxidation state can then adopt a Low Spin (LS) or High Spin (HS) electronic arrangement. The arrangement of the electrons for an octahedral complex is shown in figure 2.1.

Ultraviolet- Visible Spectroscopy

Hemes and ISCs can be probed with UV-vis spectroscopy. Hemes in the reduced state feature 3 distinct bands, called the α, β, and γ (Soret) bands. The origins of the names for the various heme groups arise from the UV-vis spectrum associated with each center (*184*). Specifically the location of α bands of each center afforded this nomenclature. The α bands are found at ~605, ~565, and ~550 nm for heme *a*, *b*, and *c* respectively. These peaks are absent in spectra of the oxidized cytochromes. $[Fe_4S_4]$ clusters also show a characteristic UV-vis spectrum with a feature at ~410nm that is present in an oxidized cluster and diminished in intensity when the cluster becomes reduced (*185*). Similar effects are seen with $[Fe_2S_2]$ clusters which exhibits features around 430nm in the oxidized state which diminish in intensity in the reduced state (*186*).

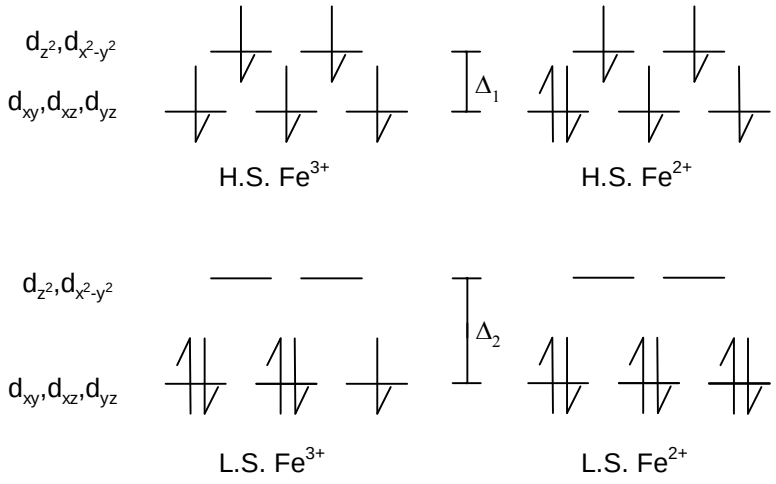

Figure 2.1. Splitting of electrons in octahedral complexes. HS vs. LS is dictated by the value of Δ. In order to obtain the LS complexes, $\Delta_2 > \Delta_1$. Orbitals are indicated by labels on the left.

Using extinction coefficients of the different heme centers, UV-vis can give a concentration of the heme components of a sample. Using this information in conjunction with ICP-MS, the percentage of iron in a sample in these types of centers can be determined. The distinct advantage of UV-vis spectroscopy compared to other biophysical techniques lies in its ability to distinguish different heme centers. Like ICP-MS, UV-vis alone cannot give a complete depiction of the iron in a cell facilitating the necessity for more methods of probing iron.

Electron Paramagnetic Resonance Spectroscopy

EPR is useful for detecting species that have unpaired electrons. Mononuclear iron centers that are found in biology are most typically found in the ferrous or ferric oxidation state. The d electrons can be arranged in a LS or HS configuration. In ISCs the spin states of the individual irons are spin-coupled to afford the system spin. Table 2.1 shows the spin state of common iron species. In cases where S = 0 the system is diamagnetic no EPR signal will result.

Typical g values for the most common biological systems are listed on table 2.1. While these serve as examples of the most common centers there are other centers which can be probed by EPR. The specific example would be a dinuclear center, such a center would feature two ions spin coupled to one another. This affords systems with the following oxidation states of the individual irons: [Fe^{2+} Fe^{2+}], [Fe^{2+} Fe^{3+}], [Fe^{3+} Fe^{3+}]. Of these only the mixed valence or the fully reduced form will result in transitions which

Table 2.1. g values of common EPR species. Spin states and oxidation states of these centers are also presented.

Iron center	Oxidation State	Spin State	Typical EPR Signals	References
Mononuclear	L.S. Fe^{2+}	S = 0	N/A	
Mononuclear	H.S. Fe^{2+}	S = 2	g ≥ 13	(*187, 188*)
Mononuclear	L.S. Fe^{3+}	S = ½	g = 2	(*189*)
Mononuclear	H.S. Fe^{3+}	S = 5/2	g = 4.3	(*190*)
Heme	L.S. Fe^{2+}	S = 0	N/A[1]	(*191*)
Heme	H.S. Fe^{2+}	S = 2	g ≥ 13	
Heme	L.S. Fe^{3+}	S = ½	g ≈ 3-3.5	(*192, 193*)
Heme	H.S. Fe^{3+}	S = 5/2	g ≈ 6.0	(*194*)
$[Fe_2S_2]$	1^+	S = ½	g = 1.96-1.91[2]	(*34, 195*)
$[Fe_2S_2]$	2^+	S = 0	N/A	
$[Fe_3S_4]$	0	S = 2	g ≥ 13	(*196*)
$[Fe_3S_4]$	1^+	S = ½	g = 1.94	(*196*)
$[Fe_4S_4]$	1^+	S = ½	g = 1.94	(*117*)
$[Fe_4S_4]$	2^+	S = 0	N/A	

[1] Although LS Fe2+ is S=0 the use of spin probes has allowed insight into systems that are typically EPR silent.
[2] Rieske centers have the smaller g values (1.91) while a typical all cysteine center would have the higher (1.96) g values.

can be probed by EPR. A well-documented dinuclear system is the diiron center in methane monooxygenase. This system has g values of 1.86 for the mixed valence system (*197, 198*) or high g values (15-16) for the fully reduced system (*199*). Less common are dinuclear centers where the metals are not spin coupled (*200, 201*).

EPR is a useful tool in studying iron due to its ability to detect systems with unpaired electrons, a common motif for redox active iron complexes. Another advantage of the technique lies in the sensitivity of the technique. EPR can detect very low concentrations of paramagnetic species. Using EPR spectroscopy signal integration using a standard of known concentration is possible (*202*). For systems with a single species ICP-MS can be used and find the extent to which a sample is active. For more complex samples EPR and signal integration can be used to find contributions of individual paramagnetic species to the entire iron content of a sample. Although much of the discussion of EPR presented here is based on its application to iron, EPR can be applied to *any* paramagnetic species giving additional information about other metal centers and radical species.

EPR also has disadvantages. First, not all samples have paramagnetic species and integer spin systems are hard to probe. This leads to several instances where signals will not be observed by EPR. In the application of EPR to a sample as complex as a cell or organelle several signals might not be observed in the native oxidation state. The addition of a reductant or oxidant can alter these oxidation states but might not be indicative of the centers in the physiologically relevant sample. The information that can

be gained by EPR might be helpful in studying iron metabolism, trafficking, and homeostasis but this technique still cannot probe all of the iron in a cell.

Mössbauer Spectroscopy

Mössbauer spectroscopy is named after Rudolf Mössbauer. He discovered the principles behind the technique in 1958 (*203*) and received the Nobel prize for this work in 1961. The experiment utilizes a source of radiation to supply energy for nuclear transitions for an element; the source is highly specific to the element being studied. In choosing a candidate element for Mössbauer experiments considerations must be made. First an appropriate source for the candidate nucleus must be available. An appropriate source is one that emits energy equal to the energy of the transition from the ground state to excited state for the candidate element. Once such a source is obtained the next consideration is the lifetime of the source. If this is inordinately short the experiment cannot be conducted. Conversely, a more stable radioactive isotope might not emit radiation at a rate fast enough to conduct the experiment. With these criteria in mind iron is a suitable nucleus for the Mössbauer experiment. The 14.4keV energy released by a ^{57}Co gamma source is equal in intensity to the energy needed for the transition to the I=3/2 excited state transition of a ^{57}Fe nucleus. Finally, the half-life of ^{57}Co is 270 days giving adequate time for scores of experiments with a single source. We shall limit the discussion of Mössbauer spectroscopy to iron although several other elements can be probed by the technique.

The source in a Mössbauer experiment emits a constant energy (14.4keV for ^{57}Co) but very few iron species will actually absorb that particular energy. For the

experiment to provide useful information the energy must be varied. This is accomplished by the use of the Doppler Effect by moving the source closer and further from the sample. By exposing the iron to a range of energies a number of different transitions can be detected in the sample.

Many Mössbauer parameters are reported in units of mm/sec in correspondence to the moving source. For iron, virtually all transitions can be observed on a velocity scale of 10-12 mm/sec. Many spectral features are observed on a narrower velocity range. In Mössbauer spectroscopy the instrument is calibrated relative to α-Fe foil. For reference the simulated spectrum of α-Fe foil is shown in figure 2.2.

Isomer Shift

The first and perhaps simplest parameter to consider in Mössbauer spectroscopy is isomer shift (δ). This parameter refers to the deviation of the transition from the 0 mm/sec velocity point. The spectral deviation is depicted in the second panel of figure 2.2. Values for δ can be either positive or negative. The value depends on the energy needed to excite the iron in the sample from the ground state to the excited state. Negative δ values do not indicate negative energy, but less energy than the 14.4 KeV emitted by the source. This parameter is related to the s-electron density at the nucleus. For this reason the oxidation state will dictate the values of δ. Comparing a $3d^5$ ferric vs. a $3d^6$ ferrous ion, the ferric system has fewer d electrons resulting in more electronic density at the nucleus compared to the ferrous system. Ferric species generally have smaller δ and ferrous species have larger δ.

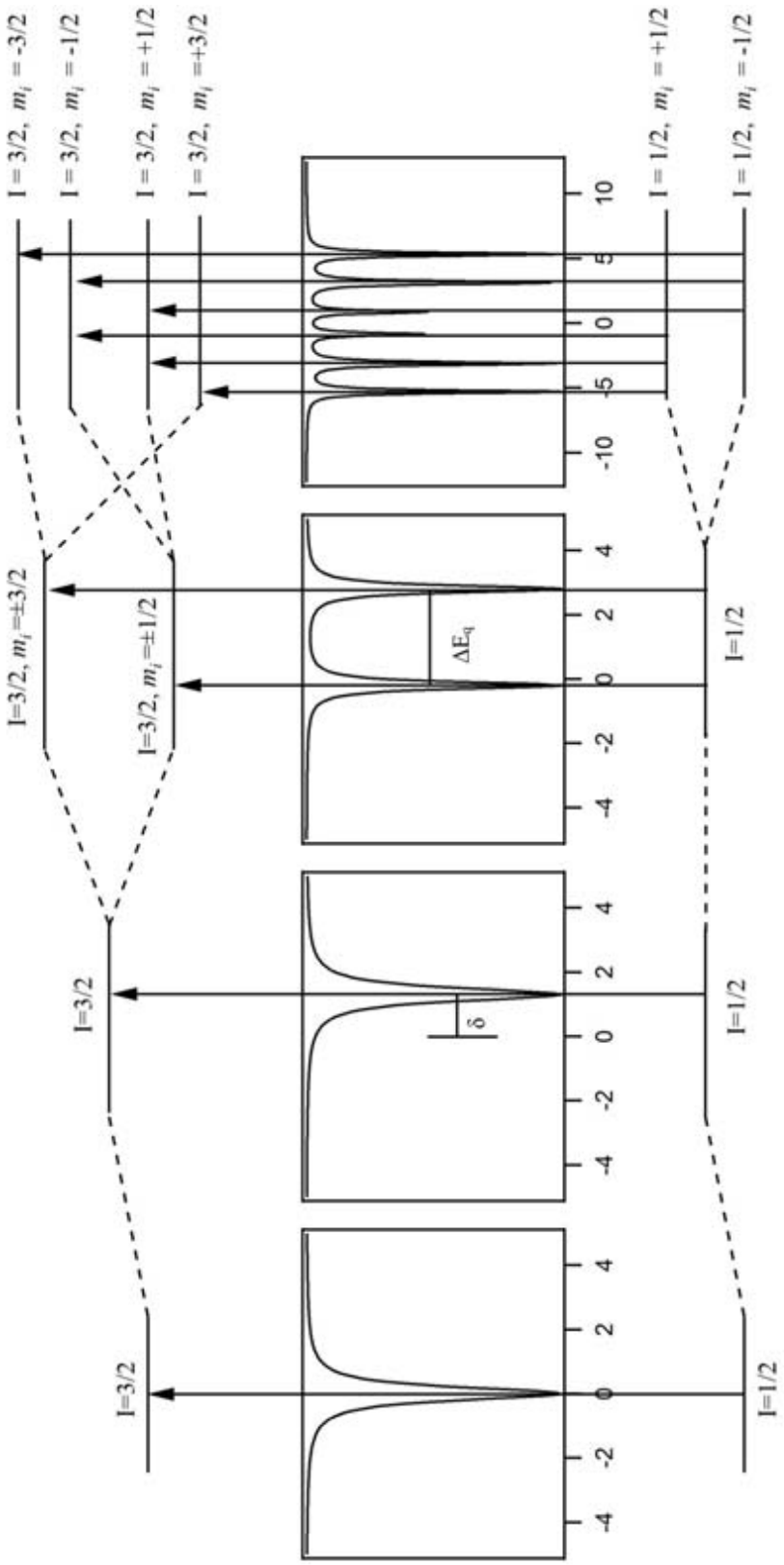

Figure 2.2. Spectral origins of Mössbauer parameters. Also indicated are allowed transitions.

Quadrupole Splitting

For iron nuclei with I=1/2, there are also effects of the electronic field gradient (EFG). Since a nuclear spin is present there will be a non-spherical distribution of the electrons around the nucleus. From the perspective of Mössbauer this will result in the splitting of the spectrum into two lines as shown in the third pane of figure 2.2. This common Mössbauer pattern is called a quadrupole doublet. In this condition the I=3/2 manifold is split into 2 different energy levels, each corresponds to two degenerate states. The distance between the two lines of the doublet in the spectrum and the difference in energy between the two levels is called the quadrupole splitting and is indicated as ΔE_q. The parameter depends on the symmetry of the nucleus. Compared to a HS ferrous ion, the 5 d electrons of a HS ferric ion will each occupy their own orbital giving rise to a more symmetrical system and therefore a smaller ΔE_q. The extra electron in the HS ferrous ion will give rise to a single doubly occupied orbital which drastically decreases the ion's symmetry resulting in a larger ΔE_q. For a quadrupole doublet the δ is measured at the center of the doublet (i.e. halfway between each line.) The value of ΔE_q can be either negative or positive. Figure 2.2 depicts a situation that would have a positive ΔE_q. Conversely, the $m_i = \pm 1/2$ could be higher in energy than the $m_i = \pm 3/2$ which would give a negative ΔE_q. The application of a magnetic field can distinguish a negative or positive ΔE_q.

Magnetic Splitting

A Mössbauer spectrum can further split by applying a magnetic field. The total number of allowed transitions is based on the relationship 2I + 1, where I is the nuclear

spin of the system. Since the Mössbauer experiment involves the transition from ground state to the excited state, or more specifically from I = 1/2 to I = 3/2, there will be 2(3/2) +1 or 6 transitions. These transitions are depicted in the fourth pane of figure 2.2. Only certain transitions are allowed, namely when I changes by 1 and m_i changes by ± 1 or 0. Thus transitions from m_i +1/2 to -3/2 and -1/2 to +3/2 are not observed. On a spectrum with 6 lines, δ is still the center of the spectrum.

Changes to Spectral Features

The appearance of a Mössbauer spectrum can change depending on experimental conditions. The most commonly altered experimental conditions are temperature and applied magnetic field. It is common to study a single sample at different temperature to determine whether the spectrum of the sample displays temperature dependence. For instance, a ferric species might be in a 6 line pattern at low temperature but collapse into a doublet at higher temperatures (*204*). Beyond a change in spectral appearance it is also possible to see temperature dependent shifts in δ and ΔE_q. For example, the splitting between the center lines of the α-Fe foil sextet shifts from 1.68 mm/sec at room temperature to 1.72 mm/sec at 4 K (*205*).

Since Mössbauer spectra are also altered as a field is applied, instruments often include a superconducting magnet capable of fields > 6 T. A magnetic field will have various effects depending on the system. For a spectrum with a six line pattern, the intensities of the lines change depending on the orientation of the field. For diamagnetic systems like LS Fe^{2+} or an oxidized [Fe_2-S_2] or [Fe_4-S_4] cluster the spectrum will be altered in predictable ways (*206*). Armed with this knowledge a Mössbauer

spectroscopist can tease apart spectral features to depending on the behavior of a sample under different conditions.

Table 2.2 shows Mössbauer parameters for many iron centers in biological systems. Relative to other techniques like EPR or UV-vis, all oxidation states and forms of iron can be probed. Herein is a strength of Mössbauer, as percentages of different forms of Fe can be determined. Furthermore, Mössbauer spectra can be obtained without damaging samples, making the identification and isolation of Fe-containing species in the sample possible.

The major drawback of Mössbauer is that it will only probe ^{57}Fe which is of low natural abundance. This means that very often biological samples will need to be enriched with ^{57}Fe to allow the experiment to be performed. Strategies for the enrichment of biological samples with ^{57}Fe will be discussed below. Among the major drawbacks of enriching samples with ^{57}Fe is the cost of the isotope which is in excess of 3000 USD per gram in 2012. Another drawback which is actually common to all the techniques discussed is the necessity for comparatively large sample sizes; this is especially unfavorable for Mössbauer in that even more ^{57}Fe will need to be used to require days or even weeks of data collection.

Making ^{57}Fe Citrate for Use in Cell Growth

^{57}Fe metal was purchased (Isoflex USA) and dissolved in a 1:1 mixture of concentrated trace metal grade (TMG) hydrochloric and nitric acid (Fisher Scientific) to ~ 0.5% v/v final concentration. The dissolved metal was then diluted to a concentration of 80 mM and stored at -20°C. To make the ^{57}Fe citrate stock, a 3-5 molar excess of

Table 2.2. Mössbauer parameters for most common biological iron centers. For rows with multiple entries the parameters reflect the individual sites of the clusters.

Iron center	Oxidation State	Spin State	δ (mm/sec)	ΔE_q (mm/sec)	References
Mononuclear	L.S. Fe^{2+}	S = 0	0.2-0.4	0.2-0.4	(*207*)
Mononuclear	H.S. Fe^{2+}	S = 2	1.0-1.4	2.8-3.7	(*207*)
Mononuclear	L.S. Fe^{3+}	S = ½	0.1-0.3	-2.0-(-3.1)	(*189*)
Mononuclear	H.S. Fe^{3+}	S = 5/2	0.4-0.6	0.6-0.8	(*208*)
Heme	L.S. Fe^{2+}	S = 0	0.4-0.6	1.0-1.1	(*209*)
Heme	H.S. Fe^{2+}	S = 2	0.7-1.0	2.1-2.5	(*210, 211*)
Heme	L.S. Fe^{3+}	S = ½	0.2-0.3	~2.0	(*212*)
Heme	H.S. Fe^{3+}	S = 5/2	~0.4	~0.8	(*212*)
$[Fe_2S_2]$	1^+	S = ½	0.4-0.6 0.2-0.4	2.5-3.2 0.4-1.0	(*213, 214*)
$[Fe_2S_2]$	2^+	S = 0	0.2-0.4	0.4-0.6	(*215*)
$[Fe_3S_4]$	0	S = 2	0.46 0.49 0.31	1.15 1.46 0.56	(*216*)
$[Fe_3S_4]$	1^+	S = ½	0.3	0.66	(*216*)
$[Fe_4S_4]$	1^+	S = ½	0.53 0.53	0.80 1.18	(*217*)
$[Fe_4S_4]$	2^+	S = 0	0.4-0.5	0.8-1.2	(*215, 216*)

sodium citrate (Fisher Scientific) was added to the stock solution, concurrently the pH was adjusted to 5.0-5.5 with sodium hydroxide (Fisher Scientific) and the solution was diluted to a final metal concentration of 40 mM. Subsequently this stock was sterilized using a 0.22μm vacuum filtration system (Millipore) and stored at 4°C for use in cell growth.

Yeast Strains Used

The wild-type *Saccharomyces cerevisiae* strain W303 (*MATα, ura3-1, ade2-1, trp1-1, his3-11,15,leu2-3,112*) was purchased from American Type Culture Collection (ATCC). The majority of the work presented utilized this strain. The experiments of chapter 5 used strain Aft1-1^{up} (*MATα, trp1-63, leu2-3,112, gcn4-101, his3-609, FRE1-HIS3::URA3, AFT1-1^{up}*), described in (*218*), a generous gift from Dr. Jerry Kaplan (University of Utah). Experiments in chapter 6 included the use of DY150 (FET3-GFP) DY150, FET3-GFP::KanMX, described in (*219*), a generous gift from Dr. Jerry Kaplan. DY150 is an isogenic strain to W303 (*220*). Aft1-1^{up} and DY150 (FET3-GFP) and W303 were maintained on YPAD (standard rich medium containing glucose (2% w/v) and 40 mg/L adenine sulfate) agar plates.

Cell Growth and Isolation of Mitochondria

Cultures (25 L) of W303-1B cells were grown on minimal medium (*107*) with 3% (v/v) glycerol, 2% (w/v) galactose, or 2% (w/v) glucose for respiring, respirofermenting, and fermenting conditions respectively. Cultures were supplemented with 40 μM ^{57}Fe unless otherwise noted. Cells were harvested at an OD_{600} of 1.0−1.4 and then transferred to a glovebox (~6 °C, ~1 ppm of O_2). Mitochondria were isolated

anaerobically as described previously (*107, 221, 222*), except that cells were treated with ~1000 units of lyticase/g of wet cells for ~50 min. Also, cells were disrupted with 20−25 strokes of the Dounce homogenizer, and a 14.5 to 18.5% Nycodenz gradient was used. In some experiments, the resuspension buffer contained chelators and/or dithionite (final concentration of 10 mM). Samples isolated with buffers that included 1 mM EGTA are termed EGTA-washed mitochondria.

[Protein] and [Metal] Determinations

Protein and metal concentrations were determined as described (*221*) except that 1−2% deoxycholate was used to disrupt membranes, and the bicinchoninic acid method (Thermo Scientific) was used to determine protein concentrations. Current samples were treated with deoxycholate rather than being sonicated prior to protein concentration determinations, and this may have released additional proteins from membranes and/or reduced the extent of protein degradation. The current metal:protein ratios (~4 nmol of Fe/mg of protein) for respiring and respiro-fermenting mitochondria are similar to those reported from other laboratories (*82, 104, 223-225*), and thus, we consider our current protein concentrations to be more accurate.

Western Blots

Western blots were obtained using specific antibodies for cellular organelles, including mitochondrial porin (Invitrogen), the vacuolar protein carboxypeptidase Y (CPY) (Invitrogen), the cytosolic protein 3-phosphoglycerate kinase (PGK) (Invitrogen), and the endoplasmic reticular protein Kar2 (Santa Cruz Biotechnology). Goat anti-mouse HRP-conjugated secondary antibodies (Invitrogen) were used with all primary

antibodies except Kar2, which used goat anti-rabbit HRP-conjugated secondary antibody (Santa Cruz Biotechnology). Thermo Scientific Enhanced Chemiluminescent (ECL) Western Blotting Substrate was then added. Images were obtained (FujiFilm LAS-4000 mini) with a 10 s standard exposure and the chemiluminescence setting. Images were analyzed using MultiGuage version 3.1.

Analysis of Mitochondrial Integrity

To assess whether isolated mitochondria were intact another western blot experiment was performed. In this experiment an antibody of cytochrome c, a kind gift from Dr. Carla Koehler (University of California, Los Angeles, CA), was used to determine the susceptibility of the protein to degradation by a protease, proteinase K (Fisher Bioreagents). This protein should be found in the IMS so mitochondria treated with a protease would respond by having lower levels of the protein vs. an untreated sample in cases where the mitochondrial membrane was compromised. Conversely if the membrane was intact the levels of cytochrome c would be similar to the untreated sample. Addition of a detergent (simulation of membrane degradation) to the latter sample should result in decreased protein levels as the protein is exposed to the protease.

Spectroscopy

EPR and Mössbauer measurements were performed as described (*107, 221*). Low temperature spectra collected at Texas A&M University varied from 4.5 K to 6 K, but these differences, relative to the 4.2 K spectra collected at Carnegie Mellon University, do not alter simulations significantly. For electronic absorption spectroscopy, samples were resuspended in 0.6 M sorbitol and 20 mM HEPES (pH 7.4); spectra were obtained

as described (*226*). Spectra of human cytochrome b_5 [Sigma, 18 μM in a buffer composed of 1.2 M sorbitol, 50 mM Tris (pH 8.5) and 1 mM dithionite] and yeast cytochrome *c* (Sigma, 20 μM in the same buffer) were also collected. The digital spectrum of bovine heart cytochrome *c* oxidase (*227*) was provided by G. Palmer (Rice University, Houston, TX). Absorbances were normalized to a 1 cm path length and divided by molar protein concentrations.

Fluorescent Determination of Interstitial Buffer Volume

The fraction of mitochondrial pellet volumes (V_{pellet}) due to buffer was determined using the cell-impermeable fluorescent Compound 5 from (*228*) a generous gift from Dr. Kevin Burgess (Texas A&M University). Initially, cells were grown to an OD (600 nm) ~ 1.2 and rinsed three times with 100 μM EDTA and then three times with deionized water. Resulting cells were packed (4000*g* for 5 min) into EPR tubes. The height of the pellet was marked on the tube, allowing V_{pellet} to be calculated from the mass of an equivalent volume of water. Pelleted cells were then resuspended in 200 μL of phosphate-buffered saline (PBS = 137 mM NaCl, 2.7 mM KCl, 10 mM Na_2HPO_4, 1.8 mM KH_2PO_4, pH 7.4) containing known concentrations of Compound 5. Cells were pelleted, and the supernatant was collected. The cells were resuspended in 200 μL of PBS without Compound 5 and pelleted; the supernatant was again collected. This process was repeated three times for each sample. The concentrations of Compound 5 in supernatant fractions were determined using a fluorescence spectrometer (Koala 90080; ISS Inc.). The volume of buffer (V_{buffer}) contributing to V_{pellet} was determined as

described, (*221*) allowing the mitochondrial packing efficiency ($V_{pellet} - V_{buffer}/V_{pellet} \times 100$) to be calculated.

BPS Experiments

Chapter 3 describes four experiments where the chelator in the isolation buffer was replaced with bathophenanthroline sulfonate (BPS.) In the first and third experiments (figures on pages 56 and 58), cells were treated with buffers containing 1 mM EGTA for the initial steps, including those used to rinse the cells and for incubation with lyticase. The buffer used just prior to homogenization and in all steps thereafter contained 3 mM BPS. Past the step in which mitochondria were collected from the density gradients, all buffers included 10 mM dithionite. The mitochondrial sample was rinsed and packed into a Mössbauer sample holder which was then frozen anaerobically. Spectra were recorded, and the sample was thawed anaerobically and sonicated for 5 × 15 s with a Branson 450 sonifier at a 60% duty load using a two-step microtip. The sample was then refrozen anaerobically, and the Mössbauer spectrum was recorded again. In the second and fourth experiments (figures on pages 56 and 58), mitochondria were collected with EGTA in all buffers. Just prior to being frozen, the sample was treated with buffer containing 3 mM BPS. Dithionite was also included in the fourth experiment, which involved deoxycholate treatment rather than sonication.

Phenanthroline Experiment

EGTA-washed mitochondria were split into two aliquots; one was left untreated, and the other was treated with 3 mM phen (ACROS Organics). After 30 min, both were packed into Mössbauer cups and frozen anaerobically.

Dithionite and Deoxycholate Experiment

A sample of EGTA-washed mitochondria was split equally and treated with dithionite (final concentration of 10 mM). Half was treated with deoxycholate (ACROS Organics) (final concentration of 0.5%) and the other half was left untreated. Samples were frozen after incubation in the glovebox for 30 min.

Whole Cells

Cells were grown on minimal medium under constant shaking and harvested at an OD_{600} of 1.0. Cells were collected by centrifugation at 4000*g* and rinsed with unbuffered 100 μM ethylenediaminetetraacetic acid (EDTA). Cells were rinsed twice with water, packed into a Mössbauer sample holder, and frozen. After spectra had been recorded, cells were thawed anaerobically, sonicated as described above, and refrozen.

Low Fe Cultures

Low Fe cultures were prepared by treating the medium with 21μM BPS. The Fe concentration of minimal media was measured to be ~7 μM by ICP-MS so 21μM BPS should have been sufficient to chelate all of this Fe as $Fe(BPS)_3$. Subsequently the media was supplemented with 1μM ^{57}Fe citrate.

Fet3 Expression Western Blot

Cells were grown to an OD(600) of 1.0-1.2 and harvested by centrifugation at 4000×g. Cells were then rinsed 3× with unbuffered EDTA (100 μM) and 3× with water. A portion of the resulting material was saved for western blot analysis and the rest was packed into EPR cuvettes and frozen in LN_2 for further analysis. Protein concentrations were measured and 60 μg of protein of each sample was added to each lane. The gel was

transferred to a PVDF membrane, incubated with antibodies for GFP and porin (as a loading control), incubated with ECL reagents, and then imaged.

CHAPTER III

IDENTIFICATION OF A NON-HEME HIGH-SPIN FERROUS POOL IN MITOCHONDRIA ISOLATED FROM *SACCHAROMYCES CEREVISIAE**

Introduction

Iron serves critical roles in cell biology, generally involving catalytic and redox processes. This transition metal is found in many prosthetic groups, including hemes and iron−sulfur clusters. These groups typically serve as enzyme active sites and redox centers. Dysfunction in cellular iron metabolism has been implicated in aging and in the pathogenesis of diseases involving reactive oxygen species (*229*). Clearly, cells need iron, but they must handle it carefully to avoid being damaged by it. Deciphering how cells do this will require a better understanding of iron trafficking in cells.

Mitochondria are traffic "hubs", used to assemble Fe−S clusters and synthesize hemes. In yeast, the Fe^{2+} ions that are used as feedstock for these processes are imported into the matrix through the high-affinity inner membrane transporters Mrs3p and Mrs4p (*79*). The ligands coordinating these species have been hypothesized to be nonproteinaceous and to have low molecular weights (*230*). The matrix-localized yeast frataxin homologue protein Yfh1p apparently shuttles these ions to the scaffold protein Isu1p for Fe−S cluster assembly, and perhaps to ferrochelatase for heme biosynthesis (*106*).

---

*This chapter is reproduced in part with permission from "A Nonheme High-Spin Ferrous Pool in Mitochondria Isolated from Fermenting *Saccharomyces cerevisiae*" by Gregory P. Holmes-Hampton, Ren Miao, Jessica Garber-Morales, Yisong Guo, Eckard Munck, Paul A. Lindahl, 2010, *Biochemistry*, 49, 4227-4234, copyright 2010 American Chemical Society.

Starting with studies by Flatmark and Tangerås (*82*), efforts have been made to characterize the low-molecular weight mononuclear nonheme Fe species in mitochondria. By exposing the organelles to BPS, a strong chelator of mononuclear Fe^{2+} ions, they estimated that ~25% of mitochondrial Fe is present as a chelatable or labile Fe pool.

Recent fluorescence-based studies in mitochondria from rat hepatocytes indicate a far lower concentration of chelatable Fe. Petrat *et al*. (*84, 231*) incubated cells with fluorescent indicators that accumulate in mitochondria. Fe binding causes fluorescence quenching, so the presence of residual fluorescence in their samples indicated that the binding reaction was limited by the Fe in mitochondria rather than by the indicator. After the subsequent addition of the tight-binding nonfluorescent chelator 1,10-phenanthroline (phen), it penetrated the mitochondria and replaced the Fe-bound indicator, thereby causing fluorescence recovery. The extent of recovery indicated that the concentration of chelatable Fe in rat liver mitochondria was 12−17 μM. The authors estimated that the chelatable Fe pool corresponded to just ~0.4% of the total Fe in the organelle. They attributed Tangerås' dramatically higher estimate to adventitious Fe generated during the isolation of the organelle.

As explained by Petrat *et al*. (*84*), the fluorescence/chelator-based approach for quantifying Fe complexes in mitochondria within a cell is superior to directly measuring Fe in isolated mitochondria. This is so because cells need not be disrupted for these experiments, such that adventitious Fe is not generated. However, this approach is disruptive in another sense; it destroys the Fe complexes of interest as an inherent part of

the detection process. Methods that would allow such complexes to be detected without destroying them would have a distinct advantage, as they could facilitate the eventual isolation and characterization of such complexes. Of course, any such method would be useful only if adventitious Fe could be distinguished from Fe that is functionally associated with mitochondria. In this study, we describe the use of Mössbauer spectroscopy to detect three pools of Fe in mitochondria from fermenting yeast cells, including nonheme high-spin (NHHS) Fe^{2+} species, magnetically isolated (i.e., noninteracting) mononuclear HS Fe^{3+} species, and Fe^{3+} nanoparticles. The major objective of this study was to establish whether these Fe-containing species are located within the mitochondria (where they might serve a metabolic role) or on the exterior of the organelle (where they would be simply artifacts of our isolation procedure and counted as adventitiously bound iron). Our results indicate that they are indeed located inside mitochondria.

Results

All samples of mitochondria were anaerobically isolated from fermenting yeast cells. This involved numerous steps in which samples were suspended in buffer, pelleted by centrifugation, and then resuspended in fresh buffer after the supernatant had been discarded. We refer to these steps as washing. Mitochondria were initially washed with buffers that did not include metal chelators. Such preparations exhibited at a low temperature (5 K) and in weak applied magnetic fields (0.05 T) Mössbauer spectra possessing quadrupole doublets typical of nonheme high-spin (NHHS) Fe^{2+} species. Such doublets had been observed in spectra of mitochondria isolated from wild-type

(WT) respiring (lactate-grown) cells (*221*). The major objective of this study was to establish whether these Fe^{2+} ions were located within fermenting mitochondria, where they might serve a metabolic role, or located on the exterior of the organelle, in which case they would probably be artifacts of our isolation procedure.

Throughout these studies, mitochondrial purity was an important consideration. Western blot analysis of our isolated mitochondria indicated an ~30-fold enrichment of the mitochondrial porin relative to the amount present in cell extracts (Figure 3.1). In fermenting cells, mitochondria occupy ~3% of the cellular volume (*232*), suggesting that our preparations were relatively pure. Western blot analysis indicated some contaminating vacuolar, endoplasmic reticular and cytosolic proteins, which is generally observed (*222*).

Samples were packed by centrifugation into Mössbauer holders (an open delrin cup) to maximize the amount of Fe examined. However, the resulting spectra (Figure 3.2) had signal-to-noise ratios lower than those readily obtained with Fe-containing proteins or small molecules, due to the low inherent concentration of Fe in mitochondria (700−800 μM Fe overall and typically 200−300 μM ^{57}Fe in samples grown on ^{57}Fe-enriched media). In spectra of mitochondria, the quality was sufficient to recognize some minor species (no less than ~10%), but insufficient to quantify such species to greater than ±5% precision.

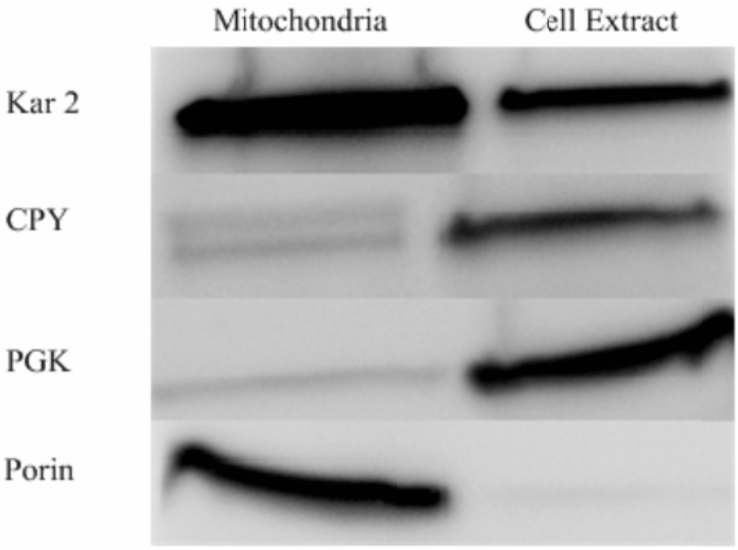

Figure 3.1. Western blot of isolated mitochondria (left lane) and corresponding cell extract (right lane) (sample F6, (29)). In both cases 60 μg of protein was loaded into the wells of a 10% SDS-PAGE gel. Kar2 is an endoplasmic reticular protein (3· increase in the amount of Kar2 in isolated mitochondria sample vs. cell extract); CPY is a vacuolar protein (1.6· decrease); PGK is a cytosolic protein (5· decrease); porin is a mitochondrial protein (32· increase).

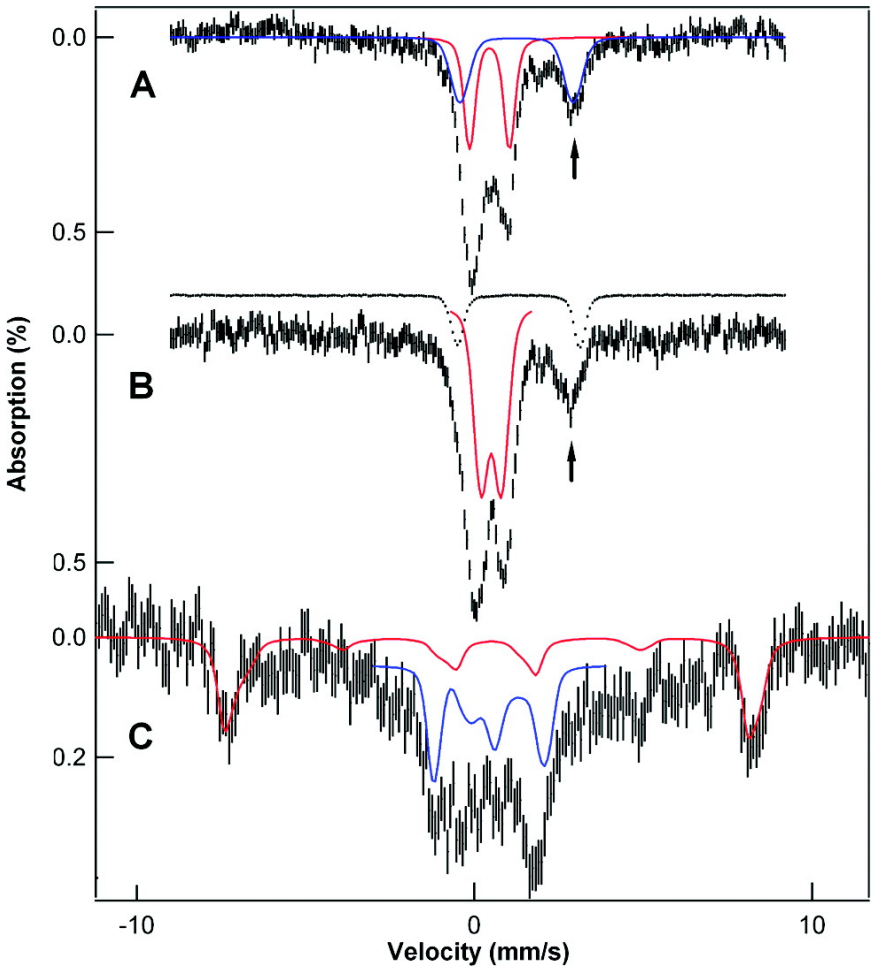

Figure 3.2. Mössbauer spectra of EGTA-washed fermenting mitochondria [sample F12 (*233*)]. Samples were recorded at 5 K and 0.05 T (A), 100 K and 0.05 T (B), and 4.2 K and 8 T (C). Solid lines simulate the contributions of NHHS Fe^{2+} species (blue line in part A, ~20% of total Fe), the central doublet (red line in part A and blue line in part C, ~ 20% of total Fe), Fe^{3+} nanoparticles (red line in part B, ~40% of total Fe), and mononuclear HS Fe^{3+} species (red line in part C, ~20% of total Fe). Shown offset above part B is the experimental spectrum of Fe^{2+}(EGTA) (black hashmarks). The black arrows in Figures 3.2, 3.4, 3.5 point to the high-energy absorption line of the NHHS Fe^{2+} species.

Nonheme High-Spin (NHHS) Ferrous Ions in EGTA-Washed Fermenting Mitochondria

Our initial strategy was to remove adventitiously bound NHHS Fe^{2+} by including 1 mM EGTA, a strong Fe^{2+} chelator, in all washing buffers used during mitochondrial isolation. Such samples were exposed to the chelator for ~6 h overall. In the packing step, all EGTA of the final wash was removed except for that residing between the packed mitochondrial particles (the residual buffer was previously estimated to occupy ~ 20% of the total volume (*221, 226*)). This quantity of residual EGTA was sufficient to coordinate ~200 μM Fe^{2+} ions. We chose EGTA because it reportedly does not penetrate mitochondrial membranes (*234*). Also, the Fe^{2+}EGTA quadruple doublet can be distinguished reasonably well from the NHHS Fe^{2+} doublet associated with our mitochondrial samples. Despite these efforts, the nonheme, non- Fe^{2+}(EGTA) HS Fe^{2+} doublet was observed in all of the ~30 independently prepared batches of EGTA-washed mitochondria examined. Spectra of four other batches (Figure 3.3) illustrate the extent of batch-to-batch variation.

The blue line in Figure 3.2A is a simulation assuming the following isomer shift, quadrupole splitting, and effective line width parameters: $\delta \approx 1.25$ mm/s, $\Delta E_Q \approx 3.35$ mm/s, and $\Gamma = -0.65$ mm/s, respectively (in WMOSS, a negative line width indicates a Voigt profile with a Lorentzian of 0.15 mm/s full width convoluted into a $\sigma = 0.65$ mm/s Gaussian). These values are typical of mononuclear $[Fe^{2+}(O)_m(N)_n]$ complexes for which $5 \leq m + n \leq 6$ and $m \geq 4$ (*235*). HS Fe^{2+} hemes have δ values ranging from 0.92 to 0.95 mm/s and ΔE_Q values ranging from 2.02 to 2.20 mm/s (*118, 236*). The low-energy

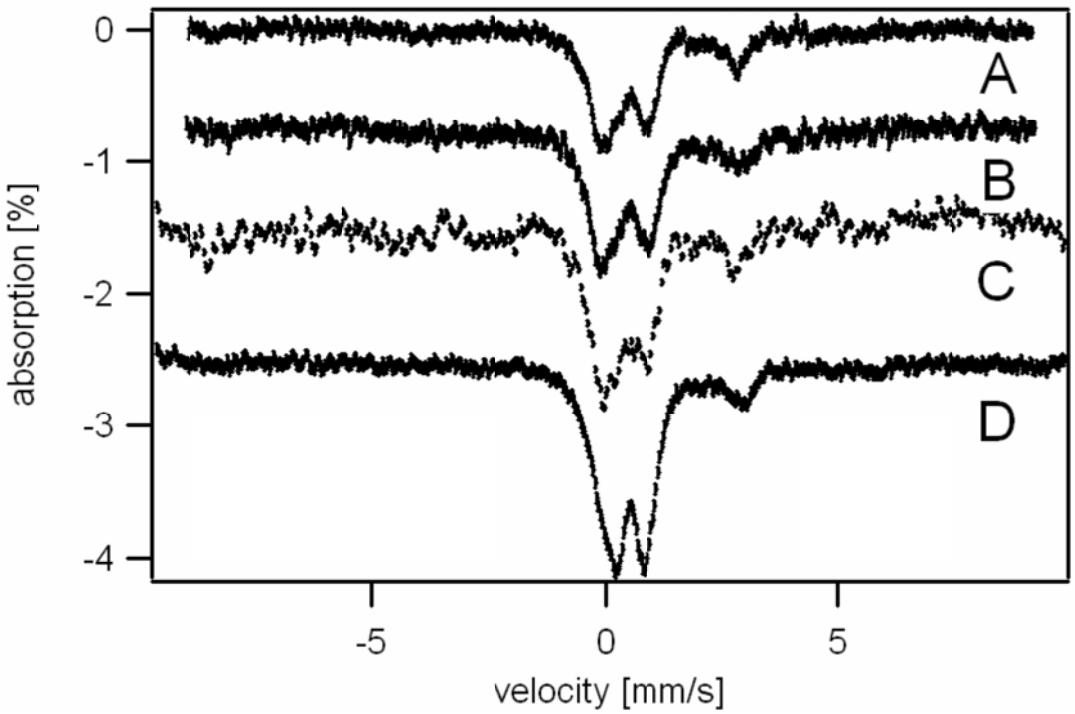

Figure 3.3. Additional Mössbauer spectra (0.05 T parallel applied field) of fermenting mitochondria.

absorption line of the NHHS Fe^{2+} doublet is hidden within the central doublet (see below), while the high-energy line, which contains half of the doublet's intensity, is generally resolved. This line is marked by the arrow in Figure 3.2A and in all other spectra. In Figure 3.2A, the spectral area of the doublet represents 20% of the Fe in the sample, corresponding to ~150 μM Fe^{2+}. The large width of the absorption lines suggests multiple species. This experiment shows that the NHHS Fe^{2+} ions in our sample are protected from EGTA chelation despite extensive washing of mitochondria with EGTA-containing buffers.

Mössbauer spectra of fermenting mitochondria also contain a quadrupole doublet representing ~20% of the total Fe (δ = 0.45 mm/s, and ΔE_Q ~ 1.15 mm/s). This species, called the central doublet, arises from unresolved $S = 0$ $[Fe_4S_4]^{2+}$ clusters and low-spin ferrous hemes (Figure 3.2A, red line) (*107, 221*). In strong applied fields, the contribution of these species can readily be simulated (Figure 3.2C, blue line) because the effective field at the nucleus arises solely from the applied field. In contrast, HS Fe^{2+} ions exhibit paramagnetic hyperfine structure spread over a wide velocity range, making it difficult to characterize in 8.0 T spectra.

EGTA-washed fermenting mitochondria also exhibited spectral features from magnetically isolated high-spin ($S = {}^5/_2$) mononuclear Fe^{3+} species with an E/D value of ~${}^1/_3$. In weak applied fields (0.05 T), magnetically isolated Fe^{3+} yields intricate Mössbauer patterns exhibiting paramagnetic hyperfine structure. With the low ^{57}Fe concentrations in these samples, such features cannot be analyzed well or easily distinguished from baseline (distorting the quantification of other species). Fortunately,

in 8 T applied fields, the outmost features of HS Fe^{3+} components are resolved (Figure 3.2C, red line), allowing an accurate estimate of their concentrations (here 20% of the spectral intensity, corresponding to ~150 μM Fe).

In 0.05 T applied fields, and at 5 K (Figure 3.2A) and 100 K (Figure 3.2B), EGTA-washed fermenting mitochondria also yielded a quadrupole doublet with a ΔE_Q of ≈0.63 mm/s and a δ of ≈0.52 mm/s (red line in Figure 3.2B). Similar doublets were present in spectra of mitochondria isolated from Yfh1p-, Yah1p-, and Atm1p-depleted cells (*105-107*); they arise from Fe^{3+} phosphate nanoparticles exhibiting superparamagnetism. In strong applied fields, these nanoparticles yield broad unresolved features (see Figure 2D of ref (*107*)). Quantification is most accurate at temperatures well above the blocking temperature, T_B; when $T \gg T_B$, spectra consist of a quadrupole doublet (in our samples, $T_B \leq 4.2$ K). The 100 K spectrum (Figure 3.2B) shows that ~40% of the Fe of the sample belongs to Fe^{3+} nanoparticles.

In summary, the Fe in EGTA-washed fermenting WT mitochondria is distributed into four major groups. Approximately 20% is NHHS Fe^{2+}, ~20% a combination of $[Fe_4S_4]^{2+}$ and LS Fe^{2+} hemes, ~40% Fe^{3+} in nanoparticles, and ~20% noninteracting mononuclear high-spin Fe^{3+}. These organelles also contain small amounts of other Fe-containing species (*233*). All of these Fe-containing species were present despite extensive exposure of the mitochondria to a strong Fe^{2+} chelator, suggesting that they are located within the organelle and protected from chelation.

BPS-Treated Mitochondria

As the difference in the positions of the high-energy lines of the NHHS Fe^{2+} doublet and the Fe^{2+}EGTA doublet is modest, we wanted more compelling evidence that the NHHS Fe^{2+} species in our samples were located within the organelle. BPS is orders of magnitude stronger than EGTA in terms of Fe^{2+} chelation, and its negative charge should also make it impenetrable to mitochondrial membranes. However, the major advantage of using BPS is that it forms a LS Fe^{2+}complex that can be easily distinguished from HS Fe^{2+} ions.

The blue line in Figure 3.4A is a 5 K Mössbauer spectrum of a mitochondrial sample washed with 3 mM BPS. It contains a NHHS Fe^{2+} doublet representing 20% of the total iron. After this spectrum had been recorded, the sample was thawed, sonicated, and refrozen, all in a glovebox containing ~1 ppm O_2. The resulting spectrum (Figure 3.4A, hash marks) lacked the NHHS Fe^{2+} doublet; rather, it exhibited a doublet with a ΔE_Q of 0.32 mm/s and a δ of 0.38 mm/s, indicating LS $Fe^{2+}(BPS)_3$. These changes are best visualized by the after-minus-before sonication difference spectrum shown in Figure 3.4B. Features pointing upward (downward) are present before (after) sonication; unchanged features offset. The spectral simulation (red line) assumes that 23% of the Fe in the sample was converted to $Fe^{2+}(BPS)_3$ by sonication, including NHHS Fe^{2+} (13%) and the central doublet (10%) (the percentage in parentheses refers to total Fe, not the percent change of the spectral species). The change corresponds to the majority of the initial NHHS Fe^{2+} species and to approximately half of the central doublet. Other experiments suggest that sonication alone can destroy $[Fe_4S_4]^{2+}$ clusters (Figure 3.5),

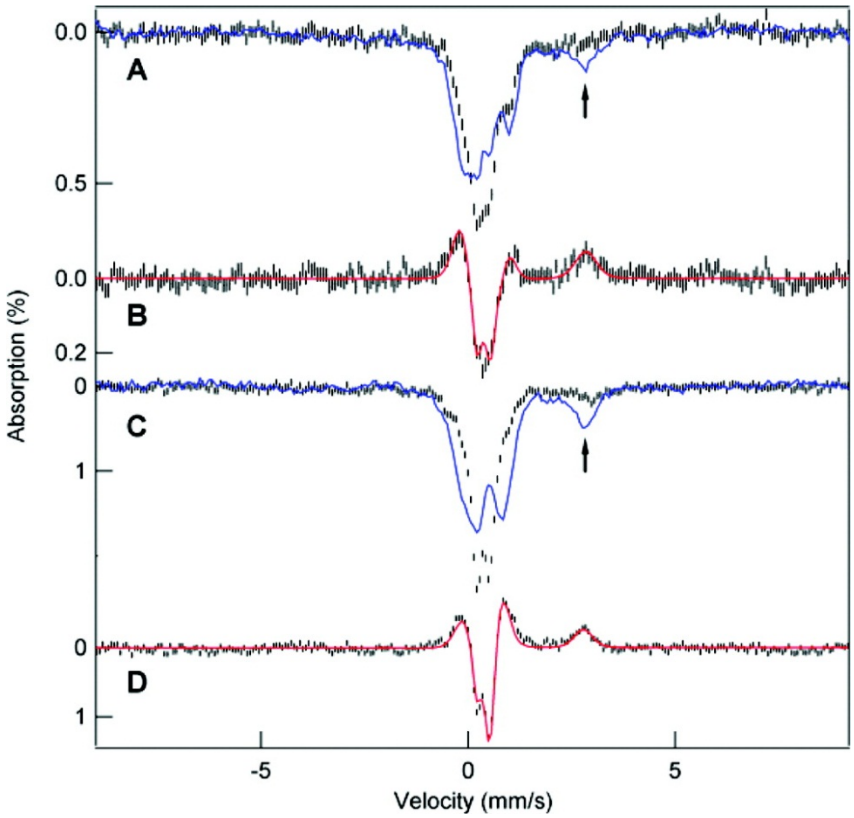

Figure 3.4. Mössbauer spectra (5 K, 0.05 T) of BPS-washed mitochondria [sample F6 (*233*)]. (A) Before (blue line) and after (hash marks) sonication. (B) After-minus-before difference spectrum. The red line is a simulation assuming that NHHS Fe^{2+} (13% of total Fe) and the central doublet Fe (10% of total Fe) were converted into the Fe^{2+}(BPS)3 complex (23% of total Fe). Parts C and D are Mössbauer spectra (100 K, 0.05 T) of a second experiment using EGTA-washed mitochondria treated in the final step with BPS [sample F13 (*233*)]. (C) Before (blue line) and after (hash marks) sonication. (D) After-minus-before difference spectrum. The red line is a simulation assuming that NHHS Fe^{2+} (12% of total Fe), Fe of the central doublet (14% of total Fe), and Fe^{3+} nanoparticles (34% of total Fe) were converted into $Fe^{2+}(BPS)_3$ (60% of total Fe).

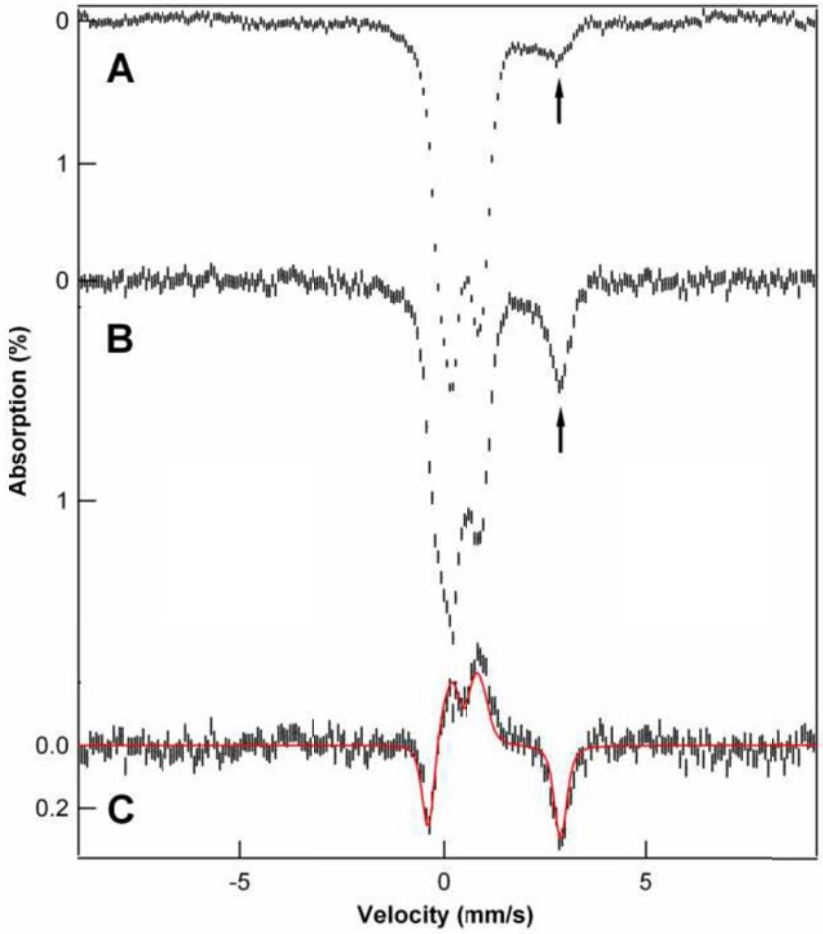

Figure 3.5. Sonication of mitochondria (Sample F7, (29)). Mössbauer spectra (100 K, 0.05 T parallel applied field) before (A), after (B) thawing, sonication, and refreezing the mitochondria sample, and the after-minus-before sonication difference spectrum (C). The red line in C is a simulation assuming that Fe^{3+} nanoparticles (8% of total Fe) and the central doublet (3% of total Fe) were converted into NHHS Fe^{2+} species (11% of total Fe). The black arrows point to the high energy absorption line of the NHHS Fe^{2+} species. The sample was isolated with 3 mM BPS and 1mM diethylene triamine pentaacetic acid in the isolation buffers, and then rinsed 4 times with buffers containing no chelator. The experiment reveals that additional NHHS Fe^{2+} ions developed as the result of sonication (13% of Fe in this form before sonication and 26% after). Some of the additional Fe^{2+} appears to have originated from $[Fe_4S_4]^{2+}$ clusters of the central doublet. Other sources of the developed Fe^{2+} may have been Fe^{3+} nanoparticles or mononuclear HS Fe^{3+}. No reductant was added so it seemsthat anaerobic sonication was sufficient for the reduction of Fe^{3+} ions released during cluster degradation to the Fe^{2+} state. The fragility of protein-bound clusters within mitochondria to sonication was unexpected, but this knowledge will be helpful in avoiding the generation of artifactual NHHS Fe^{2+} ions in future experiments.

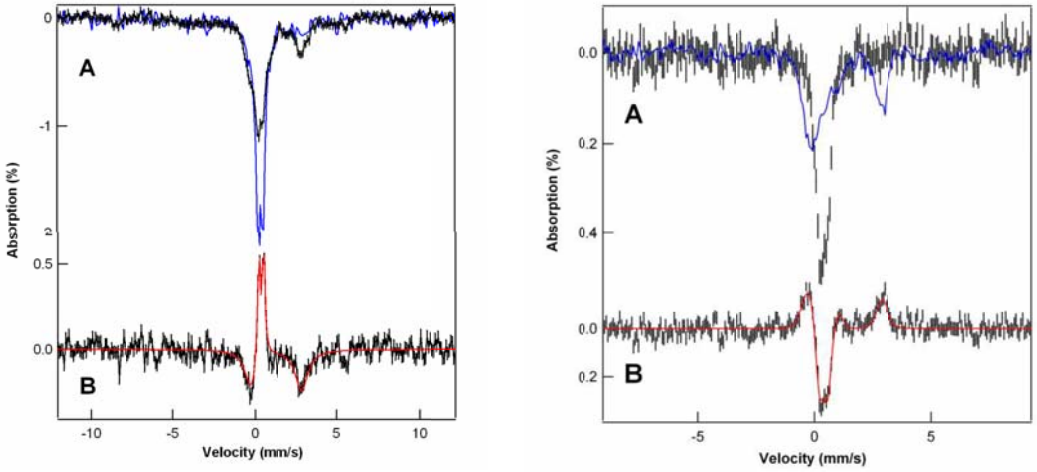

Figure 3.6. Additional Mössbauer spectra (4.5 K, 0.05T) of BPS-washed mitochondria (sample F16, (*233*)). A, before (blue line) and after (hash marks) sonication; B, after-minus-before sonication difference spectrum; The red line in B is a simulation assuming that NHHS Fe^{2+} (40% of total Fe) and the central doublet Fe (20% of total Fe) were converted into the $Fe^{2+}(BPS)_3$ complex (60% of total Fe). This was the third experiment reported in the text. In another experiment, mitochondria from ^{57}Fe-enriched fermenting cells were isolated and treated with 3 mM BPS and 1 mM dithionite (final concentrations) in the final step. Half of the sample was left untreated while the other half was treated with 0.5% deoxycholate. After 30 min incubation, both samples were frozen. A, without (hashmarks) and with (blue line) deoxycholate. B, without-minus-with difference spectrum; the red line is a simulation assuming that NHHS Fe^{2+} (25% of total Fe) was converted into $Fe^{2+}(BPS)_3$ complex (24% of total Fe). This was the fourth experiment mentioned in the text.

whereas BPS does not chelate Fe^{2+} coordinated in heme centers (*237*). We suspect that sonication degraded a large portion of mitochondrial [Fe_4S_4] clusters and that the released Fe ions were reduced by endogenous agents present in mitochondria (or generated upon sonication) to Fe^{2+} and coordinated by BPS.

Similar results were observed in a second independent experiment (Figure 3.4C,D) in which BPS was added to EGTA-washed mitochondria only in the final isolation step. Again, the majority of NHHS Fe^{2+} ions and half of the central doublet were replaced by $Fe^{2+}(BPS)_3$ after sonication. In this experiment, the majority of the iron contained in the Fe^{3+} nanoparticles was also converted to $Fe^{2+}(BPS)_3$ upon sonication (the first experiment showed a lower percentage of nanoparticles). We suspect that sonication released species (sulfide ions?) that reduced the Fe^{3+} ions of the nanoparticles to HS Fe^{2+} ions that were then coordinated by BPS. A third independent experiment (Figure 3.6) using BPS-washed mitochondria also showed the semiquantitative conversion of NHHS Fe^{2+} ions into LS $Fe^{2+}(BPS)_3$upon sonication. Other Fe-containing species in the mitochondria also converted to $Fe^{2+}(BPS)_3$, but our spectra are insufficiently resolved for their identification. A fourth experiment was conducted in which membranes were disrupted by being exposed to deoxycholate rather than by sonication. This detergent has been used to disrupt mitochondrial membranes (*238*). The spectra, also shown in Figure 3.6, again show the presence of NHHS Fe^{2+} in the BPS-washed sample, and the replacement of this doublet by the $Fe^{2+}(BPS)_3$doublet in the spectra of the sample treated with deoxycholate. The results of these four experiments establish that the NHHS Fe^{2+} ions in our samples were protected

from BPS chelation prior to sonication, and that they became susceptible to chelation after sonication. We conclude that this protection arose because these ions are encapsulated by the mitochondrial membrane across which BPS cannot penetrate. Sonication (or deoxycholate) disrupts these membranes, rendering the NHHS Fe^{2+} ions accessible to chelation. Depending on the extent of BPS exposure, a portion of the Fe in $[Fe_4S_4]^{2+}$ clusters and/or Fe^{3+} nanoparticles can also be chelated by BPS.

Mitochondria Treated with Phenanthroline

From the perspective of Fe coordination, phen and BPS have the same structure and properties; both are extremely strong bidentate chelators that bind HS Fe^{2+} to form LS Fe^{2+}complexes. However, in contrast to negatively charged BPS, phen is neutral and able to penetrate the mitochondrial inner membrane (IM) (*84*). Thus, if the NHHS Fe^{2+} species are inside mitochondrial membranes, phen should chelate these ions in unsonicated mitochondria. To test this, an EGTA-washed mitochondrial sample was divided in two; half was frozen without treatment, and the other half was treated with phen and then frozen. The untreated control (Figure 3.7A, blue line) is that of Figure 3.2; it exhibited a HS Fe^{2+} doublet representing 20% of the Fe in the sample. The matched phen-treated sample (Figure 3.7A, black hash marks) lacked the NHHS Fe^{2+} doublet but contained an intense quadrupole doublet with a ΔE_Q of 0.31 mm/s and a δ of 0.37 mm/s. These parameters are characteristic of LS $Fe^{2+}(phen)_3$. This doublet represented 25% of the total Fe in the sample. These changes are illustrated in the "after-minus-before" difference spectrum (Figure 3.7B). The red line is a simulation showing 15% NHHS Fe^{2+} ions (the features pointing upward) converting to $Fe^{2+}(phen)_3$ after being exposed to

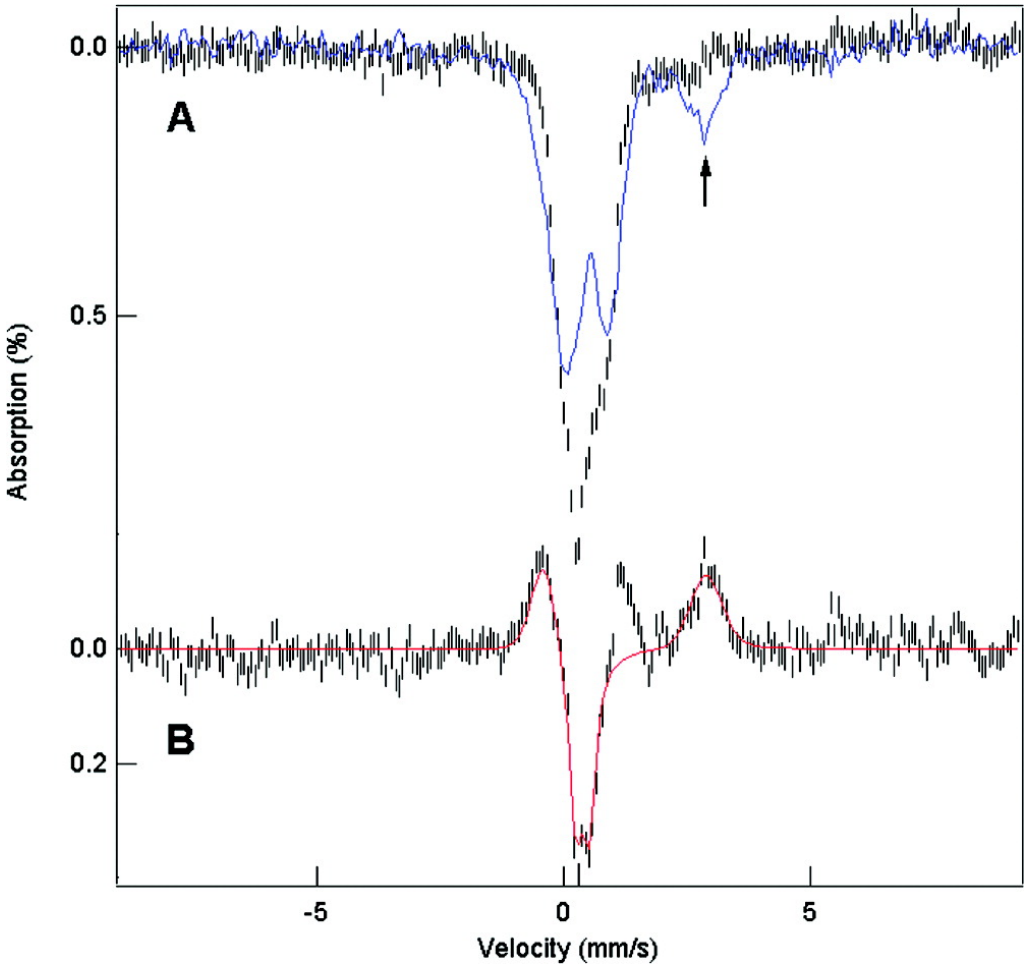

Figure 3.7. Mössbauer spectra (5 K, 0.05 T) of fermenting mitochondria [sample F14 (*233*)] incubated (A, black hash marks) or not (A, blue line) with phen. (B) Incubated-minus-not-incubated difference spectrum. The red line is a simulation assuming that NHHS Fe^{2+} ions (15% of total Fe) converted to $Fe^{2+}(phen)_3$ after being exposed to phen. The remaining $Fe^{2+}(phen)_3$ doublet (~10% of total Fe) originated from either Fe^{3+}nanoparticles, mononuclear Fe^{3+} ions, or irons of the central doublet.

phen. Some additional Fe species, representing ~10% of the total Fe, also converted to $Fe^{2+}(phen)_3$. These species exhibit the upward feature at ~1.2 mm/s in Figure 3.7B. They might be Fe^{3+}nanoparticles or Fe of the central doublet, but the spectra lack sufficient resolution to distinguish them. Phen did not cause the decline of the mononuclear HS Fe^{3+} species, perhaps due to the weaker coordination of phen to ferric ions. Regardless, our main conclusion is that phen penetrates unsonicated mitochondria and coordinates the NHHS Fe^{2+} ions located therein.

No Correlation of NHHS Fe^{2+} to Contamination Levels

One difficulty in determining the cellular location of the observed NHHS Fe^{2+} species has been to exclude the possibility that they are encapsulated by membranes other than those of mitochondria. As discussed previously (*222, 239*), the best method available for isolating large quantities of mitochondria (i.e., discontinuous density gradient centrifugation) does not remove all non-mitochondrial membranous material; the most common contaminants include endoplasmic reticulum (ER) and vacuoles (*222*). Besides having a density similar to that of mitochondria, the ER physically interacts with mitochondria for phospholipid biosynthesis and calcium signaling (*240*). These interactions might prevent the clean separation of the two organelles.

We have discovered that the percentage of NHHS Fe^{2+} differs in mitochondria isolated from cells grown on different carbon sources (*233*). In mitochondrial preparations isolated from cells grown on glucose, galactose, and glycerol, the NHHS Fe^{2+} doublet quantified to 16, 7, and 3% of the total Fe, respectively. Western blot analysis confirmed that these preparations contained some contaminating ER and

vacuolar proteins (Figure 3.8). The density of blots obtained using antibodies that bind to proteins in the ER, vacuoles, and cytosol was normalized using antibodies for the porin protein that localizes to mitochondria. We found that the normalized blot densities for contaminating organelles were not correlated to the percentage of the NHHS Fe^{2+} doublet (Figure 3.8, table). Similar analyses performed on eight different batches of mitochondria isolated from glucose-grown cells also showed no correlation (Figure 3.9). These results indicate that the NHHS Fe^{2+} ions present in chelator-washed mitochondria are contained within these organelles rather than in contaminating membranous species such as ER or vacuoles.

Dithionite- and Deoxycholate-Treated Mitochondria

We also used deoxycholate in the presence of the reductant dithionite to evaluate whether the HS Fe^{3+} species in our mitochondrial samples were contained within the organelle. We treated half of a WT EGTA-washed fermenting mitochondrial sample with dithionite; the other half was treated with dithionite and deoxycholate.

The low-field spectrum of the dithionite- and deoxycholate-treated sample (Figure 3.10A, black hashmarks) contained a doublet due to Fe^{2+}EGTA with a δ of 1.3 mm/s and a ΔE_Q of 3.6 mm/s (Figure 3.10A, blue line) that represented 40% of the total Fe. The corresponding spectrum of the dithionite-treated sample exhibited a NHHS Fe^{2+} doublet with approximately half that intensity (Figure 3.10A, blue line). The deoxycholate-treated-minus-untreated difference spectrum (Figure 3.10B) revealed that besides EGTA coordination to the 20% of the NHHS Fe^{2+} species originally in the

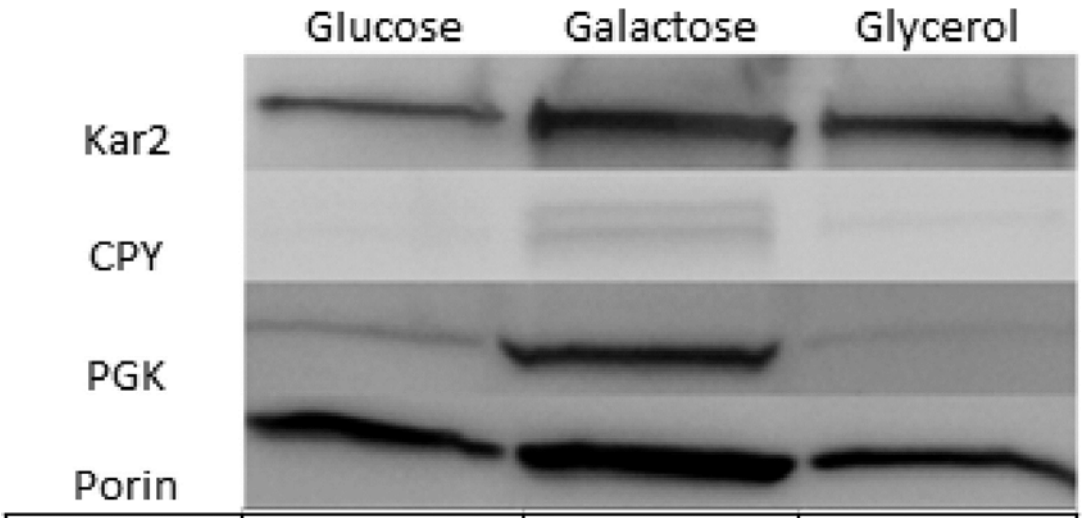

Kar2/Porin	0.57	0.73	1.06
CPY/Porin	0.042	0.15	0.045
PGK/Porin	0.18	0.51	0.2
%NHHS	16%	7%	3%

Figure 3.8. Western blots of mitochondria from various carbon sources. Includes samples grown on glucose (left), galactose (middle), and glycerol (right) [samples F5, RF1, and R1, respectively (*233*)]. For each sample, 60 μg of protein, determined by the bicinchoninic acid method (Thermo Scientific), was added to each lane of a 10% SDS−PAGE gel. Primary antibodies used in staining included Kar2p, CPY, PGK, and porin. Integrated intensities of contaminating bands were normalized to the intensity of the corresponding porin band. These ratios are given in the table along with the percentage of the NHHS Fe^{2+} doublet observed in the Mössbauer spectrum of the same material.

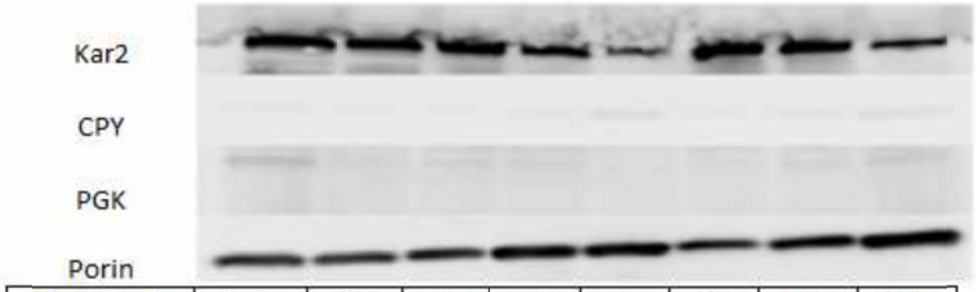

Kar2/Porin	2.01	1.32	1.87	0.72	0.38	1.2	0.92	0.45
CPY/Porin	0.15	0.14	0.07	0.11	0.14	0.22	0.12	0.11
PGK/Porin	0.47	0.32	0.24	0.17	0.32	0.16	0.19	0.23
%NHHS	32%	23%	27%	32%	27%	28%	22%	20%
Sample	N/A	F9	F6	F13	F7	F8	F11	F10

Figure 3.9. Western blot of eight independent preparations of mitochondria. Each sample was obtained by loading 60 μg of protein onto a 10% SDS-PAGE gel. Numbers given in the table are density ratios. Samples are referenced in (29).

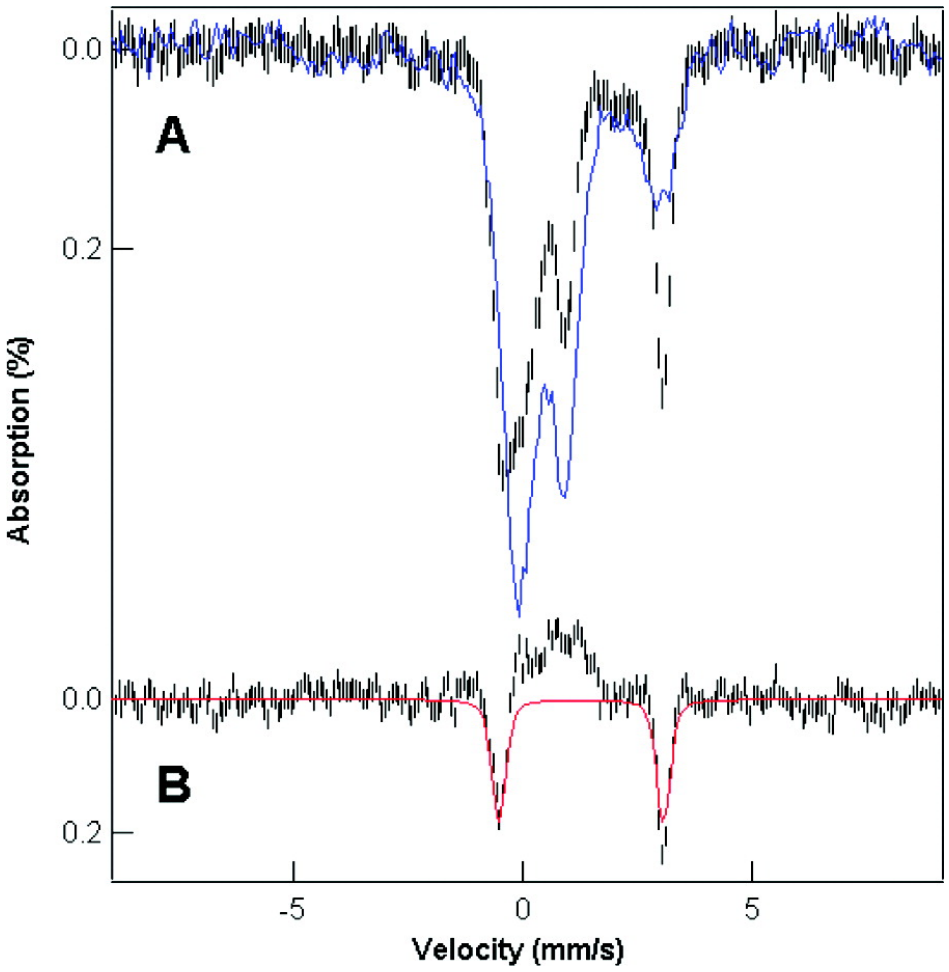

Figure 3.10. Fermenting mitochondria treated with deoxycholate and dithionite. Examines the effect of deoxycholate on the ability of dithionite to reduce Fe^{3+}species in EGTA-treated mitochondria [sample F15 (*233*)]. (A) Mössbauer spectra (100 K) of EGTA-washed, dithionite-treated, mitochondria in the absence (blue) and presence (black hashmarks) of deoxycholate. (B) Presence-minus-absence difference spectrum of deoxycholate. The red line is a simulation representing 20% of the total Fe with a δ of 1.3 mm/s and a ΔEQof 3.6 mm/s.

dithionite-treated sample, ~20% of the Fe from other species was also converted to Fe^{2+}(EGTA). High-field spectra (Figure 3.11) reveal that some (~12% of total Fe) of these other species originated from HS mononuclear Fe^{3+} species. Spectral features from such species are evident in the 8.0 T spectrum of the dithionite-treated sample but absent in that of the dithionite- and deoxycholate-treated sample. The other iron species contributing to the Fe^{2+}(EGTA) complex (~8% of total Fe) could not be identified, but they could be Fe^{3+} nanoparticles. The central doublet contribution was unchanged in the experiment, consistent with deoxycholate treatment being gentler than sonication in the disruption of membranes but not damaging Fe_4S_4 clusters. These results suggest that the mononuclear HS Fe^{3+} species (and perhaps Fe^{3+} nanoparticles) that contribute to the spectra of isolated fermenting mitochondria are contained within these organelles, protected from reduction by dithionite. Disruption of these membranes by deoxycholate removed this protection, allowing dithionite to reduce Fe^{3+} to Fe^{2+}. EGTA then chelated the Fe^{2+} ions forming the observed Fe^{2+}(EGTA) doublet.

Discussion

NHHS Fe^{2+} Pool within Isolated Mitochondria

The major conclusion of this study is that the NHHS Fe^{2+} species that are present in our isolated mitochondrial samples are located within the organelle. Three lines of evidence support this. First, such species were observed after intact mitochondria were exposed to high concentrations of strong Fe^{2+} chelators (EGTA and BPS) for extensive periods of time. EGTA is reported not to penetrate mitochondrial membranes, and BPS is unlikely to do so because of its negative charge. We have observed such species in

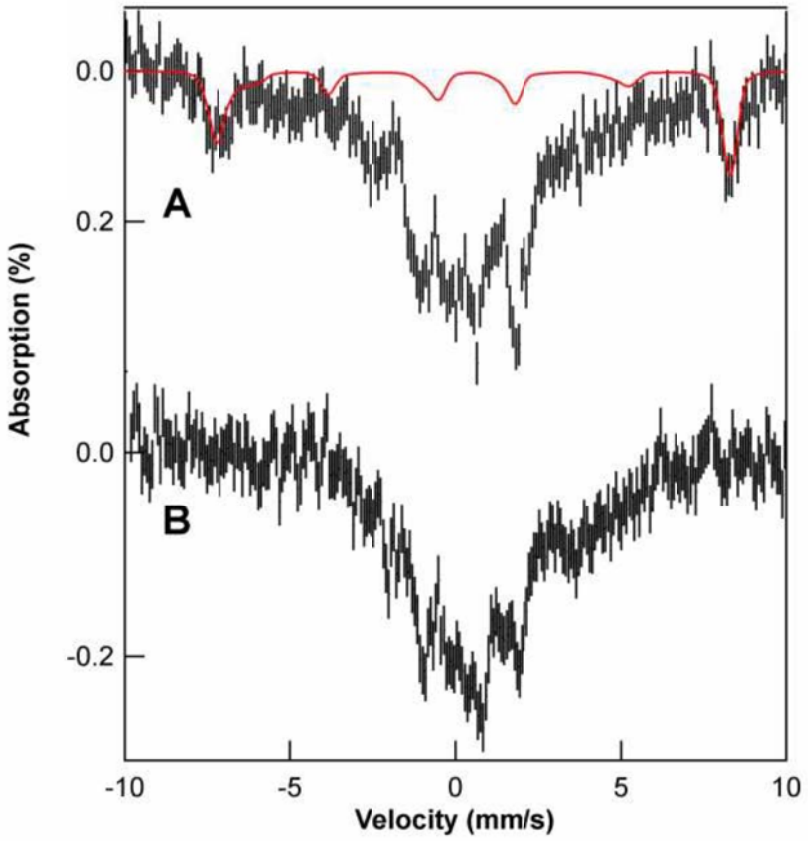

Figure 3.11. Mössbauer spectrum (4.2 K, 8.0 T parallel field) of EGTA-washed, dithionite treated fermenting mitochondria without (A) and with (B) deoxycholate (same samples as figure 3.10). The red line in (A) is a simulation of HS Fe^{3+} species representing ~12% of total Fe. This species is missing in (B). The weak signals required about 2 days of data collection per spectrum.

all ~30 batches prepared in this way over the course of the past 5 years. These Fe^{2+} species were present in samples that had not been sonicated or exposed to phen, indicating that they were not generated by the degradation of $[Fe_4S_4]$ clusters.

Second, BPS and EGTA were able to coordinate NHHS Fe^{2+} only after samples had been sonicated. As sonication disrupts mitochondrial membranes, we conclude that the NHHS Fe^{2+} species are located within the mitochondria and are protected from these chelators until the mitochondrial membranes are disrupted by sonication or by detergents such as deoxycholate. This conclusion is supported by the observation that phen (with a coordinating chemical structure similar to that of BPS but neutral and membrane permeable) can chelate the NHHS Fe^{2+} species without sonication.

Third, there was no correlation between the spectral intensity of the NHHS Fe^{2+} doublet and the level of ER or vacuolar contamination in our samples. This excludes the possibility that these Fe^{2+} species are located in a membrane-bound but non-mitochondrial organelle that contaminated our preparations.

Other scenarios have also been considered. For example, it is conceivable that during isolation, mitochondrial membranes become more permeable, allowing Fe from the isolation buffers to enter into the organelle. However, in this case, one would also expect that the strong chelators present in these buffers would have also entered the organelle and coordinated the observed HS Fe^{2+} species, and/or that Fe within the organelle would also have diffused into the buffer, draining the organelle of the observed HS Fe^{2+}. The presence of the HS Fe^{2+} species argues against these scenarios.

These Fe^{2+} components represent ~20% of the total Fe in the organelle (700−800 μM), corresponding to ~150 μM in NHHS Fe^{2+}. Given the low intensity of our signals and batch-to-batch variations, we estimate an overall relative uncertainty of ±30% (100−200 μM) for the concentration of these components in fermenting mitochondria. This concentration is 1 order of magnitude higher than previous estimates based on fluorescence studies. Comparing results is difficult because the sources of the mitochondria (yeast vs. rat liver) differed as did the metabolic conditions under which the cells were prepared. Nevertheless, our studies show that the concentration of these ions in mitochondria isolated from fermenting yeast is higher than what has been generally assumed.

Other Pools of Iron in Mitochondria

Although the focus of this paper was to establish whether the NHHS Fe^{2+} species were located within yeast mitochondria, our experiments also provide evidence of other pools of Fe in the organelle, including Fe^{3+} nanoparticles (~40% of the Fe, corresponding to ~300 μM, but somewhat variable) and mononuclear HS Fe^{3+} ions (~20% of the Fe, corresponding to ~150 μM). The combined concentration of these three pools (600 μM) represents ~80% of the total Fe in fermenting mitochondria. This is again a larger-than-expected proportion of mitochondrial Fe in the form of Fe pools. Whether these pools are independent of each other (e.g., imported through different IM transporters) or are in dynamic equilibrium with each other is unknown, but we assume the latter in the model of Figure 3.12. We have also observed a fourth pool of Fe in fermenting yeast cells, namely mononuclear HS Fe^{3+} ions located in a non-mitochondrial

region of the cell. The concentration of this pool is high, representing ~75% of all the Fe in the cell.

We have not established the metabolic role of any of these pools. Fe^{2+} ions are imported into the mitochondrial matrix via two high-affinity transporters (Mrs3p and Mrs4p), and this pool is used as feedstock for Fe−S cluster and heme biosynthesis. Studies also suggest the presence of an Fe^{3+} pool in vacuoles (*59*). It is appealing to consider that we have observed these and perhaps other Fe pools in yeast, but further studies are required to establish this. Mössbauer spectroscopy in combination with the analysis of various genetic strains of yeast will undoubtedly be useful in elucidating this and other details of iron trafficking in cells.

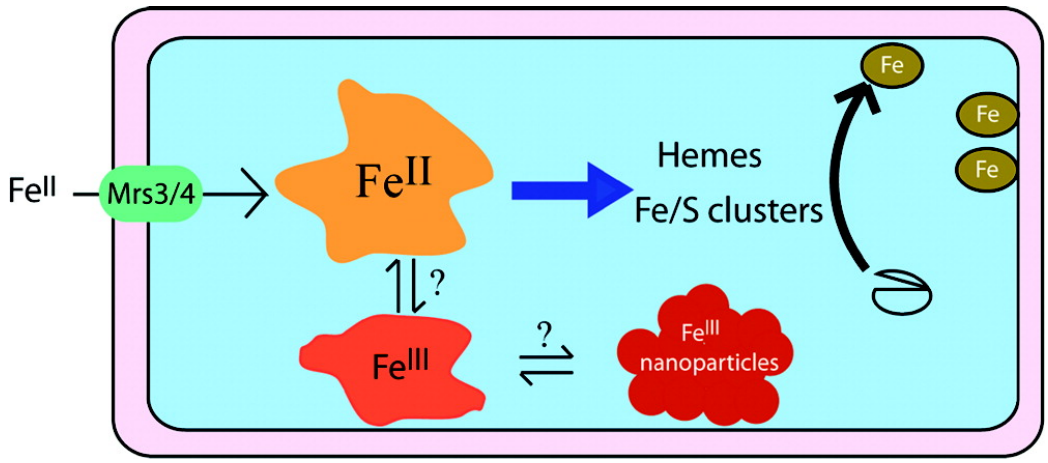

Figure 3.12. Distribution of iron pools isolated in fermenting mitochondria. Three pools composed of nonheme HS Fe^{2+} species, mononuclear HS Fe^{3+} species, and Fe^{3+} nanoparticles have been identified.

CHAPTER IV

BIOPHYSICAL CHARACTERIZATION OF IRON IN MITOCHONDRIA FROM YEAST UNDER DIFFERENT METABOLIC CONDITIONS*

Introduction

Mitochondria are cellular organelles that play critical roles in cellular physiology. Respiration and oxidative phosphorylation occur in these organelles, as do heme biosynthesis and iron−sulfur cluster assembly. As such, mitochondria are "hubs" of cellular iron trafficking (*47*). The Fe^{2+} ions used for these processes are imported by Mrs3p and Mrs4p, high-affinity transporters on the IM (*47*). Once in the matrix, these ions are delivered to Fe−S scaffold proteins and ferrochelatase (*47*). Many of these Fe−S and heme centers are inserted into respiratory complexes. Succinate dehydrogenase contains one [Fe_2S_2], [Fe_3S_4], and [Fe_4S_4] cluster each as well as a LS heme *b(4)*. Cytochrome bc_1 contains two LS *b* type hemes, one LS *c* heme, and a Rieske [Fe_2S_2] cluster (*113*). Cytochrome *c* contains one LS heme *c*. Cytochrome *c* oxidase contains two heme *a* molecules and three Cu ions (*241*). Other mitochondrial proteins

---

*This chapter is reproduced in part with permission from "Characterization of Iron in Mitochondria Isolated from Respiring and Fermenting Yeast" by Jessica Garber Morales, Gregory P. Holmes-Hampton, Ren Miao, Yisong Guo, Eckard Münck, and Paul A. Lindahl, 2010, *Biochemistry*, 49, 5436-5444,copyright 2010 American Chemical Society.
My contributions to these studies were isolation of the fermenting samples, collection of low field Mössbauer data, and analysis of the mossbauer data in collaboration with Dr. Eckard Münck and Dr. Yisong Guo at Carnegie Mellon University.

contain [Fe_4S_4] and [Fe_2S_2] clusters, hemes, and non-heme Fe^{2+} ions (see ref (*221*) for a list of mitochondrial Fe-containing proteins).

Mitochondrial dysfunction is associated with aging and various diseases, including cancer, heart disease, anemia, and neurodegeneration (*16, 242, 243*). As cells age, there is a decline in the level of Fe−S cluster biogenesis and mitochondrial membrane potential, leading with higher probability to a cellular crisis associated with loss of mitochondrial DNA, the instability and hypermutability of nuclear DNA, and cancer (*244*). Aged cells exhibit signs of iron starvation (*244*). Reactive oxygen species (ROS) generated by Fe centers within the mitochondria may damage the DNA and other cellular components (*245*), causing apoptosis (*5, 246, 247*). Ferrous ions are particularly adept at producing ROS via Fenton chemistry (*248*). In Friedreich's ataxia, the level of mitochondrial frataxin is depleted, causing a buildup of iron in the organelle (*106, 249-251*). In Parkinson's disease, there is a buildup of Fe in the *substantia nigra* portion of the brain (*252, 253*). Patients with sideroblastic anemia accumulate Fe that cannot be incorporated into hemoglobin (*47, 254*).

Much progress in understanding cellular function has been made by "omics"-level studies in which entire subsets of cellular components are measured simultaneously and analyzed as a system (*255*). We have developed an integrative biophysical approach centered on Mössbauer spectroscopy to study the systems-level distribution of iron within cells and organelles (*226*). ^{57}Fe Mössbauer spectroscopy detects all Fe species in a sample, with spectral intensities proportional to relative Fe concentrations (*119*). In complex systems, Mössbauer generally cannot resolve individual Fe species, but it can

identify groups of such species. This is not ideal, but the resolution of Fe species can be enhanced by EPR, which can detect paramagnetic species, electronic absorption spectroscopy, which can quantify heme chromophores, and ICP-MS, which can quantify the overall Fe concentration.

In this study, we have assessed the Fe content of mitochondria isolated from yeast grown under fermenting, respiro-fermenting, and respiring conditions. Mitochondria play a dominant role in respiration but not fermentation; however, they are essential for cell viability regardless of metabolic growth mode. Fermenting cells produce fewer mitochondria than respiring cells. Early in the exponential growth phase, fermenting cells are largely devoid of mitochondria; in later stages, the organelle occupies ~3% of the cell volume (*232*). Under respiration, mitochondria represent ~10% of the cell volume. Mitochondria in yeast are present as a large tubular network (*256*); the network from fermenting cells is thinner and less branched.

We report here that respiration-related Fe-containing proteins and other $[Fe_4S_4]^{2+}$ cluster-containing proteins dominate the iron content of mitochondria from respiring and respiro-fermenting cells. Under fermention, the concentrations of these species decline while those of non-heme high-spin (NHHS) Fe^{2+} ions, mononuclear HS Fe^{3+} ions, and Fe^{3+} nanoparticles increase. These changes can be rationalized by assuming that the NHHS Fe^{2+} ions constitute a pool used for Fe−S cluster and heme biosynthesis.

Results

Respiring Mitochondria

Western blots of mitochondria isolated from respiring cells showed a 10-fold enrichment of the mitochondrial porin relative to that in cell extracts (Figure 4.1). Since ~10% of the volume of respiring yeast cells is occupied by mitochondria (*232*), this observation indicates that our samples were relatively pure. The membranes of isolated mitochondria were largely intact, in that the IMS protein cytochrome *c* was protected from proteinase K-catalyzed hydrolysis unless deoxycholate was added to disrupt membranes (Figure 4.2). The metal content of samples was determined by ICP-MS (averages in Table 4.1 and individual determinations in Table 4.2).

Low-field Mössbauer spectra of respiring mitochondria were dominated by the "central doublet" (Figure 4.3C, blue line). This doublet [60% of Fe (Table 4.1)] has an isomer shift δ of $\approx$ 0.45 mm/s and a quadrupole splitting ΔE_Q of $\approx$1.15 mm/s, parameters characteristic of both $S = 0$ $[Fe_4S_4]^{2+}$ clusters and LS Fe^{2+} hemes. A minor contribution of $S = 0$ $[Fe_2S_2]^{2+}$ clusters to the central spectral region could not be excluded; fits for the 0.05 T spectra, but not the 8.0 T spectra, were improved by assuming that ~5% of the total Fe was in this form (with δ of 0.27 mm/s and ΔE_Q of 0.55 mm/s).

Respiring mitochondria exhibited a quadrupole doublet with δ of $\approx$0.83 mm/s and ΔE_Q of $\approx$2.4 mm/s, typical of HS Fe^{2+} hemes (*257*). The dashed line above the spectrum of Figure 4.3A is a simulation of this species; its low-energy line is buried under the central doublet. The spectrum also contains a paramagnetic feature, best recognized after

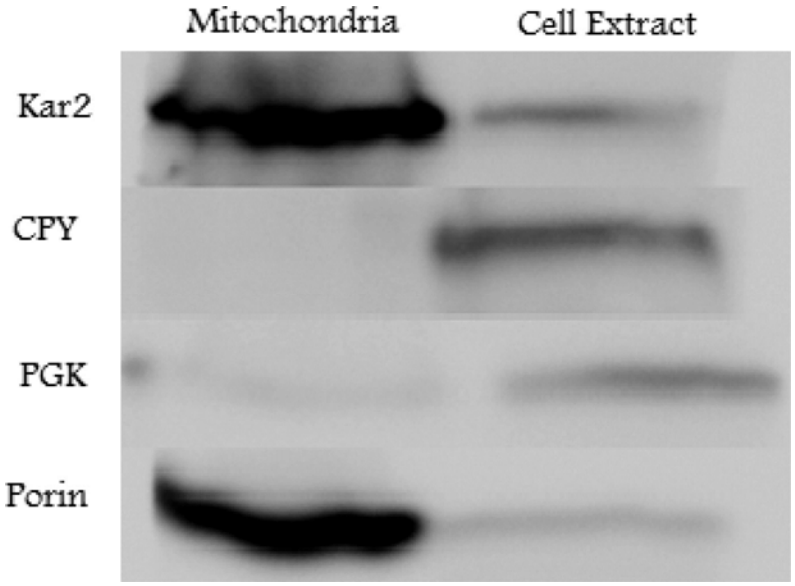

Figure 4.1. Western blot of respirinf mitochondria (left) and the corresponding cell extract (right) (batch R5). In both cases, 60 μg of protein was loaded into the wells of a 10% SDS−PAGE gel. Kar2 is an endoplasmic reticular protein (level increased 5-fold in isolated mitochondria vs cell extract). CPY is a vacuolar protein (level decreased 6-fold). PGK is a cytosolic protein (level decreased 5-fold). Porin is a mitochondrial protein (level increased 10-fold).

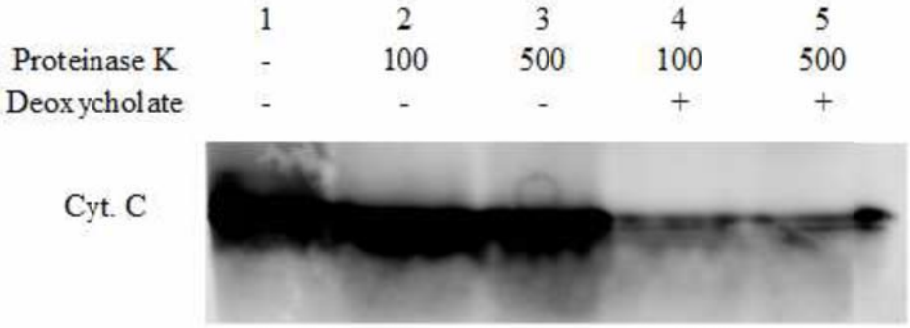

Figure 4.2. Protection of cytochrome c from protease degradation in isolated mitochondria. A sample of isolated mitochondria (50 μg of protein) was subjected to SDS-PAGE using a 12% polyacrylamide gel. Lane 1, control with no proteinase K (Fisher Scientific) added. Lanes 2 and 3, samples treated with 100 μg/mL and 500 μg/mL of proteinase K, respectively for 30 min. Samples were treated with PMSF (1 mM final concentration) for 30 min to inhibit protease activity and then with 0.5% deoxycholate prior to SDS-PAGE. Lanes 4 and 5, samples treated with 100 μg/mL and 500 μg/mL of proteinase K, respectively, in the presence of 0.5% deoxycholate.

Table 4.1. Analytical properties of isolated mitochondria. In the top part, concentrations are for "neat" mitochondria (devoid of residual interstitial solvent). Experimentally determined protein and metal concentrations of mitochondrial suspensions were multiplied by the dilution factor used to prepare these samples from the packed state. Concentrations were also divided by 0.82, the packing efficiency (*221, 226*). Values in the table are the average of the individual determinations given in Table 4.2; the number of samples evaluated is in parentheses. Indicated relative uncertainties reflect variations between samples; additional uncertainties related to fitting are estimated to be ±20%. Heme *a*, *b*, and *c* concentrations were determined from electronic absorption spectra. Entries obtained by Mössbauer spectroscopy are given as a percentage of total Fe. Percentages of HS Fe^{3+} species were determined only from 8.0 T Mössbauer spectra. The bottom part lists estimated concentrations of dominating Fe- and Cu-containing species in yeast mitochondria (in μM).

	Respiring	**respiro-fermenting**	**fermenting**
[protein] (mg/mL)	170 ± 61 (5)	200 ± 60 (2)	110 ± 30 (11)
[Fe] (μM)	720 ± 210 (5)	840 ± 120 (2)	770 ± 320 (11)
[Cu] (μM)	210 ± 170 (5)	160 ± 80 (2)	50 ± 37 (11)
[Mn] (μM)	35 ± 20 (5)	12 ± 4 (2)	15 ± 12 (11)
[Zn] (μM)	290 ± 160 (5)	230 ± 150 (2)	290 ± 210 (11)
central doublet	60 ± 2% (2)	50% (1)	25 ± 4% (5)
HS Fe^{2+} heme	7 ± 1% (2)	4% (1)	4 ± 1% (5)
NHHS Fe^{2+}	2 ± 1% (2)	3% (1)	20 ± 5% (5)
HS Fe^{3+}	0 (2)	5% (1)	15 ± 3% (3)
***S* = 1/2 $[Fe_2S_2]^{+}$**	13 ± 2% (2)	10% (1)	~0% (5)
$[Fe_2S_2]^{2+}$	<5% (2)	<5% (1)	~0% (5)
Fe^{3+} nanoparticles	<5% (2)	<5% (1)	33 ± 7% (5)
unassigned Fe	~20%	~25%	~5% (5)
[Fe^{2+} heme *a*] (μM)	51 ± 8 (4)	61 (1)	14 ± 1 (4)
[Fe^{2+} heme *b*] (μM)	52 ± 8 (4)	55 (1)	27 ± 5 (4)
[Fe^{2+} heme *c*] (μM)	120 ± 10 (4)	160 (1)	73 ± 15 (4)
g_{ave} = 1.95 (μM)	1−10 (3)	13 ± 4 (2)	1−3 (2)
g_{ave} = 1.90 (μM)	13 ± 3 (3)	29 ± 18 (2)	6 ± 2 (2)
***g* = 2.01 (μM)**	0−1 (3)	1−2 (2)	0 (2)
***g* = 2.00 (μM)**	0−2 (3)	0−6 (2)	0−1 (2)
***g* = 2.04 (μM)**	1−3 (3)	3 ± 1 (2)	1−2 (2)
***g* = 4.3 (μM)**	5−45 (3)	2−14 (2)	3 (1)
***g* = 5.8 (μM)**	1−2 (3)	0−2 (2)	~0 (1)
***g* = 6.4, 5.3 (μM)**	1−4 (3)	0−5 (2)	1 (1)
cytochrome *c* oxidase	30	35	8
succinate dehydrogenase	5	10	2
cytochrome bc_1	10	20	6
cytochrome *c*	100	140	60
other HS heme *b*	20	minor	Minor
other LS hemes combined	180	230	100
other $[Fe_4S_4]^{2+}$ only	55	36	13
other $[Fe_4S_4]^{2+}$ + $[Fe_2S_2]^{+}$	Minor	minor	Minor
other $[Fe_2S_2]^{2+}$ only	Minor	minor	Minor
Cu^{1+} pool	120	60	30

Table 4.2: Protein and metal concentrations in isolated mitochondria. Mitochondria isolated from cells grown on glycerol, galactose, and glucose are designated R# (respiring), RF# (respirofermenting) and F# (fermenting), respectively. Batches F1 – F4 were from cells grown on YPD media while F5 – F16 were from cells grown on minimal media. Sample characterizations are denoted (MB) Mössbauer, (U) UV-vis Spectroscopy, (E) EPR, (P) protein analysis and (M) metal analysis.

Batch	Protein (mg/mL)	Fe (μM)	Mn (μM)	Cu (μM)	Zn (μM)	Characterization
R1	200	750	23	360	420	MB, U, E, P, M
R2	180	600	46	63	320	MB, U, E, P, M
R3	110	600	30	59	180	U, P, M
R4	120	670	42	110	82	U, P, M
R5	80	320	6.1	270	200	E, P, M
RF1	200	770	13	80	270	MB, E, P, M
RF2	120	690	8	170	100	U, E, P, M
F1	74	640	30	36	540	U, P, M
F2	64	520	12	95	580	U, P, M
F3	86	650	11	92	220	U, P, M
F4	80	530	27	58	190	U, P, M
F5	120	850	7.2	46	180	MB, P, M
F6	96	280	2.5	14	75	MB, P, M
F7	74	620	6.3	28	220	MB, P, M
F8	120	500	4.8	25	140	MB, P, M
F9	99	560	3.9	22	140	MB, P, M
F10	120	1300	1.6	41	280	E, P, M
F11	89	470	22	4.5	89	E, P, M
F12	N/A	N/A	N/A	N/A	N/A	MB
F13	N/A	N/A	N/A	N/A	N/A	MB
F14	N/A	N/A	N/A	N/A	N/A	MB
F15	N/A	N/A	N/A	N/A	N/A	MB
F16	N/A	N/A	N/A	N/A	N/A	MB

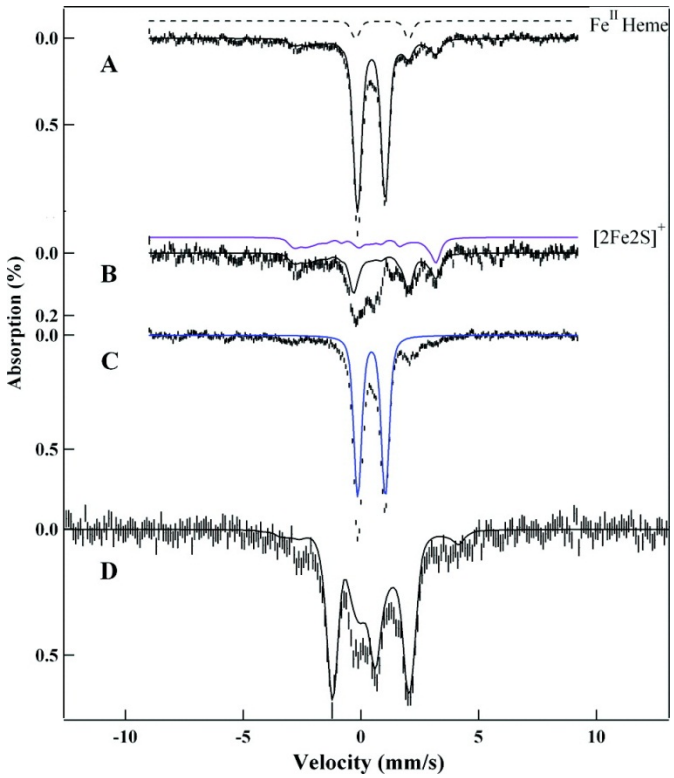

Figure 4.3. Mössbauer spectra of respiring mitochondria (batch R1). (A) At ≈5 K with a 0.05 T field applied parallel to the γ radiation. The black line is a simulation for the sum of the central doublet, HS Fe^{2+} hemes (dashed), and S = ½ $[Fe_2S_2]^+$ clusters. Table 4.1 and the bar graph on page 100 show percentages for all components. (B) Same as panel A after subtraction of the central doublet. The purple solid line is a simulation for S = ½ $[Fe_2S_2]^+$ clusters, while the black solid line is a composite simulation including these species and HS Fe^{2+} hemes. The absorption between 0 and 1 mm/s that is not covered by the black curve is unassigned. (C) Same as panel A but recorded at 100 K. The blue line outlines the contribution of the central doublet in the sample. (D) Same as panel A except at 4.2 K and with an 8.0 T parallel applied field. The black line is a simulation that includes the central doublet and contributions from S = ½ $[Fe_2S_2]^+$ clusters.

removing heme and central doublet contributions. The resulting absorption features (Figure 4.3B) at approximately 3.1 and −2.7 mm/s strongly suggest $S = {}^1/_2$ $[Fe_2S_2]^+$ clusters (due to the Rieske center in the bc_1 complex and the center in succinate dehydrogenase). Assuming the parameters of the Rieske protein (*120*) to simulate the contribution of a generic $S = {}^1/_2$ $[Fe_2S_2]^+$ cluster suggests that ~13% of the Fe in respiring mitochondria is present as such clusters. Analysis of Mössbauer and EPR spectra of another batch [R2 (Figure 4.4A and Figures 4.5 and 4.6)] both yielded ~30 μM for this cluster type. At 100 K (Figure 4.3C), a portion of the magnetic pattern observed at ~5 K has collapsed, revealing that ≤2% of spectral intensity arises from NHHS Fe^{2+} species ($\Delta E_Q \approx$ 3.0 mm/s, and $\delta \approx$ 1.3 mm/s). The black line on the 8.0 T data of Figure 4.3D simulates the central doublet and $S = {}^1/_2$ $[Fe_2S_2]^+$ clusters. After subtraction of the above-mentioned spectral features, some unresolved absorption remains at the center of the spectrum (Figure 4.3B) which could not be assigned unequivocally: a portion may be associated with Fe^{3+} phosphate nanoparticles.

We previously reported that ~22% of the total Fe was present as non-heme Fe^{2+} in respiring mitochondria grown on lactate (*221*). We now suspect that the majority of this was adventitious, as we no longer observe such features with this intensity in spectra of respiring mitochondria. Also, previously reported spectra (*221*) did not include a HS heme doublet, as we observe currently. In the initial stages of this project, samples were not isolated as rapidly as they are currently, and there may have been some heme and/or Fe−S cluster degradation that led to more intense non-heme HS Fe^{2+} doublets.

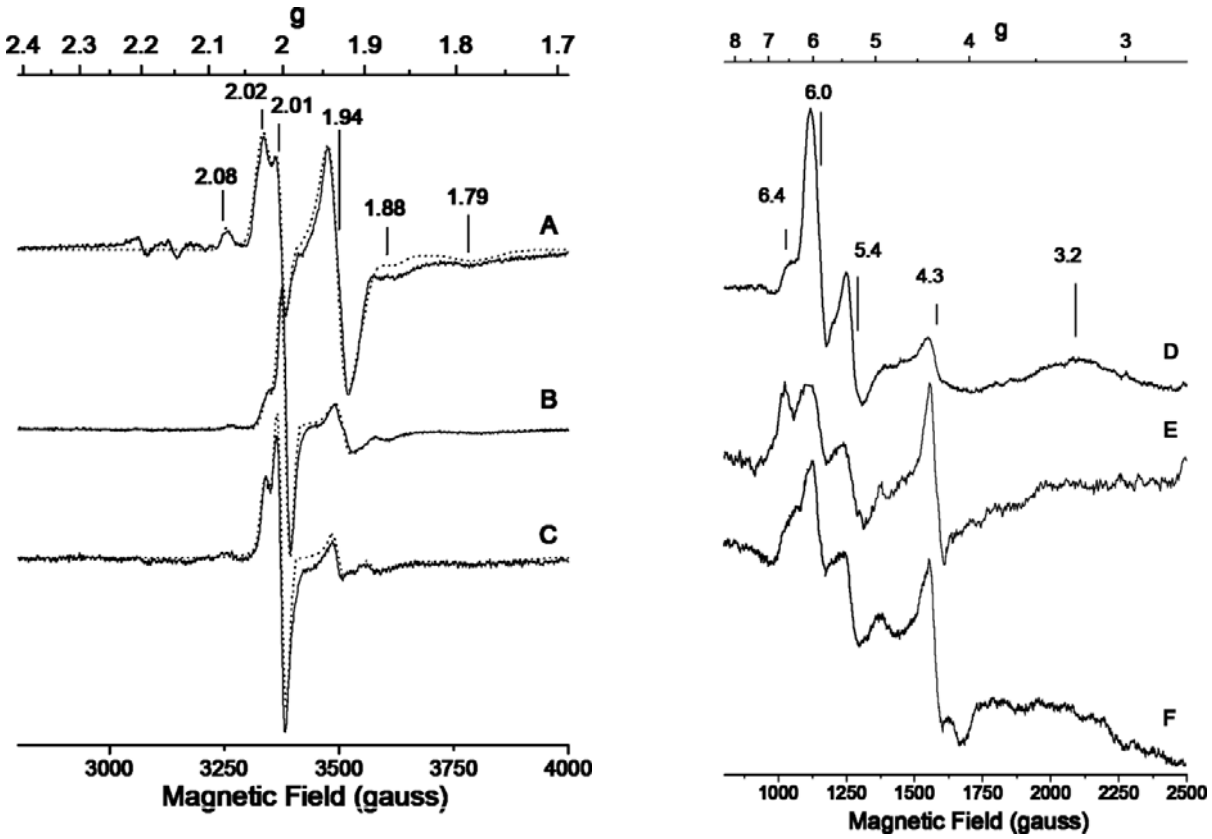

Figure 4.4. EPR spectra (10 K) of mitochondria from various carbon sources. Included are samples from respiring (A, batch R2, decomposition in S5), respiro-fermenting (B, RF1), and fermenting (C, F11) cells. Spectra A and C were recorded at 0.05 mW, and spectrum B was recorded at 0.2 mW. Dashed lines are simulations, with batch-averaged parameters given in Table 4.1. Spectra D−F show the low-field regions of spectra A−C, respectively.

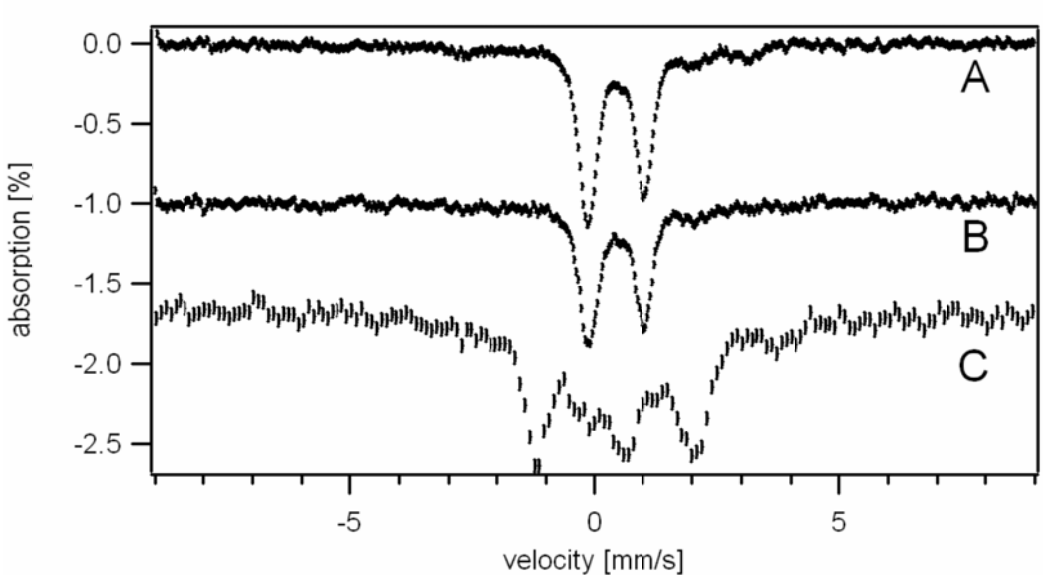

Figure 4.5. Additional Mössbauer spectra of respiring mitochondria (Batch R2). Sample was not shown in Figure 4.3 but used in constructing Table 4.1. A, 4.5 K, 0.04 T parallel field; B, 100 K 0.04 T parallel field; and C, 4.2 K, 8 T applied field.

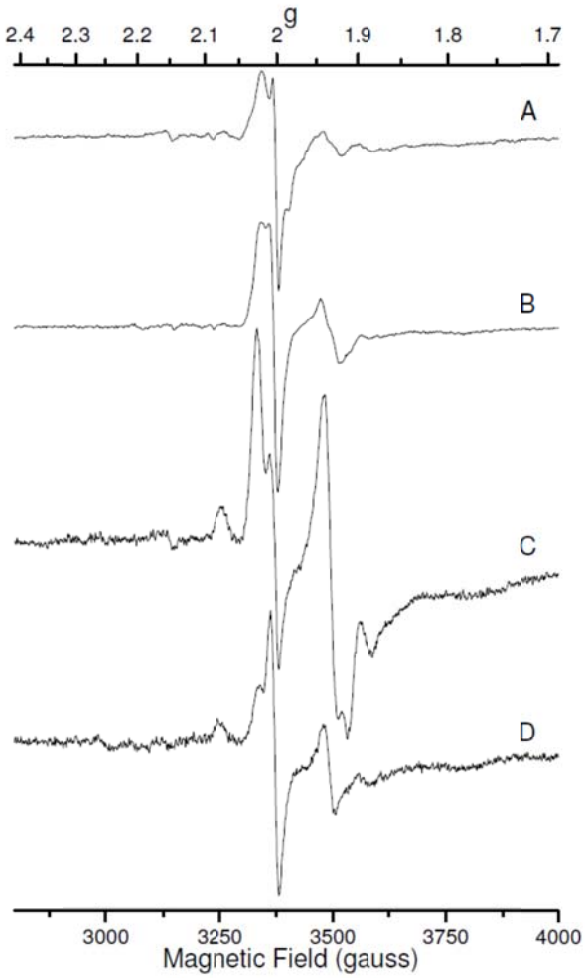

Figure 4.6. Additional EPR spectra (10K) of mitochondria from various carbon sources. Samples are not shown in Figure 4.4 but used in the construction of Table 4.1. Spectra A, B, C and D are from Batches R5, R1, RF2 and F11, respectively. Spectra A, B and D were collected at 0.05 mW microwave power while spectrum C was collected at 0.2 mW. Microwave frequency, 9.468; modulation amplitude, 10 for A, C, D and 5 for B. Spectra A and C were multiplied by 1.5 while D was multiplied by 15.

Mitochondrial suspensions are turbid, leading to electronic absorption spectra with strong sloping baselines due to light scattering (Figure 4.7). Superimposed on this are Soret bands in the 400 nm region and α and β bands in the 500−620 nm region arising from both HS and LS Fe^{2+} hemes (*227*). Spectra of respiring mitochondria were simulated (dashed lines in Figure 4.7A and Figure 4.8) by adding spectra of individual heme *a*-, *b*-, and *c*-containing proteins (Figure 4.9). Resulting concentrations (Table 4.1 and Table 4.3 for individual samples) reveal the dominance of heme *c*, with hemes *b* and *a* present in roughly equal amounts. The HS fraction of these Fe^{2+} hemes affords the heme Mössbauer doublet mentioned above, while the LS portion contributes to the central doublet.

EPR spectra of respiring mitochondria revealed additional details of the paramagnetic species observed by Mössbauer spectroscopy. The low-field region (Figure 4.4D) was dominated by $g \approx 6.0$ ($E/D = 0$) and $g = 6.4$ and 5.4 ($E/D \approx 0.021$) EPR signals; average spin concentrations are listed in Table 4.1. We assign these signals to the [a_3:Cu_b] center of cytochrome *c* oxidase in which heme a_3 is Fe^{3+} and Cu_b is Cu^{1+} (*241*). The $g = 2$ region (Figure 4.4A) was dominated by signals with $g_{ave} = 1.95$ (2.03, 1.93, 1.91), $g_{ave} = 1.90$ (2.02, 1.90, 1.78), and $g_{ave} = 2.02$ (2.08, 1.99, 1.97) and a nearly isotropic signal with $g_{ave} = 2.01$ (perhaps combined with another signal at $g = 2.00$) (*221*). The dashed line in Figure 4.4A is the composite simulation. The $g_{ave} = 1.95$ and 1.90 signals have been assigned to the $[Fe_2S_2]^+$ clusters in succinate dehydrogenase (*258*) and the Rieske protein of cytochrome bc_1, respectively (*221, 259*). The $g_{ave} = 2.01$ signal may originate from an $S = {}^1/_2[Fe_3S_4]^+$ cluster, perhaps from the

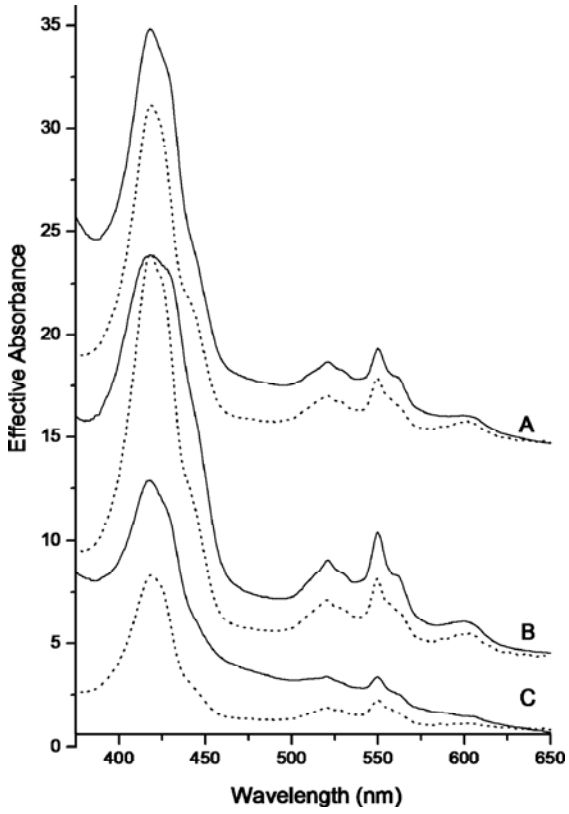

Figure 4.7. Electronic absorption spectra of mitochondrial suspensions. (A) respiring (R1), (B) respiro-fermenting (RF2), and (C) fermenting (F3) samples. Effective absorbances of neat mitochondria normalized to a 10 mm path length cuvette are plotted. These values were obtained by multiplying raw absorbances by 2.0 (the dilution factor relative to packed mitochondria) and 5.0 (path length factor due to the use of a 2 mm path length cuvette) and by dividing by 0.82 (the packing factor). Dashed lines are composites from individual heme a-, b-, and c-containing proteins, using parameters listed in Table 4.2 (averages in Table 4.1).

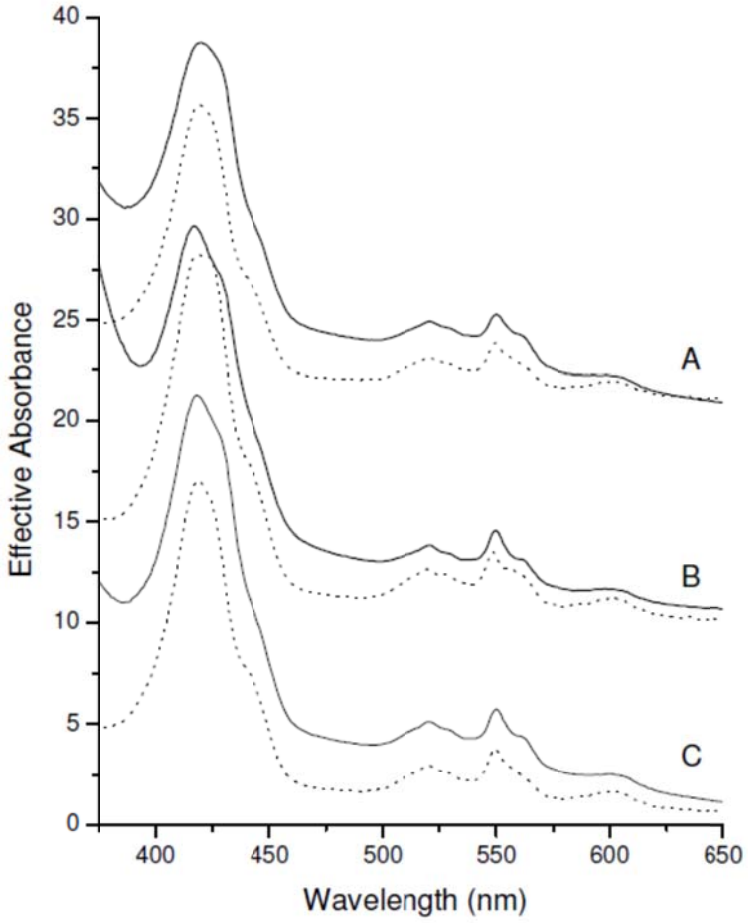

Figure 4.8. Electronic absorption spectra of respiring mitochondrial suspensions. A, Batch R3 (protein concentration, 45 mg/mL); B, Batch R4 (44 mg/mL); and C, Batch R2 (74 mg/mL). Dotted lines are composite spectra using the [Heme a], [Heme b], and [Heme c] concentrations given in Table 4.3.

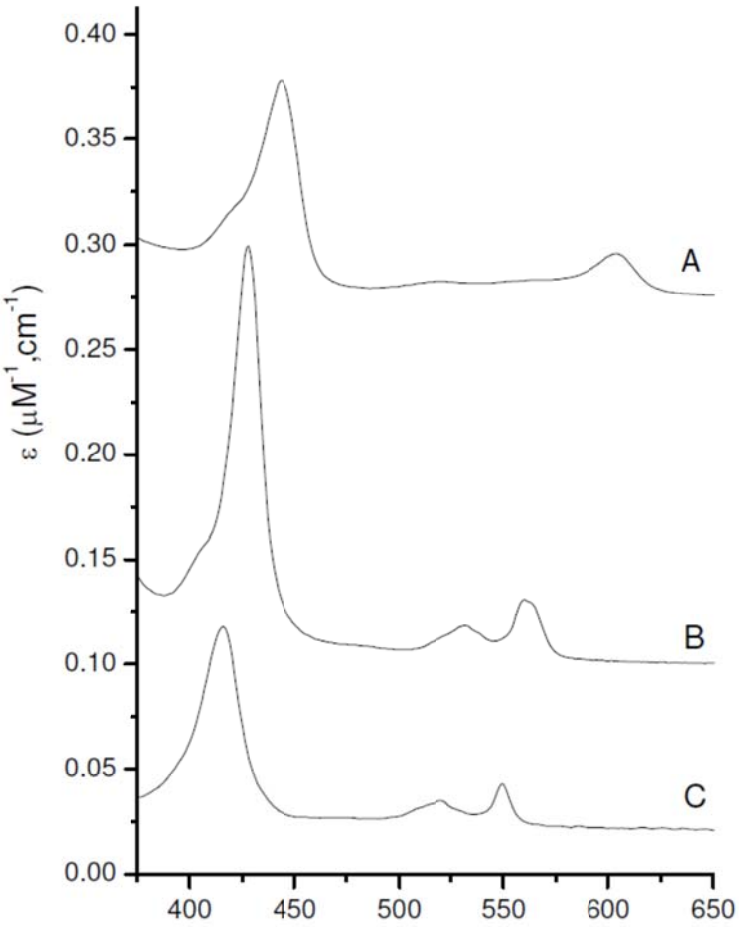

Figure 4.9. Electronic absorption spectra of heme-containing proteins. A, cytochrome c oxidase; B, cytochrome b5; C, cytochrome c. The heme b in cytochrome b5 is LS, whereas the heme b groups in mitochondria are both LS and HS. The spectrum of HS heme b differs, but the extinction coefficients in the region used in fitting (~ 560 nm) was insignificantly different. Thus, our estimate of the heme b concentration in mitochondria will not be affected by calibrating with a LS center.

Table 4.3. Concentrations of each heme component for individual samples (in μM). Values indicated are for neat mitochondria. Estimated uncertainties are ± 20% for each entry.

Batch	[Heme *a*]	[Heme *b*]	[Heme *c*]
R1	45	43	110
R2	55	44	130
R3	60	60	130
R4	44	44	120
F1	15	30	85
F2	15	33	85
F3	13	22	61
F4	12	23	61

cluster in succinate dehydrogenase. The $g = 2.00$ signal probably arises from an organic-based radical. The $g_{ave} = 2.02$ feature may arise from ET flavoprotein-ubiquinone oxidoreductase (*260*). Minor resonances between $g = 2.2$ and $g = 2.1$ are often observed but remain unassigned. The bulk of the spin concentration in the $g = 2$ region belongs to $[Fe_2S_2]^+$ clusters that are most evident in Mössbauer spectra. The remainder belongs to minor species some of which may account for the unresolved background in the Mössbauer spectra. These results were generally similar to those reported for mitochondria isolated from yeast grown on glucose and lactate (*221*).

Respiro-Fermenting Mitochondria

Metal concentrations of mitochondria isolated from respiro-fermenting cells were similar to those of respiring mitochondria, except that the Mn concentration was 2-fold lower (Table 4.1). Mössbauer spectra (Figure 4.10) were also similar. Compared to respiring mitochondria, the proportion of Fe present as the central doublet, HS Fe^{2+} hemes, and magnetic Fe in respiro-fermenting mitochondria declined slightly, while the percentages of NHHS Fe^{2+} and the unassigned absorption in the center of the spectra increased slightly. A minor contribution of NHHS Fe^{2+} (~2%) was assessed using the 100 K spectrum of Figure 4.10B. The presence of unassigned species is evident from the mismatch of the spectrum and simulation (Figure 4.10A) at ~0 mm/s. The 8.0 T spectrum reveals the presence of mononuclear HS Fe^{3+} ions (Figure 4.10C, cyan line). The black line in Figure 4.10C is a simulation of the diamagnetic Fe associated with the central doublet at low field, together with a generic $S = {}^1/_2$ $[Fe_2S_2]^+$ cluster. EPR of a well-packed sample of the same batch yielded a spin concentration of 42 μM for the sum

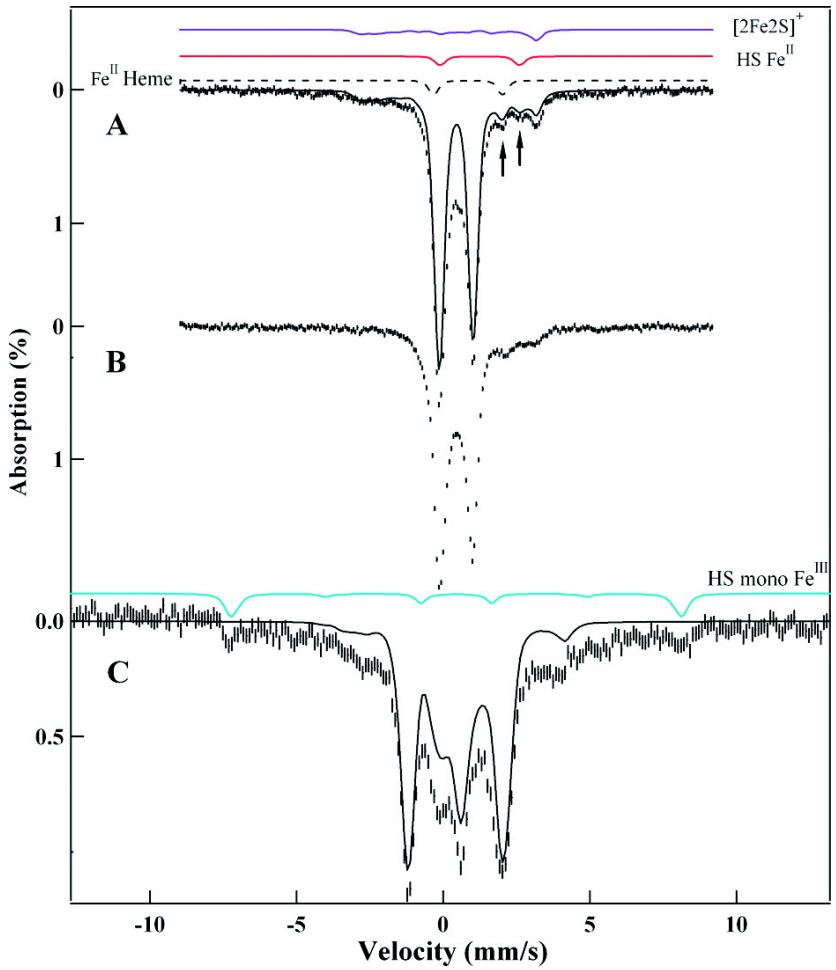

Figure 4.10. Mössbauer spectra of respirofermenting mitochondria (RF1). (A) Spectrum measured at ~5 K with a 0.05 T field applied parallel to the γ radiation. The black line is a simulation for the central doublet, HS Fe^{2+} hemes, NHHS Fe^{2+}, and S = 1/2 $[Fe_2S_2]^+$ clusters. The lines above the spectrum are simulations for S = 1/2 $[Fe_2S_2]^+$ (purple), non-heme HS Fe^{2+} (red), and HS Fe^{2+} heme (black dashed line). (B) Same as panel A but at 100 K. (C) Same as panel A but at 8.0 T and 4.2 K. The black line is a simulation for the central doublet and S = 1/2 $[Fe_2S_2]^+$ clusters. The cyan line above is a simulation for HS mononuclear Fe^{3+} species. See Table 4.1 for the concentrations of various species.

of the g_{ave}= 1.95 and 1.90 signals, suggesting that ~10% of the Fe belongs to $[Fe_2S_2]^+$ clusters. This value is similar to that suggested by the Mössbauer data. The electronic absorption spectrum of respiro-fermenting mitochondria (Figure 4.7B) revealed heme *a*, *b*, and *c* concentrations (Table 4.1) similar to those of respiring mitochondria.

Fermenting Mitochondria

Protein and Fe concentrations for fermenting mitochondria (Table 4.1) were again similar to those of respiring and respiro-fermenting mitochondria; the protein concentration might be reduced somewhat, but the variability was too high to establish this. The Mn concentration was similar to that in respiro-fermenting mitochondria and substantially lower than in respiring mitochondria. The Cu concentration was ~4-fold lower than those in respiring or respiro-fermenting mitochondria. Mössbauer spectra of fermenting mitochondria (Figure 4.11) are described in detail elsewhere (*261*); here we summarize that description. The spectra differed substantially from those of respiring or respiro-fermenting mitochondria in that there was a substantial decline in the fraction of Fe associated with the central doublet and an increase in the proportion of NHHS Fe^{2+} and Fe^{3+} nanoparticles (δ = 0.52 mm/s, and ΔE_Q = 0.63 mm/s). Electronic absorption spectra (Figure 4.7C and Figure 4.12) exhibited lower concentrations of heme centers (Table 4.1 and Table 4.3), consistent with the decline of the HS Fe^{2+} heme doublet in Mössbauer spectra. EPR spectra of fermenting mitochondria (Figure 4.4C,F) were qualitatively similar to those of respiring and respiro-fermenting mitochondria, but with lower spin concentrations (Table 4.1). The g = 6 features, assigned to the partially

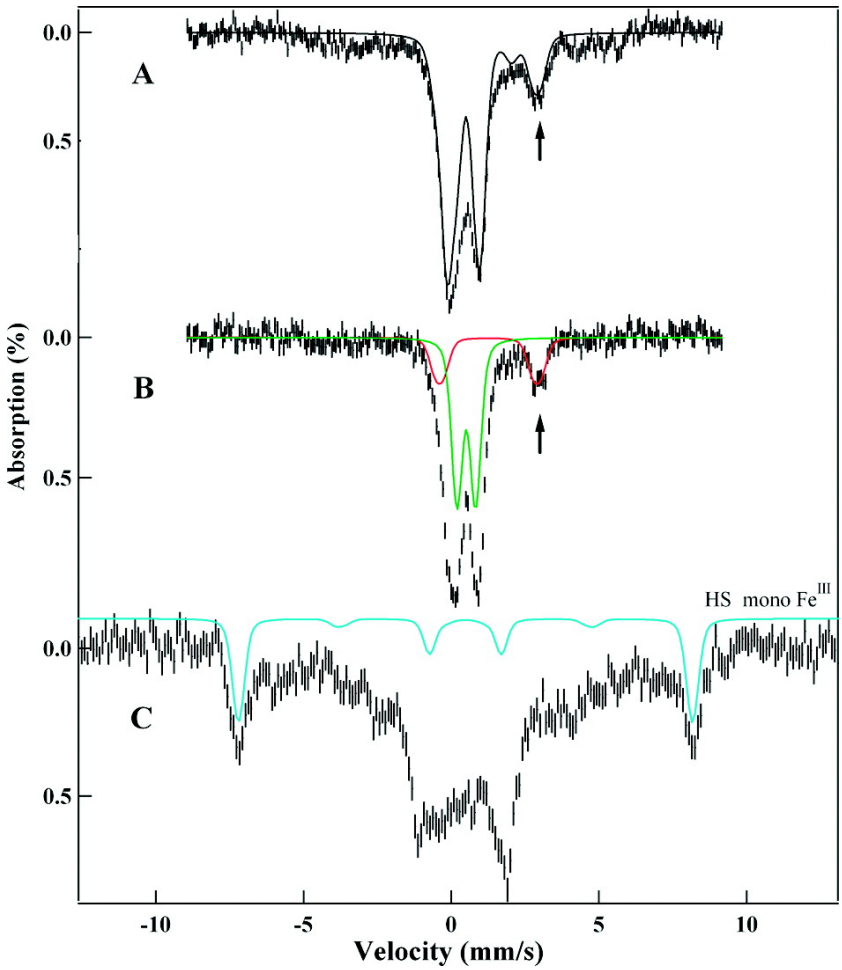

Figure 4.11. Mössbauer spectra of fermenting mitochondria (batch F9). (A) Spectrum measured at ~5 K with a 0.05 T field applied parallel to the γ radiation. The black line is a simulation for the sum of the central doublet, HS Fe^{2+} hemes, NHHS Fe^{2+} (high-energy line indicated by the arrow), and the Fe^{3+}nanoparticles. (B) Same as panel A except at 100 K. The red line indicates HS Fe^{2+}; the green line indicates the nanoparticle contribution (the doublet representing nanoparticles contains 20% of total Fe at ~5 K and 35% at 100 K; at 5 K the larger nanoparticles contribute a magnetically broadened spectrum). (C) Same as panel A except at 8.0 T and 4.2 K. The cyan line is a simulation for the HS Fe^{3+}. See Table 1 for the concentrations of various species.

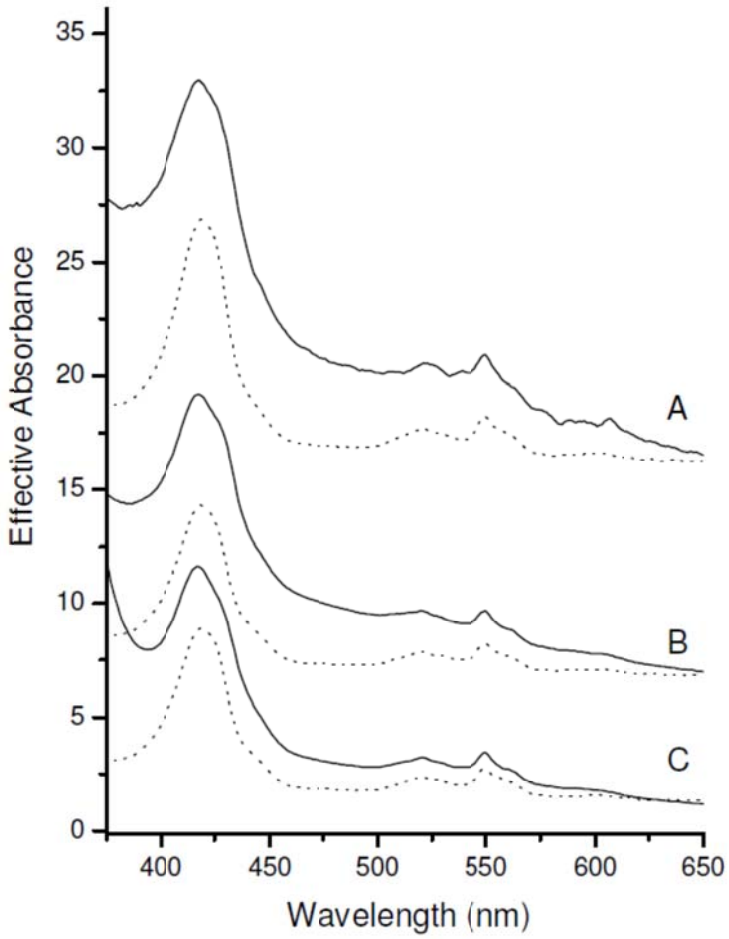

Figure 4.12. UV-vis spectra of different batches of fermenting mitochondria. A, Batch F4 (33mg/mL); B, Batch F1 (30 mg/mL) and C, Batch F2 (27 mg/mL). Dotted lines are composite spectra using the concentrations given in Table S2.

oxidized a_3:Cu_b site of cytochrome *c* oxidase, declined as expected. Summing spin concentrations of the signals in the $g = 2$ region suggests that ≤3% of the Mössbauer spectral intensity should be associated with $S = {}^1/_2$ species, a fraction too small to be detected in the presence of increased amounts of NHHS Fe^{2+} and ferric nanoparticles.

Discussion

The main objective of this study was to characterize the distribution of the major Fe species in mitochondria isolated from respiring, respiro-fermenting, and fermenting yeast cells. In the following we integrate the results from the various techniques with the known composition of proteins in mitochondria, beginning with the respiring state. Our data allow an estimate of the absolute concentration of cytochrome *c* oxidase in the organelle. As few other heme *a*-containing proteins are found in mitochondria, the heme *a* concentration essentially reflects twice the cytochrome *c* oxidase concentration. Mitochondrial heme monoxygenase may have substoichiometric amounts of heme *a* bound, but we will assume that this is insignificant. The total Fe^{2+} heme *a* concentration in respiring mitochondria (Table 4.1, top part) suggests an average concentration of ~25 μM for cytochrome *c* oxidase with reduced heme *a* species (Table 4.1, bottom part). The absence of $g \sim 3$ EPR signals indicates the lack of LS Fe^{3+} hemes in respiring mitochondria. Since cytochrome *c* oxidase contains 3 molar equiv of Cu, ~40% of the total Cu in respiring mitochondria should be in this enzyme. Most of the remainder might belong to a Cu^{1+} pool (*224*). The percentage of mitochondrial Cu that we estimate for this pool (~60%) is smaller than the previous

estimate (~90%). The absence of Cu^{2+} EPR signals in our preparations is consistent with a Cu^{1+} oxidation state for this pool.

The HS Fe^{2+} heme quadrupole doublet of respiring mitochondria should include contributions from heme a_3- and HS heme *b*-containing proteins (we are unaware of any HS heme *c*-containing proteins). After subtraction of the heme a_3 contribution, the HS heme *b* species in respiring mitochondria (Table 4.1, bottom part) are likely to be found in cytochrome *c* peroxidase, catalase, and NO oxidoreductase, among others. Subtracting the HS heme *b* concentration from the total heme *b* concentration suggests that the concentration of LS heme *b* species in mitochondria is ~30 μM. These chromophores are found in succinate dehydrogenase (one heme*b*), cytochrome bc_1 (two heme *b* molecules), and others such as cytochrome b_2 and Cox15p. This can be described by the relationship:

30μM = [succinate dehydrogenase] + 2[cytochrome bc_1] + others.

As the spin concentrations for the g_{ave} = 1.95 and 1.90 EPR signals indicate the concentrations of succinate dehydrogenase (~5 μM) and cytochrome bc_1 (~10 μM), respectively, this relationship implies that most LS heme *b* centers in mitochondria reside in these two respiratory complexes.

The known heme *c*-containing proteins in mitochondria include cytochrome c_1 and two isoforms of cytochrome *c*. Removing the cytochrome bc_1 concentration suggests that the collective concentration of the isoforms is ~110 μM. This indicates that the heme *a* and *c* contents of respiring mitochondria are dominated by cytochrome *c* oxidase and cytochrome *c*, respectively. The heme *b* content

is more evenly distributed between HS and LS, with LS forms dominated by succinate dehydrogenase and cytochrome bc_1. Concentrations in Table 4.1 (bottom part) were calculated with respect to the entire mitochondrial volume. Since species are located in particular regions of the mitochondria, their regional concentrations will be higher. Succinate dehydrogenase contains 10 molar equiv of Fe (one LS heme *b*, one Fe_2S_2 cluster, one Fe_3S_4 cluster, and one Fe_4S_4 cluster), so a concentration of ~5 μM for this respiratory complex implies an ~50 μM Fe contribution overall. Similarly, cytochrome bc_1 contains 5 molar equiv of Fe (one heme c_1, two heme *b* molecules, and one Fe_2S_2 cluster), also implying an ~50 μM overall Fe contribution. Including a 60 μM Fe contribution for cytochrome *c* oxidase and 110 μM for cytochrome *c* reveals that respiration-related complexes constitute ~40% of the iron in respiring yeast mitochondria.

The central doublet of the Mössbauer spectra of respiring mitochondria includes contributions from $[Fe_4S_4]^{2+}$ clusters and LS Fe^{2+} hemes. Table 4.1 and the relationships mentioned above suggest ~30 μM (LS heme *a*) + ~30 μM (LS heme *b*) + ~120 μM (LS heme *c*) = ~180 μM LS Fe^{2+} hemes. Subtracting this from the central doublet leaves ~35% of the mitochondrial Fe in the form of $S = 0$ $[Fe_4S_4]^{2+}$ clusters. This corresponds to ~250 μM Fe or to ~60 μM of such clusters. Subtracting an additional 5 μM contribution due to the succinate dehydrogenase $[Fe_4S_4]^{2+}$cluster leaves ~55 μM for Fe_4S_4 clusters in other mitochondrial proteins.

Some mitochondrial proteins contain only Fe_4S_4 clusters; some contain only Fe_2S_2 clusters, and some contain both cluster types. We have attempted to fit simulations

of oxidized $[Fe_2S_2]^{2+}$clusters into the Mössbauer spectra of respiring mitochondria, but we have no clear evidence of their presence. This suggests for respiring mitochondria that the majority of $[Fe_4S_4]^{2+}$clusters that are not contained in succinate dehydrogenase reside in proteins that contain only $[Fe_4S_4]^{2+}$ clusters.

Respiro-fermenting and fermenting mitochondria were analyzed similarly (Table 4.1, bottom part); results are summarized by the bar chart in Figure 4.13. In general, the total Fe concentration was similar regardless of metabolic mode. Also, the overall distribution of Fe in respiro-fermenting mitochondria was similar to that in respiring mitochondria. In contrast, the Fe distribution in fermenting mitochondria was dramatically different. This suggests that the repression of respiration by glucose, rather than the occurrence of fermentation per se, is responsible for the major shifts observed in Fe distribution. Thus, we will simplify our further analysis by averaging the Fe distributions observed for respiring and respiro-fermenting mitochondria and then compare this to the distribution obtained under fermentation.

Viewed in the respiration → fermentation direction, cytochrome *c* oxidase ↓ (declined) 4-fold, succinate dehydrogenase ↓ 3.8-fold, cytochrome bc_1 ↓ 2.5-fold, cytochrome *c* ↓ 2-fold, LS hemes generally ↓ 2-fold, and $[Fe_4S_4]^{2+}$ cluster-containing proteins ↓ 3.5-fold. The Cu^{1+} pool decreased 3-fold. The decline in the size of the Cu^{1+} pool upon shifting from respiration to fermentation contrasts with a previous report (*224*) that the concentration of this pool is independent of metabolic growth mode. In terms of Fe pools, the NHHS Fe^{2+} pool, the mononuclear HS Fe^{3+}pool, and the

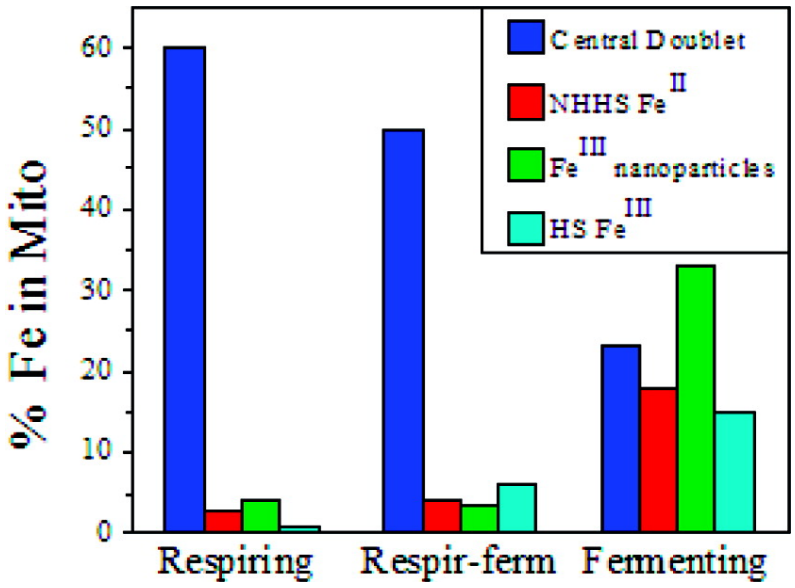

Figure 4.13. Bar graph of major forms of Fe present in mitochondria. Included are respiring, respiro-fermenting, and fermenting mitochondria. Color-coding is matched to simulated features in previous Mössbauer figures.

Fe^{3+} nanoparticles went from nearly undetectable in respiring mitochondria to representing ~75% of the Fe in the fermenting organelle. These dramatic changes reflect major differences in the way that Fe is handled by the cell, depending on metabolic mode.

We do not know the location of these pools within mitochondria but suspect that they are located in the matrix. Nor are the ligands coordinating the Fe in these pools known. The ferric ions in the Fe^{3+} nanoparticles found in Atm1-depleted mitochondria appear to be coordinated by ligands with oxygen donors but essentially lacking in N, S, or C atoms (*105*). Phosphate, water, and hydroxide ligands were suggested as likely ligands in these nanoparticles, and similar ligands might be associated with the nanoparticles observed in mitochondria from wild-type fermenting cells. The non-heme high-spin Fe^{2+} pool may consist of multiple species. Some mitochondrial proteins (e.g., frataxin, ferrochelatase, Fe−S cluster scaffold proteins, and CoQ7) may coordinate HS Fe^{2+} ions, but the collective concentration of these proteins may be insufficient to account for the overall concentration of the NHHS Fe^{2+} pool (~150 μM in fermenting mitochondria). Seguin et al. (*262*) determined that yeast cells grown under similar conditions contained ~1300 copies of Yfh1p. If we assume 60×10^{-15} L for the volume of a yeast cell (*263-266*), that 3% of that volume was due to mitochondria (*267, 268*), and that each Yfh1p bound two Fe^{2+} ions (*269*), this would correspond to a concentration of ~70 nM. Even if there were a dozen such proteins in mitochondria, their collective concentration would be 2 orders of magnitude lower than that present in the NHHS Fe^{2+} pool of fermenting mitochondria. These considerations strongly suggest that the

nonheme HS Fe^{2+} pool is dominated by nonproteinaceous low-molecular weight complexes.

The results of this study can be compared to those of proteomic studies that also indicate substantial changes in the yeast mitochondria proteome due to the diauxic shift (*255*). The concentrations of 17 proteins are significantly lower in fermenting versus respiring cells, including cytochrome *c* oxidase, cytochrome bc_1, and succinate dehydrogenase (*270*). The mitochondrial transcriptome changes more dramatically, with levels of transcripts of cytochrome *c* isoform 1 and Mn-superoxide dismutase (MnSod2) declining under fermentation (*271, 272*). Other groups have also reported lower SOD2 protein and transcript levels under fermentation (*273, 274*). Our results are consistent, including the 3-fold increase in the Mn concentration of respiring mitochondria relative to respiro-fermenting and fermenting conditions which might reflect changes in the levels of MnSod2 or associated Mn species.

The observed changes in the distribution of Fe in mitochondria isolated from cells grown under different metabolic modes can be interpreted given the known roles of mitochondria in respiring versus fermenting cells. In respiring cells, these organelles are critical for energy production, which requires the biosynthesis of Fe−S clusters and heme centers, as well as their installation into apo-respiratory complexes. Under fermentation conditions, energy production is associated with glycolysis, where no such centers are involved. Thus, the level of production of Fe−S clusters and heme centers is probably reduced in fermenting mitochondria because the metabolic need for these centers is reduced. Our results suggest a 3-fold reduction in these centers. Residual amounts of

such centers might allow fermenting cells to convert rapidly into respiration mode as environmental conditions change.

The Fe used to synthesize mitochondrial Fe−S clusters and hemes is imported into the organelle as Fe^{2+} (*80*). Neither the structure nor the composition of the imported complex(es) is(are) known, but each is probably of low molecular weight as each must pass through transporters in the IM (*47*). We propose that the non-heme HS Fe^{2+} ions present in fermenting mitochondria are these imported ions and that they serve in this capacity. The simple model of Figure 4.14 assumes this role and can rationalize the observed changes in the level of this pool. During respiration, the size of the Fe^{2+} pool is small since the biosynthesis rates of Fe−S clusters and hemes are elevated. During fermentation, the pool increases because the rate of Fe−S cluster and heme biosynthesis is diminished. Consistent with the nearly invariant Fe concentrations in respiring and fermenting mitochondria, the overall rate of Fe^{2+} import appears to be unaffected by changes in metabolic growth mode; i.e., the cell does not seem to regulate the rate of import of Fe^{2+} into mitochondria according to metabolic growth mode. Understanding Fe fluxes at the cellular level will require that the different percentage volumes occupied by mitochondria in fermenting versus respiring cells be taken into account. Another uncertainty, at the mitochondrial level, is the relationship between the NHHS Fe^{2+} pool and the other pools of Fe in fermenting mitochondria, including Fe^{3+} nanoparticles, mononuclear HS Fe^{3+} ions, and the central unresolved material. The three pools may exist in a dynamic equilibrium with each other, or they might be independent (e.g., imported by different IM transporters). Also uncertain is the cellular function of these

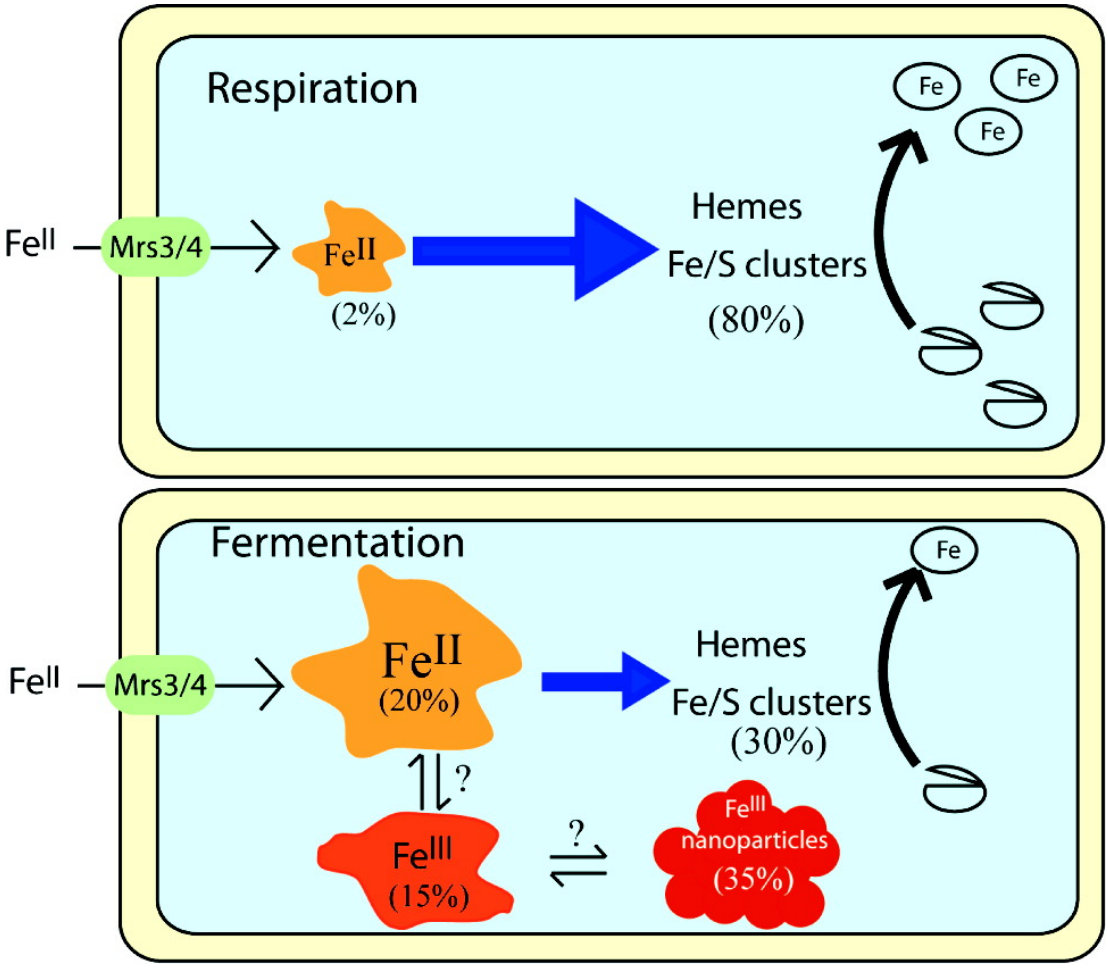

Figure 4.14. Model describing the shift in the iron content of mitochondria with metabolic growth mode. The size of the NHHS Fe^{2+} pool is dictated by the balance of input and output fluxes. During respiration, the pool is small (~15 μM). When cells ferment, the rate of Fe–S cluster and heme biosynthesis declines, causing the pool to enlarge (~150 μM). The rate of import of Fe^{2+} from the cytosol is not significantly affected by the change in metabolism. Under fermenting conditions, a portion of the NHHS Fe^{2+} pool may become oxidized to mononuclear non-heme HS Fe^{3+}, a subset of which may precipitate as Fe^{3+} nanoparticles.

other pools. They certainly store Fe in fermenting mitochondria, and the absence of these pools during respiration suggests either that these pools can be utilized under respiratory growth conditions or that they never form under these conditions. However, whether this is a cellular *strategy* for storing Fe, analogous to mitoferrin in human mitochondria (*275*), is uncertain. These pools may possibly result from an insufficient concentration of a coordinating ligand or a shift of either pH or oxidation status in fermenting mitochondria. We favor this latter characterization especially for the Fe^{3+} nanoparticle pool, in that the ligands coordinating these ions are probably not protein-bound and thus would not be under the direct genetic control of the cell. Nevertheless, this pool may indirectly impact cellular function, e.g., by generating reactive oxygen species during its formation, and it may be bioavailable under particular metabolic conditions.

CHAPTER V

BIOPHYSICAL CHARACTERIZATION OF FERMENTING YEAST CELLS, ISOLATED VACUOLES FROM FERMENTING CELLS, AND THE AFT1-1^{UP} STRAIN*

Introduction

When this project started the original motivation was to establish whether biophysical probes could be used to gain insight into processes such as iron trafficking, homeostasis, and regulation. At the onset, mitochondria were studied because of their role in such processes. We realized however that mitochondria are only one organelle in the cell, and were intrigued to apply the same methods to study iron in an entire cell. From this stemmed an additional motivation to probe iron in other organelles, namely vacuoles.

Vacuoles are the major site of cellular iron storage and detoxification. They prevent the formation of ROS by sequestering iron (*61, 276*). They have a lower pH than

---

*This chapter is reproduced in part with permission from "A Nonheme High-Spin Ferrous Pool in Mitochondria Isolated from Fermenting *Saccharomyces cerevisiae*" by Gregory P. Holmes-Hampton, Ren Miao, Jessica Garber-Morales, Yisong Guo, Eckard Munck, Paul A. Lindahl, 2010, *Biochemistry*, 49, 4227-4234, copyright 2010 American Chemical Society, "Mössbauer and EPR Study of Iron in Vacuoles from Fermenting *Saccharomyces cerevisiae"* by Allison L. Cockrell, Gregory P. Holmes-Hampton, Sean P.McCormick, Mrinmoy Chakrabarti, and Paul A. Lindahl, 2011, *Biochemistry*, 50, 10275-10283, copyright 2011 American Chemical Society, and "Biophysical Investigation of the Iron in Aft1-1^{up} and Gal-YAH1*Saccharomyces cerevisiae*" by Ren Miao, Gregory P. Holmes-Hampton, and Paul A. Lindahl, 2011, *Biochemistry*, 50, 2660-2671,copyright 2011 American Chemical Society.

the cytosol. This raises the electrochemical potential of the glutathione disulfide/glutathione couple.

The higher potential results in a more oxidizing environment. This has led previous researchers to hypothesize that the iron inside the vacuole is Fe^{3+} (*58, 59*).

There are two major pathways of iron import into the vacuole. The first involves ccc1p, the only known vacuolar iron importer (*62*). Although the exact substrate of ccc1p is still unknown, the Fe^{2+} state is assumed (*61, 64, 277*). Gene expression of *CCC1* is responsive to the iron content of the cytosol. *CCC1* mRNA is destabilized under iron deficient growth conditions (*278*).

The second pathway of iron import involves endocytosis. The majority of the iron in the vacuole appears to enter through ccc1p. Cells that are unable to endocytose have substantially higher iron content than Δccc1 cells (*62*), suggesting that the majority of the iron in the vacuole enters through ccc1p.

The vacuole has two systems of iron export, called Fth1p/Fet5p and Smf3p. Fth1p/Fet5p is homologous to the plasma membrane iron acquisition pathway involving Ftr1p/Fet3p. A similar mechanism has been implicated in the Ftr1p/Fet3p system. The Ftr1p/Fet3p system utilizes the reductase Fre6p to facilitate iron export (*59, 279*). The Smf3p system also uses this reductase. Smf3p is a divalent metal exporter of Fe^{2+}, among other substrates (*66, 280, 281*).

Iron homeostasis is controlled by both the vacuoles and mitochondria. *ΔΔmrs3/4* cells exhibit a growth defect in iron-deficient medium but they grow normally on iron-replete medium. Conversely, *Δccc1* cells grow normally in iron deficient medium but

show a growth defect on high-iron medium (*62*). Ccc1p-deficient vacuoles may be unable to import cytosolic iron, and the excess cytosolic iron inhibits cell growth, perhaps via ROS damage (*282*). Toxicity can be suppressed by overproducing Mrs3/4p (*282*), perhaps because excess Fe_{cyt} can be imported into the mitochondria which somehow detoxifies it.

A common phenotype in cells which possess mutations in the ISC biosynthetic pathway is the accumulation of nanoparticles in the mitochondria (*105-107*). However, no accumulation occurs (and there is no respiratory defect) in ISC-mutant cells in which *mrs3/4* have also been deleted (*81*), implying that this nanoparticle-forming iron enters via Mrs3/4p. Overexpressing Ccc1p also prevents Fe accumulation (*283*).

Mitochondria and vacuoles interact functionally. In *ΔΔmrs3/4* cells, mitochondria are deficient in iron and have reduced ISC and heme levels, and reduced aconitase activity, perhaps due to an inability to import sufficient iron into the organelle (*79*). Meanwhile, the vacuolar iron level is increased, via the activation of Ccc1p, so as to store iron that would otherwise be in the cytosol. The activation of Ccc1p may reduce cytosolic iron levels and thus activate Aft1p (*283*). Aconitase activities are recovered when Ccc1p is deleted, again implying that vacuoles and mitochondria draw from a common pool of cytosolic iron.

The Aft1-1^{up} strain has a mutation in Aft1p (C291F) that causes it to remain in the nucleus and constitutively activate Aft1p-controlled iron regulon genes, regardless of the iron status of the medium. This stimulates the uptake of iron regardless of the

medium Fe concentration. Aft1-1^{up} cells cultivated in rich medium (with high iron) contain higher than WT iron levels (*223*).

This chapter summarizes biophysical studies on fermenting yeast cells, vacuoles isolated from fermenting yeast cells, and the yeast strain Aft1-1^{up}. Ms. Allison Cockrell, a graduate student in the Lindahl lab, was primarily responsible for the studies involving isolated vacuoles, and Dr. Ren Miao, who at the time was a graduate student in the lab, was primarily responsible for the studies involving Aft1-1^{up}. My role on both studies was to setup, operate and maintain the Mössbauer spectrometers, help collect their spectra, and to analyze the Mössbauer spectra we obtained. I also prepared the whole cell samples for the studies on vacuoles and the wild type cell and mitochondrial samples for the Aft1-1^{up} studies. I also participated in broader discussions regarding these projects.

Results and Discussion

Whole Yeast Cells

^{57}Fe-enriched whole fermenting yeast cells grown on minimal medium supplemented with 40 μM ^{57}Fe exhibited 5 K Mössbauer spectra dominated by features indicating magnetically noninteracting mononuclear HS Fe^{3+} components (Figure 5.1). These components have vanishingly small spin-dipolar interactions with other paramagnetic iron sites. At 0.05 T (Figure 5.1A), they display paramagnetic hyperfine structure; a quadrupole doublet would be expected if spin-dipolar interactions were effective or if the Fe^{3+} component belonged to nanoparticles with a T_B of <<4 K. At 8T (Figure 5.1C),

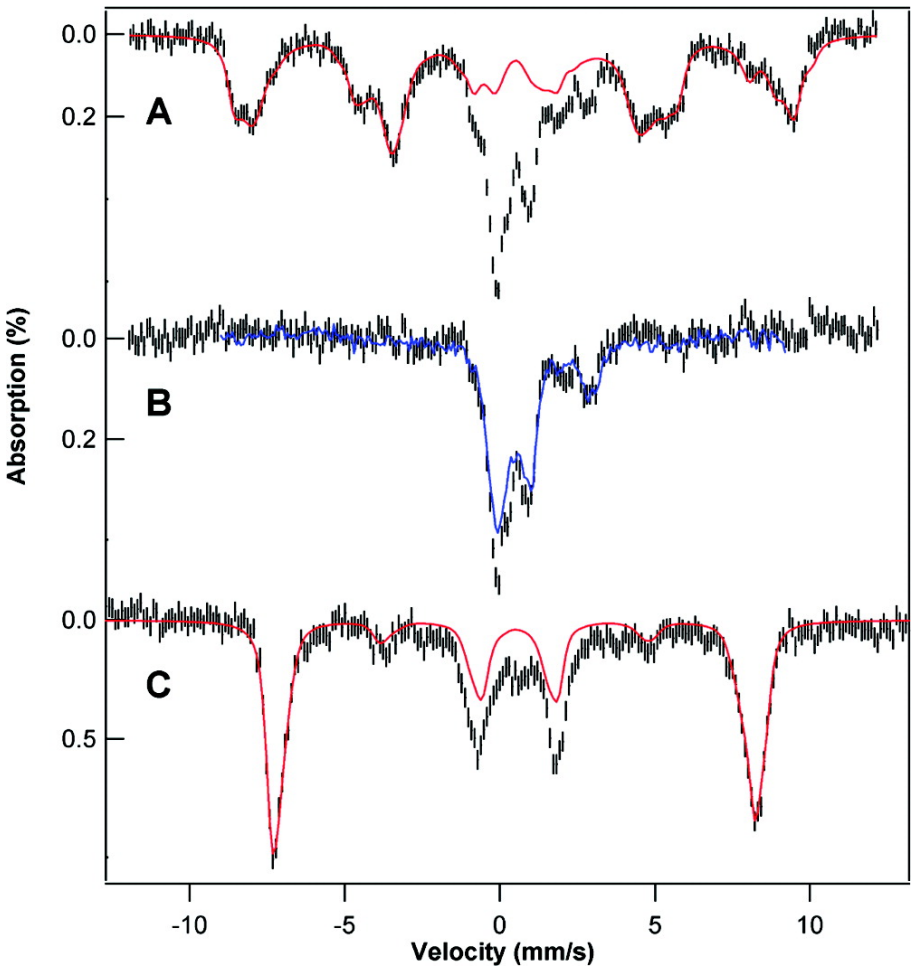

Figure 5.1. Mössbauer spectra (5 K) of whole fermenting yeast cells. Samples were grown on ^{57}Fe-enriched minimal medium. (A) Applied field of 0.05 T. The red line is a simulation with A values ranging from −21 to −23.5 T. (B) Spectrum obtained after subtraction of the simulation in part A from the data. The blue line is the spectrum of isolated mitochondria given in Figure 3.2A. (C) Same as part A, but at an applied field of 8.0 T. The red line is a simulation with A values ranging from −21.5 to −22.5 T.

such species exhibited patterns characteristic of magnetically noninteracting Fe^{3+}. This behavior implies that these components should be EPR active.

The red lines in Figure 5.1 are the sums of simulations for three mononuclear HS Fe^{3+} species, collectively representing ~75% of the spectral intensity; the actual number of species contributing to these features remains undetermined. Individual differences among the HS Fe^{3+} species are lost at 8.0 T. The difference spectrum (Figure 5.1B) obtained by subtracting the low-field simulation of Figure 5.1A from the spectrum of Figure 5.1A is similar to that obtained for isolated mitochondria (the blue line in Figure 5.1B is the spectrum of EGTA-washed mitochondria shown in Figure 3.2A).

A detailed analysis of the iron content of entire yeast cells will require a separate analysis, but our current analysis is sufficient to draw two major conclusions. First, the magnetically noninteracting mononuclear HS Fe^{3+} species (whose contribution was removed from the spectrum of Figure 5.1A) are *not* located in mitochondria. Second, the majority of the iron in fermenting yeast cells can be divided into two major groups: these non-mitochondrial mononuclear Fe^{3+} species and mitochondrial iron species.

The non-mitochondrial Fe^{3+} species were reduced to the Fe^{2+} state upon sonication of cells and treatment with dithionite (Figure 5.2). The resulting quadrupole doublet had a ΔE_q of 3.10 mm/s and a δ of 1.35 mm/s, parameters similar to those of the NHHS Fe^{2+} doublet in isolated mitochondria. This does not necessarily mean that the two doublets represent the same pool of iron, but neither can this possibility be excluded.

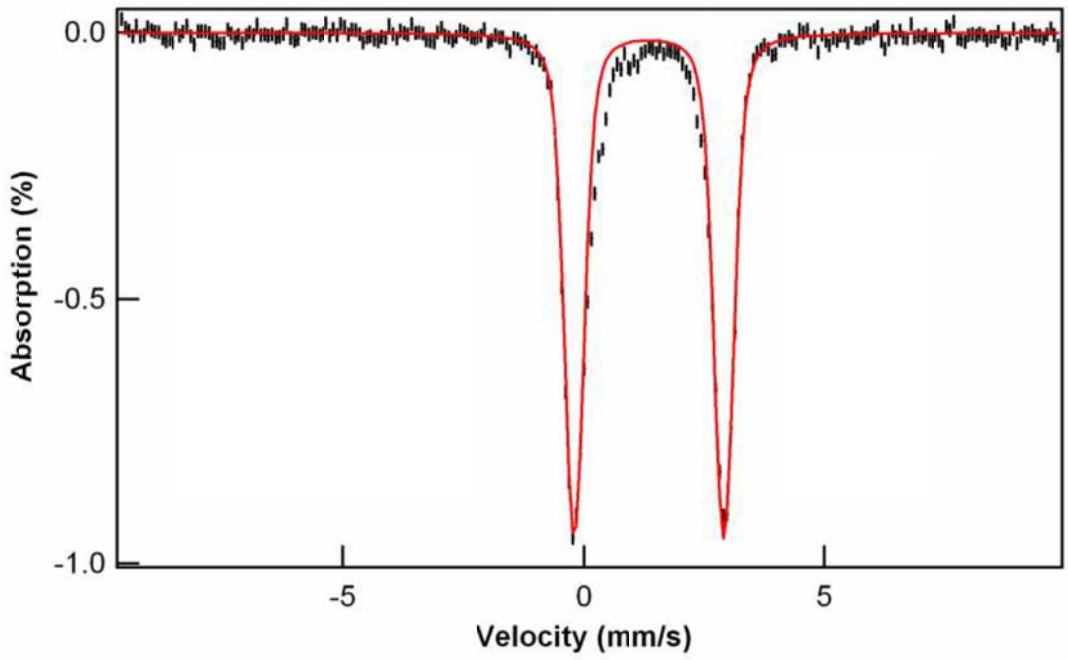

Figure 5.2. Mössbauer spectrum (4.5 K, 0.05 T parallel field) of sonicated, dithionite treated fermenting cells. The red line is the simulation for δ = 1.35 mm/s, ΔEQ = 3.10 mm/s.

Spectroscopic Characterization of Isolated Vacuoles

Vacuoles were isolated from cells grown under the same conditions used above. The fitted isomer shift, quadruple splitting, and isotropic hyperfine coupling constant (−230 kG) of the Mössbauer spectra of such samples suggest a hexacoordinated HS Fe^{3+} species (*284*). The isotropic hyperfine coupling constant is near the limit of that observed for HS Fe^{3+} systems with rhombic symmetry, and it indicates very hard/ionic donor atoms (*284*). $A_o/g_N \cdot \beta_N$ values for $[Fe^{3+}(H_2O)_6]^{3+}$ (*285*), ammonium iron alum ($NH_4Fe(SO_4)_2 \bullet 12\ H_2O$) (*286*) and HS Fe^{3+} polyphosphate are within this limiting region (ca. −238 kG), suggesting that the vacuolar HS Fe^{3+} species is coordinated by similar oxygen donors.

The spectra of all batches examined by Mössbauer included a second component in varying relative proportions. Batch 15 (*287*) exhibited the lowest proportion of this component, while batch 23 (*287*) exhibited the highest proportion. The spectra of three other batches, with intermediate levels of the second component, are shown in Figure S2 of (*287*). In batches showing greater resolution of this second feature, a quadrupole doublet was evident. These parameters were similar to those of Fe^{3+} (phosphorus) oxyhydroxo nanoparticles observed in various genetic strains of yeast (*106, 107, 226, 288*). The spectral features due to the nanoparticles could be removed, affording difference spectra that could be simulated using the same HS Fe^{3+} parameters mentioned above. A somewhat different spectral shape was reported previously (*106, 107, 226, 288*) but in those spectra the field was applied *parallel* to the γ-radiation, affording different selection rules. The magnetic features due to these nanoparticles in Figure 3 of

(*287*) were broad because the hyperfine coupling tensor *A* values were widely distributed as is typical of aggregated superparamagnetic materials.

X-band EPR spectra of isolated vacuoles supported this analysis, as all 10 batches examined displayed a dominant feature at $g_{ave} \sim 4.3$ (Figure 5.3A). Such features are typical of HS Fe^{3+} species with rhombic symmetry ($E/D \sim 1/3$). However, the quantified intensity of the signal varied considerably, with spin concentrations ranging from 110 to 175 μM in samples of packed isolated vacuoles from four separate batches (batches 14, 16, 17, and 23 of (*287*)). When normalized to the [Fe], and to the fraction of Fe associated with the six-line pattern in the Mössbauer spectra (measured to be 56% and 85% in batches 23 and 14 of (*287*), respectively, and assumed to be midway between these percentages in batches 17 and 16 of (*287*)), the ratio of [spin]/[HS Fe^{3+}] was 0.9, 0.7, 0.8, and 0.6, respectively.

Comparison of Whole Cells to Vacuolar Iron

We calculated the concentration of Fe (and other metal ions) within fermenting yeast cells grown in the same medium used to grow the cells from which vacuoles were isolated. Measured values using packed cells were normalized using the previously determined packing efficiency (*288*). Low-temperature Mössbauer spectra of whole cells (Figure 5.4) were dominated by the same pattern that was observed in spectra of isolated vacuoles, i.e., typical of a mononuclear HS Fe^{3+} species. EPR spectra of whole cells grown under the same conditions as the isolated vacuoles of Figure 5.3A were dominated by a $g_{ave} = 4.3$ signal (Figure 5.3B), essentially indistinguishable from that of isolated vacuoles.includes low-intensity features at g = 6.4 and 5.4 (*226, 289*). The low-

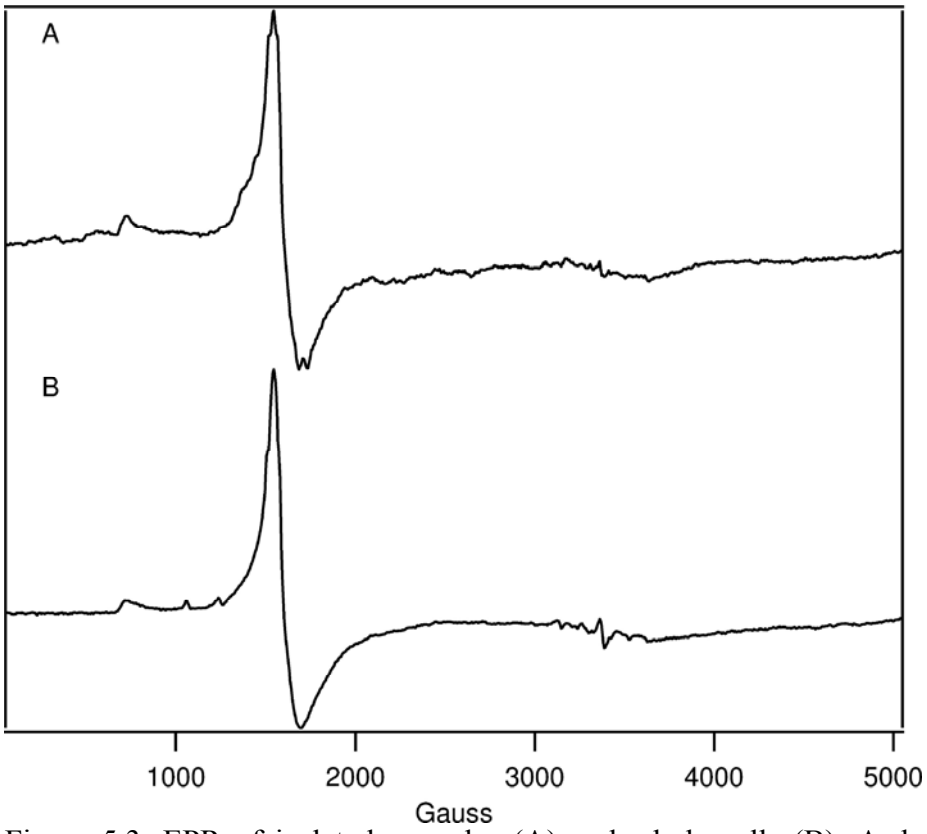

Figure 5.3. EPR of isolated vacuoles (A) and whole cells (B). A, batch 23 of (*290*); temperature, 4 K; microwave frequency, 9.46 GHz; microwave power 0.08 mW; B, temperature, 10 K; microwave frequency, 9.46 GHz; microwave power 0.2 mW. The whole-cell spectrum includes low-intensity features at g = 6.4 and 5.4 and signals in the g = 2 region which are absent or of diminished intensity in the spectrum of isolated vacuoles. These features originate from mitochondria (*226, 289*). The whole-cell spectrum

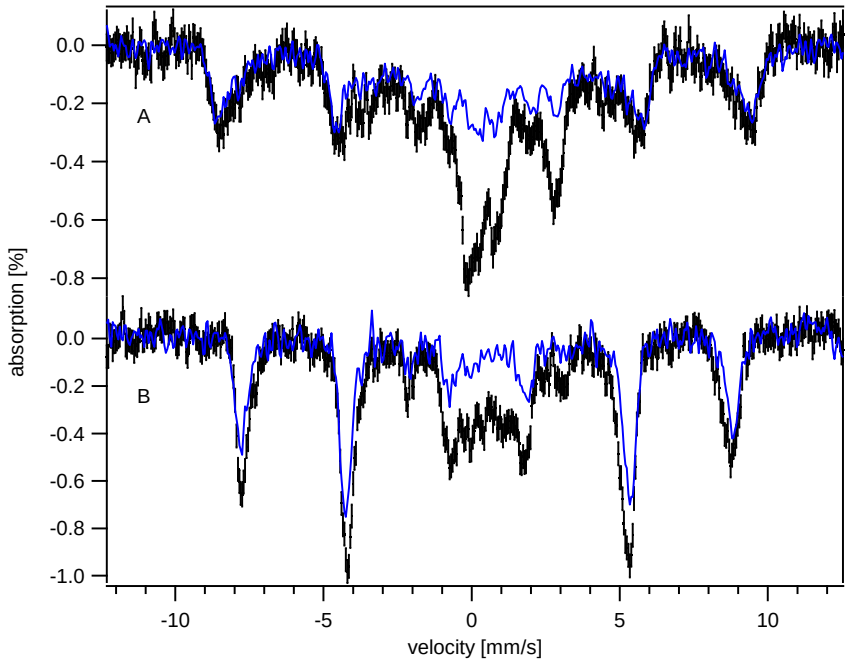

Figure 5.4. Mössbauer spectra of isolated vacuoles (Blue) and whole cells (Black). Samples were collected at A, 4.2 K and 0.05 T; B, 4.2 K and 6 T. Applied fields were perpendicular to the γ-radiation. The isolated vacuole spectra are presented in Figure 2 of (*287*).

field features probably arise from cytochrome c oxidase while the high-field features arise from other respiration-related proteins.

Determination of the Void Volume in Cell Pellet

To obtain concentrations of metals or protein in whole cells it was necessary to determine the void volume of the samples due to interstitial buffer. This value has been previously obtained for mitochondria (*221, 226*). In these studies, the contribution of interstitial buffer was determined by incubating isolated mitochondria with radiolabeled sucrose. In lieu of using radioactive materials we have altered the methods to include the use of a fluorescent molecule kindly provided by Dr. Kevin Burgess (Department of Chemistry, Texas A&M University) and monitored fluorescence with a fluorimeter kindly provided by Dr. Ryland Young (Department of Biochemistry and Biophysics, Texas A&M University). The methods have been described above in Chapter 2.

Table 5.1 shows data collected for the determination of the void volume of pellets of whole cells. We found that a pellet of yeast cells contained on average 70% cells and 30% buffer. For samples of whole cells analyzed by biophysical methods, extensive rinsing was performed to get rid of adventitious ions on the outside of the cells. Based on this and ICP-MS data, the buffer contained within the cell pellet is a minor contribution of the total metal or protein concentration in the sample. For this reason the numbers obtained were essentially used as a dilution factor to find the *actual* metal or protein concentrations inside the cell.

Table 5.1. Fluorescent data for determination of void volume in cell pellet. Experimental details are available in chapter 2. Briefly, a suspension of cells was packed into an EPR tube and the supernatant removed. The cells were resuspended in a known volume of a solution of know concentration of the fluorescent compound. The supernatant was retained and the concentration of the compound ([stock]) determined the pellet was resuspended in buffer without the compound 3 times with the supernatant of each rinse retained and the concentration of the compound determined ([super1-3]). The Value V_{buffer} was based on the dilution of the compound between rinses. *denotes [ ] after original stock (63.8 μM for 0 μM experiments, 93 μM for 1 mM experiments)was diluted with cell pellet.

Sample	0μM-1	0μM-2	0μM-3	0μM-4	1mM-1	1mM-2	1mM-3	1mM-4
[stock] (μM)	58.7	55.7	51.5	46.1	81.4	83.3	79.9	77.4
[super1] (μM)	16.7	20.4	21.2	18.9	25.4	25.5	26.3	27.0
$V_{buffer1}$ (μL)	57	73	82	82	62	61	66	70
[super2] (μM)	4.7	7.6	8.2	7.7	7.1	6.8	8.0	8.7
$V_{buffer2}$ (μL)	56	74	78	82	56	54	61	64
[super3] (μM)	1.5	2.5	3.9	4.0	2.3	2.2	2.6	4.2
$V_{buffer3}$ (μL)	64	65	89	102	64	66	65	96
V_{buffer} ave (μL)	69	71	83	89	61	60	64	77
V_{pellet} (μL)	195	239	307	286	201	190	228	240
% of buffer in pellet	30.3	29.6	27.2	31.0	30.2	31.7	28.0	32.0

Mössbauer Spectroscopy of Aft1-1^{up} Cells and Mitochondria

A detailed analysis of the Aft1-1up strain is presented elsewhere (*288*). In summary the strain exhibited features similar to WT cells; however considerably more iron is imported into these cells. Mössbauer spectra of cells grown on medium containing low (~1 μM) iron were very similar to WT cells grown on iron sufficient media. Mössbauer spectra of cells grown on medium containing 5 μM iron exhibited a more intense mononuclear HS Fe^{3+} feature and the Fe^{3+} nanoparticles accumulated. These cells also exhibited an increased absorbance indicating a higher concentration of ^{57}Fe in the sample relative to the sample obtained from medium supplemented with 1μM ^{57}Fe. Mössbauer spectra of cells grown on medium supplemented 40μM and 500μM ^{57}Fe produced spectra similar to one another both in terms of absorbance and spectral features. Both spectra exhibited a dominant mononuclear ferric feature and a substantially higher amount of Fe^{3+} nanoparticles. ICP-MS confirmed the increase in iron in the samples as the $[Fe]_{media}$ was increased. The measured concentrations of Fe in the cell were 680μM, 2.3mM, 2.8mM, and 3.4mM for 1, 5, 40, and 500μM respectively.

Mitochondria were isolated from the Aft1-1^{up} strain grown with 1μM and 40μM iron in the medium. The iron in the mitochondria isolated from cells grown with 40μM iron in the medium was dominated by Fe^{3+} nanoparticles. The spectral absorbance was high indicating a high concentration of ^{57}Fe in the sample. Comparing mitochondria isolated from Aft1-1^{up} cells with 1μM and 40μM iron in the media, the mitochondria from cells grown on lower concentration displayed a reduced absorbance indicating less iron accumulation. Features of the Mössbauer spectrum of Aft1-1^{up} mitochondria with

1μM iron in the medium were also different than the spectrum obtained from mitochondria isolated from higher iron concentration. The spectrum had a dominant feature similar to that exhibited by Fe^{3+} nanoparticles but another feature was present detracting from the resolution of the two peaks of the doublet of the nanoparticles spectrum. The second feature was unassigned but may be related to the nanoparticle feature with different spectral parameters. ICP-MS confirmed the difference in [Fe] in the samples, values of 1.4mM and 8.1mM were obtained for mitochondria isolated from cells grown on media supplemented with 1μM and 40μM iron respectively.

Comparison of Aft1-1^{up} to Gal-Yah1 Strain

In this study the iron distribution in the Aft1-1^{up} strain was also compared to the iron distribution of in cells which had YAH1 on a inducible promoter, the strain Gal-Yah1. This strain will express the protein Yah1p when galactose is used as a carbon source but not when glucose is used (*97*). Dr. Miao demonstrated that mitochondria isolated from this strain grown on glucose contained high levels of Fe^{3+} nanoparticles (*107*). Examination of the whole cells at these conditions showed that nearly all of the iron in the cell is in this same form. These cells are essentially devoid of HS Fe^{3+} (vacuolar iron).

Although ICP-MS analysis of the whole cell sample of this strain was not reported but analysis of the Mössbauer data of cells which grew for extended periods of time (~30h) would suggest an [Fe] in the whole cell of ~5-8 mM. In these studies we concluded that the Yah1-depleted strain is depositing essentially all of its iron in the mitochondria as nanoparticles and that very little iron is in the vacuole. In cells which

grow for extended periods of time, further studies will be required to confirm this. If cells under these conditions contain 5-8 mM of iron and all of it is in mitochondria which represent ~3% of the cellular volume in WT cells under fermenting conditions (*232*), we would conclude that the concentration of iron in the mitochondria would be in excess of 100mM. In light of the recent experiments on the biophysical analysis of isolated vacuoles (*290*), it also seems plausible that some portion of the iron in the whole yah1-depleted cell is in the vacuoles as nanoparticles. It is also plausible that the yah1-depleted cell contains more mitochondria by volume than a WT cell.

Conclusions

Iron Distribution of Whole Cells

In a whole fermenting yeast cell grown with 40 μM iron in the medium, ~75% of the iron is in a mononuclear HS Fe^{3+} form. The remaining ~25% of the iron is similar to those species identified in fermenting mitochondria in chapter 3. Spectroscopically, isolated vacuoles are very similar to the non-mitochondrial features observed in the whole cell sample. Further investigation is necessary to establish the effects of metabolic mode (fermenting vs. respiring) and $[Fe]_{media}$ on the distribution of iron in the cell. This will be the focus of chapter 6. A model of iron in the fermenting yeast vacuole is presented (Figure 5.5)

The Import of Iron Through Aft1 Pathways Is Not Limited by $[Fe]_{media}$

Aft1-1^{up} cells grown with high media iron contained marginally more iron than when grown on intermediate iron levels. The fractional increase was modest relative to the increase in cellular iron when $[Fe]_{medium}$ was increased from low to

intermediate levels. This suggests that the Aft1-dependent rate of iron import into the cell saturates at high $[Fe]_{medium}$. Aft1-1^{up} cells grown on medium supplemented with 40 μM iron contain 2.8 mM of iron, the same strain grown on medium supplemented with 500 μM iron contain 3.4 mM of iron.

Gal-Yah1 Cells Accumulate More Iron than Aft1-1^{up} Cells

Gal-Yah1 cells grown for extended periods of time (~30h) on medium containing 40 μM of iron and glucose contain ~3 times more iron (2.8mM vs. ~7mM) than cells in which the iron regulon is constitutively activated. This observation could result from the several situations. Iron imported into the Gal-Yah1 strain may accumulate as nanoparticles. The cell might not be able to "recognize" iron in this form and this may lead to an increased import rate in this strain. Yah1-depleted cells activate the genes of the iron regulon (*291*). This alone would not account for an increase in iron *vs*. the Aft1-1^{up} strain. Both the Gal-Yah1 and Aft1-1^{up} strains probably are not regulated to stop the import of iron through Aft1 mediated pathways. This would imply that both strains import the same amount of iron.

This difference in iron concentration may be related to the growth rate of these strains. The Aft1-1^{up} strain grows at a faster rate than the Gal-Yah1 strain. This cell growth might simply be diluting the iron in the Aft1-1^{up} strain. This could be established by further investigation. Alternatively, the Gal-Yah1 strain may be importing iron through a different transporter than the Fet3p/Ftr1p system being expressed by the upregulation of the iron regulon. This system would also have to be independent of those

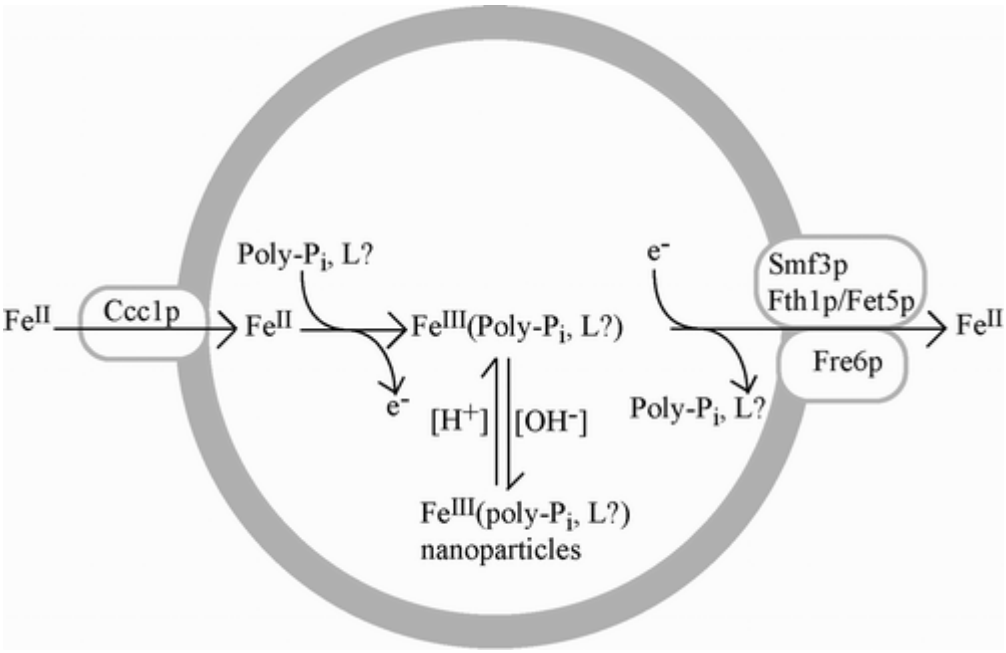

Figure 5.5 Model of iron distribution in the vacuoles of fermenting yeast cells. An unknown ferrous species enters the vacuole via Ccc1p. Associated with this import is the exchange of ligands and oxidation to HS Fe^{3+}. Polyphosphate is suggested as a possible coordinated ligand, but further studies are required to establish this. Upon export, the HS Fe^{3+} species is reduced to Fe^{2+} and ligands are again exchanged. At pH > ca. 5, some or all of the species precipitates in the form or Fe^{3+} (phosphate-based) oxyhydroxo nanoparticles perhaps associated with polyphosphate.

processes regulated by Aft1p. A model of the Aft1-1^{up} and Gal-Yah1 strains is presented (Figure 5.6).

Iron Imported by the Fet3p/Ftr1p System Can Accumulate as Nanoparticles

The Fet3p/Ftr1p pathway of iron acquisition has the highest affinity for iron of the known iron acquisition pathways implying that this should be the primary means of iron import for conditions where it is expressed (*19*). Results of a RT-PCR experiment of the Aft1-1^{up} strain indicate that the mRNA for the complex is being synthesized (*288*). Mössbauer spectra of this strain exhibit Fe^{3+} nanoparticles both in whole cells isolated mitochondria. This implies that iron imported by the Fet3p/Ftr1p pathway is being transformed into Fe^{3+} nanoparticles.

Are There Non-Aft1p Regulated Systems of Iron Import?

These studies have established that cells constitutively activating the iron regulon accumulate massive amounts of iron. In WT fermenting cells with a functional Aft1 we see that considerably less iron is imported. This raises the question of whether all the iron that is imported in WT cells is imported in an Aft1p dependent fashion. In chapter 6 we address whether this is the case. We also investigate the changes to iron distribution in WT fermenting cells and mitochondria as the $[Fe]_{medium}$ is altered from iron-starved to excessive iron conditions. Of particular interest going into to these studies was whether or not vacuoles from iron-starved fermenting cells would contain iron. If they did not, we aimed to address what $[Fe]_{media}$ was needed to fill the vacuoles with iron and whether or not this process was Aft1p dependent. Based on the observation that vacuoles and mitochondria from fermenting cells both accumulate Fe^{3+} nanoparticles we also were

curious if these species accumulated at a particular $[Fe]_{medium}$ and in an Aft1p dependent or independent fashion. Finally, we describe for the first time the iron-ome of respiring cells, demonstrate the dependence of $[Fe]_{medium}$ on this distribution, and address the role of Aft1p under these conditions.

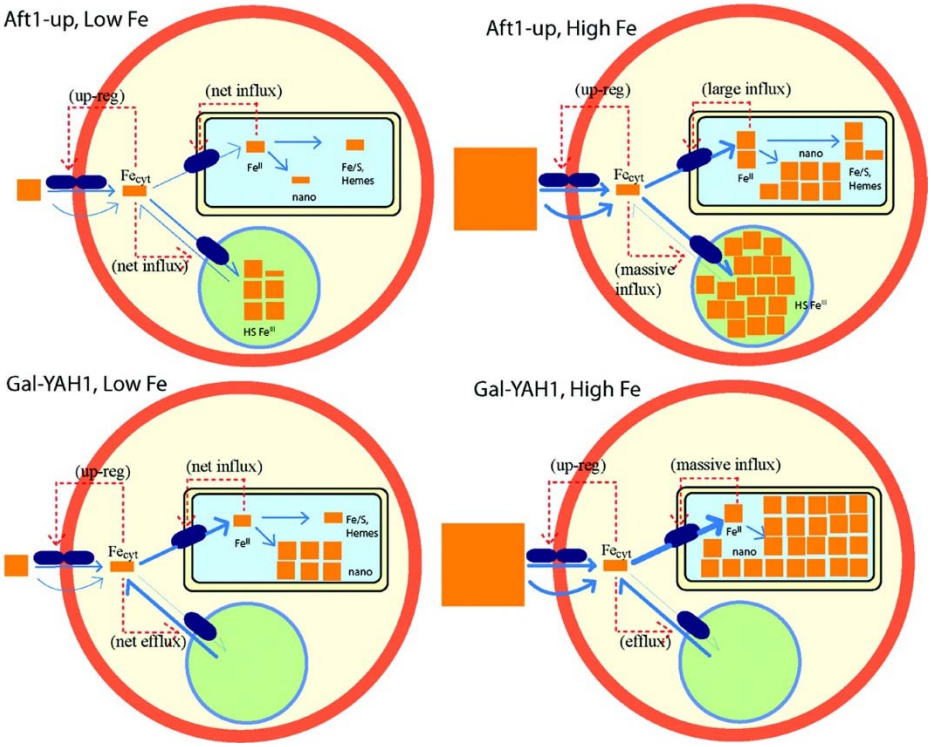

Figure 5.6 Model of iron in fermenting Aft1-1^{up} and Gal-Yah1cells. In Aft1-1^{up} cells, Aft1 is constitutively activating the iron regulon regardless of the concentration of Fe_{medium}. When grown in low $[Fe]_{medium}$, more iron is imported relative to WT cells. The majority is sent to vacuoles while much of the remainder is sent to mitochondria for heme and ISC biosynthesis. When Aft1-1^{up} cells are grown in high $[Fe]_{medium}$, the rate of import is increased, but the imported iron is distributed similarly. The flow into mitochondria is favored because nanoparticle formation depresses the concentration of the precursor iron species in the matrix that is both sensed for regulation and converted into nanoparticles. Mitochondria "feel" iron-deficient, accelerating iron import. In Yah1p-depleted cells grown at either low or high media iron, nearly all imported iron is delivered to mitochondria. This massive influx of iron into the mitochondria depresses the concentration of cytosolic iron that is sensed by the Aft1 regulatory system and by the vacuolar iron regulatory system (Fe_{cyt}). Due to this regulatory structure, these cells "feel" iron deficient, leading to an increased import of Fe_{medium} and the efflux of iron from the vacuole, as the regulatory system attempts to increase Fe_{cyt}.

CHAPTER VI

THE IRON-OME OF *SACCHAROMYCES CEREVISIAE* GROWN UNDER IRON-STARVED AND EXCESSIVE IRON CONDITIONS

Introduction

Yeast cells have an impressive capacity to grow in environments containing a wide range of iron concentrations. In the laboratory, low-iron conditions are typically obtained by adding bathophenanthroline sulfonate (BPS) (Figure 6.1) to the growth medium. BPS is a strong chelator of Fe^{2+} ions, and the resulting $[Fe^{2+}(BPS)3]4-$ complex is inaccessible for cell growth (*292*). In these "iron-starved" conditions, cells initially grow slowly and eventually stop growing (*292*). Cells inoculated into BPS-treated medium up-regulate the ca. 20 genes of the iron regulon (*293-295*). These genes, which include fet3, are under control of the transcription factors Aft1p/Aft2 (*33*). Addition of small amounts of iron to an iron starved culture recovers cell growth (*292*). Through such experiments the apparent saturation of the high affinity pathway of iron import, Fet3p/Ftr1p, was determined to be ~ 0.15 μM iron (*292, 296*). Similarly, the apparent saturation of the low affinity pathway was determined in a ΔFet3p background to be ~ 28 μM (*25*). In the same genetic background, Fet4p was identified as the low affinity pathway of iron import (*25*).

Yeast have evolved strategies to acquire iron under conditions where it is sparse but they also have mechanisms to deal with excessive concentrations of iron without showing signs of toxicity (*292, 297*). WT cells show signs of toxicity when grown in > 5

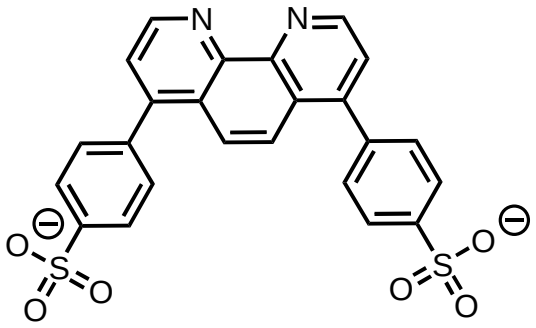

Figure 6.1 Structure of Bathophenanthroline Sulfonate.

mM for Fe^{2+} salts and 20 mM for Fe^{3+} salts (*297*). Little is known regarding the iron content of the cell under these Fe-extreme conditions.

Cobine et.al. (*224*) reports an almost 10-fold increase in cellular iron when yeast is grown under low-iron medium and medium supplemented with 100μM iron. They also observed a ~5 fold increase in mitochondrial iron. These changes are normalized to the number of cells in the whole cell samples and to mg protein in the mitochondrial samples. The latter presents a complication in that it assumes a constant [protein] in the mitochondrial samples for the different amounts of iron added.

Encouraged by the results of Cobine et al., we applied the Mössbauer-based biophysical approach method developed throughout this dissertation to probe the Fe content of such cells. These studies employed two culture conditions, one with 7-10 μM of total iron in the medium which corresponds to the endogenous concentration of Fe in minimal medium. In the other condition, there was ~ 110 μM of iron in the medium. We also examined the extremes of iron concentration, including BPS-treated, iron-starved conditions and concentrations as high as 10 mM iron in the growth medium.

Results and Discussion

Iron-Starved Fermenting Cells

Cells were grown under iron-starved conditions with glucose as the carbon source. *Iron-starved* means that 21 μM of the chelator BPS was added to the growth medium, followed by addition of 1 μM ^{57}Fe. Harvested cells were washed to remove $[Fe^{2+}(BPS)_3]^{4-}$ from solution, and then packed into Mössbauer cups for analysis. The 5 K 0.05 T Mossbauer spectrum of this material (Figure 6.2A) exhibited poor S/N due to the

low concentration of ^{57}Fe in the sample, undoubtedly the result of using such a low concentration of ^{57}Fe in the growth medium. An unresolved resonance in the center of the spectrum dominated. Authentic $[Fe^{2+}(BPS)_3]^{4-}$ exhibited a similar feature (Figure 6.2B), suggesting that the sample of packed Fe-starved cells contained $[Fe^{2+}(BPS)_3]^{4-}$ despite having washed the cells prior to packing into the Mössbauer sample holder. We subtracted the $[Fe^{2+}(BPS)_3]^{4-}$ spectrum from that of the Fe-starved fermenting cells at the level of 35% intensity; the resulting difference spectrum is given in Figure 6.3A.

We also considered that the feature could be due to Fe^{3+} oxyhydroxide nanoparticles (an authentic spectrum of which is shown in Figure 6.2C). However, only ca. 5% of spectral intensity of Fe-starved fermenting yeast could be removed by spectral subtraction, arguing against this interpretation.

This analysis indicated that about 35% of the Fe in the Fe-starved fermenting cells was due to $[Fe^{2+}(BPS)_3]^{4-}$ (~ 100 μM) and so only 65% of the concentration listed in Table 6.1 for Fe-starved fermenting cells is probably Fe within those cells. The concentration of $[Fe(BPS]_3]^{4-}$ in the harvested sample was substantially higher than the concentration of BPS added to the medium, indicating that $[Fe^{2+}(BPS)_3]^{4-}$ either adhered to the exterior of the cell, or it incorporated into it. Given the charge on the complex which should discourage membrane permeability, we favor the former possibility.

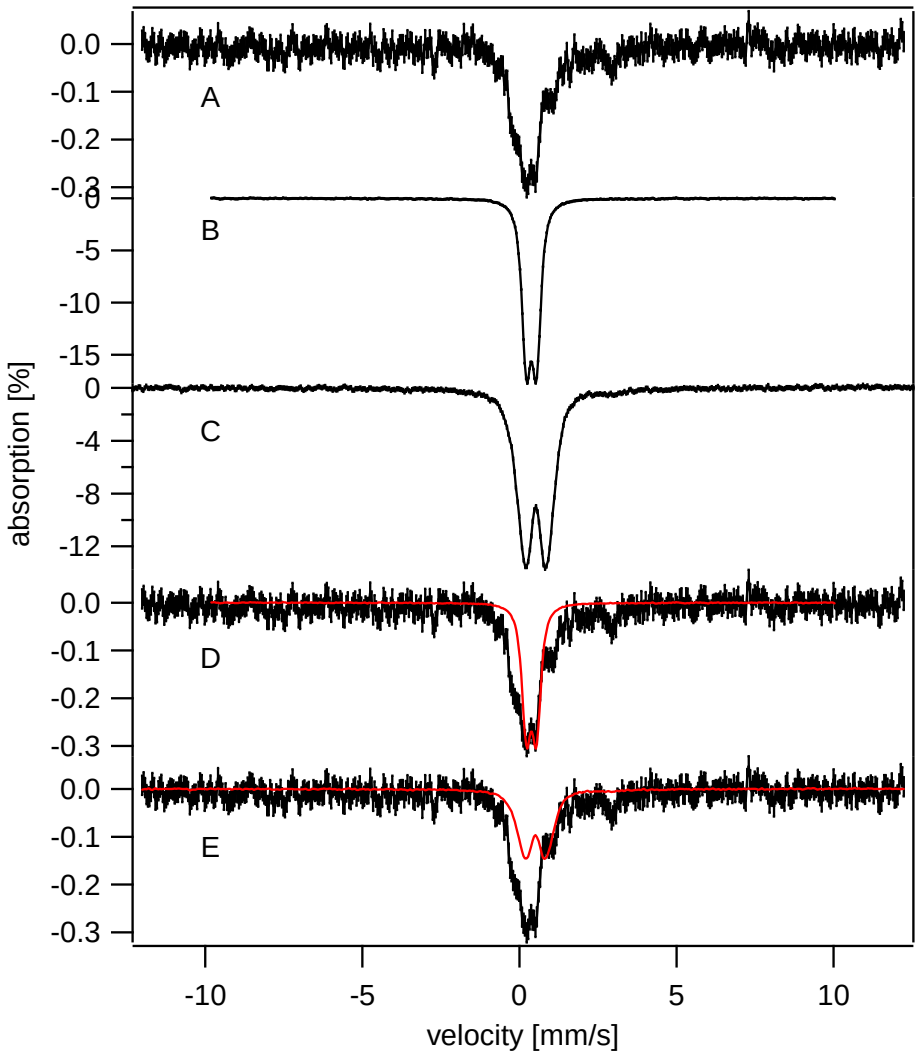

Figure 6.2. Mössbauer spectra (5 K, 0.05 T) showing the contribution of BPS in iron-starved fermenting cells. A, Iron-starved fermenting cells; B, $[Fe^{2+}(BPS)_3]^{4-}$; C, Fe^{3+} nanoparticles from Aft1-1^{UP} mitochondria published in (*290*); D, Fe-starved fermenting cells with $[Fe^{2+}(BPS)_3]^{4-}$ overlaid at 35% intensity; E, Fe-starved fermenting cells with Fe^{3+} nanoparticles overlaid at 10% intensity. Simulations were performed using WMOSS software (SEE Co, Edina MN).

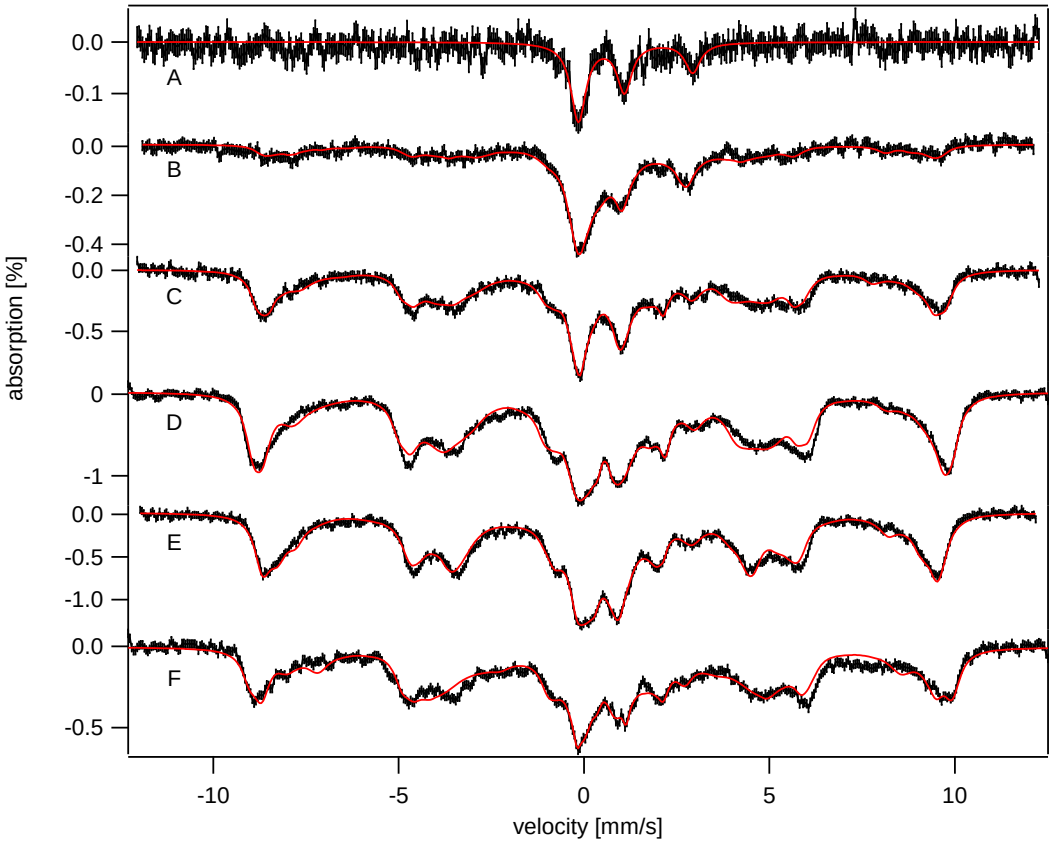

Figure 6.3. Mössbauer spectra (5K, 0.05T parallel field) of fermenting yeast cells at various $[Fe]_{medium}$. Minimal medium was treated with: A, 21 uM BPS plus 1μM ^{57}Fe; B, 1 μM ^{57}Fe; C, 10 μM ^{57}Fe; D, 100 μM ^{57}Fe; E, 1 mM ^{57}Fe; and F, 10 mM ^{57}Fe. Spectrum A is the result of removing the contribution of $[Fe^{2+}(BPS)_3]^{4-}$ from the raw spectrum, as shown in Figure 6.2A. Spectrum B has been previously published in (*288*).

Table 6.1. Analytical properties of isolated mitochondria and whole cells. Metal numbers, percentages used for Mössbauer spectral simulation, spin intensities of EPR signals, and concentrations of heme centers from UV-vis spectra. Percentages are based on corrected Mössbauer spectra where applicable. For fermenting mitochondria obtained from cells grown with 100 μM Fe in the medium, the two numbers represent percentage for each of the two batches, including the as-isolated batch and the batch treated with dithionite. EPR and ICP-MS data have been corrected for packing efficiency (*226, 288*).

[Fe] added to medium	1 μM + BPS	1 μM	10 μM	100 μM	1mM	10mM
Fermenting Whole Cells						
[Fe] (μM)	240	250	395	470	440	ND
[Cu] (μM)	280	ND	26	20	35	ND
[Mn] (μM)	17	ND	14	17	39	ND
[Zn] (μM)	560	ND	600	570	1300	ND
HS Fe^{3+} (%)	ND	40	76	80	75	84
CD (%)	58	22	18	10	5	3
HS Fe^{2+} (%)	42	26	7	5	6	5
Nanoparticles (%)	ND	12	ND	4	18	10
$[Fe^{2+}(BPS)_3]^{4-}$ (%)	38	N/A	N/A	N/A	N/A	N/A
g = 4.3 (μM)	14	---	130	360	320	290
g = 2.0 region (μM)	14	---	16	15	28	27
Fermenting Mitochondria						
[Fe] (μM)	400	---	440	660	---	---
[Cu] (μM)	80	---	41	52	---	---
[Mn] (μM)	13	---	9	11	---	---
[Zn] (μM)	570	---	330	350	---	---
HS Fe^{3+} (%)	ND	---	ND	51,0	---	---
CD (%)	59	---	11	12, 34	---	---
HS Fe^{2+} (%)	7	---	28	18, 36	---	---
HS Fe^{2+} Heme (%)	9	---	ND	ND	---	---
nanoparticles (%)	ND	---	57	27	---	---
S = 0 $[Fe_2S_2]^{2+}$ (%)	12	---	ND	ND	---	---
S = ½ $[Fe_2S_2]^{1+}$ (%)	12	---	ND	ND	---	---
[g = 4.3] (μM)		---	20	20	28	---
[g = 2.0 region] (μM)		---	low	low	low	---
[Heme *a*] (μM)	30	---	24	27	5	---
[Heme *b*] (μM)	72	---	64	78	21	---
[Heme *c*] (μM)	120	---	110	130	40	---
Respirofermenting Whole Cells						
[Fe] (μM)	200	---	350	600	350	---
[Cu] (μM)	98	---	150	280	1200	---
[Mn] (μM)	19	---	22	24	40	---
[Zn] (μM)	200	---	250	330	930	---
HS Fe^{3+} (%)	ND	---	50	52	37	---
CD (%)	43	---	12	12	25	---
HS Fe^{2+} (%)	39	---	34	29	34	---
HS Heme (%)	18	---	4	7	4	---
$[Fe^{2+}(BPS)_3]^{4-}$ (%)	12	---	11	10	5	---
g = 4.3 (μM)	low	---	low	low	Low	---
g = 2.0 region (μM)	26	---	21	22	48	---

The Fe concentration in Fe-starved fermenting cells was ~ 160 μM. This value was obtained by subtracting the contribution of $[Fe^{2+}(BPS)_3]^{4-}$ (100 μM) from the total Fe concentration as measured in packed cells (Table 6.1). Our cell pellets contained 70% cells and 30% buffer (*288*). Reported concentrations have been corrected for this packing efficiency.

The Fe-starved whole-cell difference spectrum (Figure 6.3A) was dominated by a quadruple doublet (δ = 0.45 mm/s, ΔEQ = 1.15 mm/s) previously identified as the Central Doublet (CD), arising from S = 0 $[Fe_4S_4]^{2+}$ clusters and LS Fe^{2+} heme centers (*221*). Another prominent feature was a quadrupole doublet with parameters typical of nonheme high-spin (NHHS) Fe^{2+} (δ = 1.2 mm/s and ΔE_Q = 3.1 mm/s. Percentages of these components are given in Table 6.1. We estimate that the concentrations of CD and NHHS Fe^{2+} species in Fe-starved fermenting yeast cells are ca. 70 μM and 40 μM, respectively. No other features, including those from Fe^{3+} oxyhydroxide (phosphate) nanoparticles and mononuclear HS Fe^{3+} species, were observed, though minor contributions could have escaped detection due to the poor S/N ratio.

EPR spectra of Fe-starved cells (Figure 6.4A) exhibited low-intensity signals in the g = 2 region from Mn^{2+} ions, as evidenced by the hyperfine splitting due to the I = 5/2 Mn nucleus. Also evident in the whole-cell EPR spectra were features at g ≈ 2.01 and at g ≈ 4.3. The latter is due to mononuclear HS Fe^{3+} ions with rhombic symmetry, while the former as not been assigned.

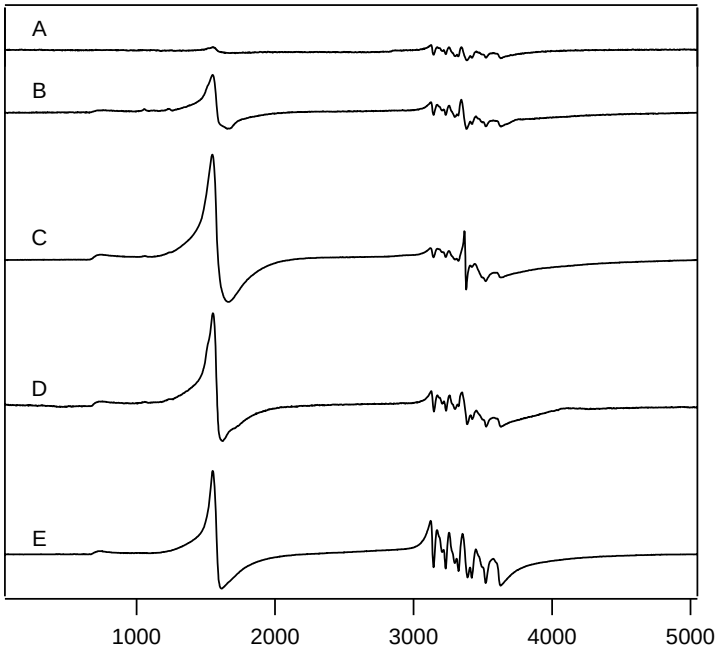

Figure 6.4. EPR spectra (10K) of fermenting whole cells at various $[Fe]_{medium}$. Minimal medium was supplemented with: A, 1μM ^{57}Fe and 21μM BPS; B, 10 μM ^{57}Fe; C, 100 μM ^{57}Fe; D, 1mM ^{57}Fe; and E, 10mM ^{57}Fe.

No signals from Cu ions were observed, despite the presence of ~ 280 μM Cu in an equivalent sample. This suggests that most Cu ions in these cells are in the diamagnetic Cu(I) state.

Mitochondria from Iron-Starved Fermenting Cells

The 5 K 0.05 T Mössbauer spectrum of mitochondria isolated from iron-starved fermenting cells (Figure 6.5B) was dominated by the CD. Also present was a feature exhibiting magnetic hyperfine interactions that probably arises from S = ½ $[Fe_2S_2]^{1+}$ clusters such as the Rieske cluster associated with cytochrome bc_1 (*259*). High energy lines of doublets arising from HS heme and nonheme Fe^{2+} species were present in the spectrum, albeit at low intensities. These mitochondria appear generally devoid of Fe^{3+} phosphate nanoparticles, as the doublet due to this species overlaps the CD, which is rather "clean" in this spectrum. Substantial concentrations of nanoparticles are evident in Fe-replete mitochondria (*261*). Interestingly, the resolution between the lines of the CD was sufficient to discern a resonance near ~ 0.6 mm/s, which we assign to the high-energy line of a quadrupole doublet arising from S = 0 $[Fe_2S_2]^{2+}$ clusters (Blue line on Figure 6.5B). Such clusters in the oxidized diamagnetic oxidation state have not been observed previously in Mössbauer spectra of isolated fermenting mitochondria, but previous spectra have always included a contribution from nanoparticles (*233, 261*) which probably obscured absorption from S = 0 $[Fe_2S_2]^{2+}$ clusters. The absence of intense NHHS Fe^{2+} and nanoparticle doublets renders this spectrum more reminiscent of mitochondria isolated from respirofermenting cells than those isolated from (Fe-replete)

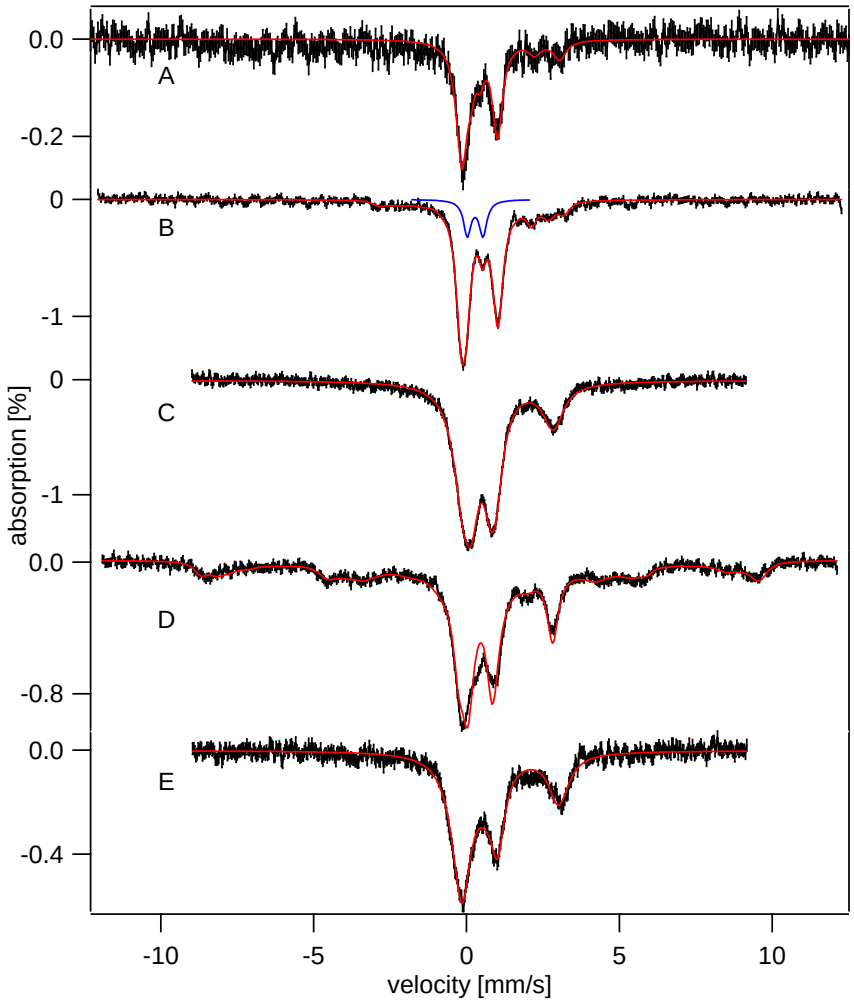

Figure 6.5. Mössbauer spectra (5K, 0.05T) of isolated mitochondria under various conditions. A, from respirofermenting cells grown on medium containing 1 μM ^{57}Fe and 21 μM BPS; B, from fermenting cells grown with 1 μM ^{57}Fe and 21 μM BPS; C, from fermenting cells, 10 μM ^{57}Fe; D, from fermenting cells, 100 μM ^{57}Fe; E, from fermenting cells, 100 μM ^{57}Fe with 1 mM dithionite added in a 0.6M sorbitol, 0.1M Trisbuffer at pH 8.5. Red lines are simulations using parameters listed on Table 6.1, the blue line is a simulation of the S = 0 $[Fe_2S_2]^{2+}$ cluster.

fermenting cells. However, even in respiring mitochondria, no feature arising from S = 0 $[Fe_2S_2]^{2+}$ clusters has been reported previously (*233*). Percentages of the features used to fit this spectrum are given in Table 6.1.

The 10 K X-band EPR spectrum (Figure 6.6B) of iron-starved mitochondria exhibited low-field signals at g = 6.5, 5.4, and 4.3. The first two signals probably arise from the a_3:Cu_b site of cytochrome c oxidase (*298*), while the g = 4.3 signal arises from HS Fe^{3+} species with rhombic symmetry. The g = 2 region signals need to be decomposed, simulated and integrated. The RT UV-vis spectrum (Figure 6.7B) of iron-starved mitochondria exhibited features due to Fe^{2+} heme centers. The concentration of heme *a*, *b*, *c* (Table 6.1) are similar to those reported for Fe-replete respiring mitochondria (*233*).

Iron-Sufficient Fermenting Cells and Mitochondria

Previously we have described the Mössbauer spectrum of whole fermenting yeast cells grown on medium containing 40 μM ^{57}Fe (*261*). In that study we assigned the iron in such cells as 25% mitochondrial iron (comprised of CD, HS hemes, NHHS Fe^{2+} and Fe^{3+} nanoparticles) and 75% "non-mitochondrial" mononuclear HS Fe^{3+}. For this study we will term cells grown on medium containing <40 μM iron but more iron than the iron-starved condition described above as "low iron".

Using Mössbauer spectroscopy, we have examined fermenting cells grown on medium containing 1μM ^{57}Fe but not treated with BPS (1μM-BPS) (Figure 6.3B). We have also examined cells grown with 10 μM ^{57}Fe (Figure 6.3C). These spectra exhibited

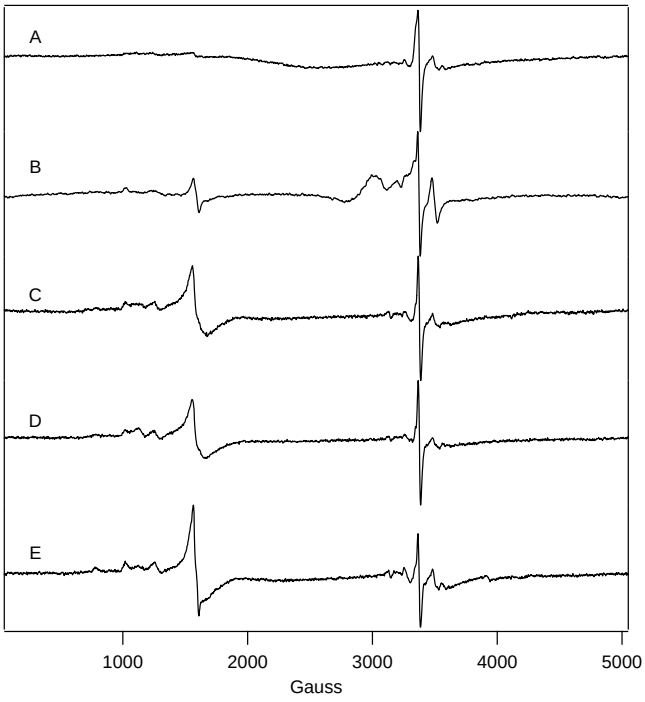

Figure 6.6. EPR (10K) of isolated mitochondria. A, from respirofermenting cells grown on medium containing 1uM ^{57}Fe and 21 μM BPS; B, same as A but fermenting cells; C, D and E, from fermenting cells grown on medium containing 10, 100, and 1000 μM ^{57}Fe respectively.

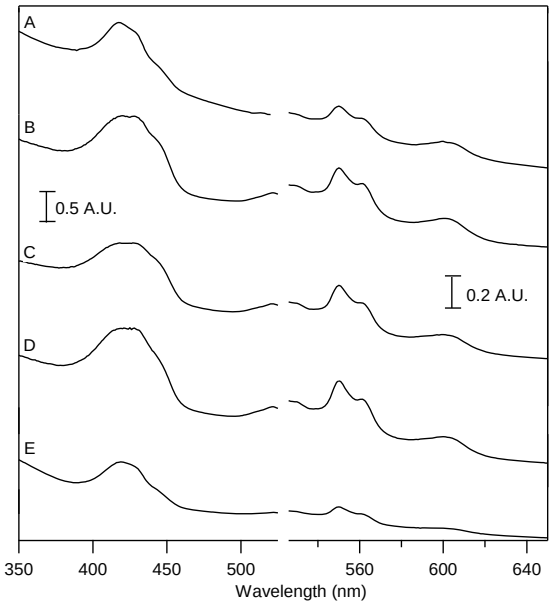

Figure 6.7. UV-vis spectra of isolated mitochondria. A, from respirofermenting cells grown on medium containing 1 μM ^{57}Fe and 21 μM BPS; B, same as A but from fermenting cells; C, D, and E. from fermenting cells grown on medium containing 10 μM,100 μM, and 1mM ^{57}Fe respectively.

features due to mononuclear HS Fe^{3+}, CD, NHHS Fe^{2+}, and Fe^{3+} nanoparticles. The percentages used to simulate these spectra are given in Table 6.1. The key differences in these spectra arise from the spectral contribution of the HS Fe^{3+} feature. In the 1μM-BPS cells, the percentage of this feature was *nearly half* that evident in the spectra of the 10 μM cells. The HS Fe^{3+} feature arises from Fe within isolated vacuoles (*290*). We concludethat vacuolar iron is accumulating in cells grown with between 1 and 10 μM of iron added to the growth medium. ICP-MS analysis indicates that a maximum of ~100 μM of the iron in the 1 μM-BPS cells and ~300 μM Fe in the 10 μM cells are associated with vacuoles.

EPR spectra of the 10 μM cells (Figure 6.4B) was similar to the iron-starved cells (Figure 6.4A) but with a more pronounced g ≈ 4.3 signal, consistent with an increased concentration of mononuclear HS Fe^{3+}. Based on ICP-MS concentrations and Mössbauer percentages, the concentrations of NHHS Fe^{2+} ions in 1μM-BPS and 10μM cells are ~65 μM and ~ 30 μM respectively.

The Mössbauer spectrum of mitochondria isolated from fermenting cells grown on medium supplemented with 10μM ^{57}Fe (Figure 6.5C) were nearly indistinguishable from the previously described mitochondria isolated from fermenting cells grown on medium supplemented with 40μM ^{57}Fe (*261*). The values used to simulate the spectrum are listed in Table 6.1. Relative to the iron-starved mitochondria described above, these mitochondria exhibited considerably more HS Fe^{2+} and Fe^{3+} nanoparticles. The Mössbauer spectrum of this sample was similar to that of mitochondria isolated from

cells grown on 40 μM Fe, yet ICP-MS analysis indicates the concentration of iron is less by a factor of ~2. Further investigation will be necessary to explain this discrepancy.

The EPR spectrum (Figure 6.6C) of mitochondria isolated from cells grown on medium supplemented with 10 μM iron were also similar to the previously reported spectra of mitochondria isolated from cells grown with 40μM iron (*233*). The UV-vis spectrum (Figure 6.7C) of these mitochondria exhibited Fe^{2+} heme concentrations similar to those seen in the iron-starved sample as indicated on Table 6.1.

Iron-Overloaded Cells and Mitochondria

We will call cells grown on medium supplemented with > 40μM iron *iron-overloaded* cells. Using Mössbauer spectroscopy, we examined fermenting cells supplemented with 100 μM, 1 mM, and 10 mM Fe (Figure 6.3D-F). The spectra exhibited similar contributions from HS Fe^{3+}, CD, HS Fe^{2+}, and Fe^{3+} nanoparticles and had similar overall Fe concentrations (see Table 6.1). These results demonstrate that yeast cells are tightly regulated such that the 3 orders of magnitude difference in iron in the growth media have only modest effects on the concentration and distribution of iron in the cell. The 100 μM sample contained a slightly lower concentration of Fe^{3+} nanoparticles relative to the other two samples; the 1mM sample exhibited the highest concentration of Fe^{3+} nanoparticles. The 10 mM sample exhibited the largest contribution of HS Fe^{3+} while the 1 mM sample exhibiting the lowest. Given the similarity of these samples we believe that the cellular import of iron (when it is not limiting) is tightly regulated.

The samples grown on 100 μM and 1mM medium Fe respectively contained ~375 and 330 μM vacuolar HS Fe^{3+} species. The total concentration of Fe in these samples was also similar to that in the 10 uM sample but ~ 1.7 times (~250 vs ~450μM) higher than the 1μM-BPS sample. These two conditions, the 1μM-BPS and the 100μM samples, best match the growth conditions of Cobine et al. (*224*). In contrast to the 10-fold change in iron concentration that they reported, we detected a 1.7-fold change.

EPR spectra of cells grown under these same conditions (Figure 6.4C-E) exhibited features similar to the iron-sufficient and iron-starved conditions. The biggest difference arises from the substantially more intense g ≈ 4.3 signals. The spin integrations of these signals are listed in Table 6.1. The calculated spin intensities for these samples are ~70% of the iron concentration which is inconsistent with the percentage of the iron in this form as identified by Mössbauer spectroscopy. The source of this apparent discrepancy is under investigation.

All three spectra also include a signal which likely arises from S = 5/2 Mn^{2+} species (spin integrations given in Table 6.1). Based on ICP-MS values and Mössbauer percentages, the concentration of NHHS Fe^{2+} in the 100 μM and 1mM cells are ~25 μM and 26 μM respectively.

We have isolated mitochondria from cells grown under the same high-iron growth conditions, and have examined two batches of mitochondria isolated from cells grown on medium supplemented with 100μM ^{57}Fe by Mössbauer spectroscopy. (We have not prepared mitochondria from cells grown with higher ^{57}Fe concentrations in the medium due to financial constraints.) The spectra (Figure 6.5C,D) were similar to those

obtained using 40 μM ^{57}Fe in the growth medium, but the amount of HS Fe^{3+} present in the two samples was quite different. We suspected that some or all of the HS Fe^{3+} in the first batch (Figure 6.5C) was an artifact of purification, but it was not chelated effectively by EGTA which is routinely added to all isolation buffers. To assess this, dithionite was included during purification of the second batch of mitochondria, such that any resulting reduced HS Fe^{2+} would become chelated by EGTA. The lack of HS Fe^{3+} features in the corresponding spectrum (Figure 6.5D) suggests that some (most) of the HS Fe^{3+} observed in the first batch was an artifact. We conclude that the iron content within mitochondria from 100 μM Fe-grown cells is nearly the same as those within mitochondria from 10 μM and 40 μM Fe-grown cells.

EPR (Figure 6.6D,E) and UV-vis spectra (Figure 6.7D,E) of mitochondria isolated from cells grown on medium supplemented with 100μM and 1mM iron have also been collected. The EPR spectra of each of these are similar to each other, the low iron EPR spectrum (Figure 6.6C) described above and the 40μM sample previously described (*233*). The UV-vis spectrum of the 100μM sample was also similar to the 10μM sample. The 1mM UV-vis sample (Figure 6.7E) however showed diminished spectral intensities relative to the other samples examined. The concentrations of these heme centers are given in Table 6.1. This may imply that under high iron the heme concentrations decline; this study should be repeated to see if the same result is obtained. In addition we should also investigate the heme centers in a 10 mM Fe-grown sample to see if these hemes centers are also lower in concentration.

Iron-Starved Respirofermenting Cells and Mitochondria

Cells were grown under iron-starved conditions with galactose as the carbon source. In previous work we have demonstrated that the respirofermenting metabolism in such cells is nearly indistinguishable from a truly respiring condition obtained by growing cells on glycerol. As with the fermenting cells, Mössbauer spectra exhibited poor S/N. The raw spectrum (Figure 6.8A) can be fit with a 12% contribution of $Fe(BPS)_3$. This contribution was subtracted and the difference spectrum (Figure 6.9A) will be used for subsequent analysis. The difference spectrum was similar to that obtained for the iron-starved fermenting cells including contributions from NHHS Fe^{2+} and CD except that an additional feature arising from HS Fe^{2+} hemes was present. Percentages used to simulate these features are given in Table 6.1.

The total Fe concentration of Fe-starved respirofermenting cells was ~ 180 μM, obtained by removing the BPS contribution. From the percentage of intensity of the NHHS Fe^{2+} doublet, we estimate that the concentration of NHHS Fe^{2+} species in these cells was ~ 31μM. EPR spectra of cells prepared in this manner (Figure 6.10A) exhibited signals from Mn^{2+} ions and a feature with $g \approx 2.01$. Based on spectral similarity, it appears the Mn^{2+} feauture for both the fermenting and respirofermenting samples is closely related. Minor features are also present in the baseline at low field corresponding to g = 6.5, 5.4, and 4.3.

Mitochondria were also isolated from iron-starved respirofermenting cells. The 5 K low-field Mossbauer spectrum (Figure 6.6A) was similar to the fermenting mitochondria isolated at the same conditions. The spectrum exhibited poor S/N

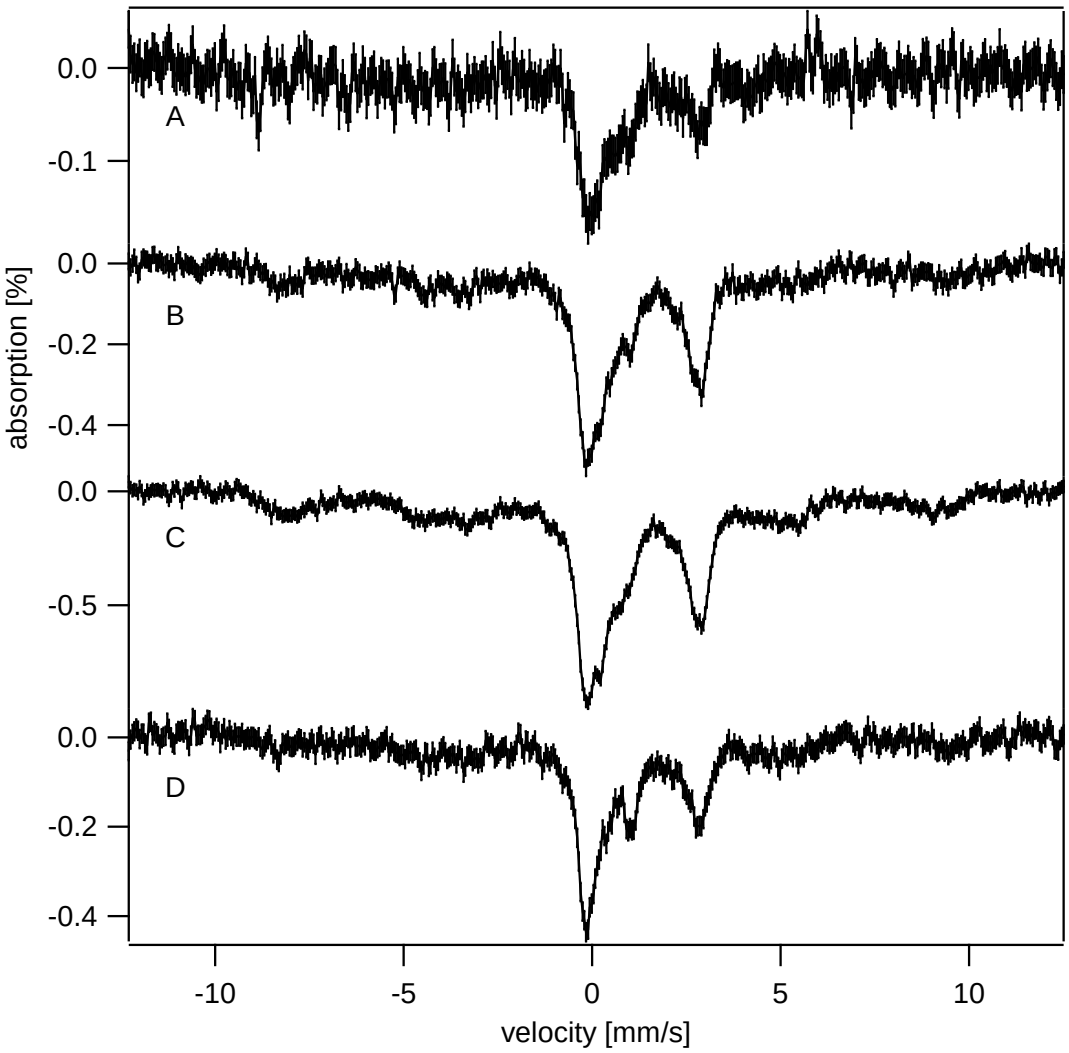

Figure 6.8. Uncorrected Mössbauer spectra of respirofermenting whole cells. Samples were grown on medium supplemented with BPS. A-D respirofermenting cells grown on medium supplemented with 21μM BPS and 1μM, 10μM, 100μM, or 1mM ^{57}Fe respectively. The corrected spectra of A-D are plotted as Figure 6.9A-D.

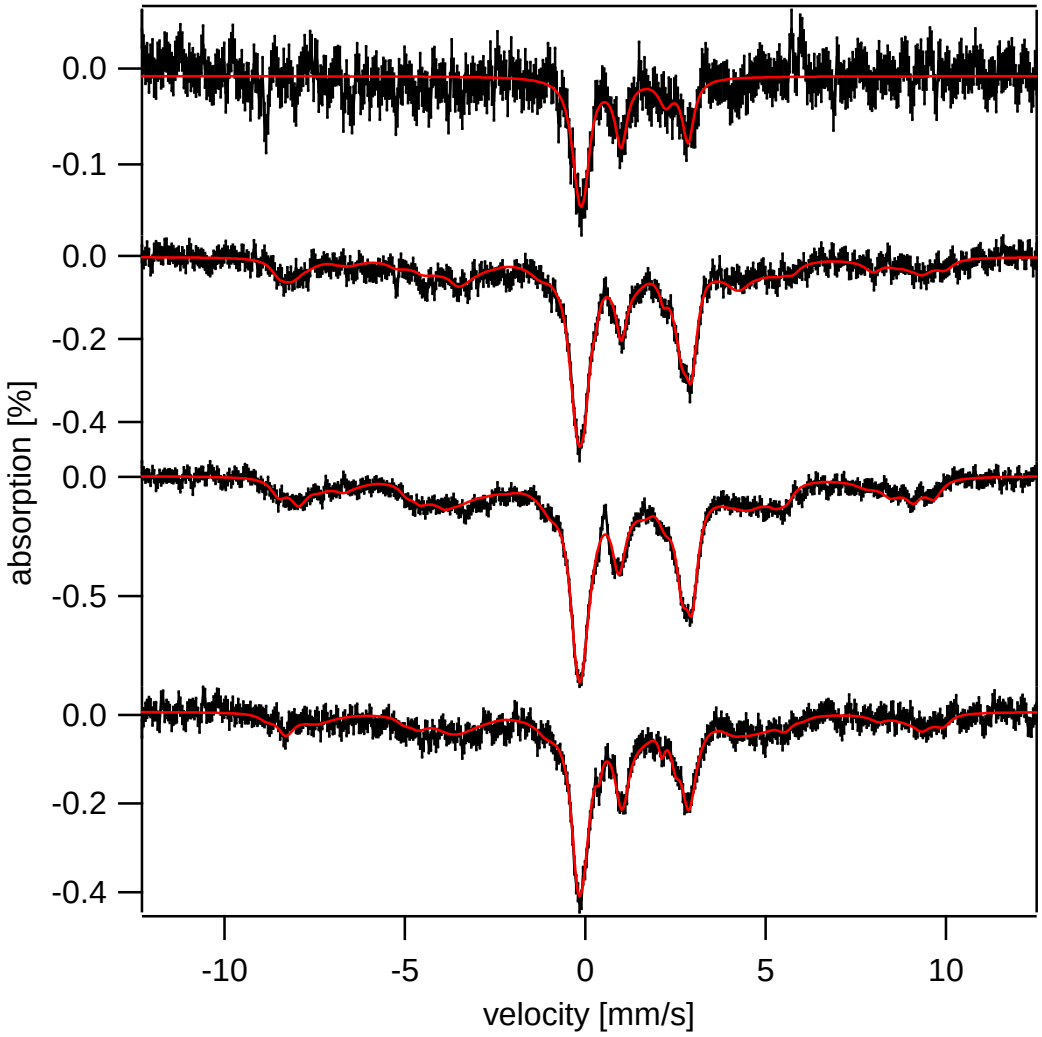

Figure 6.9. Corrected Mössbauer spectra (5K, 0.05T parallel field) of respiroferminting cells. A-D cells grown on media contain 21μM BPS and 1 μM , 10 μM , 100 μM , and 1mM ^{57}Fe respectively. Each spectrum has a contribution of $Fe(BPS)_3$ subtracted as indicated by table 6.1, the uncorrected spectra are available (Figure 6.8.)

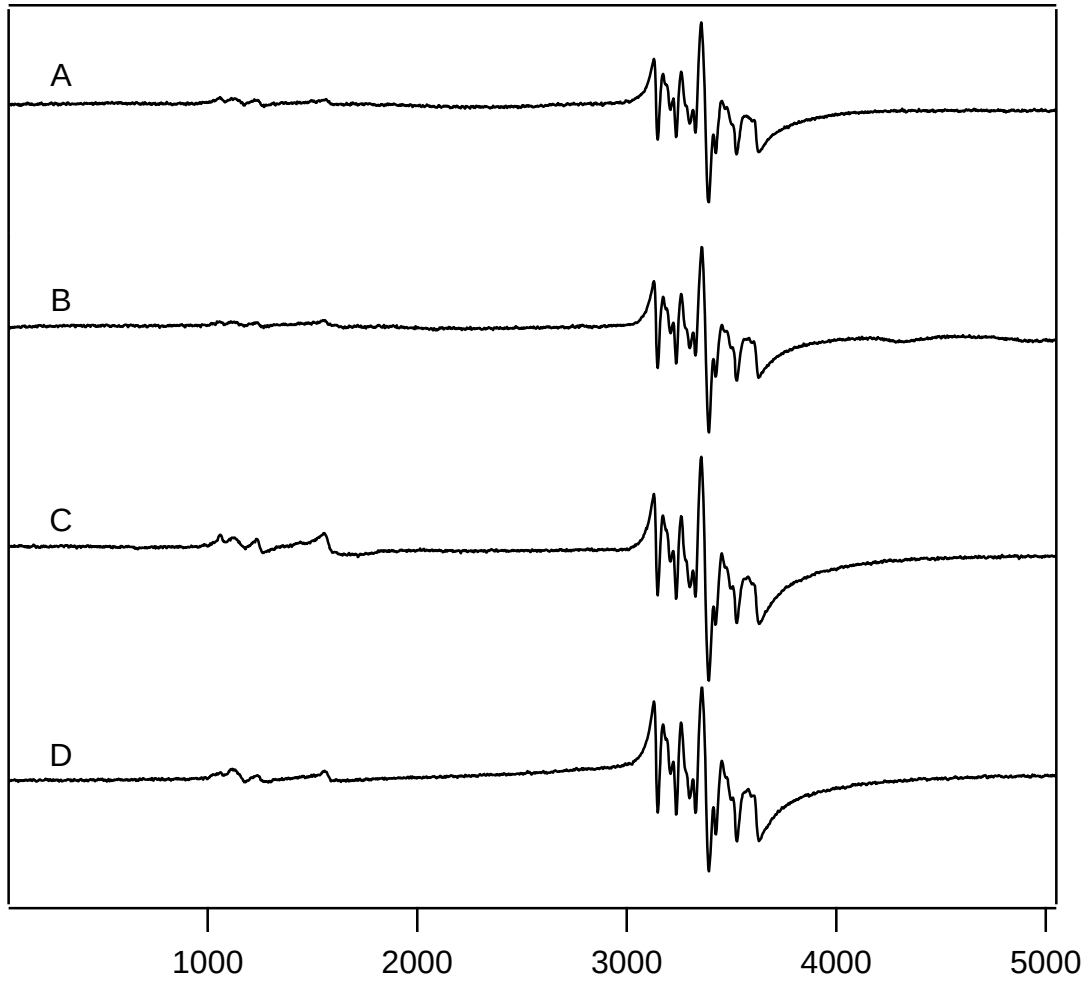

Figure 6.10. EPR spectra (10K) of respirofermenting whole cells. Samples were prepared with A. 1μM ^{57}Fe and 21μM BPS, B. 10 μM ^{57}Fe, C. 100 μM ^{57}Fe, and D.1mM ^{57}Fe, added to the growth medium. After simulating and removing the G=2.00 radical signal the spin intensities of the g =2 region for the Mn were 26 μM, 21 μM, 22 μM, and 48 μM for A-D respectively.

compared to the equivalent sample of fermenting mitochondria. Elemental analysis of these two samples for the enrichment of ^{57}Fe should be obtained to determine if more ^{57}Fe was present in the fermenting sample. Either as a result of the poor S/N or because of its absence the S = ½ $[Fe_2S_2]^{1+}$ feature was not observable in this sample. The sample was dominated by the CD (63%) also present were features arising from NHHS Fe^{2+} (14%), and heme HS Fe^{2+} (7%). As with the equivalent fermenting sample the spectrum contained very low levels of Fe^{3+} phosphate nanoparticles and mononuclear HS Fe^{3+}.

The metal content of iron-starved respirofermenting mitochondria was determined by ICP-MS, the concentrations of Fe, Cu, Mn, and Zn were 300, 270, 12, and 250μM respectively. The 10K X-band EPR spectrum (Figure 6.6A) of iron-starved respirofermenting mitochondria exhibited minor low-field signals at g = 6.5, 5.4, and 4.3. The high-field region exhibited a dominant radical at g= 2.01 as well as signals arising from respiratory complexes. Further deconvolution of these signals is necessary. The UV-vis spectrum (Figure 6.7A) of iron-starved respirofermenting mitochondria exhibited features due to Fe^{2+} heme centers. The concentration of heme *a*, *b*, *c* were 30, 70, and 120μM respectively.

Respirofermenting Cells at 10μM, 100μM, and 1mM

Respirofermenting cells were grown on medium treated with BPS and supplemented with 10μM, 100μM, and 1mM iron. Subsequently a contribution of this species as indicated in Table 6.1 was subtracted from the raw Mössbauer spectra (Figure 6.8C-E) to afford the difference spectra (Figure 6.9B-D). The Mössbauer spectra of each sample were similar; percentages of species used to simulate them are given on Table

6.1. Each of these spectra exhibited 40-50% of the intensity in the baseline similar to the HS Fe^{3+} vacuolar feature observed in Mössbauer spectra of fermenting cells grown with the same iron content. Under fermenting conditions this feature accounted for a larger percentage of the total iron in the cell. Heme HS Fe^{2+} and CD components were also present in each of these samples. A fourth feature, present in higher abundance than the equivalent fermenting samples was due to NHHS Fe^{2+}.

Using the iron numbers obtained from ICP-MS (Table 6.1) for these conditions and the percentages obtained from the Mössbauer spectra, the maximum amount of vacuolar iron was 155μM, 280μM, and 125μM for the samples supplemented with 10μM, 100μM, and 1mM iron respectively. The concentration of iron in the 100μM sample seems high relative to our expectations, and another replicate should be examined.

Following Mössbauer analysis, the cells were anaerobically thawed and transferred to EPR tubes. The spectra (Figure 6.10B-D) were similar to one another and to the iron-starved cells. All spectra exhibited features corresponding to Mn^{2+} and only minor features in the low field area. Unlike the HS Fe^{3+} feature observed in fermenting cells, the feature observed in the baseline of Mössbauer spectra of respirofermenting cells did not produce a g= 4.3 signal. This implies that the HS Fe^{3+} feature may not be vacuolar in origin. If the feature is however vacuolar it implies that the conditions inside the vacuole have changed such that different magnetic properties of the iron contained therein are observed. Alternatively it may be a different complex. To demonstrate if this

species is originating from the vacuole, the organelle should be isolated from respiring or respirofermenting cells.

Using data obtained from the Mössbauer spectra and ICP-MS analysis, the concentrations of the NHHS Fe^{2+} feature were found to be 105μM, 155μM, and 110μM for the samples supplemented with 10μM, 100μM, and 1mM iron respectively. This represents ~5 fold higher concentrations of this species in respirofermenting cells as compared to the equivalently grown fermenting cells.

Fet3-GFP Expression Levels in Fermenting and Respirofermenting Cells at Different $[Fe]_{media}$

The DY150, FET3-GFP::KanMX strain has a green fluorescent protein (GFP) fusion with Fet3p (*219*). Using an antibody against GFP we have examined the expression of GFP (and therefore Fet3p) by western blot analysis under both fermenting and respirofermenting conditions with various concentrations of iron supplemented in the growth medium. Expression of GFP was only detected for iron-starved fermenting cells. In this sample (last lane on right of Figure 6.11) 3 bands were observed with the middle band displaying the highest density and the upper band displaying the lowest density. Analysis of each of these bands individually indicates the upper band which is still visible in the blot is ~7 times less dense than the most intense middle band. This implies that the amount of Fet3-GFP in this sample is *at least* 7 times higher than any of the other samples.

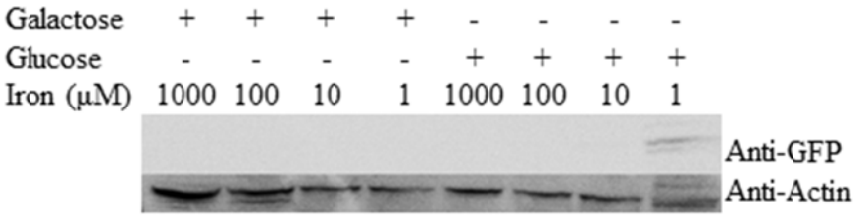

Figure 6.11 Western Blot of Fet3-GFP cells grown at various conditions. Actin is added as a loading control.

Conclusions

Iron import and distribution is tightly regulated in yeast. Under fermenting conditions we observe a downregulation of Fet3p, a product of the iron regulon at relatively low $[Fe]_{medium}$. Cells cultured on medium containing >7-8μM iron show no Fet3p expression. Conversely, cells grown on <7-8μM iron in the growth medium show a reduced HS Fe^{3+} feature arising from vacuoles. This indicates that under physiological conditions a substantial portion of cellular iron is imported by Aft1p independent processes. Cells cultured on medium containing ~17 μM Fe have vacuolar iron concentrations similar to those seen in cells cultured on medium containing > 40 μM iron. Only slight changes are observed in samples cultured on high(excessive) concentrations of iron.

Respirofermenting cells do not appear to utilize the iron regulon in the range of our experiments, as no Fet3p expression was observed in any such samples. Interestingly, these cells appear to have less iron associated with the vacuoles, iron if present in the vacuoles of these cells appears to possess different magnetic properties than the fermenting equivalent. Respirofermenting cells also contain a substantially larger NHHS Fe^{2+} component than fermenting cells. The feature is ~5 stronger in respirofermenting cells. One explanation for this is that the vacuoles have emptied their contents to the cytosol where iron will likely be in the reduced state.

The iron in mitochondria from iron-starved fermenting samples seems to be in a state more similar to respiring samples than fermenting samples. Mössbauer spectra of fermenting mitochondria exhibited spectral features primarily arising from hemes and

ISCs with very little Fe^{3+} nanoparticles, HS Fe^{3+}, and NHHS Fe^{2+}. This indicates that under iron-starved conditions the fermenting cellular response is to: a), not store iron in the vacuoles, b) insert a majority of the iron into ISCs and hemes; and c) limit forms of iron in the mitochondria which are not these centers. This reflects a situation where the cell is using iron sparingly for the most important processes, displaying an ability of the cell to redistribute available iron under conditions of iron deprivation. Iron-starved respirofermenting mitochondria were virtually indistinguishable from iron replete repirofermenting mitochondria (*233*) except they contained less iron.

CHAPTER VII

CHANGING CONTENT OF THE MOUSE BRAIN DURING DEVELOPMENT

Introduction

Iron plays a major role in generating the chemical energy required for neurological activity, in that Fe/S clusters and heme groups are abundant in mitochondrial respiratory complexes (*121*). This transition metal is found at the active sites of numerous metalloenzymes in the brain (*299*) and is required for myelin biosynthesis (*124*). Over a billion people worldwide suffer from anemia (*166*), and Fe deficiency affects neonatal brain development and cell-mediated immunity (*300*). An overabundance of Fe is also problematic, as certain forms of iron, particularly NHHS Fe^{2+} complexes, promote Fenton chemistry that generates reactive oxygen species (ROS). The brain may be particularly sensitive to ROS damage because of its high rate of O_2 consumption (*301*) and limited ability of neuronal cells to be repaired or replaced (*302*). Moreover, Fe accumulates with age and neurodegeneration (*303*).

Iron traveling into the brain must pass across the blood-brain barrier (BBB) (*304*). Fe^{3+}-bound transferrin in the blood binds to receptors on the luminal side of the endothelial cells associated with this barrier (*305*). Once inside neurons and other cells of the brain, a portion of the Fe is trafficked to mitochondria, where hemes and iron-sulfur clusters are assembled. Another portion is stored as ferritin, a spherically shaped protein complex with a hollow core into which large amounts of Fe can be deposited in the form of magnetically-interacting Fe^{3+} oxyhydroxide material (*142*). Ferritin helps

regulate cytosolic Fe concentrations and sequester Fe that might otherwise generate ROS. Fe can also be found in structurally related proteins such as mitoferritin (*306*), hemosiderin (*144*) and nueromelanin (*137*).

X-ray fluorescence (*147*), high-field magnetic resonance imaging (*149*) and high-resolution histological staining (*307*) have revealed an inhomogeneous spatial distribution of Fe in the brain. The globus pallidus, putamen, substantia nigra pars reticulata, red nucleus, cerebral dentate nucleus, the nucleus accumbens and portions of the hippocampus contain high concentrations of Fe; Fe concentrations in white matter and the cerebrospinal fluid are low. The distribution of brain Fe follows the distribution of ferritin whereas the distribution of transferrin is more homogeneous (*308*), reflecting the dominance of ferritin Fe in the brain.

These imaging methods provide excellent spatial resolution of brain Fe but their ability to resolve different types of Fe-containing species is limited. Mössbauer spectroscopy can distinguish different types of Fe (*116*), but it has barely been applied to the brain, due perhaps to the insensitivity of the technique, the low concentration of Fe in the brain, and the ability of Mössbauer to detect only ^{57}Fe (2% natural abundance).

We have used Mössbauer spectroscopy, in conjunction with EPR and UV-vis spectroscopies, and ICP-MS, to assess the Fe content of yeast mitochondria, vacuoles and whole cells (*233, 261, 290*). In those studies, our objective was to evaluate the types and relative amounts of Fe present in these organelles and cells. In yeast, the two dominant Fe “traffic hubs” include vacuoles, which store Fe, and mitochondria, which use it to obtain cellular energy.

Here we apply the same methods to study the iron content of intact ^{57}Fe-enriched mouse brains. Previous Mössbauer studies of the brain have focused on particular Fe-rich subcomponents of human brains. These studies found that virtually all Fe in these regions consists of magnetically interacting, superparamagnetic ferric species, including ferritin and nueromelanin (*137, 142, 144, 303, 306*); curiously, mitochondrial Fe, e.g. Fe/S clusters and heme groups were not observed. This is difficult to rationalize, given the enormous role of mitochondria in brain function, and the substantial proportion of yeast Fe due to this organelle. We show here that, besides ferritin-like species, the brains of mice contain substantial amounts of Fe/S clusters, much of it arising from mitochondria. Also detected were nonheme mononuclear high-spin (HS) Fe^{2+} and Fe^{3+} species, a portion of which may constitute the labile iron pool (LIP) and which may participate in ROS-generating reactions.

Results

^{57}Fe-enrichment

Low Fe concentrations in mouse brains (Table 7.1 and Figure 7.1) highlighted the need for ^{57}Fe enrichment. To evaluate enrichment rates, mice born to an ^{56}Fe-enriched mother were fed ^{57}Fe-supplemented chow immediately after weaning. Their brains enriched slowly such that only partial ^{57}Fe-enrichment was achieved after nearly 60 wks on the ^{57}Fe-supplemented diet. Other organs, including liver, spleen, heart and kidney, enriched faster and to a greater extent than the brain, with the duodenum enriching fastest (data not shown). The slow incorporation of ^{57}Fe into the brain was

Table 7.1. Summary of results of mouse studies. The concentration of heme *b* in the prenatal brain (*) was not quantified. Values obtained by EPR, UV-vis, ICP-MS and protein analyses have an estimated relative uncertainty of ± 20%. Values derived from Mössbauer analyses have an absolute estimated uncertainty of ± 4%.

Age (wks)	**-1**	**1**	**2**	**3**	**3**	**4**	**24**	**58**
Comments	Not Perfused				Iron Deficient			
Number and Sex	6 (sex not determined)	7F 2M	1F 2M	0F 3M	1F 8M	1F 3M	0F 2M	0F 1M
Average brain mass (mg)	52 ± 6	200 ± 30	350 ± 4	310 ± 40	350 ± 10	390 ± 30	377 ± 2	456
Num. used for element, protein analysis	6	4	2	3	3	2	2	1
[Protein] (mg/mL)	21	30	29	40	32	40	28	33
[Cu] (μM)	21	6	2	1	20	5	17	26
[Mn] (μM)	21	3	6	6	26	11	5	6
[Zn] (μM)	123	210	179	205	167	197	172	206
[Fe] (μM)	270	121	195	199	149	182	212	322
% 57Fe	60	72	66	73	57	85	83	58
Hemoglobin Doublet subtracted (%)	37	3	5	10	11	14	11	18
Effective [Fe] in brain (μM)	170	117	185	179	132	157	188	264
Ferritin-like sextet (% of effective Fe)	67	54	51	57	19	42	57	56
Central Doublet (% of effective Fe)	19	27	37	31	57	42	30	33
sextet/CD ratio	3.5	2.0	1.4	1.8	0.33	1.0	1.9	1.7
HS Fe^{2+} hemes (% of effective Fe)	~ 0	13	8	6	13	9	7	9
HS Fe^{2+} nonheme (% of effective Fe)	10	6	~ 4	6	10	8	6	~ 2
[Fe^{2+} heme a] (μM)	~ 0	~ 0	4	15	15	18	18	18
[Fe^{2+} heme b] (μM)	*	~ 0	6	15	12	18	18	18
[Fe^{2+} heme c] (μM)	~ 0	~ 4	12	23	25	32	32	35
gave = 4.3 (μM); HS Fe^{3+} nonheme	0.1	0.1	0.1	0.1	0.1	0.1	0.1	0.1
g = 1.90 (μM); Rieske [Fe2S2]1+	0	0.9	1.2	1.5	1.5	2.7	2.4	1.7
g = 1.93 (μM); SDH [Fe2S2]1+	0	1	1.2	1.5	1.5	2.4	2.1	1.5
g = 2.00 (μM); organic radical	0.1	0.1	0.1	0.3	0.3	0.2	0.3	0.7

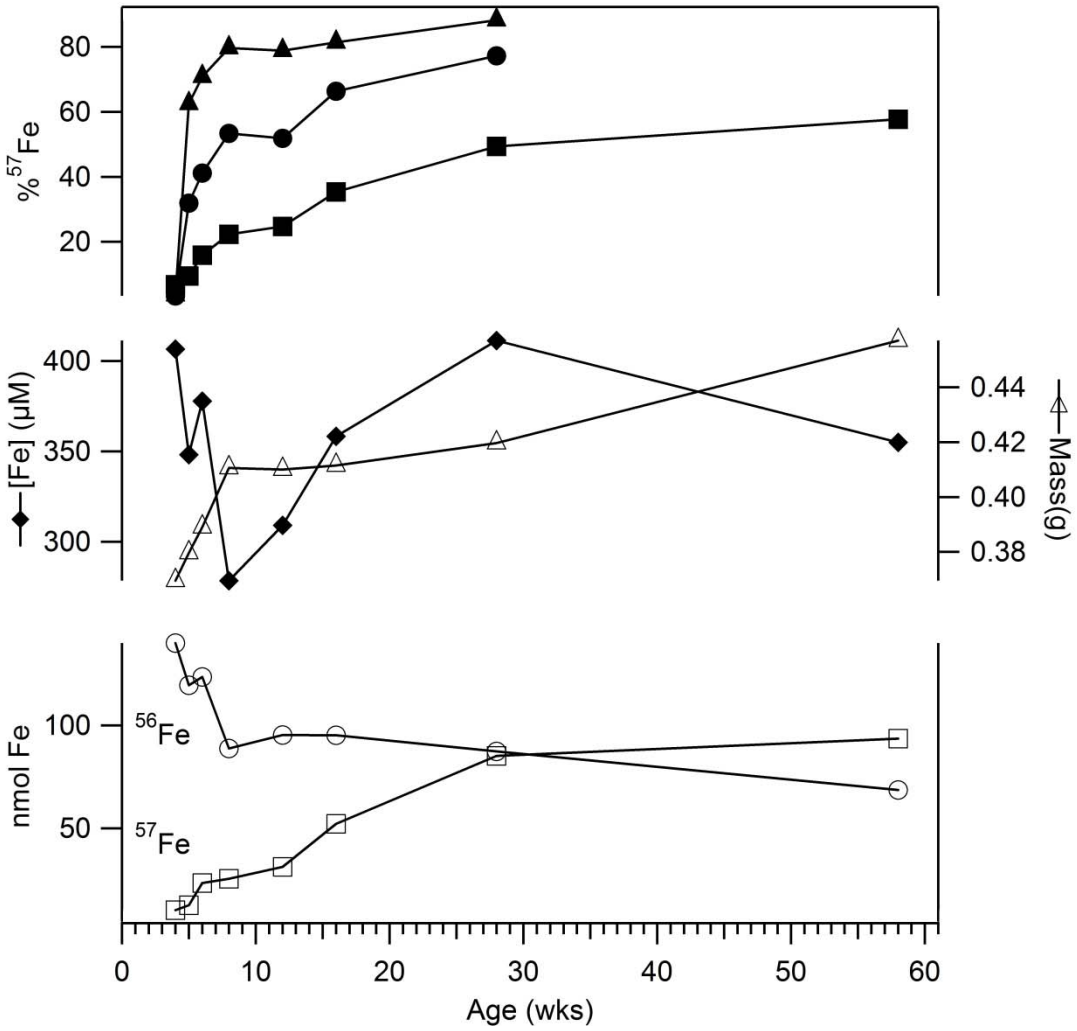

Figure 7.1. Enrichment of ^{57}Fe into ^{56}Fe-enriched mice. Upper plots refer to the % ^{57}Fe scale, including solid triangles (duodenum), solid circles (average of liver, kidney, heart and spleen) and solid squares (brain). Solid diamonds in the middle group of plots refer to total [Fe] in the brain; open triangles refer to brain mass. In the lower group, open circles and squares refer to nmoles of ^{56}Fe and ^{57}Fe in the brain, respectively.

probably due to the blood-brain barrier (*304*). Cu, Mn, Zn, Mo and P concentrations in these organs were also determined (data not shown).

The rate of Fe enrichment was biphasic, with the transition from fast to slow phase occurring 4-6 wks postpartum. During the fast-enrichment period, the total nanomoles of ^{56}Fe in the brain declined rapidly while that of ^{57}Fe increased gradually (Figure 7.1). The overall concentration of Fe in the brain declined during the fast-enrichment phase, followed by recovery in the slow-enrichment phase. Brain mass increased rapidly during the fast-enrichment phase and slowed thereafter. The concentration of ^{57}Fe in the brain increased with each generation raised under ^{57}Fe-enrichment conditions, maximizing at ~ 80% after about 3 generations. Mössbauer spectra were typically collected from animals raised under ^{57}Fe-enrichment conditions for ≥ 2 generations.

Brains from Three wk Old Mice

The low-temperature low-field Mössbauer spectrum of a 3-wk old brain exhibited 4 discernible features. A sextet typical of ferritin-bound Fe^{3+} ions dominated (Figure 7.2A); the blue line is a simulation with $\delta = 0.5$ mm/s, $\Delta E_Q = -0.3$ mm/s and $\Gamma = 0.6$ mm/s. Ferritin is an Fe-storage protein complex (*142*). At 70 K, this feature collapsed into a doublet ($\delta = 0.5$ mm/s and $\Delta E_Q = 0.7$ mm/s) (Figure 7.2B), similar to the behavior of authentic ferritin (*309*). The baseline of the 70 K spectrum did *not* reveal underlying features. When a 6 T field was applied at 4.3 K, the resulting pattern (Figure 7.2C) associated with this feature was again indistinguishable from that of ferritin. Other

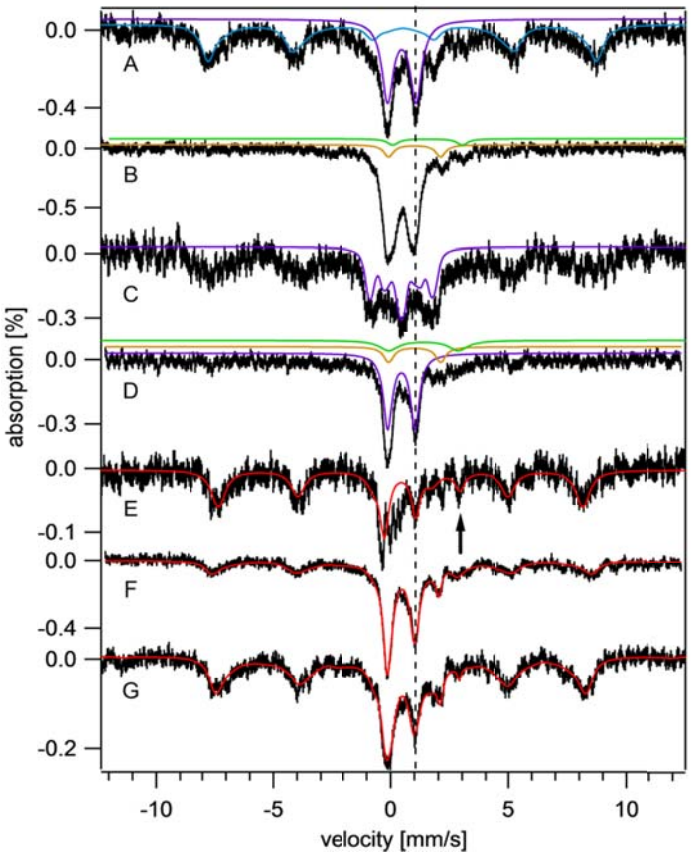

Figure 7.2. Mössbauer spectra of brains isolated at different ages. Spectra were collected at 6 K and with a 0.05 T field applied parallel to the radiation unless otherwise noted. (A), 3 wk brain; (B), same as (A) but at 70 K; (C), same as (A) but at 4.3 K and 6 T field applied perpendicular to the radiation; (D), 3wk Fe-deficient brain; (E), -1wk brain; (F), 4 wk brain; (G), 58 wk brain. Red lines are composite simulations for (E – G). Simulations assumed parameters mentioned in the text and percentages listed in Table 1. The vertical dashed line shows the position of the hi.gh-energy line of the central doublet. The arrow in (E) shows the position of the NHHS Fe^{2+} feature. H_{int} values associated with the ferritin sextet ranged from 480 – 506 kG, which may reflect subtle differences in the ferritin core structure.

magnetically interacting Fe^{3+} ions such as Fe-bound haemosiderin (*309*), neuromelanin (*137*) or mitoferritin (*306*) could have also contributed.

Another major feature in the spectrum was a quadrupole doublet with $\delta = 0.45$ mm/s and $\Delta E_Q = 1.15$ mm/s; these values are typical of S = 0 $[Fe_4S_4]^{2+}$ clusters and low-spin Fe^{2+} heme centers. At 6 T, the splitting pattern observed for this so-called *Central Doublet* (CD) was simulated (Figure 7.2C, purple line) confirming the expected diamagnetism. A doublet with identical parameters in spectra of isolated mitochondria from yeast (*233*) arises primarily from respiratory complexes, and so we assign the majority of the CD intensity in brain to mitochondrial respiratory complexes.

The spectrum also exhibited a quadrupole doublet with $\delta \sim 1.4$ mm/s, $\Delta E_Q \sim 3.3$ mm/s arising from one or more NHHS Fe^{2+} species (Figure 7.2B, simulated by the green line). These parameters are typical of such complexes with 5 – 6 O/N donor ligands. Most evident in the 70 K spectrum was the doublet from HS Fe^{2+} heme centers (Figure 7.2B, yellow line). UV-vis spectra of corresponding brain homogenate (Figure 7.3D) revealed the Soret, α and β bands indicating reduced hemes. These features were similar to those of yeast mitochondria (*233*); their concentrations were quantified and are listed in Table 7.1.

Low-temperature EPR spectra of 4-wk mouse brain homogenates (Fig. 7.3) were virtually identical to those of a 3-wk old animal but were slightly more intense. Both exhibited overlapping signals in the g = 2 region. Signals with g = 1.93 and 1.90 probably arose from the S = ½ $[Fe_2S_2]^{1+}$ cluster of succinate dehydrogenase and the reduced Rieske S = ½ $[Fe_2S_2]^{1+}$ cluster associated with cytochrome bc_1, respectively

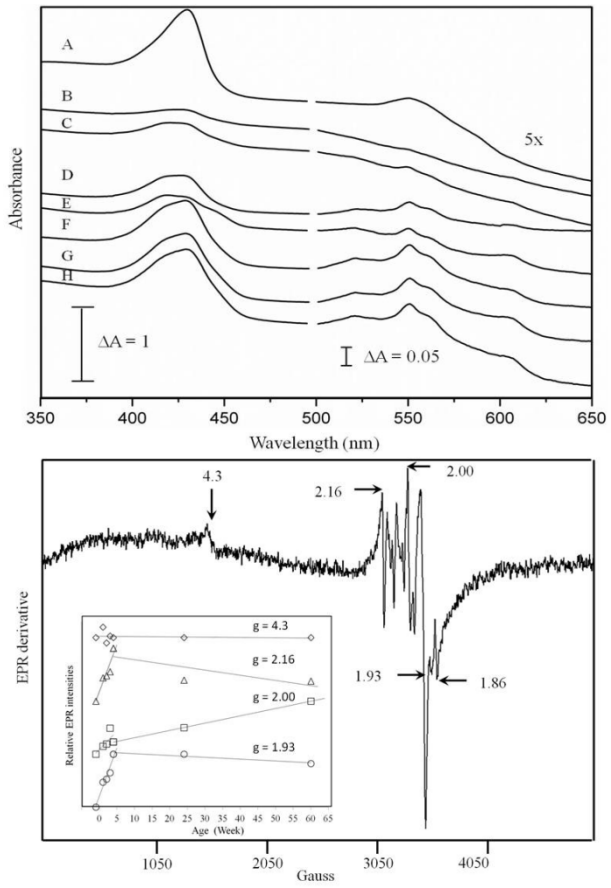

Figure 7.3. UV-vis spectra of brains isolated at different ages (top) and EPR spectrum of 4 wk brains (bottom). (A), -1 wk; (B), 1 wk; (C), 2 wks; (D), 3 wks; €, 3 wks, Fe-deficient; (F), 4 wks; (G), 24 wks; and (H), 58 wks. Intensities at wavelengths > 500 nm were multiplied by 5. Spectra shown are prior to subtracting the contributions due to hemoglobin. Bottom: Highlighted signals are indicated by arrows. Conditions: temperature, 4 K; microwave frequency, 9.43 GHz; microwave power, 0.2 mW; modulation amplitude, 10 G; sweep time, 335 sec; time constant, 164 msec. The average of 10 scans is shown. Spectra of brains isolated from animals at other ages are given in Figure 7.4. The inset shows the relative intensity of highlighted features as a function of age. Plots are offset by arbitrary amounts.

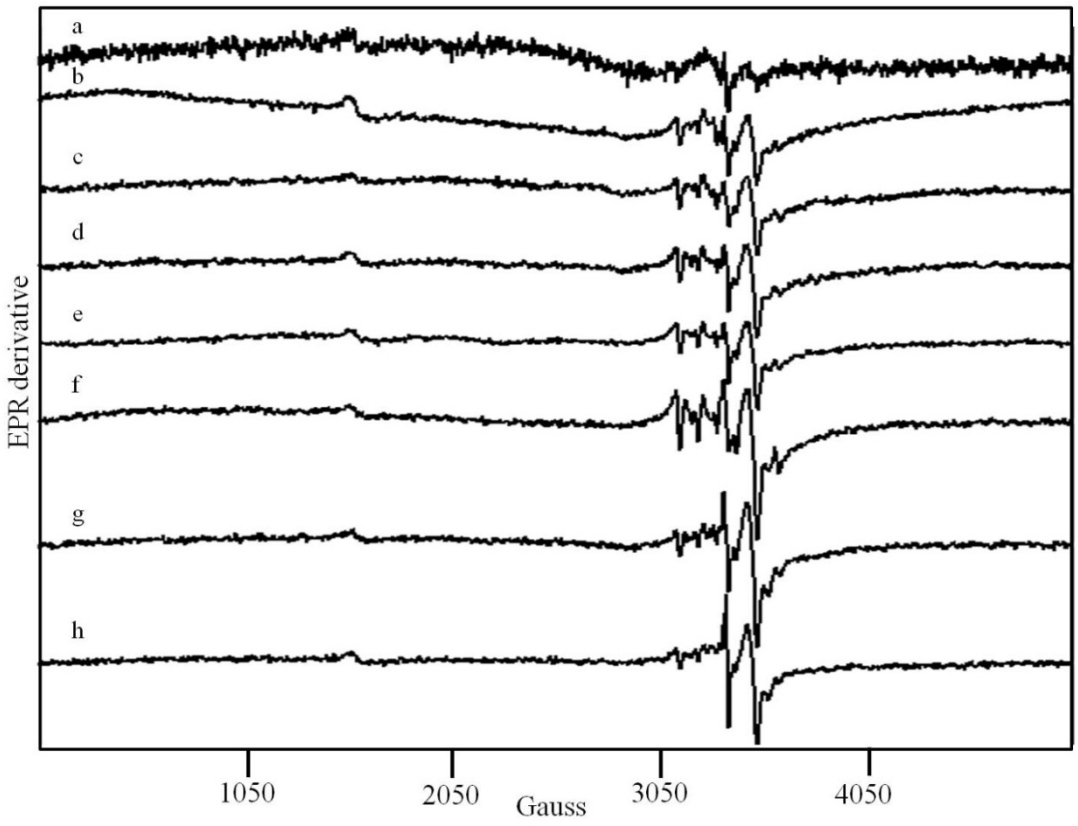

Figure 7.4. EPR spectra of packed mouse brain homogenates from mice euthanized at different ages. (A), -1 wk; (B), 1 wk; (C), 2 wks; (D), 3 wks; (E), 3 wks, Fe-deficient; (F), 4 wks; (G), 24 wks; and (H), 58 wks. EPR conditions are the same as in the Figure 7.3 legend.

(*233*). Also evident was an isotropic signal at g = 2.00, probably from an organic radical. The weak signal at g = 4.3 undoubtedly arose from mononuclear HS Fe^{3+} species with rhombic symmetry. The origin of the derivative-like feature at g = 2.16 is uncertain. Spin quantifications are listed in Table 7.1.

Brains from Iron-Deficient Mice

A pregnant ^{57}Fe-enriched mouse was switched to Fe-deficient chow 3 days prior to giving birth, and her offspring were euthanized 3 wks later at which time they displayed alopecia (Figure 7.5) (*310*). The average Fe concentration in their brains (Table 7.1) was less than in Fe-sufficient brains. Mössbauer spectra (Figure 7.2D) exhibited less of the ferritin sextet relative to Fe-sufficient brains, while the CD (purple line) was more intense. Surprisingly, the *absolute* concentration of the CD Fe in these brains was slightly *higher* than that in comparable Fe-sufficient brains (75 μM *vs*. 55 μM). A minor NHHS Fe^{2+} feature was also evident (Figure 7.2D, green line). EPR and UV-vis spectra of Fe-deficient brains exhibited the same signals and intensities as observed in spectra from brains of Fe-sufficient mice.

Prenatal Brains

Prenatal mice could not be perfused, such that the quadrupole doublet due to hemoglobin in the corresponding Mössbauer spectra was more intense than in the 3-wk brain spectra. The exact position of the heme doublet (δ = 0.96 mm/s, ΔE_Q = 2.35 mm/s) was also shifted slightly relative to that in other spectra, due to the presence of *fetal* hemoglobin in prenatal brains (*311*).

Figure 7.5. Iron-Deficient Mouse used in this study. The image is of a 3 wk old mouse nursed by a mother whose chow had been switched from ^{57}Fe-supplemented to Fe-deficient *ca*. 3 days prior to giving birth. The pup displayed significant alopecia (thinning of hair).

The average Fe concentration in the prenatal brains (Table 7.1) included a significant contribution from blood (~ 100 μM). Since the concentration of Fe in undiluted blood was 7.8 mM (data not shown), ~ 1.3% of the dissected prenatal brain volume must have been occupied by blood. This underestimates the value in living animals. Apart from the blood contribution, the Mössbauer spectrum of prenatal brains was dominated by the ferritin sextet, with only a minor percentage due to the CD (Figure 7.2E, Table 7.1) A NHHS Fe^{2+} doublet was evident (arrow), with intensity comparable to that of the 3 wk brain spectrum. The UV-vis spectrum of prenatal brain homogenate (Fig. 7.3A) was dominated by features due to fetal hemoglobin; other heme-based species (e.g. mitochondrial cytochromes) could not be discerned. Intensities of EPR signals from the prenatal brain homogenate were diminished relative to those in other spectra (Fig. 7.4A). These results indicate that *prenatal brains were deficient in mitochondria*, with most Fe present as ferritin or ferritin-like species.

Brains from Mice at Different Ages

Mössbauer spectra of brains from mice of different ages (Figure 7.2, E – G, and Figure 7.6) showed an age-dependent increase in the percentages of the CD and a relative decrease in the ferritin-like sextet. This is indicated most reliably by the ferritin:CD intensity ratios (Table 7.1) which was highest for prenatal brains and lowest at 4 wks. Mössbauer spectra of the 24 and 58 wk brains exhibited age-dependent increases in the percentage of the ferritin-like sextet and decreases in the CD. UV-vis spectra also showed an age-dependent increase in cytochromes at early ages (Fig. 7.3).

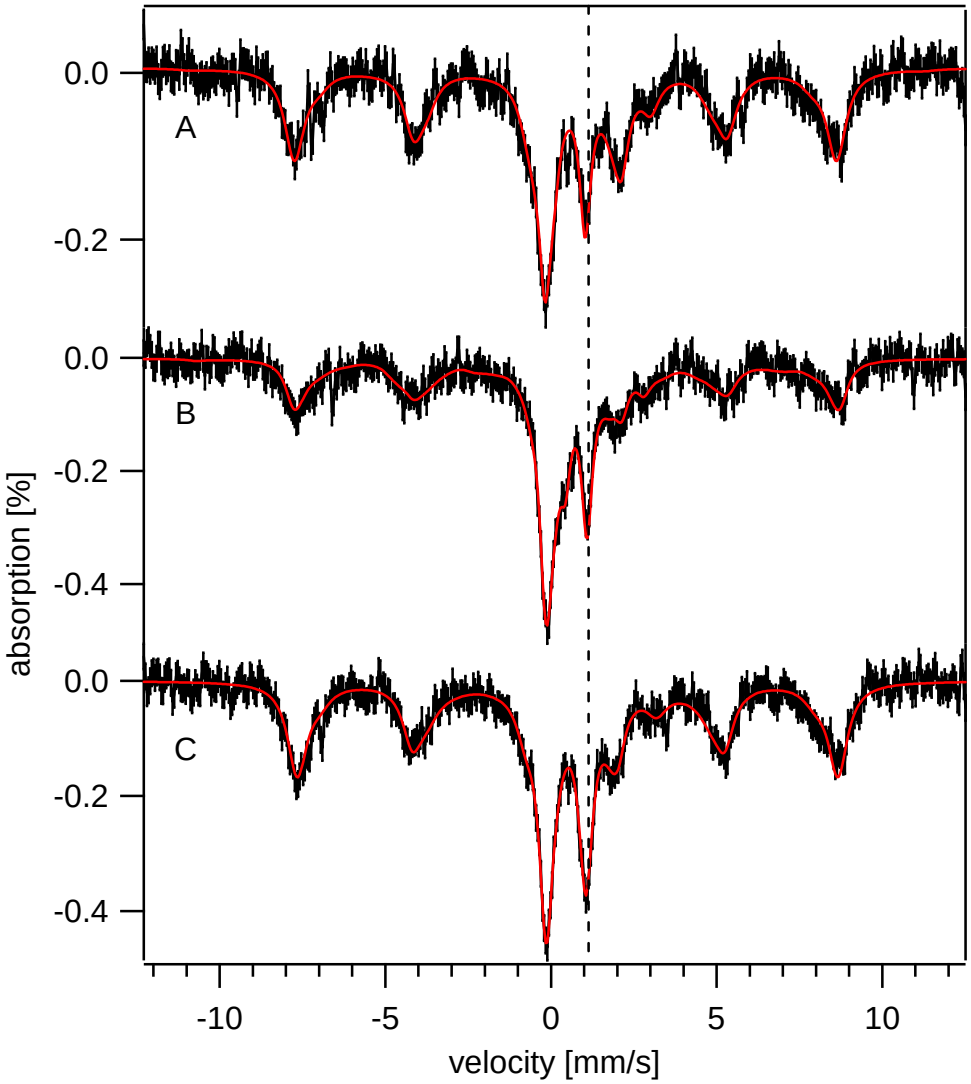

Figure 7.6. Corrected Mössbauer spectra of mice brains. Samples are brains at (A), 1 wk, (B), 2 wks, and (C), 24 wks. The dashed line indicates the position of the high energy line of the central doublet. Simulations in red use parameters from the text and percentages from Table 7.1. Spectra were collected at 6 K with a 0.05 T field applied parallel to the radiation. Uncorrected spectra are presented in Figure 7.7.

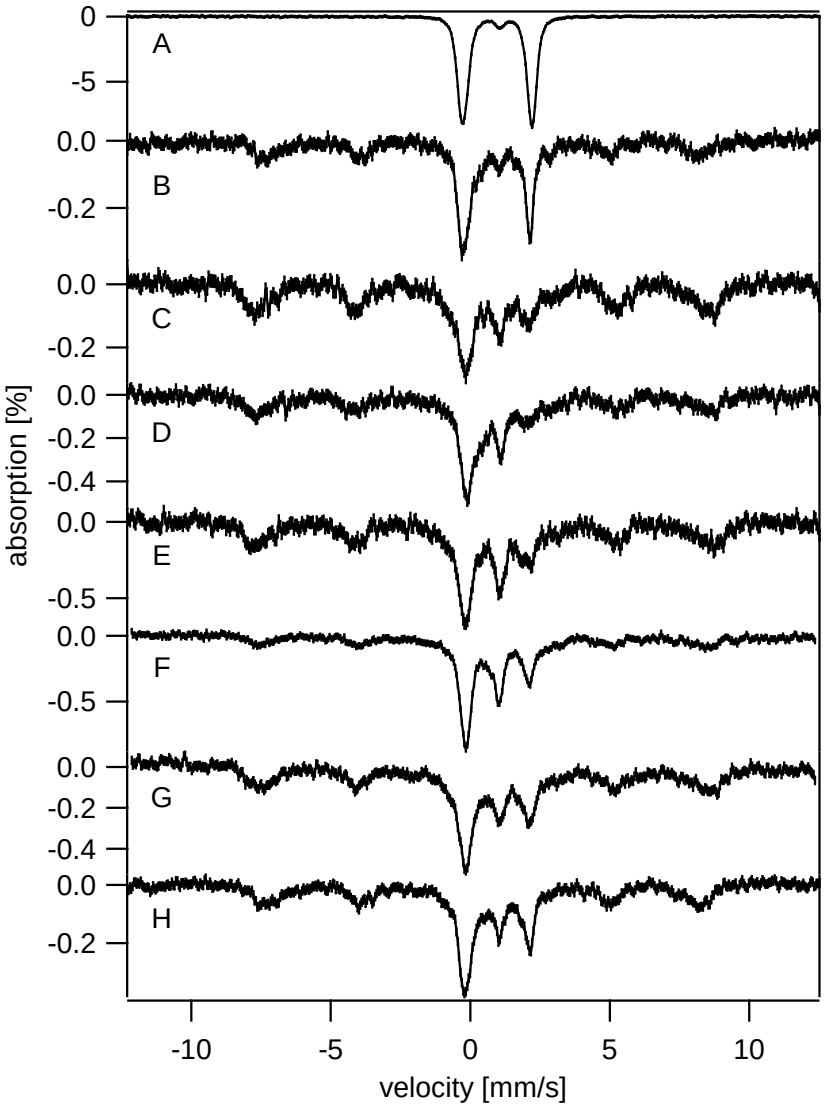

Figure 7.7. Uncorrected Mössbauer spectra of mouse brains at different ages. (A), blood from a 4 wk mouse; (B), unperfused prenatal brain (corresponds to corrected spectrum, Figure 7.2E); (C), uncorrected spectrum of perfused 1 wk brain (corrected spectrum is Figure 7.6A); (D), uncorrected spectrum of perfused 2 wk brain (corrected spectrum is Figure 7.6B); (E), uncorrected spectrum of perfused 3 wk brain (corrected spectrum is Figure 7.2A); (F), uncorrected spectrum of perfused 4 wk brain (corrected spectrum is Figure 7.2F); (G), uncorrected spectrum of perfused 24 wk brain (corrected spectrum, Figure 7.6C); (H), uncorrected spectrum of perfused 58 wk brain (corrected spectrum, Figure 7.2G); Spectra were collected at 5-6 K and 0.05 T magnetic field applied parallel to the direction of the radiation. Total Mössbauer data collection times (in hrs), including 70 K data, were (A), 40; (B), 330; (C), 435; (D), 390; (E), 240; (F), 390; (G), 570; and (H), 400.

EPR spectra exhibited increasing intensities of the signals in the g = 2 region (Fig. 7.4), including features that likely originate from mitochondria. The radical signal at g = 2.00 also increased with age, while the g = 4.3 signal intensity was age-invariant.

Discussion

Comparison to Previous Mössbauer Studies

The Mössbauer spectra presented here are significantly different from previous reports (*142, 158, 312*) in that the only feature observed previously was the sextet due to ferritin or neuromelanin. Why none of the previously published spectra of brain displayed a CD, a heme quadrupole doublet, or NHHS Fe^{2+} species can partially rationalized. Previous studies utilized human brains which were unenriched in ^{57}Fe; this diminished the spectral quality such that minor species, e.g. NHHS Fe^{2+}, could have gone undetected. The human donors were generally near the end of their natural lifespan, and older brains may contain more ferritin than younger ones (*313*). The concentration of Fe in the average human diet may be higher, relatively speaking, than in our mouse chow, which could possibly translate into relatively more ferritin and less CD in the human brain. Further studies are required to examine these possibilities.

Incorporation of Fe into Brain

In this study, we found that young mouse brains exchanged Fe rapidly during the rapid growth phase, including the *export* of Fe. This resulted in an overall *decline* in the concentration of Fe in the brain. During this period, the brain appears to grow faster than could be maintained by the rate of Fe import, such that ferritin stores were activated. With age, the dynamic exchange of Fe slows, brain growth slows, and the concentration

of Fe in the brain recovers. Similar effects have been reported (*314-316*). During the first month of life, the proportion of stored Fe declines while the proportion of mitochondrial Fe increases. As the animals become adults, the proportion of stored Fe increases again. In our study, the concentration of mitochondria did not decline noticeably up to 58 wks; we are currently investigating whether mitochondrial levels decline towards the end of the animal's natural lifespan, as has been reported (*302*).

Burst of Mitochondriogenesis.

In yeast cells, the Mössbauer CD and HS heme doublet, the g = 1.94 and 1.90 EPR signals and the heme *a*, *b*, and *c* UV-vis signals arise primarily from the mitochondrial respiratory complexes (*233*), and so we have assigned the analogous features in brain spectra similarly. The intensity of these signals, considered collectively, undoubtedly reflects the concentration of mitochondria in the brain. The ferritin-like sextet in the Mössbauer spectrum reflects brain Fe that is stored. These assignments are supported by a recent study of the ironome of human Jurkat cells and their isolated mitochondria (*317*).

Our results show that most of the Fe in the brain of prenatal and newborn mice is stored, and that during the first month of life, the proportion of stored Fe declines while the proportion of mitochondrial Fe increases. As the animals move into adulthood, the proportion of stored Fe in the brain increases again. We did not detect an overall decline in the concentration of mitochondria with age up to 58 wks; further studies are underway to determine whether mitochondrial levels decline towards the end of the animal's

natural lifespan. Mitochondrial levels have been reported to decline with age due to mitophagy (*302*).

These results, in conjunction with those of the ^{57}Fe incorporation study, suggest a connection between this burst of mitochondriogenesis and an increase in brain activity (Figure 7.8). Before birth and immediately thereafter, the level of brain activity is low and so might be the demand for energy. During this period, Fe is slowly imported into the brain where most of it is stored as ferritin or ferritin-like material. During the first few weeks of life, there is an increased level of brain activity as the animal's eyes open and they explore their environment. The increased brain activity increases the demand for more chemical energy, prompting a burst of mitochondriogenesis. This demand for Fe is beyond that at which Fe can be imported into the brain. Thus, the brain draws upon its Fe stores to build the requisite Fe/S clusters and heme centers. The scarcity of Fe is exacerbated by the rapid increase of brain volume during the same period, resulting in the overall decline in the Fe concentration in the brain. Eventually, the burst of mitochondriogenesis slows, as does the rate of brain growth. The brain replenishes its Fe stores, via the slow import of Fe from the blood, and it reestablishes a higher overall Fe concentration.

This model is consistent with previous results. Pysh and co-workers used electron microscopy to determine the proportion of rat cell volume (in the inferior colliculus) due to mitochondria during different stages of development (*318*). The mitochondrial profile number was relatively low during the first few postnatal days but it increased rapidly thereafter, leveling off at ca. 25 days postnatal.

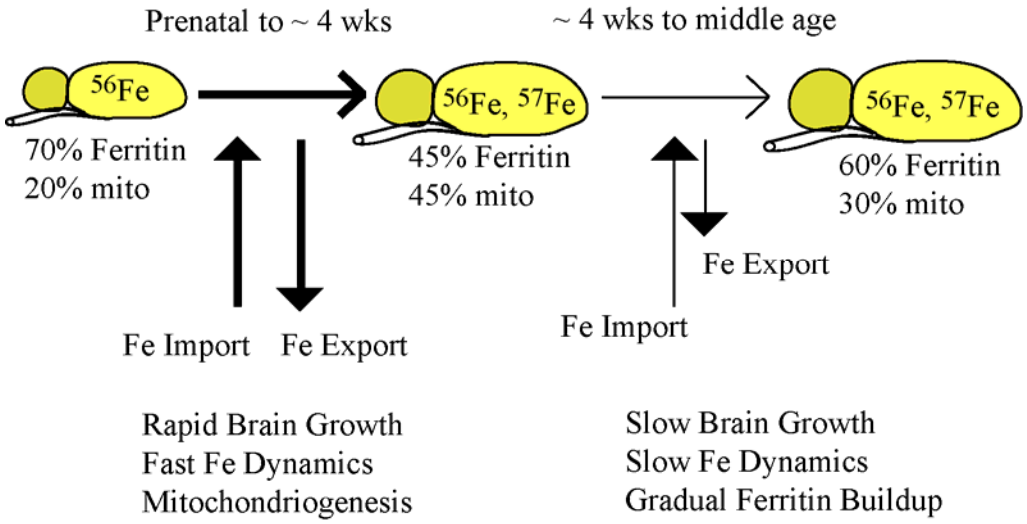

Figure 7.8. Model of Fe utilization in the developing mouse brain. During the first ~ 4 wks of life, the mouse brain grows rapidly and exhibits a rapid dynamic exchange of Fe with the blood including both import and export of Fe to/from the brain. Early during this period most of the Fe in the brain is present as ferritin or ferritin-like material. During the first week or so of life, brain growth and mitochondriogenesis are so fast that Fe cannot be imported rapidly enough to maintain the overall [Fe] in the brain. The decline in [Fe] within neuronal cells causes some ferritin-like Fe to be released, with much of that Fe used for mitochondriogenesis. Gradually, the [Fe] recovers, rates of dynamic Fe import/export slow, and a greater proportion of Fe becomes stored as ferritin.

The mitochondrial volume fraction increased 6-fold, reaching 9% of tissue volume in adults. Interestingly, there was no correlation of mitochondria with synapse concentrations; rather, the rate of mitochondriogenesis was thought to correlate with increased levels of synaptic *activity*.

Effect of Iron deficiency

Our results indicate that the regulation of brain Fe is sensitive to dietary changes. The brain responds to an Fe deficiency by reducing levels of stored Fe such as ferritin and by maintaining normal mitochondria levels. Interestingly, the concentration of mitochondria in Fe-deficient brains was *higher* than observed in Fe-sufficient animals at any developmental stage examined. Explaining this counterintuitive result will require further studies, but Fe regulation in the brain is undoubtedly complex, and the brain may be protected from an organism-level Fe deficiency. Conceivably, the brain may become loaded with mitochondria under Fe-deficient conditions to sustain the increased brain activity required for the animal to seek more (Fe-rich) food. In other studies, levels of the brain Fe-containing proteins tyrosine hydroxlase, tryptophan hydroxylase, monoamine oxidase, succinate hydroxylase and cytochrome c in Fe deficient animals were also normal (*319*). Mackler et al. (*320*) reported that the levels of cytochromes a and c were normal under Fe deficient conditions, and that that the level of cytochrome b was only slightly reduced relative to in Fe-sufficient mitochondria. Perhaps neurological problems arise only if the Fe deficiency is so severe that all storage forms of Fe in the animal have been exhausted and the brain can no longer be protected from the deficiency.

Mononuclear Nonheme High-Spin Ferrous and Ferric Species

Our results indicate the presence of substantial amounts of NHHS Fe^{2+} in the mouse brain. NHHS Fe^{2+} complexes are generally less tightly coordinated than low-spin complexes and they exhibit more rapid ligand-exchange. Such properties would be expected for trafficking Fe complexes and for complexes that undergo Fenton chemistry which may damage cells and contribute to aging and neurodegeneration. Three of our Mössbauer spectra clearly indicate the presence of substantial concentrations of NHHS Fe^{2+} species in the brain (-1 wk, 3 wks, and Fe-deficient). In these cases, the concentration of all NHHS Fe^{2+} species in the mouse brain was ~ 20 μM. The NHHS Fe^{2+} doublets were broad, suggesting that many NHHS Fe^{2+} species contribute. The NHHS Fe^{2+} doublet in the other brain Mössbauer spectra were present but less well resolved. The g = 4.3 EPR signal was present in every brain homogenate examined. The quantified intensity of this signal indicates that NHHS Fe^{3+} species are present in the mouse brain at a collective concentration of ~ 100 nM.

A portion of these species are Fe^{2+} and Fe^{3+} ions bound tightly in the active site of enzymes in the brain, while another portion are probably involved in trafficking and/or the Labile Iron Pool (LIP) (*82, 85, 86*). Such species have not been observed in previous Mössbauer and EPR studies of the brain (*153, 155, 321*). On the other hand, Meguro et al. (*307*) found substantial amounts of nonheme Fe^{2+} and Fe^{3+} distributed inhomogeneously throughout the rat brain. Using high-resolution histological staining methods, they determined that the levels of these species increased with the age of the animal. Sohal et al. (*322*) observed an age-dependent increase of nonheme Fe^{2+} species

in mouse brain, but that Fe was not chelatable by bleomyosin. Our results do not support such an age-dependent increase, though small changes could have gone undetected using our methods.

Spin Radical Species

The radical species detected here may be physiologically relevant since samples were prepared in the strict absence of O_2 which minimizes the possibility of generating artifactual radical signals. Transient radicals in the brain have been detected using spin-probes (*323*) but the radical detected here was stable in the absence of such probes. Radical species are cleared from the brain faster in young mice than in old, suggesting that the reducing capacity of the brain decreases with age (*324*). These changes may be related to the age-dependent increase in the intensity of the radical EPR signal that we observed. Most theories of ageing involve the age-dependent accumulation of ROS (*325*), which could be responsible for the radical signal. ROS are generated primarily by mitochondria, and can damage these organelles.

Conclusions

Our study provides new insights into Fe trafficking and homeostasis in the brain. We have enriched mice with ^{57}Fe and have used Mössbauer spectroscopy, along with EPR, UV-vis and ICP-MS, as biophysical probes of the Fe content of the mouse brain. We quantified the rates of Fe incorporation into the brain, and have shown that Fe is slowly imported, relative to the incorporation rate into other organs. The slow rate of Fe incorporation into the brain is probably due to the tight regulation at the BBB. The rate of Fe incorporation is biphasic, with a rapid phase occurring in very young animals,

following by a slower phase in older animals. During this rapid Fe-incorporation phase, the brain is growing rapidly, and its activity is increasing. As such, mitochondria are rapidly being generated, which creates a high demand for Fe. This demand cannot be met exclusively with newly imported Fe, such that the concentration of Fe in the brain declines and some ferritin-stored Fe is used for mitochondriogenesis. As brain growth and mitochondriogenesis slow, the Fe import rate becomes sufficient to allow some of the imported Fe to be stored once again. The brain contains substantial concentrations of NHHS Fe^{2+} and Fe^{3+} species a portion of which may be used in trafficking and homeostasis. This form of Fe is known to undergo the Fenton reaction to generate reactive oxygen species and be associated with aging. Further studies are required to determine whether the detected Fe species participate in such reactions. We observed an organic radical EPR signal which increased with age, consistent with the ROS theory of aging. Only ferritin-like Fe was observed in previous Mössbauer studies of the human brain, possibly because of differences in the age and/or diets of the mice vs. human donors. We showed that the Fe content of the brain is sensitive to diet, in that stored Fe is preferentially utilized when mice are raised on an Fe-deficient diet. The methods developed here are widely applicable, and could be applied to any and all mouse organs, including those found in transgenic animals with various Fe-associated disorders. This approach may reveal differences in Fe trafficking and/or regulatory homeostasis, and thus significantly impact the mechanistic study of Fe-related diseases.

CHAPTER VIII

CONCLUSIONS AND FUTURE WORK

Conclusions

The major objective of this study was to establish whether an integrated biophysical analysis centered on Mössbauer spectroscopy could be developed to study the iron contained in complex biological systems, and to apply that methodology to an organelle, a cell, and a whole organ. Specifically we wanted to establish whether these methods could provide new insights into processes such as iron trafficking, metabolism, and homeostasis.

The initial focus was to apply this systems-level analysis to mitochondria because of their extensive role in iron metabolism. These studies, presented in Chapters 3 and 4, probed iron metabolism in fermenting, respirofermenting and respiring mitochondria isolated from cells grown on 40 μM iron. The studies on fermenting mitochondria revealed that the iron in this organelle was primarily distributed in 4 species. These included a contribution of CD, NHHS Fe^{2+}, HS Fe^{3+}, and Fe^{3+} nanoparticles with contributions of ~25%, 20%, 15%, and 35% respectively. The concentrations of iron in the mitochondria (~800 μM) suggested that the concentrations of the NHHS Fe^{2+} and HS Fe^{3+} species were beyond what would be expected of mononuclear iron containing proteins.

We thus rationalized that these species likely contributed to a pool of ions which may be utilized in the production of ISCs and hemes. For this reason we performed

experiments to demonstrate that these features were indeed mitochondrial. To establish the NHHS Fe^{2+} was associated with the mitochondria we incubated mitochondria with the chelator BPS which drives HS Fe^{2+} to LS Fe^{2+}. Initially we saw no formation of the LS complex. Upon addition of detergent or use of physical methods to disrupt the membranes, there was a nearly quantitative transfer to the LS feature. This led to the conclusion that the NHHS Fe^{2+} feature observed in Mössbauer spectra of purified fermenting mitochondria was protected from chelation, most likely due to the feature being encapsulated by a membrane. To establish that this membrane was mitochondrial, we analyzed several batches of mitochondria by both Mössbauer spectroscopy and western blot analysis. The Mössbauer data revealed that the amount of NHHS Fe^{2+} in each sample was nearly constant. The western blot, as expected, revealed that contributions of other organelles were contained in samples of purified mitochondria. Interestingly, the amount of contamination was not always constant, and individual preperations contained increased or decreased levels of specific contaminants. This led to the conclusion that the NHHS Fe^{2+} ions were most likely in the mitochondria, as the concentrations of these ions did not correlate to an increase or decrease of contaminating organelles.

Similar methods were used to establish that the HS Fe^{3+} was mitochondrial. We treated mitochondrial samples with dithionite. These HS Fe^{3+} ions were only reduced when the membranes were disturbed. As with the NHHS Fe^{2+} species, these ions showed no correlation to differential levels of non- mitochondrial contamination as observed by western blot analysis.

The presence of Fe^{3+} nanoparticles in WT mitochondria were initially a surprise. We assigned the feature as such based on the spectral similarity to nanoparticles present in mitochondria of ISC mutants (*105-107*). This feature, as with HS Fe^{3+}, was susceptible to reduction only when the mitochondrial membranes were disrupted.

Following these studies we wanted to establish whether these distributions of iron changed if the metabolic mode of growth changed. In a collaborative effort with two graduate students in the Lindahl lab, Dr. Jessica Garber Morales and Dr. Ren Miao, we studied both respiring and respirofermenting mitochondria and found that the distribution of iron in the mitochondria of these cells was similar to one another but quite different from the distributions observed in fermenting mitochondria. Under respiring and respirofermenting conditions, Mössbauer spectroscopy revealed 50-60% of the iron was observed as CD, with minor contributions of NHHS Fe^{2+} , HS Fe^{3+}, and Fe^{3+} nanoparticles. We concluded that these features were serving as storage in the fermenting mitochondria where ISC and heme biosynthesis should be less prevalent than in the repirofermenting and respiring conditions. In the latter conditions we concluded that the majority of the ions are being utilized. In the resirofermenting and respiring mitochondrial samples, unlike the fermenting samples a considerable contribution (~10%) of the iron was present as heme HS Fe^{2+}.

Following these studies we were interested in whether the same analysis could be applied to the cell, an undoubtedly more complex system. In chapter 5 we presented Mössbauer data collected on fermenting cells grown on medium containing 40μM ^{57}Fe. This spectrum revealed that ~75% of the cellular iron was present in a HS Fe^{3+} species

which was non-mitochondrial. A difference spectrum (subtracting a simulation of the HS Fe^{3+}) revealed that the final 25% was very similar to isolated mitochondria. We hypothesized the HS Fe^{3+} feature would likely arise from vacuoles, a storage site of iron in the cell.

Another graduate student in the Lindahl lab, Ms. Allison Cockrell, isolated vacuoles and in a collaborative project showed that the iron found in vacuoles was primarily HS Fe^{3+}, spectroscopically similar to the non-mitochondrial iron observed in whole cells. This strengthened our original hypothesis on the origin of this feature. In the study of isolated vacuoles, Fe^{3+} nanoparticles were also observed. These particles had, spectroscopic properties similar to those found in mitochondria.

In another collaborative effort with Dr. Ren Miao we studied the distribution of iron in cells which constitutively activate the iron regulon, the Aft1-1^{up} strain. Studies on this strain revealed that such cells import massive amounts of iron consist with the activated pathways of iron import. Mössbauer spectra of these cells demonstrated that the iron in this strain was distributed into several features including strongest contributions from Fe^{3+} nanoparticles and HS Fe^{3+}. The mitochondria of these cells were dominated by Fe^{3+} nanoparticles indicating that a substantial portion of this feature present in whole cells originated from mitochondria. These studies demonstrated that a constitutively activated iron regulon led to the accumulation of iron in the cell in features we had previously observed in WT cells. This prompted a further investigation to establish whether all iron in a WT cell is imported in an Aft1p dependent fashion.

In the final yeast studies, described in Chapter 6, we collected biophysical data on yeast cells grown on medium differently supplemented with iron. At the lowest levels of iron supplementation, medium supplemented with BPS and 1μM ^{57}Fe and medium not treated with BPS but still supplemented with 1μM ^{57}Fe we observed dimished $[Fe]_{cell}$. In Mössbauer spectra of these samples, we observed less of the total iron in the feature associated with the vacuoles. We hypothesize that under such conditions the cell is iron-starved and provides the majority of imported iron to processes involved in ISC and heme biosynthesis. Further confirmation of this study came from studies on isolated mitochondria from cells grown on medium supplemented with BPS and 1μM ^{57}Fe. These mitochondria were rich in CD material and lacked additional features (HS Fe^{3+}, HNNS Fe^{2+}, and Fe^{3+} nanoparticles) observed in fermenting mitochondria from cells supplemented with higher $[Fe]_{medium}$. In cells grown on medium supplemented with 10μM to 10mM iron, we observed only modest changes to the iron distribution of both whole cells and isolated mitochondria.

We also studied whole cells grown on medium with the same supplementation of iron but with galactose, a respirofermenting carbon source. Mössbauer spectra of these cells were similar to one another for all the concentrations of iron added, but all were different relative to the fermenting state. Mössbauer spectra of respirofermenting cells contained an altered feature reminiscent of the HS Fe^{3+} observed in Mössbauer spectra of fermenting cells. This feature, which was not as abundant as in fermenting samples, lacked a g = 4.3 EPR signal which was present in the fermenting samples and in isolated vacuoles. This indicates the possibility that this HS Fe^{3+} species is different from that

observed in fermenting cells. We also observed much stronger features originating from HS Fe^{2+} in Mössbauer spectra of respirofermenting cells.

Using a strain of yeast that have the gene for GFP fused to FET3 we investigated whether or not iron imported into fermenting and respirofermenting cells was imported in an Aft1p dependent fashion. Studying the range of $[Fe]_{medium}$ from BPS treated with 1μM up to 1mM we only observed expression of GFP-Fet3p under the iron-starved fermenting conditions. This indicates that a substantial portion of the iron in cells is imported independent of Aft1p.

The final studies, discussed in Chapter 7, investigated the iron distribution of brains of mice at different developmental stages from prenatal to 58 weeks in age. Previous Mössbauer-based studies on human brains revealed that the only observable features in the sections of brain studied were those arising from ferritin and related forms. This was intriguing in that brains contain mitochondria and should therefore contain Mössbauer spectral features associated with them. Starting from prenatal brains up to brain 4 weeks in age we observed a CD in addition to the previously observed ferritin in the Mössbauer spectra of these samples. In this age range we saw the ratio of CD:ferritin increasing indicating increased biosynthesis of ISCs and hemes during that timeframe. Additionally, we observed features arising from NHHS and heme HS Fe^{2+} in these spectra. Beyond 4 weeks in age we saw the ratio of CD:ferritn decrease. We hypothesize that this decline in the ratio of CD:ferritin is a result of additional import of iron without additional biosynthesis of ISCs and hemes. We also studied mice fed an iron deficient diet. The Mössbauer spectra of these brains exhibited the largest ratio of

CD:ferritin, arising from decreased ferritin levels. As with yeast under iron deficient conditions we hypothesize that the iron is obligatorily used for ISC and heme biosynthesis rather than being stored when available iron is low.

Future Studies

In essentially all samples studied in this dissertation, mononuclear HS Fe^{2+} or HS Fe^{3+} species or both were observed. In many cases the concentrations of these species are beyond what would be expected if they were associated with protein. We believe that these species represent iron ligated by small molecules which may play an important role in trafficking. One intriguing field of study would include the development and application of experiments to identify the ligands of such species. Studying these species in cells and isolated organelles has the potential for great insight into iron trafficking. Such methods which are currently the focus of other graduate students in the lab, will undoubtedly utilize chromatographic separation followed by chemical characterization.

Along these lines, interesting studies on mitochondria should be conducted. Currently two high affinity importers of iron in yeast mitochondria have been identified, Mrs3p and Mrs4p. Establishing whether these importers are trafficking the same or different species into the mitochondria is an important question worthy of further investigation. If these importers do not use the same substrate, it would also be interesting to identify if a particular iron complex is more conducive to the formation of ISC, hemes, or Fe^{3+} nanoparticles.

Studying the formation of Fe^{3+} nanoparticles is also an exciting area of research. In this study we have observed such species in WT mitochondria. We attributed this to

the presence of additional iron, beyond the mitochondrial necessity becoming oxidized and percipating out of solution. It may also be that certain conditions within the mitochondria (or vacuole) make the organelle more susceptible to the formation of nanoparticles. Such conditions might include a change in pH of the organelle, a more oxidizing environment, or a limitation of stabilizing ligands. Establishing if any or all of these processes (or others) play a role in the formation of Fe^{3+} nanoparticle would be an exciting advance in the current understanding of iron metabolism.

Based on the studies in whole yeast cells, it appears that a substantial portion of iron is imported into the cell through Aft1p-independent processes. Further studies and the identification of such processes would provide insight into iron regulation and trafficking. Further studies should be conducted on the regulation of these processes. These studies will almost certainly involve mutations of potential importers of iron.

As many of the current yeast-based studies involve WT strains, they should be regarded as control experiments. As such they not only demonstrate the applicability of the methods used but also provide a comparison for cells with genetic mutations involved in iron metabolism. Using this systems level analysis of cells in conjunct with mutations to individual proteins can probe mechanistic questions of the protein. This has been demonstrated by previous work in the Lindahl lab (*105, 107*).

An exciting avenue of research will certainly involve the study of higher eukaryotes. The studies presented here on the mouse brain, like the studies on yeast, establish the applicability of the methods but should be supplemented by more extensive investigation. In brains, older animals should be studied. This would help establish

whether or not iron accumulates with age. If iron does accumulate with age it would be interesting to observe the form which accumulates. As with yeast, studies of WT mice will also serve as a control for genetically altered animals, this is another area which warrants future study. Beyond studying the brain other organs should also be probed with these methods.

In the current study on mice brains we have hypothesized that the CD observed in the Mössbauer spectra of brain samples belongs to mitochondria. To establish this mitochondria should be isolated from mouse brains (and eventually other organs). This, coupled with experiments to establish the purity and integrity of the mitochondrial material, will help to establish the current hypothesis that these features arise from mitochondria. This will require a large number of animals to obtain sufficient quantities of mitochondrial material. Taking this in consideration it *might* also be interesting to study mice of different ages to establish age dependent variations in the iron distribution of mitochondria isolated from mouse brains.

During the past decades substantial progress has been made towards understanding processes involved in iron metabolism, trafficking, and homeostasis. In spite of this there are still many questions to be answered. The work presented here demonstrated a biophysical methodology which will certainly play an important future role in this process.

REFERENCES

1. Beinert, H., and Kennedy, M. C. (1993) Aconitase, a two-faced protein: enzyme and iron regulatory factor. *Faseb Journal 7*, 1442-1449.
2. Beinert, H., Kennedy, M. C., and Stout, C. D. (1996) Aconitase as Iron-Sulfur Protein, Enzyme, and Iron-Regulatory Protein. *Chem Rev 96*, 2335-2374.
3. Flint, D. H., and Allen, R. M. (1996) Iron-Sulfur Proteins with Nonredox Functions. *Chem Rev 96*, 2315-2334.
4. Beinert, H. (2002) Spectroscopy of succinate dehydrogenases, a historical perspective. *Biochimica Et Biophysica Acta 1553*, 7-22.
5. Raha, S., McEachern, G. E., Myint, A. T., and Robinson, B. H. (2000) Superoxides from mitochondrial complex III: the role of manganese superoxide dismutase. *Free Radic Biol Med 29*, 170-180.
6. Zitomer, R. S., Montgomery, D. L., Nichols, D. L., and Hall, B. D. (1979) Transcriptional Regulation of the Yeast Cytochrome-C Gene. *P Natl Acad Sci USA 76*, 3627-3631.
7. Alseth, I., Eide, L., Pirovano, M., Rognes, T., Seeberg, E., and Bjoras, M. (1999) The Saccharomyces cerevisiae homologues of endonuclease III from Escherichia coli, Ntg1 and Ntg2, are both required for efficient repair of spontaneous and induced oxidative DNA damage in yeast. *Mol Cell Biol 19*, 3779-3787.

8. Boal, A. K., Yavin, E., and Barton, J. K. (2007) DNA repair glycosylases with a [4Fe-4S] cluster: a redox cofactor for DNA-mediated charge transport? *Journal of Inorganic Biochemistry 101*, 1913-1921.

9. Klinge, S., Hirst, J., Maman, J. D., Krude, T., and Pellegrini, L. (2007) An iron-sulfur domain of the eukaryotic primase is essential for RNA primer synthesis. *Nat Struct Mol Biol 14*, 875-877.

10. Lukianova, O. A., and David, S. S. (2005) A role for iron-sulfur clusters in DNA repair. *Curr Opin Chem Biol 9*, 145-151.

11. Perutz, M. F. (1960) Structure of hemoglobin. *Brookhaven Symp Biol 13*, 165-183.

12. Cary, S. P. L., Winger, J. A., Derbyshire, E. R., and Marletta, M. A. (2006) Nitric oxide signaling: no longer simply on or off. *Trends Biochem.Sci. 31*, 231-239.

13. Shelver, D., Kerby, R. L., He, Y., and Roberts, G. P. (1997) CooA, a CO-sensing transcription factor from Rhodospirillum rubrum, is a CO-binding heme protein. *Proceedings of the National Academy of Sciences 94*, 11216-11220.

14. Fenton, H. J. H. (1894) LXXIII.-Oxidation of tartaric acid in presence of iron. *Journal of the Chemical Society, Transactions 65*, 899-910.

15. Drake, I. M., Mapstone, N. P., Schorah, C. J., White, K. L., Chalmers, D. M., Dixon, M. F., and Axon, A. T. (1998) Reactive oxygen species activity and lipid peroxidation in Helicobacter pylori associated gastritis: relation to gastric mucosal ascorbic acid concentrations and effect of H pylori eradication. *Gut 42*, 768-771.

16. Irazusta, V., Moreno-Cermeno, A., Cabiscol, E., Ros, J., and Tamarit, J. (2008) Major targets of iron-induced protein oxidative damage in frataxin-deficient yeasts are magnesium-binding proteins. *Free Radic Biol Med 44*, 1712-1723.

17. Wiseman, H., and Halliwell, B. (1996) Damage to DNA by reactive oxygen and nitrogen species: role in inflammatory disease and progression to cancer. *Biochem J 313 (Pt 1)*, 17-29.

18. Rieske, J. S., Maclennan, D. H., and Coleman, R. (1964) Isolation and Properties of Iron-Protein from (Reduced Coenzyme Q) -Cytochrome C Reductase Complex of Respiratory Chain. *Biochem Bioph Res Co 15*, 338-344.

19. Kwok, E. Y., Severance, S., and Kosman, D. J. (2006) Evidence for iron channeling in the Fet3p-Ftr1p high-affinity iron uptake complex in the yeast plasma membrane. *Biochemistry 45*, 6317-6327.

20. Martins, L. J., Jensen, L. T., Simon, J. R., Keller, G. L., and Winge, D. R. (1998) Metalloregulation of FRE1 and FRE2 homologs in Saccharomyces cerevisiae. *Journal of Biological Chemistry 273*, 23716-23721.

21. Yuan, D. S., Stearman, R., Dancis, A., Dunn, T., Beeler, T., and Klausner, R. D. (1995) The Menkes/Wilson disease gene homologue in yeast provides copper to a ceruloplasmin-like oxidase required for iron uptake. *Proc Natl Acad Sci U S A 92*, 2632-2636.

22. Stearman, R., Yuan, D. S., Yamaguchi-Iwai, Y., Klausner, R. D., and Dancis, A. (1996) A permease-oxidase complex involved in high-affinity iron uptake in yeast. *Science 271*, 1552-1557.

23. Hassett, R. F., Romeo, A. M., and Kosman, D. J. (1998) Regulation of high affinity iron uptake in the yeast Saccharomyces cerevisiae. Role of dioxygen and Fe. *Journal of Biological Chemistry 273*, 7628-7636.

24. Kwok, E., and Kosman, D. (2006) Iron in yeast: Mechanisms involved in homeostasis, In *Molecular Biology of Metal Homeostasis and Detoxification* (Tamas, M., and Martinoia, E., Eds.), pp 495-495, Springer Berlin / Heidelberg.

25. Dix, D. R., Bridgham, J. T., Broderius, M. A., Byersdorfer, C. A., and Eide, D. J. (1994) The FET4 gene encodes the low affinity Fe(II) transport protein of Saccharomyces cerevisiae. *The Journal of biological chemistry 269*, 26092-26099.

26. Dix, D., Bridgham, J., Broderius, M., and Eide, D. (1997) Characterization of the FET4 protein of yeast - Evidence for a direct role in the transport of iron. *Journal of Biological Chemistry 272*, 11770-11777.

27. Heymann, P., Ernst, J. F., and Winkelmann, G. (2000) Identification and substrate specificity of a ferrichrome-type siderophore transporter (Arn1p) in Saccharomyces cerevisiae. *FEMS Microbiol Lett 186*, 221-227.

28. Heymann, P., Ernst, J. F., and Winkelmann, G. (1999) Identification of a fungal triacetylfusarinine C siderophore transport gene (TAF1) in Saccharomyces cerevisiae as a member of the major facilitator superfamily. *Biometals 12*, 301-306.

29. Heymann, P., Ernst, J. F., and Winkelmann, G. (2000) A gene of the major facilitator superfamily encodes a transporter for enterobactin (Enb1p) in Saccharomyces cerevisiae. *Biometals 13*, 65-72.

30. Yun, C. W., Bauler, M., Moore, R. E., Klebba, P. E., and Philpott, C. C. (2001) The role of the FRE family of plasma membrane reductases in the uptake of siderophore-iron in Saccharomyces cerevisiae. *Journal of Biological Chemistry 276*, 10218-10223.

31. Lesuisse, E., Blaiseau, P. L., Dancis, A., and Camadro, J. M. (2001) Siderophore uptake and use by the yeast Saccharomyces cerevisiae. *Microbiology 147*, 289-298.

32. Philpott, C. C., Protchenko, O., Kim, Y. W., Boretsky, Y., and Shakoury-Elizeh, M. (2002) The response to iron deprivation in Saccharomyces cerevisiae: expression of siderophore-based systems of iron uptake. *Biochem Soc Trans 30*, 698-702.

33. Yamaguchi-Iwai, Y., Dancis, A., and Klausner, R. D. (1995) AFT1: a mediator of iron regulated transcriptional control in Saccharomyces cerevisiae. *EMBO J 14*, 1231-1239.

34. Li, H. R., Mapolelo, D. T., Dingra, N. N., Naik, S. G., Lees, N. S., Hoffman, B. M., Riggs-Gelasco, P. J., Huynh, B. H., Johnson, M. K., and Outten, C. E. (2009) The Yeast Iron Regulatory Proteins Grx3/4 and Fra2 Form Heterodimeric Complexes Containing a [2Fe-2S] Cluster with Cysteinyl and Histidyl Ligation. *Biochemistry 48*, 9569-9581.

35. Li, H., Mapolelo, D. T., Randeniya, S., Johnson, M. K., and Outten, C. E. (2012) Human Glutaredoxin 3 Forms [2Fe-2S]-Bridged Complexes with Human BolA2. *Biochemistry*.

36. Balk, J., Pierik, A. J., Netz, D. J., Muhlenhoff, U., and Lill, R. (2004) The hydrogenase-like Nar1p is essential for maturation of cytosolic and nuclear iron-sulphur proteins. *Embo Journal 23*, 2105-2115.

37. Netz, D. J., Pierik, A. J., Stumpfig, M., Muhlenhoff, U., and Lill, R. (2007) The Cfd1-Nbp35 complex acts as a scaffold for iron-sulfur protein assembly in the yeast cytosol. *Nat Chem Biol 3*, 278-286.

38. Zhang, Y., Lyver, E. R., Nakamaru-Ogiso, E., Yoon, H., Amutha, B., Lee, D. W., Bi, E., Ohnishi, T., Daldal, F., Pain, D., and Dancis, A. (2008) Dre2, a conserved eukaryotic Fe/S cluster protein, functions in cytosolic Fe/S protein biogenesis. *Mol Cell Biol 28*, 5569-5582.

39. Goto-Ito, S., Ishii, R., Ito, T., Shibata, R., Fusatomi, E., Sekine, S. I., Bessho, Y., and Yokoyama, S. (2007) Structure of an archaeal TYW1, the enzyme catalyzing the second step of wye-base biosynthesis. *Acta Crystallogr D Biol Crystallogr 63*, 1059-1068.

40. Rudolf, J., Makrantoni, V., Ingledew, W. J., Stark, M. J., and White, M. F. (2006) The DNA repair helicases XPD and FancJ have essential iron-sulfur domains. *Mol Cell 23*, 801-808.

41. Yeeles, J. T., Cammack, R., and Dillingham, M. S. (2009) An iron-sulfur cluster is essential for the binding of broken DNA by AddAB-type helicase-nucleases. *Journal of Biological Chemistry 284*, 7746-7755.

42. Bard, M., Bruner, D. A., Pierson, C. A., Lees, N. D., Biermann, B., Frye, L., Koegel, C., and Barbuch, R. (1996) Cloning and characterization of ERG25, the Saccharomyces cerevisiae gene encoding C-4 sterol methyl oxidase. *Proc Natl Acad Sci U S A 93*, 186-190.

43. Luo, M., Jiang, Y. L., Ma, X. X., Tang, Y. J., He, Y. X., Yu, J., Zhang, R. G., Chen, Y., and Zhou, C. Z. (2010) Structural and biochemical characterization of yeast monothiol glutaredoxin Grx6. *J Mol Biol 398*, 614-622.

44. Ali, A., Zhang, Q., Dai, J., and Huang, X. (2003) Calcein as a fluorescent iron chemosensor for the determination of low molecular weight iron in biological fluids. *Biometals 16*, 285-293.

45. Thomas, F., Serratrice, G., Beguin, C., Aman, E. S., Pierre, J. L., Fontecave, M., and Laulhere, J. P. (1999) Calcein as a fluorescent probe for ferric iron. Application to iron nutrition in plant cells. *Journal of Biological Chemistry 274*, 13375-13383.

46. Bigelis, R., and Umbarger, H. E. (1976) Yeast alpha-isopropylmalate isomerase. Factors affecting stability and enzyme activity. *Journal of Biological Chemistry 251*, 3545-3552.

47. Lill, R., and Muhlenhoff, U. (2008) Maturation of iron-sulfur proteins in eukaryotes: Mechanisms, connected processes, and diseases. *Annu Rev Biochem 77*, 669-700.

48. Dong, J. S., Lai, R., Nielsen, K., Fekete, C. A., Qiu, H. F., and Hinnebusch, A. G. (2004) The essential ATP-binding cassette protein RLI1 functions in translation by promoting preinitiation complex assembly. *Journal of Biological Chemistry 279*, 42157-42168.

49. Fekete, Z., Sipos, K., Lange, H., Nagy, J., Netz, D. J. A., Balk, J., Rotte, C., Lill, R., and Kispal, G. (2005) The iron-sulphur protein Rli1p and mitochondria play an essential role in the biogenesis of cytosolic ribosomes. *Febs J 272*, 54-54.

50. Yarunin, A., Panse, V. G., Petfalski, E., Dez, C., Tollervey, D., and Hurt, E. C. (2005) Functional link between ribosome formation and biogenesis of iron-sulfur proteins. *Embo Journal 24*, 580-588.

51. Ge, J., Perlstein, D. L., Nguyen, H. H., Bar, G., Griffin, R. G., and Stubbe, J. (2001) Why multiple small subunits (Y2 and Y4) for yeast ribonucleotide reductase? Toward understanding the role of Y4. *Proc Natl Acad Sci U S A 98*, 10067-10072.

52. Huang, M., and Elledge, S. J. (1997) Identification of RNR4, encoding a second essential small subunit of ribonucleotide reductase in Saccharomyces cerevisiae. *Mol Cell Biol 17*, 6105-6113.

53. Roy, A., Solodovnikova, N., Nicholson, T., Antholine, W., and Walden, W. E. (2003) A novel eukaryotic factor for cytosolic Fe-S cluster assembly. *EMBO J 22*, 4826-4835.

54. Hausmann, A., Aguilar Netz, D. J., Balk, J., Pierik, A. J., Muhlenhoff, U., and Lill, R. (2005) The eukaryotic P loop NTPase Nbp35: an essential component of the cytosolic and nuclear iron-sulfur protein assembly machinery. *Proc Natl Acad Sci U S A 102*, 3266-3271.

55. Srinivasan, V., Netz, D. J., Webert, H., Mascarenhas, J., Pierik, A. J., Michel, H., and Lill, R. (2007) Structure of the yeast WD40 domain protein Cia1, a component acting late in iron-sulfur protein biogenesis. *Structure 15*, 1246-1257.

56. Li, S. C., and Kane, P. M. (2009) The yeast lysosome-like vacuole: endpoint and crossroads. *Biochimica Et Biophysica Acta 1793*, 650-663.

57. Kaplan, C. D., and Kaplan, J. (2009) Iron acquisition and transcriptional regulation. *Chem Rev 109*, 4536-4552.

58. Raguzzi, F., Lesuisse, E., and Crichton, R. R. (1988) Iron storage in Saccharomyces cerevisiae. *Febs Letters 231*, 253-258.

59. Singh, A., Kaur, N., and Kosman, D. J. (2007) The metalloreductase Fre6p in Fe-Efflux from the yeast vacuole. *Journal of Biological Chemistry 282*, 28619-28626.

60. Paz, Y., Shimoni, E., Weiss, M., and Pick, U. (2007) Effects of iron deficiency on iron binding and internalization into acidic vacuoles in *Dunaliella salina*. *Plant Physiol 144*, 1407-1415.

61. Li, L. T., Chen, O. S., Ward, D. M., and Kaplan, J. (2001) A yeast vacuolar membrane transporter CCC1 facilitates iron storage. *Mol Biol Cell 12*, 206a-206a.

62. Li, L. T., Chen, O. S., Ward, D. M., and Kaplan, J. (2001) CCC1 is a transporter that mediates vacuolar iron storage in yeast. *Journal of Biological Chemistry 276*, 29515-29519.

63. Lapinskas, P. J., Lin, S. J., and Culotta, V. C. (1996) The role of the *Saccharomyces cerevisiae* CCC1 gene in the homeostasis of manganese ions. *Mol Microbiol 21*, 519-528.

64. Lin, H. L., Burton, D., Li, L. T., Warner, D. E., Phillips, J. D., Ward, D. M., and Kaplan, J. (2009) Gain-of-function mutations identify amino acids within transmembrane domains of the yeast vacuolar transporter Zrc1 that determine metal specificity. *Biochemical Journal 422*, 273-283.

65. Urbanowski, J. L., and Piper, R. C. (1999) The iron transporter fth1p forms a complex with the Fet5 iron oxidase and resides on the vacuolar membrane. *Journal of Biological Chemistry 274*, 38061-38070.

66. Cohen, A., Nelson, H., and Nelson, N. (2000) The family of SMF metal ion transporters in yeast cells. *Journal of Biological Chemistry 275*, 33388-33394.

67. Li, L., Bagley, D., Ward, D. M., and Kaplan, J. (2008) Yap5 is an iron-responsive transcriptional activator that regulates vacuolar iron storage in yeast. *Molecular and Cellular Biology 28*, 1326-1337.

68. Puig, S., Askeland, E., and Thiele, D. J. (2005) Coordinated remodeling of cellular metabolism during iron deficiency through targeted mRNA degradation. *Cell 120*, 99-110.

69. Mannella, C. A. (1992) THE INS AND OUTS OF MITOCHONDRIAL-MEMBRANE CHANNELS. *Trends Biochem.Sci. 17*, 315-320.

70. Abe, Y., Shodai, T., Muto, T., Mihara, K., Torii, H., Nishikawa, S., Endo, T., and Kohda, D. (2000) Structural basis of presequence recognition by the mitochondrial protein import receptor Tom20. *Cell 100*, 551-560.

71. Koehler, C. M., Merchant, S., and Schatz, G. (1999) How membrane proteins travel across the mitochondrial intermembrane space. *Trends Biochem.Sci. 24*, 428-432.

72. Neupert, W. (1997) Protein import into mitochondria. *Annu Rev Biochem 66*, 863-917.

73. Bauer, M. F., Sirrenberg, C., Neupert, W., and Brunner, M. (1996) Role of Tim23 as voltage sensor and presequence receptor in protein import into mitochondria. *Cell 87*, 33-41.

74. Komiya, T., Rospert, S., Koehler, C., Looser, R., Schatz, G., and Mihara, K. (1998) Interaction of mitochondrial targeting signals with acidic receptor domains along the protein import pathway: evidence for the 'acid chain' hypothesis. *EMBO Journal 17*, 3886-3898.

75. Bolliger, L., Junne, T., Schatz, G., and Lithgow, T. (1995) Acidic receptor domains on both sides of the outer membrane mediate translocation of precursor proteins into yeast mitochondria. *EMBO Journal 14*, 6318-6326.

76. Moczko, M., Bomer, U., Kubrich, M., Zufall, N., Honlinger, A., and Pfanner, N. (1997) The intermembrane space domain of mitochondrial Tom22 functions as a trans binding site for properties with N-terminal targeting sequences. *Molecular and Cellular Biology 17*, 6574-6584.

77. Alberts, B., Johnson, A., Lewis, J., Raff, M., Roberts, K., and Walter, P. (1994) *Essential Cell Biology*, Garland Publishing, New York.

78. Söllner, T., Schmidt, C., and Schmelzer, C. (1987) Amplification of the yeast nuclear gene <i>MRS3</i> confers suppression of a mitochondrial RNA splice defect. *Current Genetics 12*, 497-501.

79. Muhlenhoff, U., Stadler, J. A., Richhardt, N., Seubert, A., Eickhorst, T., Schweyen, R. J., Lill, R., and Wiesenberger, G. (2003) A specific role of the yeast mitochondrial carriers Mrs3/4p in mitochondrial iron acquisition under iron-limiting conditions. *Journal of Biological Chemistry 278*, 40612-40620.

80. Lange, H., Kispal, G., and Lill, R. (1999) Mechanism of iron transport to the site of heme synthesis inside yeast mitochondria. *Journal of Biological Chemistry 274*, 18989-18996.

81. Foury, F., and Roganti, T. (2002) Deletion of the mitochondrial carrier genes MRS3 and MRS4 suppresses mitochondrial iron accumulation in a yeast frataxin-deficient strain. *Journal of Biological Chemistry 277*, 24475-24483.

82. Tangeras, A., Flatmark, T., Backstrom, D., and Ehrenberg, A. (1980) Mitochondrial Iron Not Bound in Heme and Iron-Sulfur Centers - Estimation, Compartmentation and Redox State. *Biochimica Et Biophysica Acta 589*, 162-175.

83. de Groot, H., Bramey, T., Freitag, P., Fandrey, J., Rauen, U., Pamp, K., Erhard, J., Frede, S., and Petrat, F. (2009) No evidence for protective erythropoietin alpha signalling in rat hepatocytes. *Bmc Gastroenterol 9*.

84. Petrat, F., de Groot, H., Sustmann, R., and Rauen, U. (2002) The chelatable iron pool in living cells: A methodically defined quantity. *Biol. Chem. 383*, 489-502.

85. Rauen, U., Petrat, F., and de Groot, H. (2001) Subcellular distribution of chelatable iron: a laser scanning microscopic study in isolated hepatocytes and liver endothelial cells. *Biochemical Journal 356*, 61-69.

86. Rauen, U., Petrat, F., and de Groot, H. (1999) Determination of the chelatable iron pool of isolated rat hepatocytes by digital fluorescence microscopy using the fluorescent probe, phen green SK. *Hepatology 29*, 1171-1179.

87. Tamarit, J., Irazusta, V., Moreno-Cermeno, A., and Ros, J. (2006) Colorimetric assay for the quantitation of iron in yeast. *Anal Biochem 351*, 149-151.

88. Wang, T., and Craig, E. A. (2008) Binding of yeast frataxin to the scaffold for Fe-S cluster biogenesis, Isu. *Journal of Biological Chemistry 283*, 12674-12679.

89. Bencze, K. Z., Kondapalli, K. C., Cook, J. D., McMahon, S., Millan-Pacheco, C., Pastor, N., and Stemmler, T. L. (2006) The structure and function of frataxin. *Crit Rev Biochem Mol Biol 41*, 269-291.

90. Gerber, J., Muhlenhoff, U., and Lill, R. (2003) An interaction between frataxin and Isu1/Nfs1 that is crucial for Fe/S cluster synthesis on Isu1. *EMBO Rep 4*, 906-911.

91. Tsai, C. L., and Barondeau, D. P. (2010) Human frataxin is an allosteric switch that activates the Fe-S cluster biosynthetic complex. *Biochemistry 49*, 9132-9139.

92. Adinolfi, S., Iannuzzi, C., Prischi, F., Pastore, C., Iametti, S., Martin, S. R., Bonomi, F., and Pastore, A. (2009) Bacterial frataxin CyaY is the gatekeeper of iron-sulfur cluster formation catalyzed by IscS. *Nat Struct Mol Biol 16*, 390-396.

93. Beinert, H., Holm, R. H., and Münck, E. (1997) Iron-Sulfur Clusters: Nature's Modular, Multipurpose Structures. *Science 277*, 653-659.

94. Pandey, A., Yoon, H., Lyver, E. R., Dancis, A., and Pain, D. (2011) Isd11p protein activates the mitochondrial cysteine desulfurase Nfs1p protein. *Journal of Biological Chemistry 286*, 38242-38252.

95. Li, J., Saxena, S., Pain, D., and Dancis, A. (2001) Adrenodoxin reductase homolog (Arh1p) of yeast mitochondria required for iron homeostasis. *Journal of Biological Chemistry 276*, 1503-1509.

96. Manzella, L., Barros, M. H., and Nobrega, F. G. (1998) ARH1 of Saccharomyces cerevisiae: A new essential gene that codes for a protein homologous to the human adrenodoxin reductase. *Yeast 14*, 839-846.

97. Lange, H., Kaut, A., Kispal, G., and Lill, R. (2000) A mitochondrial ferredoxin is essential for biogenesis of cellular iron-sulfur proteins. *Proc Natl Acad Sci U S A 97*, 1050-1055.

98. Strain, J., Lorenz, C. R., Bode, J., Garland, S., Smolen, G. A., Ta, D. T., Vickery, L. E., and Culotta, V. C. (1998) Suppressors of superoxide dismutase (SOD1) deficiency in Saccharomyces cerevisiae. Identification of proteins predicted to mediate iron-sulfur cluster assembly. *Journal of Biological Chemistry 273*, 31138-31144.

99. Dutkiewicz, R., Schilke, B., Knieszner, H., Walter, W., Craig, E. A., and Marszalek, J. (2003) Ssq1, a mitochondrial Hsp70 involved in iron-sulfur (Fe/S) center biogenesis. Similarities to and differences from its bacterial counterpart. *Journal of Biological Chemistry 278*, 29719-29727.

100. Voisine, C., Schilke, B., Ohlson, M., Beinert, H., Marszalek, J., and Craig, E. A. (2000) Role of the mitochondrial Hsp70s, Ssc1 and Ssq1, in the maturation of Yfh1. *Mol Cell Biol 20*, 3677-3684.

101. Voisine, C., Cheng, Y. C., Ohlson, M., Schilke, B., Hoff, K., Beinert, H., Marszalek, J., and Craig, E. A. (2001) Jac1, a mitochondrial J-type chaperone, is involved in the biogenesis of Fe/S clusters in Saccharomyces cerevisiae. *P Natl Acad Sci USA 98*, 1483-1488.

102. Ikeda, E., Yoshida, S., Mitsuzawa, H., Uno, I., and Toh-e, A. (1994) YGE1 is a yeast homologue of Escherichia coli grpE and is required for maintenance of mitochondrial functions. *Febs Letters 339*, 265-268.

103. Rodriguez-Manzaneque, M. T., Tamarit, J., Belli, G., Ros, J., and Herrero, E. (2002) Grx5 is a mitochondrial glutaredoxin required for the activity of iron/sulfur enzymes. *Mol Biol Cell 13*, 1109-1121.

104. Kispal, G., Csere, P., Prohl, C., and Lill, R. (1999) The mitochondrial proteins Atm1p and Nfs1p are essential for biogenesis of cytosolic Fe/S proteins. *EMBO J 18*, 3981-3989.

105. Miao, R., Kim, H., Koppolu, U. M., Ellis, E. A., Scott, R. A., and Lindahl, P. A. (2009) Biophysical characterization of the iron in mitochondria from Atm1p-depleted Saccharomyces cerevisiae. *Biochemistry 48*, 9556-9568.

106. Lesuisse, E., Santos, R., Matzanke, B. F., Knight, S. A., Camadro, J. M., and Dancis, A. (2003) Iron use for haeme synthesis is under control of the yeast frataxin homologue (Yfh1). *Hum Mol Genet 12*, 879-889.

107. Miao, R., Martinho, M., Morales, J. G., Kim, H., Ellis, E. A., Lill, R., Hendrich, M. P., Munck, E., and Lindahl, P. A. (2008) EPR and Mossbauer spectroscopy of intact mitochondria isolated from Yah1p-depleted Saccharomyces cerevisiae. *Biochemistry 47*, 9888-9899.

108. Camadro, J. M., and Labbe, P. (1988) Purification and properties of ferrochelatase from the yeast Saccharomyces cerevisiae. Evidence for a precursor form of the protein. *Journal of Biological Chemistry 263*, 11675-11682.

109. Mogi, T., Saiki, K., and Anraku, Y. (1994) Biosynthesis and Functional-Role of Heme-O and Heme-A. *Mol Microbiol 14*, 391-398.

110. Dumont, M. E., Cardillo, T. S., Hayes, M. K., and Sherman, F. (1991) Role of Cytochrome-C Heme Lyase in Mitochondrial Import and Accumulation of Cytochrome-C in Saccharomyces-Cerevisiae. *Molecular and Cellular Biology 11*, 5487-5496.

111. de Vries, S., and Grivell, L. A. (1988) Purification and characterization of a rotenone-insensitive NADH:Q6 oxidoreductase from mitochondria of Saccharomyces cerevisiae. *European Journal of Biochemistry 176*, 377-384.

112. Luttik, M. A., Overkamp, K. M., Kotter, P., de Vries, S., van Dijken, J. P., and Pronk, J. T. (1998) The Saccharomyces cerevisiae NDE1 and NDE2 genes encode separate mitochondrial NADH dehydrogenases catalyzing the oxidation of cytosolic NADH. *Journal of Biological Chemistry 273*, 24529-24534.

113. Hunte, C., Koepke, J., Lange, C., Rossmanith, T., and Michel, H. (2000) Structure at 2.3 A resolution of the cytochrome bc(1) complex from the yeast Saccharomyces cerevisiae co-crystallized with an antibody Fv fragment. *Structure 8*, 669-684.

114. Taanman, J. W., and Capaldi, R. A. (1992) Purification of yeast cytochrome c oxidase with a subunit composition resembling the mammalian enzyme. *Journal of Biological Chemistry 267*, 22481-22485.

115. Raha, S., and Robinson, B. H. (2000) Mitochondria, oxygen free radicals, disease and ageing. *Trends Biochem Sci 25*, 502-508.

116. Glaser, T. (2011) Mössbauer Spectroscopy and Transition Metal Chemistry. Fundamentals and Applications. Edited by Philipp Gütlich, Eckhard Bill and

Alfred X. Trautwein. *Angewandte Chemie International Edition 50*, 10019-10020.

117. Emptage, M. H., Kent, T. A., Kennedy, M. C., Beinert, H., and Munck, E. (1983) Mossbauer and EPR studies of activated aconitase: development of a localized valence state at a subsite of the [4Fe-4S] cluster on binding of citrate. *Proc Natl Acad Sci U S A 80*, 4674-4678.

118. Kent, T. A., Munck, E., Dunham, W. R., Filter, W. F., Findling, K. L., Yoshida, T., and Fee, J. A. (1982) Mossbauer Study of a Bacterial Cytochrome-Oxidase - Cytochrome C1aa3 from Thermus-Thermophilus. *Journal of Biological Chemistry 257*, 2489-2492.

119. Münck, E. (1978) [20] Mössbauer spectroscopy of proteins: Electron carriers, In *Methods in Enzymology* (Sidney, F., and Lester, P., Eds.), pp 346-379, Academic Press.

120. Pikus, J. D., Studts, J. M., Achim, C., Kauffmann, K. E., Munck, E., Steffan, R. J., McClay, K., and Fox, B. G. (1996) Recombinant toluene-4-monooxygenase: Catalytic and Mossbauer studies of the purified diiron and Rieske components of a four-protein complex. *Biochemistry 35*, 9106-9119.

121. Greenamyre, J. T., and Horowitz, M. P. (2010) Mitochondrial Iron Metabolism and Its Role in Neurodegeneration. *J Alzheimers Dis 20*, S551-S568.

122. Furukawa, Y. (2003) Genetics and biochemistry of dopa-responsive dystonia: significance of striatal tyrosine hydroxylase protein loss. *Adv Neurol 91*, 401-410.

123. Martinez, A., Knappskog, P. M., and Haavik, J. (2001) A structural approach into human tryptophan hydroxylase and its implications for the regulation of serotonin biosynthesis. *Curr Med Chem 8*, 1077-1091.

124. Ortiz, E., Pasquini, J. M., Thompson, K., Felt, B., Butkus, G., Beard, J., and Connor, J. R. (2004) Effect of manipulation of iron storage, transport, or availability on myelin composition and brain iron content in three different animal models. *J Neurosci Res 77*, 681-689.

125. Kwik-Uribe, C. L., Gietzen, D., German, J. B., Golub, M. S., and Keen, C. L. (2000) Chronic marginal iron intakes during early development in mice result in persistent changes in dopamine metabolism and myelin composition. *J Nutr 130*, 2821-2830.

126. Huebers, H. A., and Finch, C. A. (1987) The physiology of transferrin and transferrin receptors. *Physiol Rev 67*, 520-582.

127. Aisen, P. (2004) Transferrin receptor 1. *Int J Biochem Cell Biol 36*, 2137-2143.

128. Klausner, R. D., Ashwell, G., van Renswoude, J., Harford, J. B., and Bridges, K. R. (1983) Binding of apotransferrin to K562 cells: explanation of the transferrin cycle. *Proc Natl Acad Sci U S A 80*, 2263-2266.

129. Moos, T., Rosengren Nielsen, T., Skjorringe, T., and Morgan, E. H. (2007) Iron trafficking inside the brain. *J Neurochem 103*, 1730-1740.

130. Abboud, S., and Haile, D. J. (2000) A novel mammalian iron-regulated protein involved in intracellular iron metabolism. *Journal of Biological Chemistry 275*, 19906-19912.

131. Burdo, J. R., Menzies, S. L., Simpson, I. A., Garrick, L. M., Garrick, M. D., Dolan, K. G., Haile, D. J., Beard, J. L., and Connor, J. R. (2001) Distribution of divalent metal transporter 1 and metal transport protein 1 in the normal and Belgrade rat. *J Neurosci Res 66*, 1198-1207.

132. McKie, A. T., Marciani, P., Rolfs, A., Brennan, K., Wehr, K., Barrow, D., Miret, S., Bomford, A., Peters, T. J., Farzaneh, F., Hediger, M. A., Hentze, M. W., and Simpson, R. J. (2000) A novel duodenal iron-regulated transporter, IREG1, implicated in the basolateral transfer of iron to the circulation. *Mol Cell 5*, 299-309.

133. Klomp, L. W. J., Farhangrazi, Z. S., Dugan, L. L., and Gitlin, J. D. (1996) Ceruloplasmin gene expression in the murine central nervous system. *J Clin Invest 98*, 207-215.

134. Liu, Y., Hong, L., Kempf, V. R., Wakamatsu, K., Ito, S., and Simon, J. D. (2004) Ion-exchange and adsorption of Fe(III) by Sepia melanin. *Pigment Cell Res 17*, 262-269.

135. Zecca, L., Fariello, R., Riederer, P., Sulzer, D., Gatti, A., and Tampellini, D. (2002) The absolute concentration of nigral neuromelanin, assayed by a new sensitive method, increases throughout the life and is dramatically decreased in Parkinson's disease. *Febs Letters 510*, 216-220.

136. Sulzer, D., Mosharov, E., Talloczy, Z., Zucca, F. A., Simon, J. D., and Zecca, L. (2008) Neuronal pigmented autophagic vacuoles: lipofuscin, neuromelanin, and

ceroid as macroautophagic responses during aging and disease. *J Neurochem 106*, 24-36.

137. Gerlach, M., Trautwein, A. X., Zecca, L., Youdim, M. B., and Riederer, P. (1995) Mossbauer spectroscopic studies of purified human neuromelanin isolated from the substantia nigra. *J Neurochem 65*, 923-926.

138. Jellinger, K., Kienzl, E., Rumpelmair, G., Riederer, P., Stachelberger, H., Ben-Shachar, D., and Youdim, M. B. (1992) Iron-melanin complex in substantia nigra of parkinsonian brains: an x-ray microanalysis. *J Neurochem 59*, 1168-1171.

139. Oshiro, S., Morioka, M. S., and Kikuchi, M. (2011) Dysregulation of Iron Metabolism in Alzheimer's Disease, Parkinson's Disease, and Amyotrophic Lateral Sclerosis. *Advances in Pharmacological Sciences 2011*.

140. Theil, E. C. (1987) Ferritin: structure, gene regulation, and cellular function in animals, plants, and microorganisms. *Annu Rev Biochem 56*, 289-315.

141. Andrews, S. C., Arosio, P., Bottke, W., Briat, J. F., von Darl, M., Harrison, P. M., Laulhere, J. P., Levi, S., Lobreaux, S., and Yewdall, S. J. (1992) Structure, function, and evolution of ferritins. *Journal of Inorganic Biochemistry 47*, 161-174.

142. Zecca, L., Gallorini, M., Schunemann, V., Trautwein, A. X., Gerlach, M., Riederer, P., Vezzoni, P., and Tampellini, D. (2001) Iron, neuromelanin and ferritin content in the substantia nigra of normal subjects at different ages: consequences for iron storage and neurodegenerative processes. *J Neurochem 76*, 1766-1773.

143. Levi, S., Corsi, B., Bosisio, M., Invernizzi, R., Volz, A., Sanford, D., Arosio, P., and Drysdale, J. (2001) A human mitochondrial ferritin encoded by an intronless gene. *Journal of Biological Chemistry 276*, 24437-24440.

144. Bell, S. H., Weir, M. P., Dickson, D. P., Gibson, J. F., Sharp, G. A., and Peters, T. J. (1984) Mossbauer spectroscopic studies of human haemosiderin and ferritin. *Biochimica Et Biophysica Acta 787*, 227-236.

145. Wang, X., Ong, W., and Connor, J. (2002) Increase in ferric and ferrous iron in the rat hippocampus with time after kainate-induced excitotoxic injury. *Experimental Brain Research 143*, 137-148.

146. Sutton, S. R., Rivers, M. L., and Smith, J. V. (1986) Synchrotron x-ray fluorescence: diffraction interference. *Anal Chem 58*, 2167-2171.

147. Pushie, M. J., Pickering, I. J., Martin, G. R., Tsutsui, S., Jirik, F. R., and George, G. N. (2011) Prion protein expression level alters regional copper, iron and zinc content in the mouse brain. *Metallomics 3*, 206-214.

148. Duyn, J. H., van Gelderen, P., Li, T. Q., de Zwart, J. A., Koretsky, A. P., and Fukunaga, M. (2007) High-field MRI of brain cortical substructure based on signal phase. *Proc Natl Acad Sci U S A 104*, 11796-11801.

149. Rodrigue, K. M., Haacke, E. M., and Raz, N. (2011) Differential effects of age and history of hypertension on regional brain volumes and iron. *Neuroimage 54*, 750-759.

150. Haacke, E. M., Cheng, N. Y., House, M. J., Liu, Q., Neelavalli, J., Ogg, R. J., Khan, A., Ayaz, M., Kirsch, W., and Obenaus, A. (2005) Imaging iron stores in the brain using magnetic resonance imaging. *Magn Reson Imaging 23*, 1-25.

151. Duyn, J. H. (2011) High-field MRI of brain iron. *Methods in molecular biology 711*, 239-249.

152. Galazka-Friedman, J., Bauminger, E. R., Koziorowski, D., and Friedman, A. (2004) Mossbauer spectroscopy and ELISA studies reveal differences between Parkinson's disease and control substantia nigra. *Biochim Biophys Acta 1688*, 130-136.

153. Friedman, A., Arosio, P., Finazzi, D., Koziorowski, D., and Galazka-Friedman, J. (2011) Ferritin as an important player in neurodegeneration. *Parkinsonism Relat Disord 17*, 423-430.

154. Sadowski, K., Szlachta, K., Serafin-Krol, M., Galazka-Friedman, J., and Friedman, A. (2011) Brain tissue echogenicity-implications for substantia nigra studies in parkinsonian patients. *J Neural Transm*.

155. Wypijewska, A., Galazka-Friedman, J., Bauminger, E. R., Wszolek, Z. K., Schweitzer, K. J., Dickson, D. W., Jaklewicz, A., Elbaum, D., and Friedman, A. (2010) Iron and reactive oxygen species activity in parkinsonian substantia nigra. *Parkinsonism Relat Disord 16*, 329-333.

156. Koziorowski, D., Friedman, A., Arosio, P., Santambrogio, P., and Dziewulska, D. (2007) ELISA reveals a difference in the structure of substantia nigra ferritin

in Parkinson's disease and incidental Lewy body compared to control. *Parkinsonism Relat Disord 13*, 214-218.

157. Friedman, A., Galazka-Friedman, J., and Bauminger, E. R. (2007) Iron as a trigger of neurodegeneration in Parkinson's disease. *Handb Clin Neurol 83*, 493-505.

158. Dubiel, S. M., Zablotna-Rypien, B., and Mackey, J. B. (1999) Magnetic properties of human liver and brain ferritin. *Eur Biophys J 28*, 263-267.

159. McNeill, A., Birchall, D., Hayflick, S. J., Gregory, A., Schenk, J. F., Zimmerman, E. A., Shang, H., Miyajima, H., and Chinnery, P. F. (2008) T2* and FSE MRI distinguishes four subtypes of neurodegeneration with brain iron accumulation. *Neurology 70*, 1614-1619.

160. Pietrangelo, A. (2010) Hereditary hemochromatosis: pathogenesis, diagnosis, and treatment. *Gastroenterology 139*, 393-408, 408 e391-392.

161. Niederau, C., Fischer, R., Sonnenberg, A., Stremmel, W., Trampisch, H. J., and Strohmeyer, G. (1985) Survival and Causes of Death in Cirrhotic and in Noncirrhotic Patients with Primary Hemochromatosis. *New England Journal of Medicine 313*, 1256-1262.

162. Oerter, K. E., Kamp, G. A., Munson, P. J., Nienhuis, A. W., Cassorla, F. G., and Manasco, P. K. (1993) Multiple hormone deficiencies in children with hemochromatosis. *The Journal of clinical endocrinology and metabolism 76*, 357-361.

163. Balcerzak, S. P., Mintz, D. H., and Westerman, M. P. (1968) Diabetes Mellitus and Idiopathic Hemochromatosis. *The American Journal of the Medical Sciences 255*, 53-62.

164. Cutler, D. J., Isner, J. M., Bracey, A. W., Hufnagel, C. A., Conrad, P. W., Roberts, W. C., Kerwin, D. M., and Weintraub, A. M. (1980) Hemochromatosis heart disease: An unemphasized cause of potentially reversible restrictive cardiomyopathy. *The American Journal of Medicine 69*, 923-928.

165. Ganz, T. (2004) Hepcidin in iron metabolism. *Curr Opin Hematol 11*, 251-254.

166. Ramakrishnan, U., Rivera, J., Villalpando, S., Gonzalez-Cossio, T., Martorell, R., and Neufeld, L. M. (2001) Prevalence of anemia and iron deficiency during pregnancy of women supplemented with iron or iron and multiple micronutrients. *Faseb Journal 15*, A641-A641.

167. Allen, L. H. (2000) Anemia and iron deficiency: effects on pregnancy outcome. *The American Journal of Clinical Nutrition 71*, 1280S-1284S.

168. Rogers, J. T., Mikkilineni, S., Cantuti-Castelvetri, I., Smith, D. H., Huang, X. D., Bandyopadhyay, S., Cahill, C. M., Maccecchini, M. L., Lahiri, D. K., and Greig, N. H. (2011) The alpha-synuclein 5 ' untranslated region targeted translation blockers: anti-alpha synuclein efficacy of cardiac glycosides and Posiphen. *Journal of Neural Transmission 118*, 493-507.

169. Danzeisen, R., Achsel, T., Bederke, U., Cozzolino, M., Crosio, C., Ferri, A., Frenzel, M., Gralla, E. B., Huber, L., Ludolph, A., Nencini, M., Rotilio, G.,

Valentine, J. S., and Carri, M. T. (2006) Superoxide dismutase 1 modulates expression of transferrin receptor. *J Biol Inorg Chem 11*, 489-498.

170. Zecca, L., Youdim, M. B. H., Riederer, P., Connor, J. R., and Crichton, R. R. (2004) Iron, brain ageing and neurodegenerative disorders. *Nat Rev Neurosci 5*, 863-873.

171. Duce, J. A., Tsatsanis, A., Cater, M. A., James, S. A., Robb, E., Wikhe, K., Leong, S. L., Perez, K., Johanssen, T., Greenough, M. A., Cho, H. H., Galatis, D., Moir, R. D., Masters, C. L., McLean, C., Tanzi, R. E., Cappai, R., Barnham, K. J., Ciccotosto, G. D., Rogers, J. T., and Bush, A. I. (2010) Iron-export ferroxidase activity of beta-amyloid precursor protein is inhibited by zinc in Alzheimer's disease. *Cell 142*, 857-867.

172. Delatycki, M. B., Williamson, R., and Forrest, S. M. (2000) Friedreich ataxia: an overview. *J Med Genet 37*, 1-8.

173. Camaschella, C. (2008) Recent advances in the understanding of inherited sideroblastic anaemia. *Br J Haematol 143*, 27-38.

174. Campuzano, V., Montermini, L., Molto, M. D., Pianese, L., Cossee, M., Cavalcanti, F., Monros, E., Rodius, F., Duclos, F., Monticelli, A., Zara, F., Canizares, J., Koutnikova, H., Bidichandani, S. I., Gellera, C., Brice, A., Trouillas, P., De Michele, G., Filla, A., De Frutos, R., Palau, F., Patel, P. I., Di Donato, S., Mandel, J. L., Cocozza, S., Koenig, M., and Pandolfo, M. (1996) Friedreich's ataxia: autosomal recessive disease caused by an intronic GAA triplet repeat expansion. *Science 271*, 1423-1427.

175. Harding, A. E. (1981) Friedreich Ataxia - a Clinical and Genetic-Study of 90 Families with an Analysis of Early Diagnostic-Criteria and Intrafamilial Clustering of Clinical-Features. *Brain 104*, 589-620.

176. Puccio, H., and Kœnig, M. (2000) Recent advances in the molecular pathogenesis of Friedreich ataxia. *Human Molecular Genetics 9*, 887-892.

177. Savary, S., Allikmets, R., Denizot, F., Luciani, M. F., Mattei, M. G., Dean, M., and Chimini, G. (1997) Isolation and chromosomal mapping of a novel ATP-binding cassette transporter conserved in mouse and human. *Genomics 41*, 275-278.

178. Hallgren, B., and Sourander, P. (1958) The Effect of Age on the Non-Haemin Iron in the Human Brain. *Journal of Neurochemistry 3*, 41-51.

179. Bartzokis, G., Mintz, J., Sultzer, D., Marx, P., Herzberg, J. S., Phelan, C. K., and Marder, S. R. (1994) In vivo MR evaluation of age-related increases in brain iron. *AJNR Am J Neuroradiol 15*, 1129-1138.

180. Meechan, D. W., Maynard, T. M., Wu, Y., Gopalakrishna, D., Lieberman, J. A., and LaMantia, A. S. (2006) Gene dosage in the developing and adult brain in a mouse model of 22q11 deletion syndrome. *Mol Cell Neurosci 33*, 412-428.

181. Schipper, H. M. (2004) Heme oxygenase expression in human central nervous system disorders. *Free Radic Biol Med 37*, 1995-2011.

182. Hahn, P., Song, Y., Ying, G. S., He, X., Beard, J., and Dunaief, J. L. (2009) Age-dependent and gender-specific changes in mouse tissue iron by strain. *Exp Gerontol 44*, 594-600.

183. Spizzo, T., Byersdorfer, C., Duesterhoeft, S., and Eide, D. (1997) The yeast FET5 gene encodes a FET3-related multicopper oxidase implicated in iron transport. *Mol Gen Genet 256*, 547-556.

184. Keilin, D. (1925) On Cytochrome, a Respiratory Pigment, Common to Animals, Yeast, and Higher Plants. *Proceedings of the Royal Society of London. Series B, Containing Papers of a Biological Character 98*, 312-339.

185. Albrecht, A. G., Netz, D. J., Miethke, M., Pierik, A. J., Burghaus, O., Peuckert, F., Lill, R., and Marahiel, M. A. (2010) SufU is an essential iron-sulfur cluster scaffold protein in Bacillus subtilis. *Journal of Bacteriology 192*, 1643-1651.

186. Cárdenas, J., Mortenson, L. E., and Yoch, D. C. (1976) Purification and properties of paramagnetic protein from clostridium pasteurianum W5. *Biochimica et Biophysica Acta (BBA) - Protein Structure 434*, 244-257.

187. Telser, J., van Slageren, J., Vongtragool, S., Dressel, M., Reiff, W. M., Zvyagin, S. A., Ozarowski, A., and Krzystek, J. (2005) High-frequency/high-field EPR spectroscopy of the high-spin ferrous ion in hexaaqua complexes. *Magn Reson Chem 43 Spec no.*, S130-139.

188. Werth, M. T., Kurtz, D. M., Howes, B. D., and Boi, H. H. (1989) Observation of S = 2 EPR signals from ferrous iron-thiolate complexes. Relevance to rubredoxin-type sites in proteins. *Inorganic Chemistry 28*, 1357-1361.

189. Popescu, V.-C., Münck, E., Fox, B. G., Sanakis, Y., Cummings, J. G., Turner, I. M., and Nelson, M. J. (2001) Mössbauer and EPR Studies of the Photoactivation of Nitrile Hydratase†. *Biochemistry 40*, 7984-7991.

190. Zhang, Y., Gan, Q. F., Pavel, E. G., Sigal, E., and Solomon, E. I. (1995) Epr Definition of the Nonheme Ferric Active-Sites of Mammalian 15-Lipoxygenase - Major Spectral Difference Relative to Human 5-Lipoxygenases and Plant Lipoxygenases and Their Ligand-Field Origin. *J Am Chem Soc 117*, 7422-7427.

191. Sun, J., Wilks, A., Ortiz de Montellano, P. R., and Loehr, T. M. (1993) Resonance Raman and EPR spectroscopic studies on heme-heme oxygenase complexes. *Biochemistry 32*, 14151-14157.

192. Bertrand, P., Janot, J. M., Benosman, H., Gayda, J. P., and Labeyrie, F. (1987) An EPR study of the interactions between heme and flavin in yeast flavocytochrome b2. *Eur Biophys J 14*, 273-278.

193. Brautigan, D. L., Feinberg, B. A., Hoffman, B. M., Margoliash, E., Preisach, J., and Blumberg, W. E. (1977) Multiple low spin forms of the cytochrome c ferrihemochrome. EPR spectra of various eukaryotic and prokaryotic cytochromes c. *Journal of Biological Chemistry 252*, 574-582.

194. Fujii, H., Finnegan, M. G., and Johnson, M. K. (1999) The active form of the ferric heme in neutrophil cytochrome b(558) is low-spin in the reconstituted cell-free system in the presence of amphophil. *J Biochem 126*, 708-714.

195. Flint, D. H., and Emptage, M. H. (1988) Dihydroxy acid dehydratase from spinach contains a [2Fe-2S] cluster. *Journal of Biological Chemistry 263*, 3558-3564.

196. Knaff, D. B., Hirasawa, M., Ameyibor, E., Fu, W. G., and Johnson, M. K. (1991) Spectroscopic Evidence for a [3fe-4s] Cluster in Spinach Glutamate Synthase. *Journal of Biological Chemistry 266*, 15080-15084.

197. Davydov, R., Valentine, A. M., Komar-Panicucci, S., Hoffman, B. M., and Lippard, S. J. (1999) An EPR study of the dinuclear iron site in the soluble methane monooxygenase from Methylococcus capsulatus (Bath) reduced by one electron at 77 K: the effects of component interactions and the binding of small molecules to the diiron(III) center. *Biochemistry 38*, 4188-4197.

198. Smoukov, S. K., Kopp, D. A., Valentine, A. M., Davydov, R., Lippard, S. J., and Hoffman, B. M. (2002) Product binding to the diiron(III) and mixed-valence diiron centers of methane monooxygenase hydroxylase studied by (1,2)H and (19)F ENDOR spectroscopy. *J Am Chem Soc 124*, 2657-2663.

199. Jang, H. G., Hendrich, M. P., and Que, L. (1993) Insight into the G Approximate-to 16 Epr Signals of Reduced Diiron Oxo Proteins - Structure and Properties of [Feii2bpmp(O2p(Oc6h5)2)2]Cl. *Inorganic Chemistry 32*, 911-918.

200. Kamat, S. S., Bagaria, A., Kumaran, D., Holmes-Hampton, G. P., Fan, H., Sali, A., Sauder, J. M., Burley, S. K., Lindahl, P. A., Swaminathan, S., and Raushel, F. M. (2011) Catalytic Mechanism and Three-Dimensional Structure of Adenine Deaminase. *Biochemistry 50*, 1917-1927.

201. Kamat, S. S., Holmes-Hampton, G. P., Bagaria, A., Kumaran, D., Tichy, S. E., Gheyi, T., Zheng, X. J., Bain, K., Groshong, C., Emtage, S., Sauder, J. M.,

Burley, S. K., Swaminathan, S., Lindahl, P. A., and Raushel, F. M. (2011) The catalase activity of diiron adenine deaminase. *Protein Sci 20*, 2080-2094.

202. Orme-Johnson, N. R., and Orme-Johnson, W. H. (1978) Detection and quantitation of free cytochrome P-450 and cytochrome P-450 complexes by EPR spectroscopy. *Methods Enzymol 52*, 252-257.

203. Mossbauer, R. L. (1962) Recoilless Nuclear Resonance Absorption of Gamma Radiation: A new principle yields gamma lines of extreme narrowness for measurements of unprecedented accuracy. *Science 137*, 731-738.

204. Schulz, C. E., Rutter, R., Sage, J. T., Debrunner, P. G., and Hager, L. P. (1984) Moessbauer and electron paramagnetic resonance studies of horseradish peroxidase and its catalytic intermediates. *Biochemistry 23*, 4743-4754.

205. Violet, C. E., and Pipkorn, D. N. (1971) Mossbauer Line Positions and Hyperfine Interactions in Alpha Iron. *J Appl Phys 42*, 4339-&.

206. Bridges, H. R., Bill, E., and Hirst, J. (2011) Mössbauer Spectroscopy on Respiratory Complex I: The Iron–Sulfur Cluster Ensemble in the NADH-Reduced Enzyme Is Partially Oxidized. *Biochemistry 51*, 149-158.

207. Sanakis, Y., Petrouleas, V., and Diner, B. A. (1994) Cyanide Binding at the Non-Heme Fe2+ of the Iron-Quinone Complex of Photosystem II: At High Concentrations, Cyanide Converts the Fe2+ from High (S = 2) to Low (S = 0) Spin. *Biochemistry 33*, 9922-9928.

208. Tsang, C. P., Boyle, A. J. F., and Morgan, E. H. (1975) Mossbauer-Spectra of Bicarbonate-Free Ferric-Transferrin Complex. *Biochimica Et Biophysica Acta 386*, 32-40.

209. Lipscomb, J. D., Andersson, K. K., Munck, E., Kent, T. A., and Hooper, A. B. (1982) Resolution of Multiple Heme Centers of Hydroxylamine Oxidoreductase from Nitrosomonas .2. Mossbauer-Spectroscopy. *Biochemistry 21*, 3973-3976.

210. Champion, P. M., Chiang, R., Muenck, E., Debrunner, P., and Hager, L. P. (1975) Moessbauer investigations of high-spin ferrous heme proteins. II. Chloroperoxidase, horseradish peroxidase, and hemoglobin. *Biochemistry 14*, 4159-4166.

211. Spartalian, K., Lang, G., and Yonetani, T. (1976) Low temperature photodissociation studies of ferrous hemoglobin and myoglobin complexes by Mössbauer spectroscopy. *Biochimica et Biophysica Acta (BBA) - General Subjects 428*, 281-290.

212. Costa, C., Moura, J. J., Moura, I., Liu, M. Y., Peck, H. D., Jr., LeGall, J., Wang, Y. N., and Huynh, B. H. (1990) Hexaheme nitrite reductase from Desulfovibrio desulfuricans. Mossbauer and EPR characterization of the heme groups. *The Journal of biological chemistry 265*, 14382-14388.

213. Barata, B. A. S., Liang, J., Moura, I., Legall, J., Moura, J. J. G., and Hanh Huynh, B. (1992) Mössbauer study of the native, reduced and substrate-reacted Desulfovibrio gigas aldehyde oxido-reductase. *European Journal of Biochemistry 204*, 773-778.

214. Schunemann, V., Trautwein, A. X., Illerhaus, J., and Haehnel, W. (1999) Mossbauer and electron paramagnetic resonance studies of the cytochrome bf complex. *Biochemistry 38*, 8981-8991.

215. Tse Sum Bui, B., Florentin, D., Marquet, A., Benda, R., and Trautwein, A. X. (1999) Mössbauer studies of Escherichia coli biotin synthase: evidence for reversible interconversion between [2Fe-2S]2+ and [4Fe-4S]2+ clusters. *Febs Letters 459*, 411-414.

216. Surerus, K. K., Kennedy, M. C., Beinert, H., and Munck, E. (1989) Mossbauer study of the inactive Fe3S4 and Fe3Se4 and the active Fe4Se4 forms of beef heart aconitase. *Proc Natl Acad Sci U S A 86*, 9846-9850.

217. Xia, J., Hu, Z., Popescu, C. V., Lindahl, P. A., and Münck, E. (1997) Mössbauer and EPR Study of the Ni-Activated α-Subunit of Carbon Monoxide Dehydrogenase from Clostridium thermoaceticum. *J Am Chem Soc 119*, 8301-8312.

218. Yamaguchiiwai, Y., Dancis, A., and Klausner, R. D. (1995) Aft1 - a Mediator of Iron-Regulated Transcriptional Control in Saccharomyces-Cerevisiae. *Embo Journal 14*, 1231-1239.

219. Felice, M. R., De Domenico, I., Li, L. T., Ward, D. M., Bartok, B., Musci, G., and Kaplan, J. (2005) Post-transcriptional regulation of the yeast high affinity iron transport system. *Journal of Biological Chemistry 280*, 22181-22190.

220. Thomas, B. J., and Rothstein, R. (1989) Elevated Recombination Rates in Transcriptionally Active DNA. *Cell 56*, 619-630.

221. Hudder, B. N., Morales, J. G., Stubna, A., Munck, E., Hendrich, M. P., and Lindahl, P. A. (2007) Electron paramagnetic resonance and Mossbauer spectroscopy of intact mitochondria from respiring Saccharomyces cerevisiae. *J Biol Inorg Chem 12*, 1029-1053.

222. Diekert, K., De Kroon, A. I. P. M., Kispal, G., and Lill, R. (2001) Isolation and subfractionation of mitochondria from the yeast saccharomyces cerevisiae, pp 37-51.

223. Babcock, M., deSilva, D., Oaks, R., DavisKaplan, S., Jiralerspong, S., Montermini, L., Pandolfo, M., and Kaplan, J. (1997) Regulation of mitochondrial iron accumulation by Yfh1p, a putative homolog of frataxin. *Science 276*, 1709-1712.

224. Cobine, P. A., Ojeda, L. D., Rigby, K. M., and Winge, D. R. (2004) Yeast contain a non-proteinaceous pool of copper in the mitochondrial matrix. *The Journal of biological chemistry 279*, 14447-14455.

225. Foury, F., and Cazzalini, O. (1997) Deletion of the yeast homologue of the human gene associated with Friedreich's ataxia elicits iron accumulation in mitochondria. *FEBS Lett 411*, 373-377.

226. Lindahl, P. A., Morales, J. G., Miao, R., and Holmes-Hampton, G. (2009) Isolation of Saccharomyces Cerevisiae Mitochondria for Mossbauer, Epr, and Electronic Absorption Spectroscopic Analyses. *Method Enzymol 456*, 267-285.

227. Liao, G. L., and Palmer, G. (1996) The reduced minus oxidized difference spectra of cytochromes a and a(3) *Biochimica et Biophysica Acta-Bioenergetics 1274*, 109-111.

228. Jose, J., Loudet, A., Ueno, Y., Barhoumi, R., Burghardt, R. C., and Burgess, K. (2010) Intracellular imaging of organelles with new water-soluble benzophenoxazine dyes. *Org Biomol Chem 8*, 2052-2059.

229. Atamna, H. (2004) Heme, iron, and the mitochondrial decay of ageing. *Ageing Research Reviews 3*, 303-318.

230. Shvartsman, M., Kikkeri, R., Shanzer, A., and Cabantchik, Z. I. (2007) Non-transferrin-bound iron reaches mitochondria by a chelator-inaccessible mechanism: biological and clinical implications. *American Journal of Physiology-Cell Physiology 293*, C1383-C1394.

231. Petrat, F., Weisheit, D., Lensen, M., de Groot, H., Sustmann, R., and Rauen, U. (2002) Selective determination of mitochondrial chelatable iron in viable cells with a new fluorescent sensor. *Biochemical Journal 362*, 137-147.

232. Stevens, B. J. (1977) Variation in Number and Volume of Mitochondria in Yeast According to Growth-Conditions - Study Based on Serial Sectioning and Computer Graphics Reconstitution. *Biologie Cellulaire 28*, 37-56.

233. Garber Morales, J., Holmes-Hampton, G. P., Miao, R., Guo, Y., Munck, E., and Lindahl, P. A. (2010) Biophysical characterization of iron in mitochondria isolated from respiring and fermenting yeast. *Biochemistry 49*, 5436-5444.

234. Luo, Y., Bond, J. D., and Ingram, V. M. (1997) Compromised mitochondrial function leads to increased cytosolic calcium and to activation of MAP kinases. *P Natl Acad Sci USA 94*, 9705-9710.

235. Dickson, D. P. E., and Berry, F. J. (1986) *Mossbauer spectroscopy*, Cambridge University Press, Cambridge ; New York.

236. Wikstrom, M., Krab, K., and Saraste, M. (1981) Proton-Translocating Cytochrome Complexes. *Annu Rev Biochem 50*, 623-655.

237. Flatmark, T., and Tangeras, A. (1976) Mitochondrial 'non-heme non-FeS iron' and its significance in the cellular metabolism of iron., In *Proteins of Iron Metabolism* (E.B. Brown, P. A., J. Fielding, and R.R. Crichton, Ed.), pp 349 – 358., Grune & Stratton, New York, USA.

238. Green, D. E., Tisdale, H. D., Criddle, R. S., and Bock, R. M. (1961) Structural Protein and Mitochondrial Organization. *Biochem Bioph Res Co 5*, 81-&.

239. Glick, B. S., and Pon, L. A. (1995) Isolation of highly purified mitochondria from Saccharomyces cerevisiae. *Methods in Enzymology 260*, 213-223.

240. Goetz, J. G., and Nabi, I. R. (2006) Interaction of the smooth endoplasmic reticulum and mitochondria. *Biochemical Society Transactions 34*, 370-373.

241. Beinert, H., and Shaw, R. W. (1977) On Identitiy of High-Spin Heme Components of Cytochrome-C Oxidase. *Biochimica et Biophysica Acta 462*, 121-130.

242. Barrientos, A. (2003) Yeast models of human mitochondrial diseases. *Iubmb Life 55*, 83-95.

243. Rouault, T. A., and Tong, W. H. (2008) Iron-sulfur cluster biogenesis and human disease. *Trends in genetics : TIG 24*, 398-407.

244. Veatch, J. R., McMurray, M. A., Nelson, Z. W., and Gottschling, D. E. (2009) Mitochondrial dysfunction leads to nuclear genome instability via an iron-sulfur cluster defect. *Cell 137*, 1247-1258.

245. Huang, M. E., and Kolodner, R. D. (2005) A biological network in Saccharomyces cerevisiae prevents the deleterious effects of endogenous oxidative DNA damage. *Mol Cell 17*, 709-720.

246. Barja, G. (1998) Mitochondrial free radical production and aging in mammals and birds. *Annals of the New York Academy of Sciences 854*, 224-238.

247. Turrens, J. F. (1997) Superoxide production by the mitochondrial respiratory chain. *Bioscience reports 17*, 3-8.

248. Scheffler, I. E. (1999) *Mitochondria*, Wiley-Liss.

249. Babcock, M., de Silva, D., Oaks, R., Davis-Kaplan, S., Jiralerspong, S., Montermini, L., Pandolfo, M., and Kaplan, J. (1997) Regulation of mitochondrial iron accumulation by Yfh1p, a putative homolog of frataxin. *Science 276*, 1709-1712.

250. Carraway, M. S., Suliman, H. B., Madden, M. C., Piantadosi, C. A., and Ghio, A. J. (2006) Metabolic capacity regulates iron homeostasis in endothelial cells. *Free Radic Biol Med 41*, 1662-1669.

251. Napoli, E., Taroni, F., and Cortopassi, G. A. (2006) Frataxin, iron-sulfur clusters, heme, ROS, and aging. *Antioxidants & redox signaling 8*, 506-516.

252. Hare, D., Reedy, B., Grimm, R., Wilkins, S., Volitakis, I., George, J. L., Cherny, R. A., Bush, A. I., Finkelstein, D. I., and Doble, P. (2009) Quantitative elemental

bio-imaging of Mn, Fe, Cu and Zn in 6-hydroxydopamine induced Parkinsonism mouse models. *Metallomics 1*, 53-58.

253. Lee, D. W., Kaur, D., Chinta, S. J., Rajagopalan, S., and Andersen, J. K. (2009) A Disruption in Iron-Sulfur Center Biogenesis via Inhibition of Mitochondrial Dithiol Glutaredoxin 2 May Contribute to Mitochondrial and Cellular Iron Dysregulation in Mammalian Glutathione-Depleted Dopaminergic Cells: Implications for Parkinson's Disease. *Antioxidants & redox signaling 11*, 2083-2094.

254. Camaschella, C., Campanella, A., De Falco, L., Boschetto, L., Merlini, R., Silvestri, L., Levi, S., and Iolascon, A. (2007) The human counterpart of zebrafish shiraz shows sideroblastic-like microcytic anemia and iron overload. *Blood 110*, 1353-1358.

255. Schonauer, M. S., and Dieckmann, C. L. (2004) Mitochondrial genomics and proteomics. *Curr. Genomics 5*, 575-588.

256. Egner, A., Jakobs, S., and Hell, S. W. (2002) Fast 100-nm resolution three-dimensional microscope reveals structural plasticity of mitochondria in live yeast. *P Natl Acad Sci USA 99*, 3370-3375.

257. Wang, H., Sauke, T., Debrunner, P. G., and Chan, S. I. (1988) The CO Adduct of Yeast Cytochrome-C Oxidase - Mossbauer and Photolysis Studies. *Journal of Biological Chemistry 263*, 15260-15263.

258. Maguire, J. J., Johnson, M. K., Morningstar, J. E., Ackrell, B. A. C., and Kearney, E. B. (1985) Electron-Paramagnetic Rresonance Studies of Mammalian

Succinate-Dehyrogenase Detection of the Tetranuclear Cluster S2. *Journal of Biological Chemistry 260*, 909-912.

259. Fee, J. A., Findling, K. L., Yoshida, T., Hille, R., Tarr, G. E., Hearshen, D. O., Dunham, W. R., Day, E. P., Kent, T. A., and Munck, E. (1984) Purification and characterization of the Rieske iron-sulfur protein from Thermus thermophilus. Evidence for a [2Fe-2S] cluster having non-cysteine ligands. *Journal of Biological Chemistry 259*, 124-133.

260. Swanson, M. A., Usselman, R. J., Frerman, F. E., Eaton, G. R., and Eaton, S. S. (2008) The iron-sulfur cluster of electron transfer flavoprotein-ubiquinone oxidoreductase is the electron acceptor for electron transfer flavoprotein. *Biochemistry 47*, 8894-8901.

261. Holmes-Hampton, G. P., Miao, R., Morales, J. G., Guo, Y. S., Münck, E., and Lindahl, P. A. (2010) A Nonheme High-Spin Ferrous Pool in Mitochondria Isolated from Fermenting *Saccharomyces cerevisiae*. *Biochemistry 49*, 4227-4234.

262. Seguin, A., Bayot, A., Dancis, A., Rogowska-Wrzesinska, A., Auchere, F., Camadro, J. M., Bulteau, A. L., and Lesuisse, E. (2009) Overexpression of the yeast frataxin homolog (Yfh1): Contrasting effects on iron-sulfur cluster assembly, heme synthesis and resistance to oxidative stress. *Mitochondrion 9*, 130-138.

263. Jorgensen, P., Nishikawa, J. L., Breitkreutz, B. J., and Tyers, M. (2002) Systematic identification of pathways that couple cell growth and division in yeast. *Science 297*, 395-400.

264. Sherman, F. (2002) Getting started with yeast. *Guide to Yeast Genetics and Molecular and Cell Biology, Pt B 350*, 3-41.

265. Tamaki, H., Yun, C. W., Mizutani, T., Tsuzuki, T., Takagi, Y., Shinozaki, M., Kodama, Y., Shirahige, K., and Kumagai, H. (2005) Glucose-dependent cell size is regulated by a G protein-coupled receptor system in yeast Saccharomyces cerevisiae. *Genes Cells 10*, 193-206.

266. Tyson, C. B., Lord, P. G., and Wheals, A. E. (1979) Dependency of size of Saccharomyces cerevisiae cells on growth rate. *J Bacteriol 138*, 92-98.

267. Polakis, E. S., Bartley, W., and Meek, G. A. (1964) Changes in Structure + Enzyme Activity of Saccharomyces Cerevisiae in Response to Changes in Environment. *Biochemical Journal 90*, 369-&.

268. Polakis, E. S., Bartley, W., and Meek, G. A. (1965) Changes in Activities of Respiratory Enzymes during Aerobic Growth of Yeast on Different Carbon Sources. *Biochemical Journal 97*, 298-&.

269. Cook, J. D., Bencze, K. Z., Jankovic, A. D., Crater, A. K., Busch, C. N., Bradley, P. B., Stemmler, A. J., Spaller, M. R., and Stemmler, T. L. (2006) Monomeric yeast frataxin is an iron-binding protein. *Biochemistry 45*, 7767-7777.

270. Ohlmeier, S., Kastaniotis, A. J., Hiltunen, J. K., and Bergmann, U. (2004) The Yeast Mitochondrial Proteome, a Study of Fermentative and Respiratory Growth. *Journal of Biological Chemistry 279*, 3956-3979.

271. Costa, V., Amorim, M. A., Reis, E., Quintaniha, A., and Moradas-Ferreira, P. (1979) Mitochondrial superoxide dismutase is essential for ethanol tolerance of Saccharomyces cerevisiae in the post-diauxic phase. *Microbiology 143*, 1649-1656.

272. Zitomer, R. S., Montgomery, D. L., Nichols, D. L., and Halo, B. D. (1979) Transcriptional regulation of the yeast cytochrome c gene. *P Natl Acad Sci USA 76*, 3627-3631.

273. Macierzynska, E., Grzelak, A., and Bartosz, G. (2007) The effect of growth medium on the antioxidant defense of Saccharomyces cerevisiae. *Cellular & molecular biology letters*.

274. Maris, A. F., Assumpcao, A. L., Bonatto, D., Brendel, M., and Henriques, J. A. (2001) Diauxic shift-induced stress resistance against hydroperoxides in Saccharomyces cerevisiae is not an adaptive stress response and does not depend on functional mitochondria. *Curr Genet 39*, 137-149.

275. Paradkar, P. N., Zumbrennen, K. B., Paw, B. H., Ward, D. M., and Kaplan, J. (2009) Regulation of Mitochondrial Iron Import through Differential Turnover of Mitoferrin 1 and Mitoferrin 2. *Molecular and Cellular Biology 29*, 1007-1016.

276. Corson, L. B., Folmer, J., Strain, J. J., Culotta, V. C., and Cleveland, D. W. (1999) Oxidative stress and iron are implicated in fragmenting vacuoles of

Saccharomyces cerevisiae lacking Cu,Zn-superoxide dismutase. *Journal of Biological Chemistry 274*, 27590-27596.

277. Kaplan, C. D., and Kaplan, J. (2009) Iron Acquisition and Transcriptional Regulation. *Chem Rev 109*, 4536-4552.

278. Kumanovics, A., Chen, O. S., Li, L. T., Bagley, D., Adkins, E. M., Lin, H. L., Dingra, N. N., Outten, C. E., Keller, G., Winge, D., Ward, D. M., and Kaplan, J. (2008) Identification of FRA1 and FRA2 as genes involved in regulating the yeast iron regulon in response to decreased mitochondrial iron-sulfur cluster synthesis. *Journal of Biological Chemistry 283*, 10276-10286.

279. Rees, E. M., and Thiele, D. J. (2007) Identification of a vacuole-associated metalloreductase and its role in Ctr2-mediated intracellular copper mobilization. *Journal of Biological Chemistry 282*, 21629-21638.

280. Portnoy, M. E., Liu, X. F., and Culotta, V. C. (2000) *Saccharomyces cerevisiae* expresses three functionally distinct homologues of the Nramp family of metal transporters. *Molecular and Cellular Biology 20*, 7893-7902.

281. Nelson, N. (1999) Metal ion transporters and homeostasis. *Embo Journal 18*, 4361-4371.

282. Li, L. T., and Kaplan, J. (2004) A mitochondrial-vacuolar signaling pathway in yeast that affects iron and copper metabolism. *Journal of Biological Chemistry 279*, 33653-33661.

283. Chen, O. S., and Kaplan, J. (2000) CCC1 suppresses mitochondrial damage in the yeast model of Friedreich's ataxia by limiting mitochondrial iron accumulation. *Journal of Biological Chemistry 275*, 7626-7632.

284. Que, L. (2000) *Physical methods in bioinorganic chemistry : spectroscopy and magnetism*, University Science Books, Sausalito, Calif.

285. Sinnecker, S., Slep, L. D., Bill, E., and Neese, F. (2005) Performance of nonrelativistic and quasi-relativistic hybrid DFT for the prediction of electric and magnetic hyperfine parameters in 57Fe Mossbauer spectra. *Inorg Chem 44*, 2245-2254.

286. Greenwood, N. N., and Gibb, T. C. (1971) High-spin Iron Complexes, In *Mössbauer spectroscopy*, pp 112-159, Chapman and Hall, London,.

287. Cockrell, A. L., Holmes-Hampton, G. P., McCormick, S. P., Chakrabarti, M., and Lindahl, P. A. (2011) Mössbauer and EPR Study of Iron in Vacuoles from Fermenting Saccharomyces cerevisiae. *Biochemistry*.

288. Miao, R., Holmes-Hampton, G. P., and Lindahl, P. A. (2011) Biophysical Investigation of the Iron in Aft1-1(up) and Gal-YAH1 Saccharomyces cerevisiae. *Biochemistry 50*, 2660-2671.

289. Hudder, B. N., Morales, J. G., Stubna, A., Münck, E., Hendrich, M. P., and Lindahl, P. A. (2007) Electron paramagnetic resonance and Mössbauer spectroscopy of intact mitochondria from respiring *Saccharomyces cerevisiae*. *J Biol Inorg Chem 12*, 1029-1053.

290. Cockrell, A. L., Holmes-Hampton, G. P., McCormick, S. P., Chakrabarti, M., and Lindahl, P. A. (2011) Mössbauer and EPR Study of Iron in Vacuoles from Fermenting Saccharomyces cerevisiae. *Biochemistry 50*, 10275-10283.

291. Hausmann, A., Samans, B., Lill, R., and Mühlenhoff, U. (2008) Cellular and Mitochondrial Remodeling upon Defects in Iron-Sulfur Protein Biogenesis. *Journal of Biological Chemistry 283*, 8318-8330.

292. Eide, D., Daviskaplan, S., Jordan, I., Sipe, D., and Kaplan, J. (1992) Regulation of Iron Uptake in Saccharomyces-Cerevisiae - the Ferrireductase and Fe(Ii) Transporter Are Regulated Independently. *Journal of Biological Chemistry 267*, 20774-20781.

293. Casas, C., Aldea, M., Espinet, C., Gallego, C., Gil, R., and Herrero, E. (1997) The AFT1 transcriptional factor is differentially required for expression of high-affinity iron uptake genes in Saccharomyces cerevisiae. *Yeast 13*, 621-637.

294. Courel, M., Lallet, S., Camadro, J. M., and Blaiseau, P. L. (2005) Direct activation of genes involved in intracellular iron use by the yeast iron-responsive transcription factor Aft2 without its paralog Aft1. *Molecular and Cellular Biology 25*, 6760-6771.

295. Rutherford, J. C., Jaron, S., and Winge, D. R. (2003) Aft1p and Aft2p mediate iron-responsive gene expression in yeast through related promoter elements. *Journal of Biological Chemistry 278*, 27636-27643.

296. Askwith, C., Eide, D., Van Ho, A., Bernard, P. S., Li, L., Davis-Kaplan, S., Sipe, D. M., and Kaplan, J. (1994) The FET3 gene of S. cerevisiae encodes a multicopper oxidase required for ferrous iron uptake. *Cell 76*, 403-410.

297. Nishida, K., and Silver, P. A. (2012) Induction of Biogenic Magnetization and Redox Control by a Component of the Target of Rapamycin Complex 1 Signaling Pathway. *PLoS Biol 10*, e1001269.

298. Aasa, R., Albracht, S. P. J., Falk, K.-E., Lanne, B., and Vänngård, T. (1976) EPR signals from cytochrome c oxidase. *Biochimica et Biophysica Acta (BBA) - Enzymology 422*, 260-272.

299. Fitzpatrick, P. F. (1999) Tetrahydropterin-dependent amino acid hydroxylases. *Annu Rev Biochem 68*, 355-381.

300. Beard, J., Erikson, K. M., and Jones, B. C. (2003) Neonatal iron deficiency results in irreversible changes in dopamine function in rats. *J Nutr 133*, 1174-1179.

301. Halliwell, B. (2006) Oxidative stress and neurodegeneration: where are we now? *J Neurochem 97*, 1634-1658.

302. Green, D. R., Galluzzi, L., and Kroemer, G. (2011) Mitochondria and the autophagy-inflammation-cell death axis in organismal aging. *Science 333*, 1109-1112.

303. Gerlach, M., Ben-Shachar, D., Riederer, P., and Youdim, M. B. (1994) Altered brain metabolism of iron as a cause of neurodegenerative diseases? *J Neurochem 63*, 793-807.

304. Wu, L. J., Leenders, A. G., Cooperman, S., Meyron-Holtz, E., Smith, S., Land, W., Tsai, R. Y., Berger, U. V., Sheng, Z. H., and Rouault, T. A. (2004) Expression of the iron transporter ferroportin in synaptic vesicles and the blood-brain barrier. *Brain Res 1001*, 108-117.

305. Fishman, J. B., Rubin, J. B., Handrahan, J. V., Connor, J. R., and Fine, R. E. (1987) Receptor-mediated transcytosis of transferrin across the blood-brain barrier. *J Neurosci Res 18*, 299-304.

306. Bou-Abdallah, F., Santambrogio, P., Levi, S., Arosio, P., and Chasteen, N. D. (2005) Unique iron binding and oxidation properties of human mitochondrial ferritin: a comparative analysis with Human H-chain ferritin. *J Mol Biol 347*, 543-554.

307. Meguro, R., Asano, Y., Odagiri, S., Li, C., and Shoumura, K. (2008) Cellular and subcellular localizations of nonheme ferric and ferrous iron in the rat brain: a light and electron microscopic study by the perfusion-Perls and -Turnbull methods. *Arch Histol Cytol 71*, 205-222.

308. Connor, J. R., Menzies, S. L., St Martin, S. M., and Mufson, E. J. (1992) A histochemical study of iron, transferrin, and ferritin in Alzheimer's diseased brains. *J Neurosci Res 31*, 75-83.

309. Bell, S. H., Weir, M. P., Dickson, D. P., Gibson, J. F., Sharp, G. A., and Peters, T. J. (1984) Mossbauer spectroscopic studies of human haemosiderin and ferritin. *Biochim Biophys Acta 787*, 227-236.

310. Vanderford, D. A., Greer, P. K., Sharp, J. M., Chichlowski, M., Rouse, D. C., Selim, M. A., and Hale, L. P. (2010) Alopecia in IL-10-deficient mouse pups is c-kit-dependent and can be triggered by iron deficiency. *Exp Dermatol 19*, 518-526.

311. Oshtrakh, M. I. (1998) The features of Mossbauer spectra of hemoglobin in relation to the quadrupole splitting and heme iron stereochemistry. *Z Naturforsch A 53*, 608-614.

312. Galazka-Friedman, J., Bauminger, E. R., Friedman, A., Barcikowska, M., Hechel, D., and Nowik, I. (1996) Iron in parkinsonian and control substantia nigra--a Mossbauer spectroscopy study. *Mov Disord 11*, 8-16.

313. Bartzokis, G., Tishler, T. A., Shin, I. S., Lu, P. H., and Cummings, J. L. (2004) Brain ferritin iron as a risk factor for age at onset in neurodegenerative diseases. *Annals of the New York Academy of Sciences 1012*, 224-236.

314. Keen, C. L., and Hurley, L. S. (1980) Developmental changes in concentrations of iron, copper, and zinc in mouse tissues. *Mech Ageing Dev 13*, 161-176.

315. Moos, T., and Morgan, E. H. (2000) Transferrin and transferrin receptor function in brain barrier systems. *Cell Mol Neurobiol 20*, 77-95.

316. Connor, J. R., Menzies, S. L., Burdo, J. R., and Boyer, P. J. (2001) Iron and iron management proteins in neurobiology. *Pediatr Neurol 25*, 118-129.

317. Jhurry, N. D., Chakrabarti, M., McCormick, S. P., Holmes-Hampton, G. P., and Lindahl, P. A. (2012) Ironome of Human Jurkat Cells and Isolated Mitochondria. *Proc Natl Acad Sci U S A Sumbitted for Review*.

318. Pysh, J. J. (1970) Mitochondrial changes in rat inferior colliculus during postnatal development: an electron microscopic study. *Brain Res 18*, 325-342.

319. Ashkenazi, R., Ben-Shachar, D., and Youdim, M. B. (1982) Nutritional iron and dopamine binding sites in the rat brain. *Pharmacol Biochem Behav 17 Suppl 1*, 43-47.

320. Mackler, B., Person, R., and Grace, R. (1985) Iron deficiency in the rat: effects on energy metabolism in brown adipose tissue. *Pediatr Res 19*, 989-991.

321. Galazka-Friedman, J. (2009) Iron as a risk factor in neurological diseases, In *ICAME 2007* (Gajbhiye, N. S., and Date, S. K., Eds.), pp 31-44, Springer Berlin Heidelberg.

322. Sohal, R. S., Wennberg-Kirch, E., Jaiswal, K., Kwong, L. K., and Forster, M. J. (1999) Effect of age and caloric restriction on bleomycin-chelatable and nonheme iron in different tissues of C57BL/6 mice. *Free Radic Biol Med 27*, 287-293.

323. Sano, H., Naruse, M., Matsumoto, K., Oi, T., and Utsumi, H. (2000) A new nitroxyl-probe with high retention in the brain and its application for brain imaging. *Free Radic Biol Med 28*, 959-969.

324. Gomi, F., Utsumi, H., Hamada, A., and Matsuo, M. (1993) Aging retards spin clearance from mouse brain and food restriction prevents its age-dependent retardation. *Life Sci 52*, 2027-2033.

325. Cadenas, E., and Davies, K. J. (2000) Mitochondrial free radical generation, oxidative stress, and aging. *Free Radic Biol Med 29*, 222-230.

APPENDIX A

INSTALLING, OPERATING AND MAINTAINING MÖSSBAUER INSTRUMENTS IN THE LINDAHL LAB

Description of the Instruments

The Lindahl lab at Texas A&M University currently houses 4 Mössbauer spectrometers (SEE Co, Edina, MN, USA). Three are low-field instruments; one allows applied magnetic fields as high as 6 T. Two low-field instruments employ CCR4K closed cycle He gas refrigerator cryostats, while the third (an SVT300 LHe/LN2 cryostat) uses liquid helium as a cryogen. The CCR4K helium compressors cool the sample to temperatures between 4.6 and 325 K. The SVT300 can operate as low as 1.3 K under pumped He conditions. The remaining spectrometer has a LHe6T LHe/LN2 superconducting magnet cryostat. This instrument also uses liquid helium and operates between 1.3 to 325 K.

The majority of the components of each of these systems is identical. Each uses a VT400 velocity transducer, a W302 resonant γ-ray spectrometer with integrated servo control interfaced with the VT400, and a W202 γ-ray spectrometer with high voltage supply for the detector. The detector on each system is a proportional counter (LND, INC. #45431). See figure A.1 for a sketch of the instrument setup.

The basic experiment starts with the W302 box. This box sends signals to servos in the VT400 to control the velocity scale for sample collection. The servos move the ^{57}Co source (Ritverc, GmbH, St. Petersburgh, Russia) towards and away from the

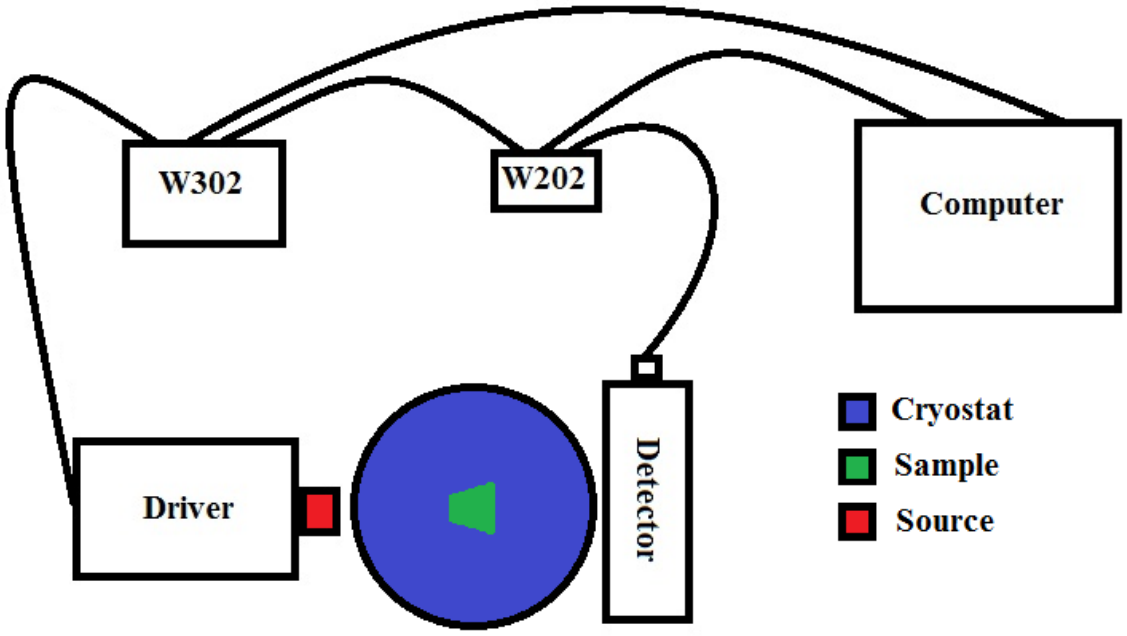

Figure A.1. Basic instrument setup.

stationary sample mounted inside the cryostat. The sample will absorb a small percentage of the γ-rays produced by the source. The remaining γ-rays will continue on to the detector biased at a voltage supplied by the W202. Channels embedded in the W302 hardware will then locally store counts of radiation which correspond to energies at different velocities. This information is then transferred to a PC where the data is plotted as 1024 discrete points corresponding to the range of energies exposed to the sample. The counts will be highest at energies where none of the γ-rays has been absorbed and lowest where the absorption is maximal.

On the low-field instruments, a magnet with a field strength of ~500 G is placed around the sample on the outside of the dewar. This is accomplished with stand-alone magnets which must be mounted on the instruments as shown in figure A.2.

Using Air Pads to Minimize External Vibrations on the System

Mössbauer spectroscopy is extremely sensitive to vibrations which can cause lines to broaden and resolution to decline. The CCR4K systems present additional challenges as they require a refrigerator which constantly generates vibrations. Strategies for isolating these vibrations from the sample will follow. For all instruments the best monitor for vibrational isolation is to measure linewidths on a reference spectrum which is typically obtained using α-Fe Foil. We have found The floor can be a significant source of vibrations. To eliminate theses, air pads have been installed on the bottoms of the legs of all 4 instrument frames (Figure A.3). Use of these air pads reduced vibrations significantly.

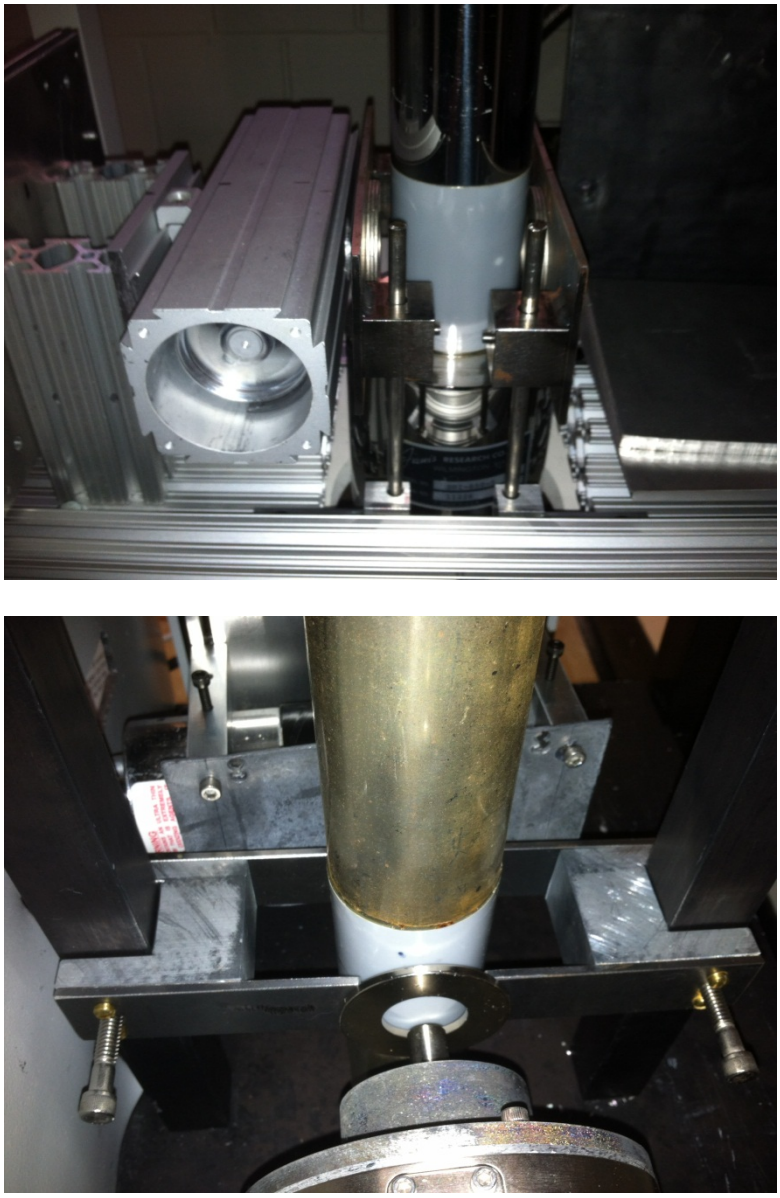

Figure A.2. Mounting of magnets on Mössbauer instruments. Top, mounting of the magnet on the CCR4K the detector can be seen on the left the driver (absent in the image) would be positioned on the right. Bottom, mounting of the magnet on the SVT300 the driver is shown on the bottom of the figure and the detector is at the top.

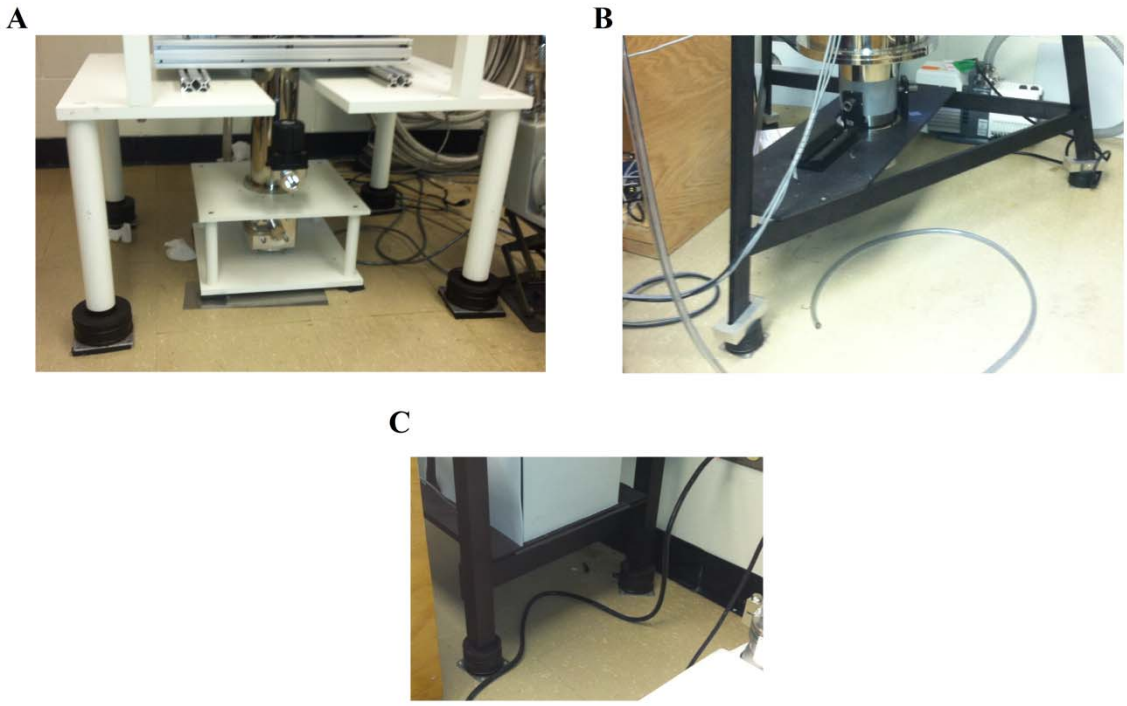

Figure A.3. Air pads on Mössbauer instruments. Systems are A. CCR4K, B. LHE6T, and C. SVT300.

Leveling the Instrument

The instrument should be level prior to collecting data. The instrument frame is first leveled by adjusting the air pressure in the pads. The dewer should be leveled next. The LHe6T dewar rests directly on the frame, so if the frame is level, the dewar will generally also be level. If not, the dewer can be leveled by shimming the instrument. On the SVT300 dewar also rests on frame. Unlike the previous system this one has 4 adjusting screws under the top table of the frame which allow the instrument to be adjusted. These screws have a thin piece of rubber between the blunt end of the screw and the dewar to avoid damage to the dewar. The dewar of the CCR4K systems is isolated from the mounting platform. In this case the dewar should be leveled by adjusting the separate frame associated with the dewar.

Mounting the Source and Detector and Adjusting the Height

For each system the source driver and detector are mounted on tables on the frame. A picture of this area on each instrument is included in Figure A.4. These components are mounted a little different on each system. On the LHe6T system the driver is mounted in a cradle which is attached directly to the bottom table of the frame. The detector is mounted on a sliding bracket to the same surface. The ideal setup with this and the other system will have the source and detector positioned in the center of the windows. In the initial setup of this system it was found that the windows of the instrument were lower than the position of the source and detector. To alleviate this, the instrument was shimmed with an aluminum plate cut to fit the contour of the dewar. This

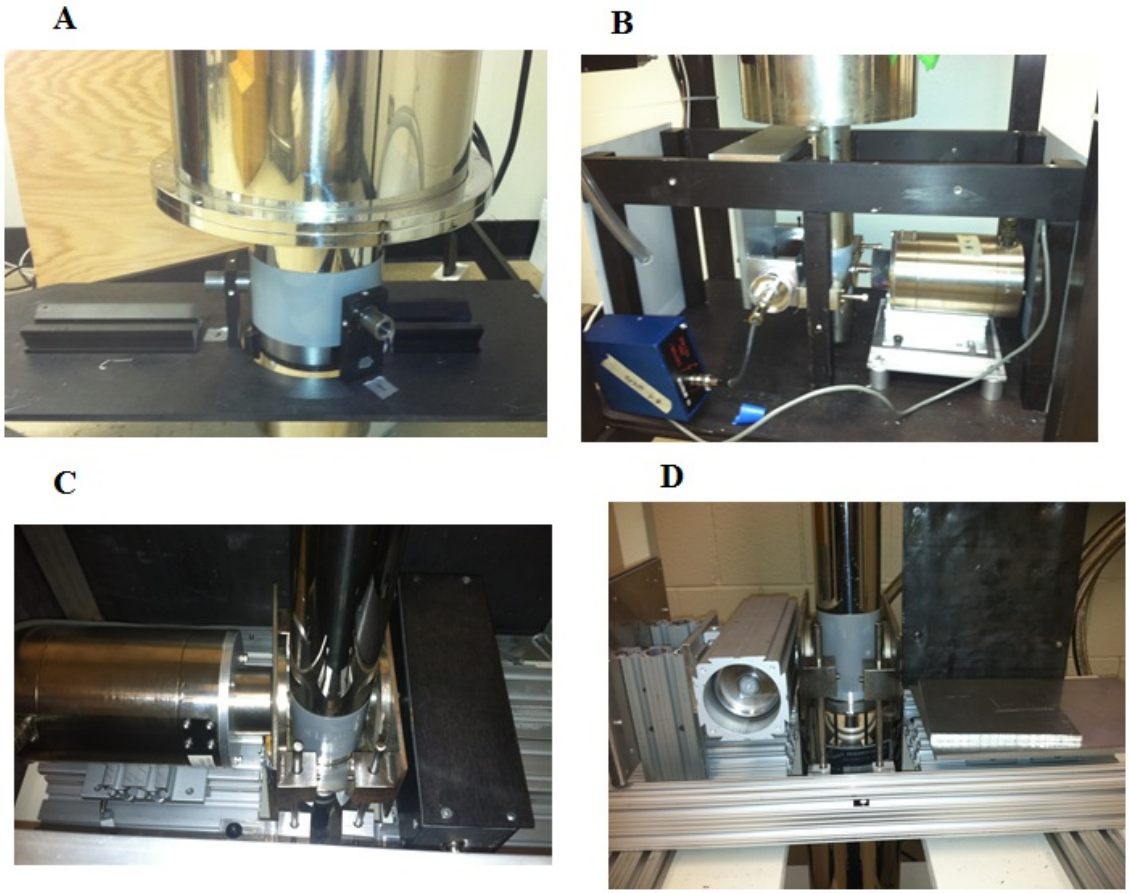

Figure A.4. Source and driver mounts on Mössbauer instruments. A, mounting area for the LHe6T system, the driver rests in the cradle on the left and the detector mounts in the bracket on the right. B, mounting area on the SVT-300 system, the driver mounts to a cradle that has been shimmed to the correct height the detector hangs from above on the left. C,D mounting area for the CCR4K systems, the newer system, C the detector mounts on the right and the driver mounts on the left. The older system D the detector mounts on the left and the driver rests on the platform on the right.

adjusted the height of the source and detector to the correct position relative to the windows of the dewar. If the position of the windows is higher than the position of the source and detector the shim under the dewar could be removed (and perhaps replace with one not as thick). Instead, the source and detector could be shimmed to the correct height. If the windows are lower than the source and detector, the instrument could be raised or the source and detector could be lower. The former approach is preferred.

The driver for the SVT300 system is mounted in a cradle similar to that of the LHe6T system. The detector is mounted on a frame built from the bottom table of the frame. In this configuration the detector hangs, suspended from the top. The detector is mounted in an adjustable configuration such that it can move up or down. In the initial setup of this instrument the driver was shimmed to the correct height. If the position needs to be adjusted such that the source is in the middle of the windows one can either adjust the height of the shims on the driver or adjust the vertical orientation of the instrument. Aside from the 4 leveling screws under the upper table, this dewar also sits on two adjustable screws at the point where the dewar tapers into the tail. These screws can be adjusted to move the entire dewar up or down.

The CCR4K instruments feature similar construction however the mounting of the source and driver are somewhat different on each of these instruments. The instruments will be distinguished as the newer instrument (originally installed in room 1137 in March of 2009) or the older instrument (originally installed in room 1136 in December of 2007). The newer instrument has the brackets on the source and detector which slide onto a complimentary bracket mounted to the lower table of the frame. The

height of these should be adjusted by inflating or deflating the air pads. The older instrument has the detector mounted in a similar configuration. The driver on the older instrument is fitted with legs extending from the cylindrical body. These allow the source to rest on a plate which slides onto a mounting bracket. Since the source is not mounted on this instrument it is necessary to ensure the driver is sitting in line with the detector. This issue could be alleviated by mounting the driver to the mounting bracket.

Installing and Changing of the Source, and RSO Source Regulations

Further optimization of the instruments will require that the source has been installed. For day-to-day operation of these instruments, lead shielding has been installed to reduce radiation exposure. Operations involving changing or installing a source will feature the highest exposure to radiation. It is best to evaluate the procedure to be accomplished prior to starting them. To minimize exposure one should use a lead vest during all procedures. Work with the source as far from your body as possible, with arms stretched out.

To change a source, remove shielding from the instrument as necessary to remove the driver. The source is incased in lead at the top of the driver except for the top where radiation is emitted. Place a sheet of lead over this opening to minimize personal exposure to radiation. With the driver sitting with the flat bottom on a benchtop, remove the three screws from the lead shielding top and remove the top lifting it vertically. Working quickly once the top is removed. Unscrew the source using a long 7/16” socket (normally used with a socket wrench) in which the inside surfaces are lined with strips of duct tape to unscrew the source. Place the assembly in a lead storage container (a “pig”),

jiggle the socket free of the source, and place the lead cover on the pig. Pigs should be stored with their lids on when a source is inside, and with their lids off when the source is installed on the driver. The steps in installing the new source are essentially the reverse of those for removing the source. The only difference would be that the source will need to be removed from the pig with a tweezers and unwrapped before it can be inserted into the socket tool.

The sources themselves do not retain identifying features so it is best to store the pig with the lid off in an area close to the instrument containing the source from that pig. Official TAMU paperwork should similarly be kept near the instrument and source to aid in the final disposal of the source. To remove a source from the lab it should be placed back into the cardboard box in which it was received. If the paperwork is kept with the source adequate information should be available to identify which source is in the box. The company to which the old source is shipped (SEE Co.) should be notified of the shipment. Then the Radiological Safety Office at TAMU (RSO) should be contacted, and they will come to the lab, pick up the source, inspect it, and then ship it to SEE Co.

Once per month the RSO will request a “leak-test” of each source. Remove the cotton swap that they provide from the bag, rinse it with ethanol and rub on or near the source. Replace it in the bag and sent to RSO. RSO staff will also conduct surveys of rooms which contain radiation by swabbing areas of the room with cotton pads. Rooms containing sources should be kept shut and locked.

Optimization of Source-Detector Distance

The intensity of the γ-rays which reach the detector is proportional to the square root of the distance between the source and the detector. Thus, optimal counts will be achieved when the detector and source are as close to one another as possible. This distance is limited by the diameter of the cryostat and the configuration of the mounts for the magnets. The optimal configuration for minimizing this distance has been incorporated in the design of the mounts in Figure A.2. For the CCR4K mounts, the brackets were incorporated into the mounting bracket that mounts the driver and detector. For the SVT300 no such brackets are present so the magnet was mounted on the vertical support beam. In each case the magnet mounts to 1/16" piece of steel to provide a surface on which the magnet will adhere. After mounting the magnet as close to the cryostat as possible without touching the cryostat, the source and detector are moved in as close to the cryostat as possible. Care should be taken to make sure the source is not inside of the magnetic field as this will affect the γ-rays.

Identifying the Height of the Sample Relative to the Windows of the Cryostat

To ensure that the sample is maximally exposed to γ-rays ensure that the height of the sample is optimally positioned in the path of the γ-rays. This can be accomplished by carefully finding the distance from the γ path relative to the top of the cryostat and adjusting the height of the sample rod relative to this measurement. A simple method to accomplish this involves using a rod that is longer than the height of the cryostat and attaching a flat sheet of lead to one end. The γ-rays will not penetrate the lead so a hole should be placed in this lead. While monitoring the counts on the software for the

spectrometer, move the rod up and down to maximize counts. This should indicate the height where the γ-rays are passing through the hole in the lead. This height should be carefully measured and the sample rod should be adjusted to the same height.

Positioning the Sample Rod.

Once the height of the sample is established, rotate the sample so that the γ-rays go through the sample. Once again, maximize counts on the software for the spectrometer. Counts should decrease as more hit the copper sample foot. By orienting the sample such that optimal counts are obtained more radiation is exposed to the sample resulting in a quicker collection time. While several different sample cups have been utilized in the lab, the majority of samples are put into cups which are tapered as depicted in figure A.1 and discussed in (*226*). When using tapered cups one should orient the sample such that bottom end of the cup is closest to the source and the top of the cup is closest to the counter.

The second aspect of positioning involves centering the sample within the cryostat cross-section (Figure A.5E). If the sample is to the left or right (Figure A.5A and Figure A.5B) of the γ path, it will be exposed to less radiation, decreasing the efficiency of the measurement. If the sample is positioned closer to the source or detector (Figure A.5C and Figure A.5D) the geometry of the cup will be less efficient and less radiation will be exposed to the sample. For the LHe6T and SVT300 instruments this positioning should be set. These dewars are both constructed such that the sample rod is fixed relative to the instrument. Once the dewar is positioned, the

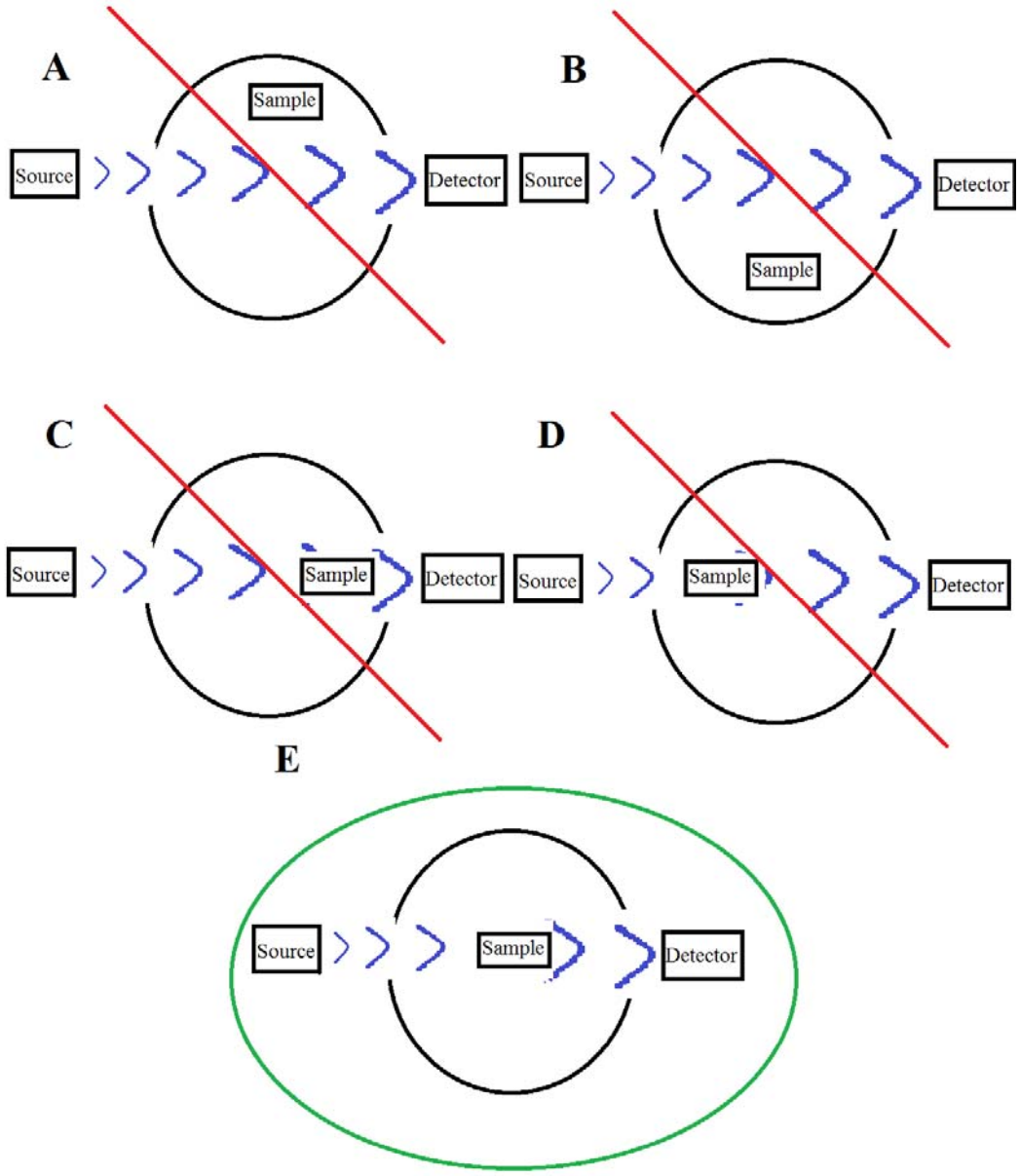

Figure A.5. Incorrect A-D, and correct E positioning of the sample in the γ path.

sample rod should also be properly positioned. Essentially, the only way this positioning will deviate is if the sample rod becomes bent.

This type of positioning is a more critical issue on the CCR4K dewars, as the sample is essentially dangling within the cryostat, not touching the walls or floor of the cryostat besides the entrance hole (which is isolated from the rest of the cryostat via the bellows). Unlike the LHe6T or SVT600, these dewers do not use cryogen to cool the sample; they use a closed cycle refrigerator which vibrates significantly. As a result, the dewar is connected to a source of vibration. To alleviate this, the instrument is designed with a rubber bellows located between the mounting of the sample rod and the dewar. This means that installation of the sample rod into the instrument no longer implies a solid construction as in the other dewars.

To ensure the position of the sample rod is in the center of the γ path a simple method has been developed. First, remove the clamp which connects the bellows used to isolate the vibration of the dewar from the table which is used to mount the sample. The bellows should be compressed such that the sample rod becomes visible as is shown in figure A.6. The rubber portion of the baffles is taped to the bottom side of the top table. With the sample rod visible, inspect the orientation and move the dewar relative to the bottom table housing the source, detector and upper table for sample mounting. Orient the dewar such that the sample rod is in the middle of the dewar. As long as the sample rod has not become bent this should adjust the sample to the middle of the γ path.

Calibrating the Instrument

At this point the α-Fe foil should be placed in the instrument attached to the sample foot. To ensure the instrument is free of vibrations the spectrum of the foil should be obtained on a 2mm/sec velocity scale at RT. Once the spectrum has been collected to a sufficient signal-to-noise ratio (S/N), the data can be analyzed. This typically takes 15-60 min depending on the age and strength of the source. On this scale only the inner lines of the sextet of the α-Fe foil will be visible. The data should be folded without using a calibration file. Next the data can be fit with the "quadpr" parameter file on WMOSS. This doublet should have δ values around 250 channels (varies by instrument), ΔE_q values around 200 channels (also varies by instrument), and Γ values around 30 channels. Using known properties of α-Fe foil (*205*), divide the ΔE_q value in channels by the known value of 1.68 mm/sec to obtain a step (in channels/mm/sec.) This step can be multiplied by the value obtained for Γ. If this value is ~0.260 mm/sec or under, the linewidths are acceptable. If this value is greater than this, refer to the section below on line broadening.

The next step is to calibrate the instrument. This is done at RT, ideally with the α-Fe foil at the sample position. Data should be collected for all spectral velocity scales on which data will be collected; typically 5, 7, 9, and 12. Once spectra at each velocity scale have been collected to adequate S/N, the data can be analyzed using the WMOSS

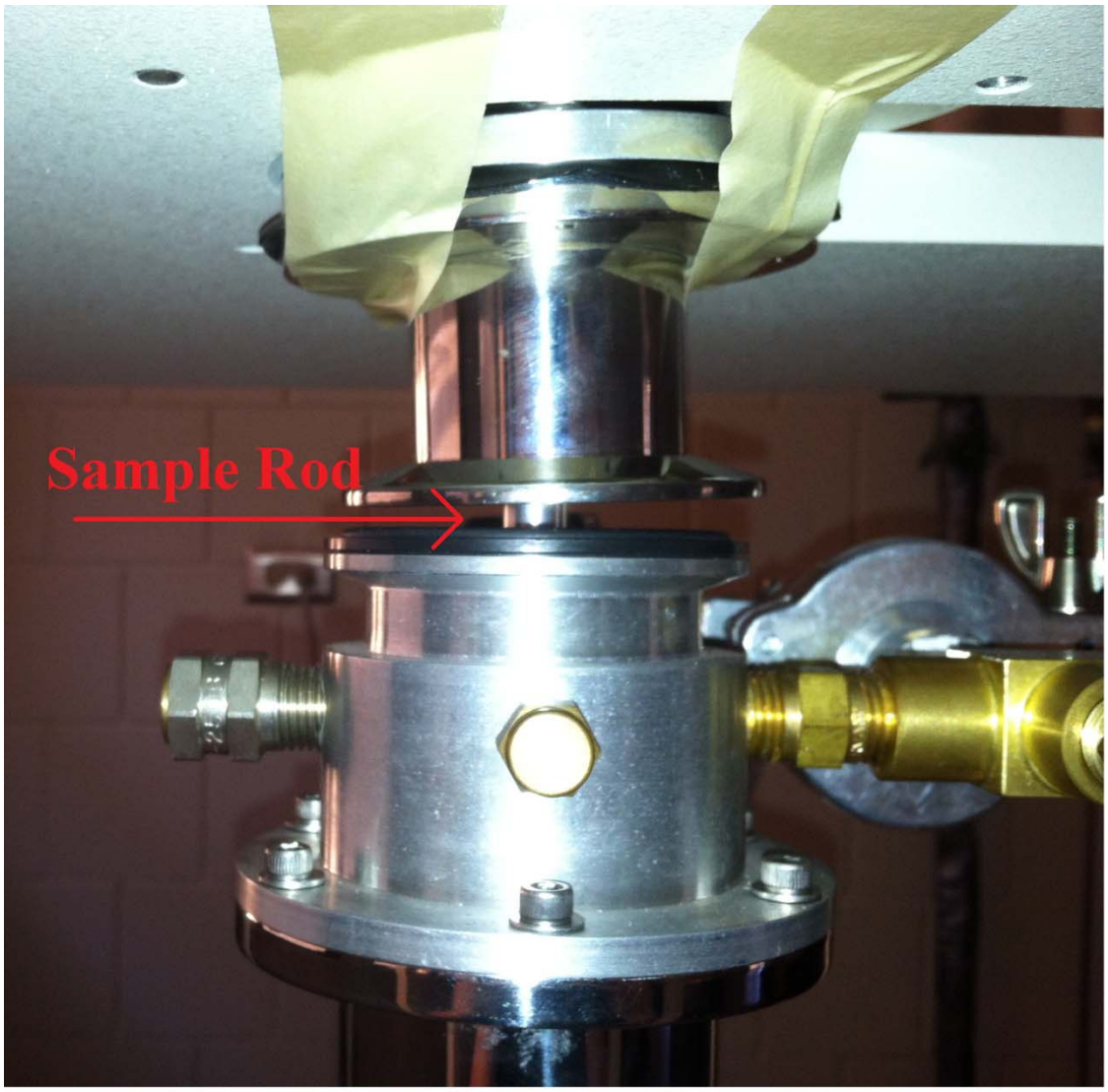

Figure A.6. The baffles taped to the top plate. This method is used for centering of the sample rod in the dewar.

femetl4 or femetl6 parameter file (these files fit lines 4 and 6 respectively) depending on the velocity scale. These fits can then be saved on WMOSS to be made available for the "Use Previous Calibration?" option on the data folding function.

Cooling the Instruments

Data can be collected at this point. Most spectra will be collected at cryogenic temperatures. The cooling procedure for the two CCR4K systems is identical; that for the LHe6t and SVT300 systems differs somewhat. Prior to cooling any of the systems it is necessary to establish a vacuum on the cryostats; a few days are typically required for the pressure to drop to ~1-3 x 10^{-6} mbar. At that pressure, the CCR4K refrigerators may be turned on. Allow the temperature to drop to ~150K and then close the valve to the turbo vacuum pump. The pump efficiency is such that it will not drop much below 5-7x 10^{-7} mbar. Assuming ideal gas behavior, Gay-Lussac's law ($P_1/T_1 = P_2/T_2$) is applicable for a change in pressure and temperature at constant volume. For a system cooling currently at 7.0 x 10^{-7} mbar and 150K, closing the valve to the vacuum should reach a final pressure of 2.33 x 10^{-8} mbar once the system reaches 5K. This phenomenon is referred to as *cryopumping*. This is lower than the pressure which would be reached by leaving the system under pumping conditions.

For the LHe6T and SVT300 systems, the final temperature of 4.2K is reached by cooling the system with liquid He (LHe). The LHe cannot be added until the system has been precooled with liquid N_2 (LN2). If the system is allowed to pump until it equilibrates at 77 K then cryopumping will only be in effect for the final 73 degrees. Therefore it is best to allow these systems to pump a longer time and close the valve at

room temperature. A system at 1.0 x 10^{-6} mbar at 298 K will drop to a pressure of 1.4 x 10^{-8} mbar at 4.2K. On the other hand leaving the valve open until the system equilibrates at 77K will result in a pressure of ~ 7 x 10^{-7} mbar. Once equilibrated to LHe temperatures this system will only reach 3.8 x 10^{-8} mbar.

Sample cooling in the CCR4K and LHe6T systems relies on exchange gas. In these instruments the sample chamber is isolated from the atmosphere and low pressures of He gas are put back into the system. This gas is cooled by the cryogen in the LHe6T system or by contact with the cold head in the CCR4K system. In the SVT300 system, the sample chamber is connected to the He reservoir by a needle valve. The introduction of the cryogen to the sample space keeps the sample cold. The sample space in this system is open to the atmosphere but positive pressure from the cryogen introduced to the sample space keeps this chamber full of helium gas.

Loading Samples into the Mössbauer Instruments

The process is different for each system, and is most involved for the LHe6T system. Since the sample chamber is cooled by exchange gas it is still under vacuum relative to the atmosphere. This means the sample space needs to be filled to atmospheric pressure prior to putting the sample rod into the instrument. This can be done with 99.997% He gas. However it is best to precool this gas by passing it through a coil of tubing chilled in LN2. Once the sample chamber has been equilibrated to atmospheric pressure the system is ready for the sample rod. A sample should be inserted into the sample foot and tightened with the set screw. This should all be done in a dewar filled with LN2. Once the sample is inserted in the sample rod it may be inserted

into the instrument. The relatively warm sample rod will boil the LHe so gas will be exhausted as the rod is inserted. The sample rod should be mounted using 4 screws. At this time a vacuum should be pulled on the sample space. It is best to pull a vacuum on the system until the gauge on the front of the instrument reaches the minimum pressure. This should be done in a short period of time (~1 min). At this point the tubing system used to prechill the refill gas should be removed to increase the efficiency of the vacuum. Then, the system should be left under vacuum until a pressure of ~10 mtorr is reached as monitored by the external pressure gauge.

To put a sample into the SVT300 dewar, simply remove the retaining collar and pull the sample rod out. The sample can then be inserted in the sample foot, and the sample rod can be replaced into the instrument. Finally the retaining collar should be re-affixed to the instrument.

To put a sample into the CCR4K systems, pressurize the system with 99.997% He gas. With these systems it is not necessary to prechill the gas. The sample should be inserted into the sample foot, and then the sample rod can be inserted into the instrument. The 4 screws should be tightened and a vacuum should be pulled on the sample space. Pull a vacuum until the gauge on the instrument reaches a minimum value. The system should be refilled with He gas until the gauge reads ~ -25 mmHg. Fill the system to this pressure as the system equilibrates, as adding gas when the instrument is warm will result in a lower pressure upon equilibration.

For all systems, once the sample has been installed, the W202 program should be opened. This program is used to define the windows of radiation which will be counted.

An appropriate voltage should be sent to the detector (typically ~1500-2000V depending on the system). Once the spectrometer stabilizes, a plot of the radiation will display. Two windows are used including one which corresponds to 2KeV of energy and one at 14.4 KeV. The 2KeV peak should be the first peak on the left and the 14.4KeV should be the third peak. Windows should be set on these peaks and then sent to the W202 using the "send windows" button.

At this time the W302 program should be opened. If a sample was in the instrument prior to loading the current sample, the user should ensure the previous data has been saved and renamed according to the file name on the log. Once this has been accomplished the appropriate velocity scale should be selected. If a different scale is chosen than the previous scale the software will prompt you to "wait" and then begin data collection. If the same scale is desired the user will need to choose the "clear data" option and the spectrum will begin to collect. Wait until the temperature of the sample has equilibrated prior to the start of data collection.

Changing the Temperature of the Instrument

All four spectrometers have temperature controllers to allowing the collection of spectra at different temperatures. High-temperature data should be collected using the CCR4K systems as heating the other systems will consume additional He thereby increasing costs. Each CCR4K systems has a different temperature controller and a slightly different procedure. The older system is equipped with the SEE Co. W106 temperature controller. This hardware is capable of heating two channels at once. Identify which channel the sample rod is attached to prior to adjusting the data. Once the

channel has been identified, press the “menu” button; this will begin to toggle through available options. Press the button several times until you see the option for the desired channel set point. Press the “ok” button input the desired temperature and press the “ok” button again. This should take the controller back to the main display. To increase the temperature flip the toggle switch for the appropriate channel to “on.” The temperature should increase to the set point.

The newer CCR4K system is equipped with the LakeShore 325 temperature controller. This system only allows heating on one channel, input A. For this reason make sure that the sample rod is connected to input A and that the cold head is connected to input B. To increase the temperature, press the “set point” button, and then the desired temperature. Press the “enter” button followed by the “heater range” button. There are two heater ranges; the low setting will only be effective for small increases in temperature (up to ~30K) so the high range should be used for heating to e.g. 100 K. Following this the user should see the temperature increase to the set point.

Applying a Magnetic Field on the LHe6T System

The LHe6T system has a LakeShore 625 superconducting magnet power supply for charging the superconducting magnet. To avoid quenching the magnet and losing LHe, it is important to always know the field at the magnet. This value should always be reported in the log file. It is also good practice to be able to identify the field at the magnet using an alternative method such as writing it down and leaving the information near the power supply. Once the user is confident of the field at the magnet, the power supply should be turned on. Once the power supply has reached the main screen, the user

can press the “output setting” button. This will allow the user to type the current field into the power supply. The user should the press the “enter” button if the field is not 0; the value of Output 1 should change to the entered value. Once the power supply is at the same field as the magnet, press the “PSH On” switch. The blue light above this switch will blink for ~10 sec then stay on solid. This will turn the persistent switch heater on. At this time the field at the magnet will match the output field on the power supply. To increase or decrease this value, choose the “output setting” and input the desired field. After pressing “enter” the field will change to the desired setting. Once the desired field has been met, press the “PSH off” switch. The blue light will blink again, then stay off. At this time the power supply can be turned off.

Increasing S/N with an Altered Sample Foot

Sample feet allowing larger sample volumes have been designed for situation where the quantity of sample is not limited. The standard cup holds 1 mL while the larger cups developed here (along with a larger sample foot) hold ~3 mL. Figure A.7 shows the various sample feet used in the instruments. The larger sample cup will absorb more of the γ-rays which will result in a better S/N.

Common Problems Experienced with the LHe Systems

When lines appear broadened, the first thing to check is whether the air pads have deflated. If so, they should be inflated; a manual bicycle type air pump is preferable as this give maximal control. When inflating it will be necessary to level the instrument again and realign. If this does not solve the problem it may be indicative of a more serious problem which would need to be diagnosed individually.

Figure A.7. Different sample feet used on the TAMU instruments.

Another commonly encountered problem is a decrease in counts beyond that associated with the decay of the source. This problem may arise from the accumulation of snow-like material in the dewar which may be absorbing γ-rays. In this case the dewar should be warmed to room temperature and pumped dry; while warm, an increase in the count rate should be observed if this was the problem. Another problem may be increased use of the cryogen. This may be indicate that the dewar's vacuum has gone soft. The system should be warmed to room temperature and a rigorous vacuum should be reestablished.

Common Problems with the CCR4K Systems

The inherent vibrations associated with these systems render them more susceptible to line broadening. These vibrations can cause the instrument to move out of alignment gradually. Another common problem will be an increase in the minimum temperature the system can obtain. At times the refrigerator will fail to turn on. Occasionally there will be a knocking sound produced at the cold head. Each of these problems and potential solutions will be discussed in the following sections.

Line Broadening: Causes and Solutions

Occasionally, the CCR4K system will show linewidth broadening. The linewidths should be checked periodically with the α-Fe Foil. By performing periodic checks not only will it help to identify the problem but it will also serve as a gauge of the integrity of the data collected when line broadening is observed (i.e. the user will know data collected prior to the last linewidth check which produced good results was

reliable.) All diagnosis listed below includes collecting spectra of α-Fe Foil at a velocity scale of 2 mm/sec.

Line broadening is most commonly the result of a component of the instrument mounted to the bottom table of the frame making contact with the vibration producing cold head. Most commonly one will find the magnet mounts in contact with the dewar where it flares out for the cold head. This typically results from the air pads becoming deflated. If this is found to be the case, add air to the pads. On the CCR4K instruments the height should be adjusted such that it is 113 mm from the bottom of the upper table to the center of the junction located immediately below the vacuum gauge (refer to figure A.8). Once this height is correctly adjusted, ensure that no components from the mounting table are in contact with the cryostat. Concurrent with height adjustment the instrument should be leveled and the alignment checked.

If linewidth broadening persists a good strategy is to remove the clasp at the bellows and tape them to the upper table. Collecting a spectrum in this fashion will indicate if contact to the cryostat is being made in a location other than this union. If this produces a spectrum devoid of broadening the user should inspect the cold head position and ensure that it is concentric with the baffles. Reattach the baffles and inspect the instrument from above the upper table. By looking down into the sample space one should see the top of the inner walls of the sample chamber centered in reference to the opening of the sample mount. The dewar should be adjusted if this is not the case. If broaden lines are obtained in the previous step and no contact to the cryostat is visible on the outside of the instrument it is possible there is contact between the sample rod and

the walls of the cryostat on the inside of the instrument. Use great care to ensure both the mounting platform and the cold head are level. If the linewidths are still broadened the sample rod should be inspected for visible damage such as a bend which might cause such contact.

If none of these strategies produces an acceptable linewidth measurement it may be an indication of a more serious problem. Such problems require further diagnosis for a solution.

Increases in the Minimum Obtainable Temperature

Over time the minimum temperature of the CCR4K system will slowly increase. Several problems may result in this condition. The first and simplest problem may be the vacuum in the dewar going soft. To fix this the refrigerator should be turned off and the instrument should be warmed to room temperature. With the instrument warm the vacuum should be re-established. Often the dewar going soft will result in condensation on the outside of the dewar. If this is observed the preceding steps will typically be effective.

If re-establishing the vacuum does not result in lowering of the minimum temperature it may be an indication of contaminating gas in the system. The refrigerator features an absorber to deal with this. The manufacturer (Sumitomo Cryogenics)

Figure A.8. Height of the CCR4K systems. The air pads on the CCR4K systems should be inflated such that the junction indicated by the bottom horizontal red line is 113mm from the bottom of the upper table.

suggests the absorber should be replaced every 15,000 hours of operation. If the system has become contaminated it may also be necessary to purge the system. The manufacturer has provided instructions for such purposes. Finally total equipment failure might be the culprit for increase in temperature. This will typically include damage to the cold head or refrigerator. In such cases the appropriate part will need to be shipped to Sumitomo for repair. For the refrigerator one simply needs remove the He lines and ship the compressor to the manufacturer. If the cold head is damaged the user will need to remove it from the instrument using the procedure outlined below.

The Refrigerator Will Not Turn On

A few issues may result in the refrigerator not turning on. If this problem is experienced the user should first ensure that power is being supplied to the unit and that the circuit breaker on the back of the instrument has not tripped. Another situation which will result in this problem is the absence of chilled water. The user should ensure that the refrigerator is supplied with chilled water. Another cause for the refrigerator to stop working is inadequate pressure of He gas in the system. This can be checked at the gauge on the front of the instrument. Only 99.999 He gas should be added to the system. The pressure of He gas in the system should be ~1.7 mPa when the refrigerator is off and ~2.3 mPa when the system is on. If the compressor still does not turn on it may have become damaged and will likely need to be repaired or replaced.

Knocking at the Cold Head

After several months of continuous operation it is common to hear a knocking noise coming from the cold head. Initially this noise will be intermittent. Changing the

pressure in the sample space by adding or removing He gas will typically alleviate this problem. This is usually an indication that the cold head is beginning to fail. After this noise has begun the cold head will eventually reach a state where the knocking persists. If this is the case it will need to be removed from the instrument and sent to the manufacturer to be repaired or replaced.

Removing the Cold Head from the Instrument

In cases where the cold head needs to be repaired or replaced the following procedure should be used to remove the cold head. Prior to starting this repair the sample rod should be removed and the instrument should be warmed to room temperature. Pull the dewar out from under the mounting platform to remove the cold head. First remove the mounting brackets on the bottom plate of the frame which would otherwise prohibit this process. Next remove the He gas return and supply lines from the back of the unit. Prior to pulling the dewar out, the clasp connecting the dewar to the baffles should be removed. Remove the screws at the top of the upper table and completely remove the baffles to stop them from hanging in the absence of the support of the dewar. The gas line for refilling the sample chamber should be pulled off of the hose barb. The dewar should now be free and can be removed from beneath the mounting platform. At this point the dewar will be mounted on a smaller double-tiered frame.

The CCR4K dewar comes apart into several pieces. The first step in deconstructing the dewar involves removing the outer vacuum shielding. The user should ensure that the vacuum has been released from this space before continuing. To remove the outer shield the wired connection for the temperature sensor should be

removed first. This is a round receptacle on the rear of the instrument near the bottom. The receptacle is attached to the outer shield by 3 screws. The wires should be long enough to pull the receptacle out of the dewar several inches. The receptacle will be connected to the instrument with 6 wires. To maintain the length of the wires, use a soldering iron to remove the wires from the receptacle. Allow the iron to warm up and simply touch the solder pool on the lead of the wire you wish to remove. It is best to do the process systematically, removing one wire at a time and labeling it with masking tape. The wires will be connected to leads A-D, J, and K. Once all the wires have been disconnected, feed the wires back through the hole on the dewar. Make sure that the labels are not lost during this and subsequent steps.

Remove the six screws holding the sample chamber refill manifold that is attached to the thermal shielding located at the top of the dewar (the junction referred to in figure A.8). One screw is located under the vacuum gauge, and it may be necessary to rotate the gauge 90° to access it. Lift the part/piece and free it from the instrument. Remove the 8 screws which mount the shielding to the upper table of the small platform. Lift the vacuum shielding until it is free from the rest of the system.

The thermal shielding should now be visible. This part is wrapped in foil and attached to the cold head on a small circular structure incorporated in the cold head design by 6 screws. A small clamp on top of this shielding should be loosened to allow the thermal shielding to be removed. Then remove the 6 screws and lift the entire shield free from the instrument. These screws attach to the thermal shielding in a bottom up configuration, with threads oriented away from the floor.

After the thermal shield is removed the final part attached to the cold head is the sample chamber. This chamber houses the temperature sensor so it is a good idea to wrap the wires around the chamber and place a small piece of tape on them to keep them out of the way. Six more screws attach the copper portion of the sample chamber to the copper portion of the cold head. Removing these screws allows the sample chamber to be removed. After this step only the cold head mounted on the small frame will remain.

To remove the cold head, first remove the 8 screws which go through the cold head and into the bottom of the upper table of the small frame. Two of these screws are difficult to remove because of the protrusion on the cold head where the He gas lines connect. Removing these will require a modified hex key which has a shortened end. Once these screws are removed, the cold head will be loose on the small frame. To remove the cold head the 4 screws holding the small frame together must be removed. The cold head can then be removed and packed in the box supplied by the manufacturer. All screws and parts should be cataloged and stored until the instrument is reassembled.

Putting the Instrument Back Together

After the cold head has been repaired the instrument must reassembled. The first step is to mount the cold head on the frame. Prior to doing this, clean the surfaces (both the cold head and the top plate of the frame which will make contact) with an ethanol-moistened Chemwipe. The O-ring and corresponding groove on the platform should be greased to ensure a good seal; this part of the system will be under high vacuum. After the cold head has been placed on the small frame, the top table can be carefully lowered over the cold head. The 8 holes on the top side of this table are spaced such that there are

two orientations for the holes. The outer vacuum shield should be inspected to ensure this piece is installed correctly. It is easiest to reattach this table to the platform and then replace the 8 screws which mount the cold head to this surface. It is best to install these and all subsequent screws in an alternating fashion to allow proper seating of the various components.

Once the cold head is mounted the sample chamber can be attached. At this point the tape on the wires of the temperature sensor, used to affix the wires to the sample chamber, should be removed. The wires should be wrapped around the cold head until the ends are approximately located near the hole in the vacuum shield. The wires can be attached to the cold head using dental floss. With the sample chamber back in place, the thermal shield and its retaining clamp should be reinstalled. Next the vacuum shield should be reinstalled. Prior to installing this, the O-ring on the top side of the upper table of the small platform should be greased. As the vacuum shielding is being replaced, pull the wires for the temperature sensor through the hole for the receptacle.

Next the wires should be re-soldered to the receptacle. Typically the solder retained on each lead is adequate for this process. Reattach each wire carefully, making sure it is returned to the proper lead and that the connection to the lead is solid. Once the receptacle has been rewired, apply grease to the O-ring and tighten the three screws. Finally, reinstall the sample chamber refill manifold which couples to the thermal shielding. Identify 4 O-ring grooves and three O-rings on this piece. Each O-ring should be greased and replaced in the proper position. This piece can be lowered down onto the top of the instrument and the final 6 screws tightened.

The dewar should next be moved back into place under the mounting platform. The He gas lines should be attached to the back of the cold head. The cold head should be leveled and aligned and then the baffles can be reinstalled and clamped to the dewar. Following these steps the system can be setup as outlined above.

VITA

Name: Gregory Paul Holmes-Hampton

Address: Department of Chemistry
Texas A&M University
3255 TAMU
College Station, Texas 77843-3255

Email Address: gholmes-hampton@chem.tamu.edu

Education: Ph.D., Chemistry, Texas A&M University, 2012
B.S., Chemistry, Illinois State University, 2007

Selected Publications:

Miao, R., Holmes-Hampton, G. P., and Lindahl, P. A. (2011) Biophysical Investigation of the Iron in Aft1-1(up) and Gal-YAH1 *Saccharomyces cerevisiae*, *Biochemistry 50*, 2660-2671.

Lindahl, P. A., and Holmes-Hampton, G. P. (2011) Biophysical probes of iron metabolism in cells and organelles, *Current Opinion in Chemical Biology 15*, 342-346.

Cockrell, A. L., Holmes-Hampton, G. P., McCormick, S. P., Chakrabarti, M., and Lindahl, P. A. (2011) Mossbauer and EPR Study of Iron in Vacuoles from Fermenting Saccharomyces cerevisiae, *Biochemistry 50*, 10275-10283.

Holmes-Hampton, G. P., Miao, R., Morales, J. G., Guo, Y. S., Münck, E., and Lindahl, P. A. (2010) A Nonheme High-Spin Ferrous Pool in Mitochondria Isolated from Fermenting *Saccharomyces cerevisiae*, *Biochemistry 49*, 4227-4234.

Garber Morales, J., Holmes-Hampton, G. P., Miao, R., Guo, Y., Munck, E., and Lindahl, P. A. (2010) Biophysical characterization of iron in mitochondria isolated from respiring and fermenting yeast, *Biochemistry 49*, 5436-5444.

Lindahl, P. A., Morales, J. G., Miao, R., and Holmes-Hampton, G. (2009) Isolation of Saccharomyces Cerevisiae Mitochondria for Mossbauer, Epr, and Electronic Absorption Spectroscopic Analyses, *Method Enzymol 456*, 267-285.